Ru(II) PNX (X = O,N,S) Complexes in Homogeneous Catalysis for Sustainable Development

Elizabeth Ellison

March 2025

Abstract

Ruthenium pincer complexes have shown substantial promise as homogeneous catalysts in reactions involving hydrogen transfer processes. Designer ligands provide excellent control over electronic and steric environment, allowing tuning of catalysts to control reactivity. Several authors have demonstrated their activity in useful transformations such as small molecule activation, asymmetric hydrogenations, hydrogenative cleavages, dehydrogenative couplings and activation of alcohols. However, reported pincer ligands are frequently difficult to make and highly air intolerant. The design of practical yet effective complexes for such reactions continues to be relevant.

In this work, a series of bis-ligated Ru(II) complexes are prepared using imine-based PNX (X = O, N, S) ligands readily prepared from commercially available starting materials, producing a family of complexes of the structure $[RuCl_2(PNX)_2]$. These complexes contained fixed PN moieties and featured a variable pendant arm to demonstrate variable binding modes and showed hemilability in solution. Ligand structures were modified by pendant arm length, bulk, and donor atom. Several complexes were produced readily in good yields as single products, with single crystal X-ray crystallography confirming ligand binding mode. PNO alcohol ligands predominantly demonstrate a bis-tridentate binding mode. Extension of alcohol chain or substitution at the oxygen donor changes binding mode to bis-tridentate. Use of substituted N or S donors gives mixed binding modes within the same complex.

These complexes are applied in the Guerbet coupling of ethanol with either ethanol or methanol to produce different isomers of butanol. This reaction is of industrial interest for application in biofuel upgrading and operates through a hydrogen borrowing mechanism. The family of $[RuCl_2(PNX)_2]$ are found effective in the production of isobutanol, with the best performing PNS complex [RuCl(**L14**)]Cl yielding 70 % isobutanol at 96 % selectivity. The system shows good tolerance to reduced base loading and use of alternative cheaper base NaOH.

The activity scope of these species is expanded in the hydrogenative cleavage of esters for future application in plastics degradation. The novel species are found active towards hydrogenative cleavage but also catalyse competitive transesterification reactions. The most effective systems feature PNN ligands. Further investigation of complexes demonstrates that the activity of symmetrical PNP, SNS and NNN ligands is dependent on the presence of a Ru-N-H moiety.

Acknowledgements

Contents

Abbreviations

1,4-BDM	1,4-Benzenedimethanol
2-MeTHF	2-Methyltetrahydrofuran
ABE	Acetone-Butanol-Ethanol
AEA	N-Acetylethylenediamine
AKI	Anti-Knock Index
AP+	Atmospheric Pressure Chemical Ionisation
BHT	Butylated hydroxytoluene
BPA	Bisphenol A
BPA-PC	Poly(bisphenol-A carbonate)
CFT	Crystal Field Theory
DAE	N,N'-Diacetylethylenediamine
DCM	Dichloromethane
DFT	Density Functional Theory
DMSO	Dimethyl Sulfoxide
dppm	1,1-Bis(diphenylphosphino)methane
dppp	1,3-Bis(diphenylphosphino)propane
ED	Ethylenediamine
EG	Ethylene glycol
ES+	Electrospray Ionisation
ESI-MS	Electrospray Ionisation Mass Spectrometry
EV	Electric Vehicle
FBA	4-Fluorobenzyl alcohol
FTIR	Fourier-Transform Infrared Spectroscopy

GC	Gas Chromatography
GC-FID	Gas Chromatography Flame Ionisation Detector
GCMS	Gas Chromatography-Mass Spectrometry
HGV	Heavy Goods Vehicle
HRMS	High Resolution Mass Spectrometry
IPCC	Intergovernmental Panel on Climate Change
IR	Infrared Spectroscopy
LDA	Lithium diisopropylamide
LFT	Ligand Field Theory
LRMS	Low Resolution Mass Spectrometry
MAHB	Millennium Alliance for Humanity and the Biosphere
MFB	Methyl 4-fluorobenzoate
MLC	Metal-Ligand Cooperation
MOT	Molecular Orbital Theory
NHC	N-Heterocyclic Carbene
NMR	Nuclear Magnetic Resonance
PET	Polyethylene Terephthalate
PLA	Polylactic acid
Q-TOF	Quadrupole Time of Flight
TFA	Trifluoroacetic acid
THF	Tetrahydrofuran

1 A Brief History of Ruthenium Pincer Complexes in Catalysis

Ruthenium pincer complexes and their use in catalysis is highly relevant to industrial and academic interests. Their development and use guides the work presented in this thesis. In this introduction, focus is given to the history of transition metals in catalysis and the subsequent development of interesting ligand structures, with some brief demonstration of their applications. Fuller introductions to the types of catalysis performed in this work are provided in their relevant results and discussion chapters.

1.1 Transition metal catalysis

The fundamental purpose of a catalyst is to reduce the activation energy required for a chemical transformation. Despite not being recognised or named as such until 1836, catalysts have been used for thousands of years: the enzymes employed in fermentation are a type of biocatalyst[1,2]. In modern times, catalysis is a key cornerstone of industrial chemistry, enabling large scale reactions at reduced energy consumption, increased rate, and higher turnover. An estimated 75 % of current industrial processes use catalysts, increasing to 90 % in new processes[3].

Transition metals, here defined as all elements found in the d-block of the periodic table, are commonly used in catalysts. They typically possess partially filled d-orbitals, allowing them to form variable oxidation states. This flexibility enables them to donate and accept electrons readily, interacting with substrates and activating them towards bond-making and bond-breaking processes that would otherwise be inefficient or unfeasible under conventional conditions.

The use of transition metals in catalysis dates to the 1823 discovery of platinum black as a catalyst for oxidation of hydrogen gas to form water by Johann Wolfgang Döbereiner[4,5], commercialised for use in the Döbereiner lamp. Later major breakthroughs include the Sabatier process for reduction of carbon dioxide over a nickel catalyst to produce methane and water[6,7] (for which Paul Sabatier won the 1912 Nobel Prize[8]), and the early Ziegler-Natta catalysts using titanium and aluminium for polyolefin production, which revolutionised the plastics industry in the 1950s and remains the most popular industrial catalyst for ethylene polymerisation[9,10]. Transition metal catalysed processes are so common that in many reactions they remain the most effective: the Haber-Bosch process uses an iron catalyst to produce ammonia and remains the method of production of almost 175 million tonnes of ammonia annually.

1.1.1 Heterogeneous vs. Homogeneous Catalysts

Most early systems using transition metals focus on heterogeneous catalysis, either metallic transition metals or their oxides. Heterogeneous systems are where the catalyst exists in a different phase, such as a solid interacting with gaseous or liquid reactants. Functionally, a heterogeneous catalyst supplies an infinite surface upon which a chemical reaction may occur by adsorption to a surface. However, frequently these systems are poorly selective and require forcing conditions, including high pressures and temperatures. They are additionally limited by available surface area for reaction[11]. Given the propensity for transition metals to form stable coordination complexes of many different oxidation states, there has been substantial more recent exploration of transition metal complexes as homogeneous catalysts.

Homogeneous catalysis is the branch of catalysis in which the catalyst and reactants exist in the same phase, typically in solution. Homogeneous catalysts operate as single, usually well characterised, molecules, so may also be known as single-site or molecular catalysts. Although a broad range of chemicals, including organic molecules, enzymes, Brønsted and Lewis acids and bases all can behave as homogeneous catalysts, the term is frequently used to specifically refer to transition metal complexes, given this is the area with the largest recent growth[12].

1.2 Transition Metal Complexes

The earliest examples of characterised transition metal complexes are what were previously referred to as "complex salts", metal salts which could not be structurally resolved due to the notion that metals, like carbon, had fixed valency and thus fixed number of available bonds. The two concepts were first proposed to exist separately by Alfred Werner, with the deduction that many metal ions such as Fe(III) and Co(III) were able to form six bonds with coordinating molecules. His coordination theory of primary valency (formal charge) and secondary valency (coordination number) was published in 1893, before the discovery of the electron, and forms the basis for modern coordination chemistry[13–15]. To understand the benefits of transition metal complexes as catalysts, a consideration of this coordination chemistry at play is necessary.

A transition metal complex is a type of coordination complex, where a central atom – the coordination centre – is surrounded by a selection of coordinated inorganic or organic ligands. In a transition metal complex, the coordination centre is a transition metal atom or ion and ligands may be organic or inorganic molecules. Various bonding models exist to describe these interactions and explain geometries and magnetic behaviours. It is possible to consider bonding as either fully ionic, as in crystal field theory (CFT), where ligands are described as point charges, or fully covalent, as in molecular orbital theory (MOT), where bonds are formed through overlap between ligand orbitals and coordination centre orbitals of appropriate symmetry (σ or π). An additional model involves classification of covalent bonds such that ligands are described as one, two or zero electron donors (X, L or Z type ligands, respectively). In this way, a metal centre and coordinating L type ligand may be considered as a Lewis adduct[13] (Figure 1.1). In reality, metal-ligand bonding is somewhere between covalent and ionic in character and ligand field theory (LFT) incorporates aspects of both models to describe bonding with greater detail.
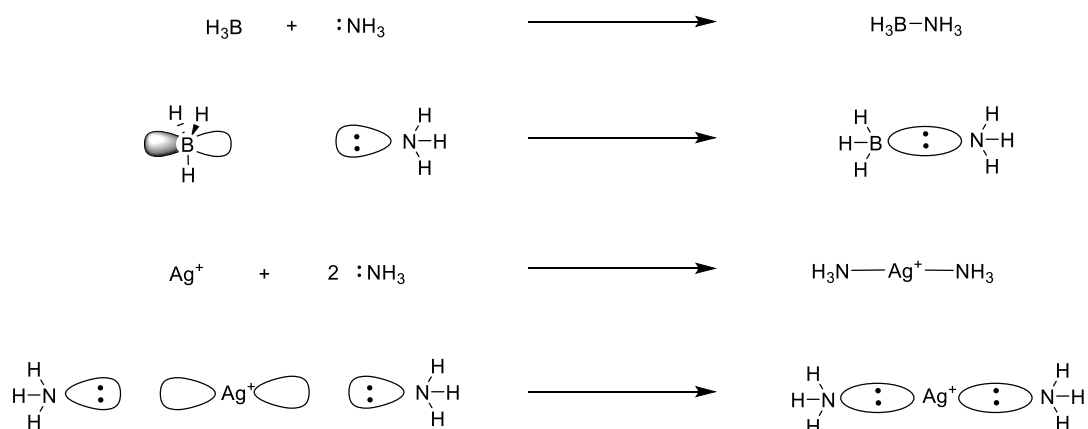
Figure 1.1 – Top: Lewis adduct formation. Bottom: Analogous metal-ligand σ binding in a transition metal coordination complex with an L type ligand. Figure adapted from literature[16].

The application scope of complexes of transition metal ions has exploded. Complexes may be overall neutral or charged. Neutral ligands are most commonly heteroatoms featuring lone pairs (O, N, S, P), and halogen ions are common monoatomic ligands. Ligands may bind to multiple metal atoms as bridging ligands, creating dimeric or trimeric coordination complex clusters. Carbon atoms may also behave as ligands; carbon monoxide is a common monodentate ligand which coordinates through the carbon in a more traditionally covalent type bond, whereas a carbene donates in the traditional lone pair donor style. It is noted that a direct M-C bond is required for a complex to be categorised as organometallic, regardless of if other ligands carry additional carbon atoms[13].

Denticity and hapticity are additional ligand binding considerations. Denticity refers to the number of bonds a single ligand forms with a metal centre. Many common ligands are monodentate (i.e. have one binding site), but thermodynamic stability is gained in a polydentate binding mode where chelate rings are formed. Generally speaking, the most stable chelate ring size is 5-membered, though ring systems from 3-membered to 7-membered are known in the literature. Hapticity is similar but distinct, referring to the number of contiguous atoms which are bound to a metal centre: ferrocene is an exemplar of this, with two η^5 cyclopentadiene ligands (Figure 1.2d). Ideal conformation around a transition metal coordination centre depends on electronic configuration of the d orbitals. Octahedral complexes are most common[17], though many tetrahedral, square planar and even two coordinate linear complexes are also known. A selection of coordination complexes chosen to showcase this wide variance is shown in Figure 1.2, demonstrating both synthetic and naturally occurring examples.
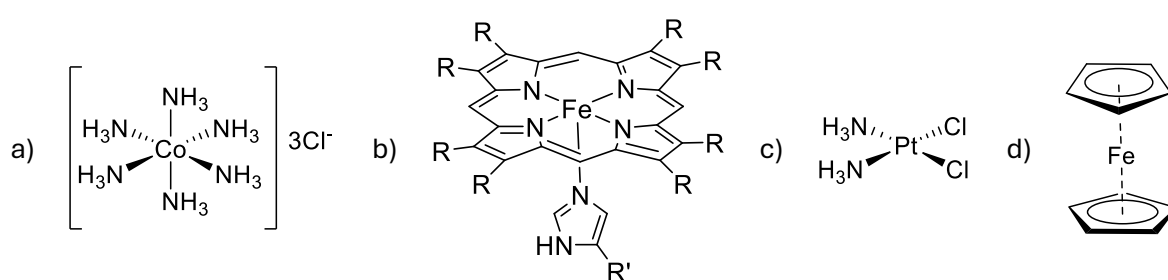
Figure 1.2 - Selection of transition metal coordination complexes. a) Hexaamminecobalt(III) chloride, an archetypal Werner complex. b) Haem, the iron-containing section of hemoglobin. c) Cisplatin, a chemotherapy medication. d) Ferrocene, first known metallocene.

As has been established, the extremely broad scope of existent ligands results in a vast array of different interactions with transition metal centres. Hence, a family of compounds are created with a vast array of different electronic and steric properties, even with the same metal centre. The variation of ligands stabilises or destabilises oxidation states, and modifies access to the

metal by changing steric effects. Such fine control of properties is extremely desirable for creating selective catalysts.

1.2.1   Discrete Transition Metal Complexes in Catalysis

As expected, transition metal complexes are well established as catalysts in many industrial processes, particularly in the production of fine chemicals, pharmaceuticals, and polymers. A selection of chemical products which are produced industrially using homogeneous catalysis are presented in Figure 1.3.
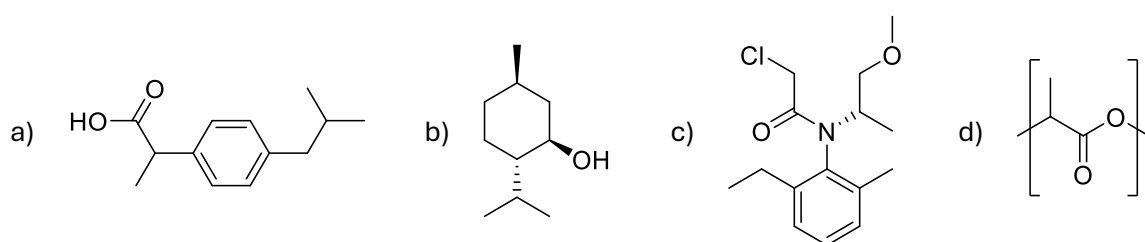
Figure 1.3 - Selected fine chemical products produced using homogeneous catalysis. a) Ibuprofen, an anti-inflammatory drug produced using [PdCl$_2$(PPh$_3$)$_2$] catalyst for a carbonylation step[18]. b) L-menthol, a widely used flavouring which is produced enantiospecifically using a BINAP rhodium homogeneous catalyst[19]. c) (S)-Metolachlor is a herbicide produced using a chiral iridium phosphine-phosphoramidite catalyst. d) Polylactic acid (PLA), a biodegradable polymer frequently produced using tin(II) 2-ethylhexanoate[20].

Not all mechanisms involving transition metal complexes as catalysts are well established. However, the typical process involves an initial coordination of a substrate to a metal centre. This may happen by exchange with an existing ligand which is lost, substitution of a hemilabile portion of a multidentate ligand, or direct coordination with no replacement of existing ligands. This coordination donates electron density to the metal centre, activating bonds towards further reaction. In many instances, a bond may be fully cleaved upon coordination in an oxidative addition type step. An example of this is demonstrated with the use of the well-known Wilkinson's catalyst, known since the 1960s as a catalyst for hydrogenation of alkenes[21]. The reaction mechanism is well understood and presented in Scheme 1.1.

Wilkinson's catalyst is a coordinatively unsaturated Rh(I) complex with the formula [RhCl(PPh$_3$)$_3$] (Figure 1.4a), adopting a distorted square planar geometry. This structure is a pre-catalyst, with initial spontaneous dissociation of a single PPh$_3$ creating the active species **I** in the reaction (Scheme 1.1). H$_2$ then reacts with this species by oxidative addition, to create a formal Rh(III) dihydride species **II**. This is followed by the η^2 coordination of an alkene, then its migratory insertion into the Rh-H bond, and finally the reductive elimination of the resultant alkane to reform the formal Rh(I) active catalyst. Such mechanisms are common and well-established for transition metal complex catalysis.
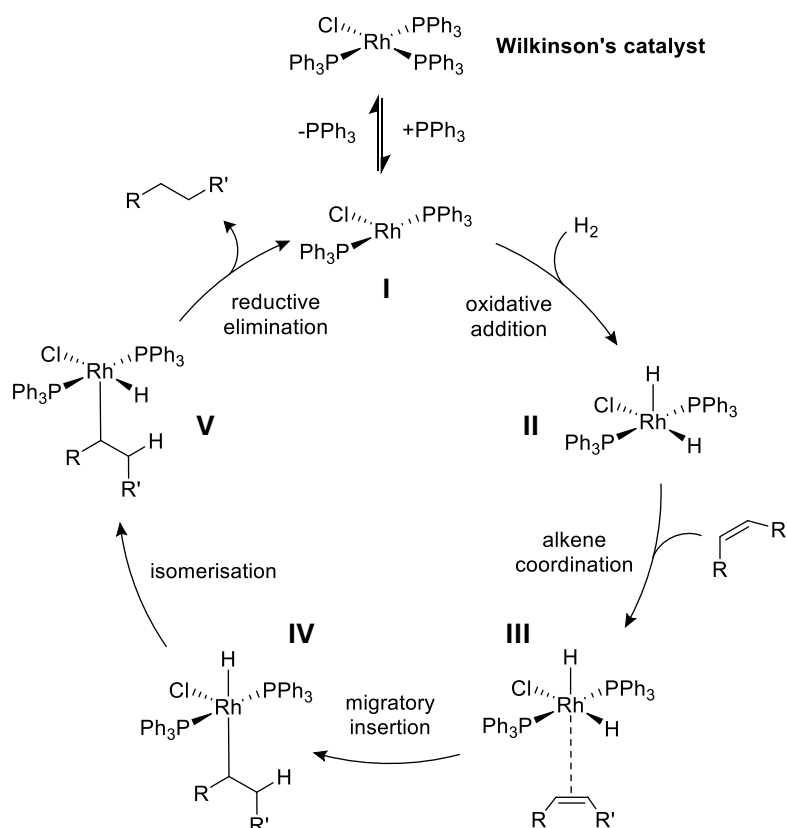
Scheme 1.1 - Reaction mechanism of alkene hydrogenation using Wilkinson's catalyst[21–23].

Several landmark processes rely on homogeneous catalysis. Hydroformylation, the production of aldehydes from alkenes using carbon monoxide and hydrogen gas, originally used the cobalt complex $[HCo(CO)_4]$[24] (Figure 1.4a) and, since its development in the 1960s, now often uses Wilkinson's catalyst[25]. This process plays a crucial role in the production of detergents and other speciality chemicals. The industrial production of acetic acid has also long used homogeneous catalysis: the Monsanto process used a rhodium catalyst (Figure 1.4c) with an iodide co-catalyst for the carbonylation of methanol to acetic acid. This process has been largely replaced by the Cativa process, which uses an iridium catalyst (Figure 1.4d) with an iodide cocatalyst in an analogous mechanism, as the catalyst showed greater stability[26]. Note that in these two processes the anionic complexes shown in Figure 1.4 are the catalytically active species formed *in situ*.
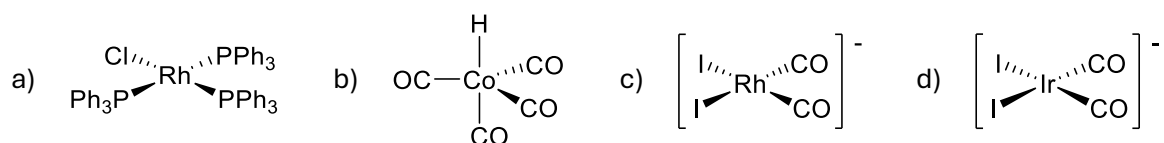
Figure 1.4 - Selected homogeneous catalysts and their industrial applications. a) Wilkinson's catalyst. b) [HCo(CO)₄].
c) [RhI₂(CO)₂]⁻ - Active species of catalyst in Monsanto process. d) [IrI₂(CO)₂]⁻ - Active species of catalyst in Cativa
process.

1.2.2   Pincer Complexes
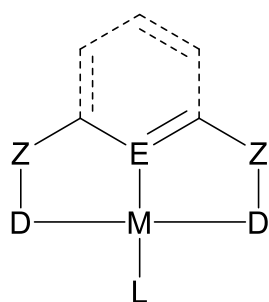
M = transition metal centre

E = central donor atom

D = pendant donor arms

Z = spacer atoms, non-coordinated

L = ancillary ligand

Figure 1.5 - General structure of a transition metal pincer complex.

A notable subcategory of catalytically relevant complexes – and of particular academic interest – are pincer ligand complexes. A pincer ligand is a tridentate ligand which binds to a metal centre by three adjacent sites, creating two chelate rings. Typically, rigid ligand structure enforces meridional geometry, though some flexible linkers permit facial coordination[27,28], but this is less common, and species demonstrating this facial geometry are not always discussed as pincer complexes. The chelate ring sizes vary, but most commonly are five-membered and 6-membered. Pincer ligands may be aliphatic or aromatic and are reported with a wide range of different donor atoms. Ligands are commonly described by the combination of donor atoms, e.g. PNP, NNC or PNS. The general structure of a pincer complex is shown in Figure 1.5.

The earliest identified reports of pincer complexes were in 1971[29], with five-coordinate systems of Fe(II), Ni(II) and Co(II) reported by the Nelson group featuring a pyridine-based ligand system with two phosphine side arms – a ligand structure which has remained extremely popular. Later work by Shaw and coworkers in 1976 demonstrates organometallic pincer complexes with PCP type ligands[30], which informed much of the early pincer complex research[31–33].

M = Ni, Fe, Co
X = Cl, Br, I, NCS, ClO$_4$
Nelson, 1971

M = Ni, Pd, Pt, Rh
X = Cl, Br, I, H, CN, CO
Shaw, 1976
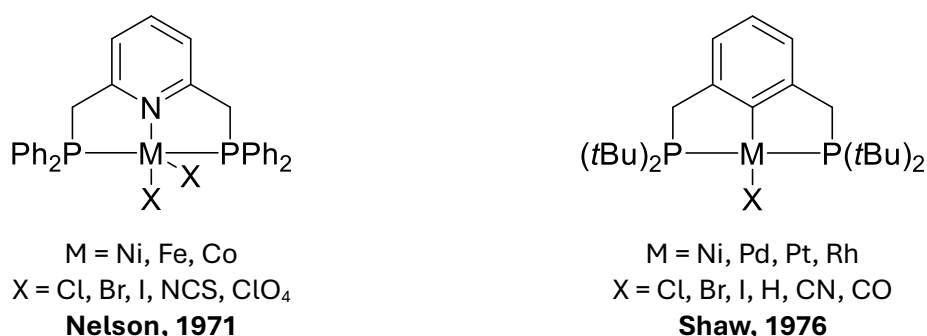
Figure 1.6 - Early examples of transition metal pincer complexes featuring PNP and PCP ligands.

The potential application of pincer ligands for catalysis was noted at the time due to the ability of the ligands to tune the reactivity of the metal centre, without necessarily taking part in reactivity at the metal centre or being dissociated[34]. Different donors provide finely tuneable electronic

variation in the metal centre, whilst the ligand backbone modifies the sterics of the system. The chelation mode allows retention of the ligand system throughout a catalytic cycle. Additionally, pincer complexes have been shown to incorporate the ligand into reaction mechanisms in what is known as metal-ligand cooperativity, with multiple reports demonstrating ligand non-innocence in catalytic pathways.

An additional benefit of pincer ligands is the incorporation of hemilability. A term originally coined in 1979 by Jeffrey and Rauchfuss[35], this refers to the ability of a donor atom to reversibly dissociate from the metal centre to facilitate reactivity, modifying the electronics of the metal centre and the sterics of the coordination sphere[27]. In a pincer ligand, the retention of two binding atoms permits the reversibility of this dissociation, whereas with a mono- or bidentate ligand, the ligand is more likely to be lost to solvation. The degree of hemilability of a donor atom is influenced by the rigidity and length of a donor arm, as well as the type of donor[36]. Several systems have been shown to demonstrate hemilability in catalytic cycles, such as in the NNN-ligated nickel catalysed Sonogashira coupling of alkyl halides with terminal alkynes reported by Hu and coworkers in 2015 (Scheme 1.2)[37].
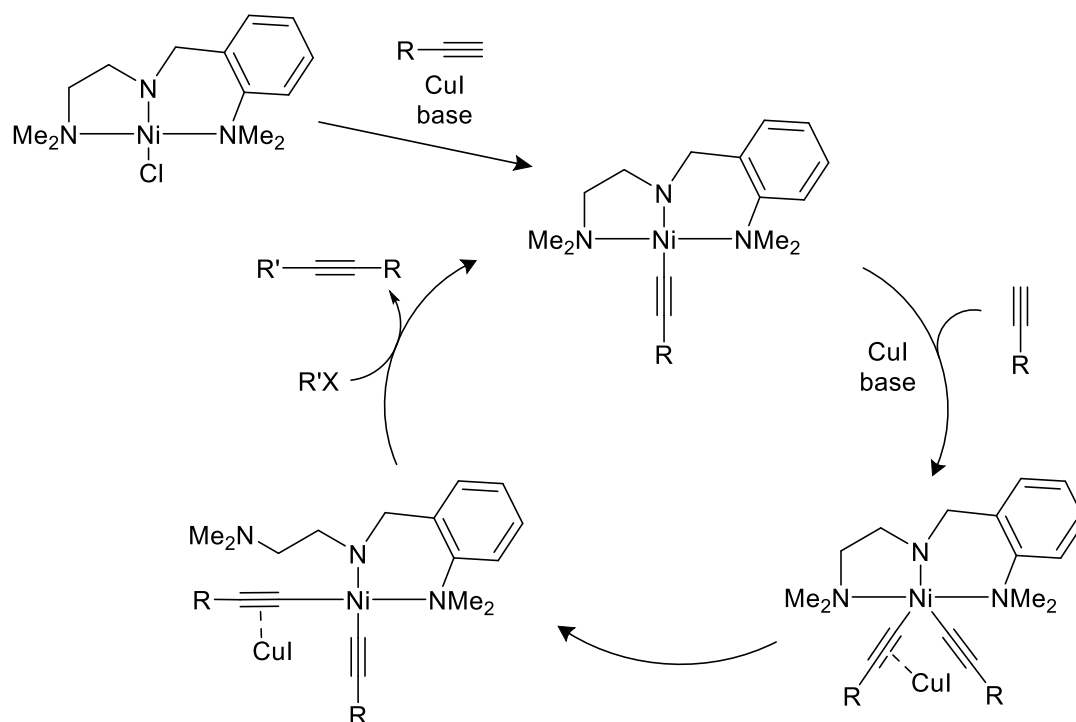
Scheme 1.2 - Simplified mechanism of nickel-catalysed coupling of terminal alkynes with alkyl halides demonstrating hemilability of the NNN pincer ligand.

Since the turn of the century there has been vast expansion of research on pincer complexes[38], with several recent reviews published on catalytic applications which focus on different metal

centres and ligand types[28,38–43]. Some pincer systems are now available and used commercially, with examples presented in Figure 1.7.
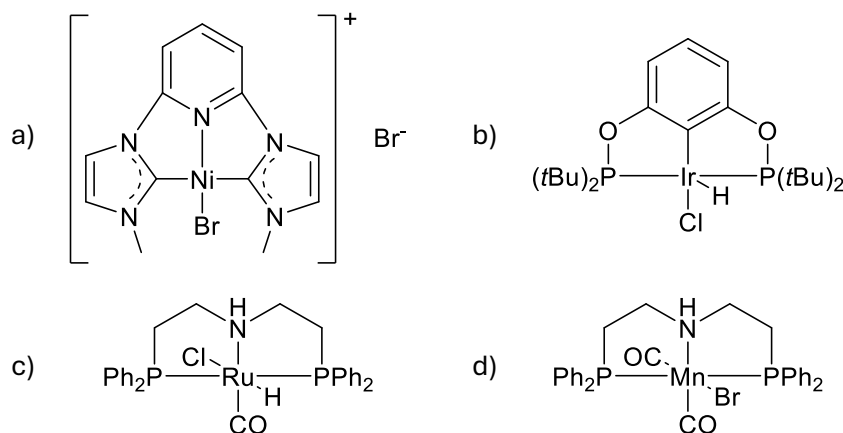
Figure 1.7 – Commercially available pincer complexes used as catalysts.

Figure 1.7a shows a commercially available nickel CNC complex first reported by Inamoto *et al.* which has been used for the formation of C-C bonds in both the Heck reaction and Suzuki coupling[44]. This complex demonstrates the use of N-heterocyclic carbenes (NHCs) as donor species. Figure 1.7b shows an iridium PCP complex reported for C-H activation, initially applied to transfer dehydrogenation of alkanes[45] and subsequently nitrile formation by a similar mechanism[46]. The two catalysts shown in Figure 1.7c and Figure 1.7d respectively both have the same ligand type applied to different metal precursors. Figure 1.7c shows a ruthenium PNP complex known as RuMACHO®, reported by Kuriyama and coworkers[47] for direct hydrogenation of esters to alcohols. This PNP ligand type was applied more recently to manganese by Beller and coworkers (Figure 1.7d). The Beller group has subsequently demonstrated its efficacy in direct hydrogenation[48], dehydrogenation[49] and N-alkylation by a hydrogen borrowing mechanism[50].

1.3   Ruthenium Pincer Complexes

Precious metals take centre stage in homogeneous catalysis, in particular the platinum group[40,51]. It is therefore unsurprising that there in increasing study in the use of abundant earth metals in transition metal catalysis; cheap and readily accessible materials are obviously convenient. Interest in the first row metals such as cobalt[52], nickel[53] and iron[54] is increasing, with recent reviews of these metals and their pincer complexes in catalysis. However, ruthenium complexes continue to provide some of the best cost efficiency[38]. Ruthenium is relatively low cost, compared to popular homogeneous catalysis based on palladium, rhodium and iridium, and is also relatively non-toxic[55]. It has many accessible oxidation states but both Ru(II) and Ru(III) are stable with different ligand systems[56,57]. Ruthenium has also shown to be highly effective in catalysis, in particular hydrogenations, C-H bond activation and olefin metathesis[58,59]. Almost all commercially available transition metal complex catalysts for asymmetric hydrogenation are ruthenium catalysts.

The field of ruthenium pincer complexes in catalysis is thus very broad, with a number of excellent reviews on their synthesis and catalytic application in recent years[38,60–63]. A non-exhaustive selection of the types of complexes and the catalysis performed by such species is presented below, with the intention of demonstrating the range of systems available and their potential utility. In the following selection, a key theme of metal-ligand cooperative catalysis mechanisms is noted, where – particularly in hydrogen borrowing type systems – the metal and ligand are proposed to work in tandem to activate substrates.

1.3.1   PCP complexes

Some of the earliest examples of pincer systems were the aromatic organometallic PCP complexes featuring a stable M-C σ bond[30]. Later applied to ruthenium by van Koten and coworkers, these new Ru(II) complexes were demonstrated to be effective for reduction by transfer hydrogenation of ketones to alcohols[64]. Increases in turnover were observed with substitution of the chloride ancillary ligand, though both systems were vastly more efficient than the similarly tested NCN analogue. Later work from the same group demonstrated an impact of substitution on phosphine R groups, with increased activity with strongly electron-withdrawing substituent p-CF$_3$[65].

X = Cl
X = OSO₂CF₂
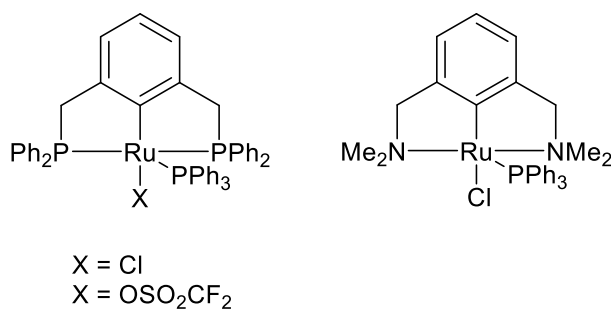
van Koten, 2000

Figure 1.8 - Left: Ruthenium PCP complexes demonstrated as effective hydrogen transfer catalysts. Right: Analogous ruthenium NCN complex also tested.

Backbone structural modifications have been made to such systems, such as the introduction of non-binding heteroatoms by Bedford and coworkers[66], though the only identified reports of catalytic activity for this ligand include an ancillary norbornadiene ligand, with reports from the Huang group in 2016 of both silylation of heteroarenes[67] and unusual acceptor-less alkane dehydrogenation[68].

R = Ph, iPr
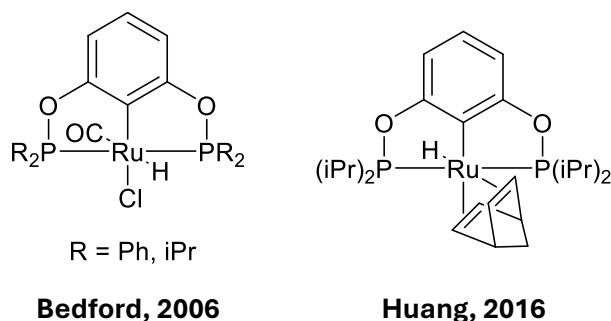
Bedford, 2006   **Huang, 2016**

Figure 1.9 - Ruthenium PCP complexes.

1.3.2   PNP complexes

As established, PNP ligated complexes are the earliest examples of pincer complexes known so have substantial catalytic research and development, including when applied to ruthenium. A robust summary of these species was reported by Milstein and coworkers in 2014 with significant discussion of their catalytic activities[61].

Many ruthenium PNP complexes have been prepared: the commercially available example RuMACHO® has already been noted in Section 1.2.2 (Figure 1.7c), first reported in 2012 by Takasago chemists and also available as the borane adduct RuMACHO-BH. However, aromatic backbones are particularly popular in this series, with three such examples presented in Figure 1.10.
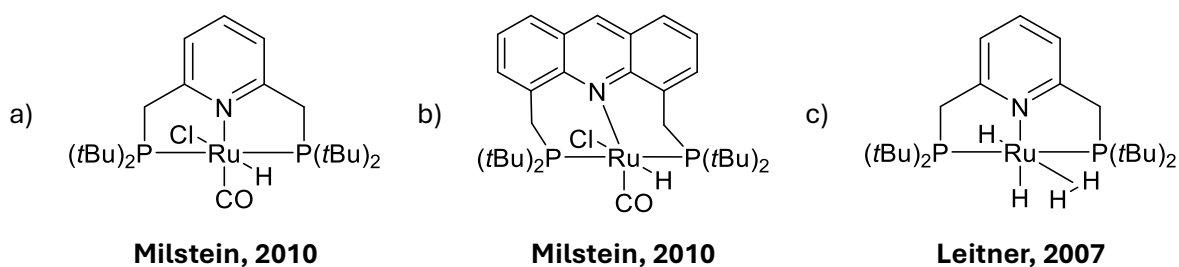
Figure 1.10 - Aromatic PNP ruthenium complexes.

The complex presented in Figure 1.10a is also commercially available and reported as active for a range of reactions. Milstein and coworkers reported the direct synthesis of azines by dehydrogenative coupling of alcohols with hydrazine[69]. It may be pre-activated with a base to give the isolatable dearomatized complex **II** shown inScheme 1.3.
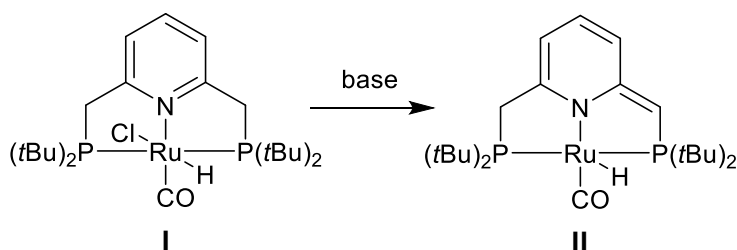
Scheme 1.3 - Treatment of Milstein PNP complex with base to produce the catalytically active species, featuring a dearomatised backbone.

This base-treated species (Scheme 1.3 **II**) is active for the direct hydrogenation of nitriles to primary amines under neutral conditions; the extended aromatic PNP complex (Figure 1.10b) required catalytic base[70]. Later DFT studies by Pidko and coworkers supported a mechanism involving metal-ligand cooperativity in direct hydrogenation of CO_2 (Scheme 1.4), wherein initial heterolytic cleavage of H_2 across ruthenium centre and activated ligand was the rate determining step. Interestingly, they noted a deactivating pathway of similar coordination of CO_2, which could be disfavoured by increasing H_2 concentrations[71]. The coordination mode of CO_2 is analogous to stable coordination of aldehydes previously reported by Milstein and coworkers[72].
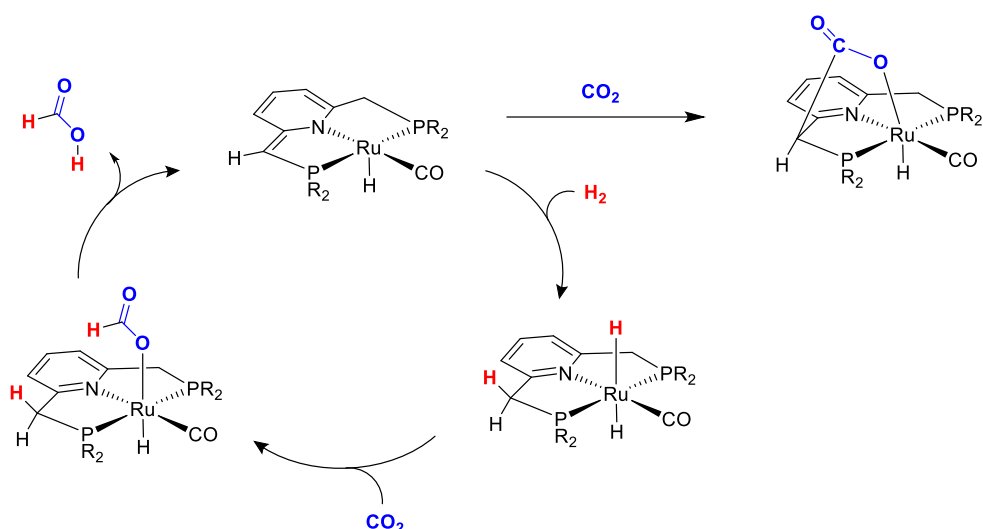
Scheme 1.4 – Metal-ligand cooperativity in simplified catalytic cycle of reduction of CO_2 to formic acid including deactivating coordination of CO_2. R = tBu.

The similar ruthenium PNP complex presented in Figure 1.10c is an example of the impact of alternative ancillary ligands: Leitner and coworkers reported an aromatic PNP complex with an unusual nonclassical hydride H_2 ligand for successful hydroboration of terminal alkynes[73]. Interestingly, when this complex was applied to direct reduction of nitriles, water as an additive was found to increase selectivity and rate[74].
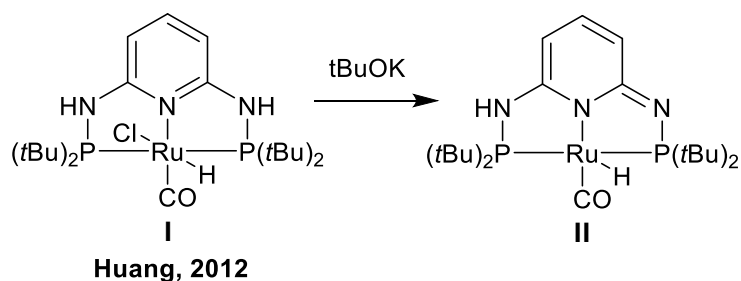
Scheme 1.5 - Activation with base of ruthenium PN^{3}P complex.

PNP complexes featuring nitrogen linker atoms are also known, and similarly reported to be isolable as dearomatized active species, as demonstrated in Scheme 1.5. The PN^{3}P complex (Scheme 1.5 **I**) first reported by Huang and coworkers in 2012[75] has a planar ligand backbone and demonstrated activity for the reduction of ketones using 2-propanol as hydrogen source when used with base.

13

1.3.3 SNS and NNN complexes

a) Gusev, 2013   b) Messerle, 2010
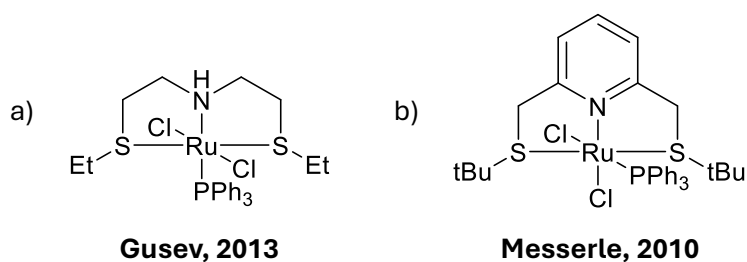
Figure 1.11 - Ruthenium SNS complexes.

Phosphine free ligands have been investigated in ruthenium catalysis for their air tolerance. Sulfur especially is explored as a direct alternative to phosphorus due to its large soft donor character. In 2013, Gusev and coworkers reported an SNS type complex analogous to RuMACHO® (Figure 1.11a) which was also found to be highly effective for the direct hydrogenation of multiple substrates. Cleavage of esters, reduction of imines, ketones and alkenes were all reported, with reactivity reducing when ancillary ligand PPh$_3$ was substituted with AsPh$_3$ or CO[76]. Interestingly, the active species was proposed to be a dihydride species featuring a facially coordinated SNS ligand, with coordination mode confirmed by single crystal X-ray crystallography. Conversely, the complexes of the aromatic equivalents (Figure 1.11b), first reported by Messerle and coworkers in 2010 as effective transfer hydrogenation catalysts[77], were later reported by Waser and coworkers to be entirely ineffective direct hydrogenation catalysts under identical conditions[78]. This difference in behaviour was also noted in a recent report by Chirdon *et al.* comparing analogous aromatic and aliphatic SNS and PNP pincer complexes of the form [RuCl$_2$CO(XNX)] (X = S, P)[79]. They found that the sulfur species were generally less electron rich than their phosphorus counterparts, and exhibited more structural variation due to variability in the position of sulfur, with a tendency towards *cis* halide arrangement over the *trans* arrangement seen in PNP species. Therefore, more careful consideration of ligand design was considered necessary for property replication.

a) Periana, 2010   b) Hong, 2010
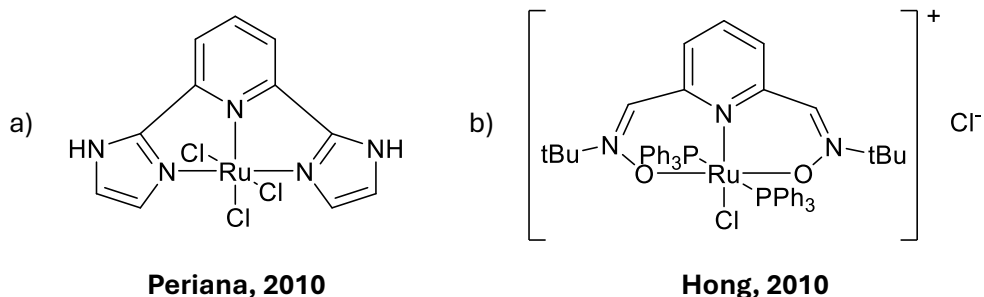
Figure 1.12 - NNN and ONO ruthenium complexes.

Nitrogen-based ligands are typically less stable than phosphine or sulfur ligands in ruthenium complexes due to the steric hindrance of short C-N bonds; cone angles for such ligands are large and on a hindered complex such species are unstable. However, the stabilising effect of a pincer system has allowed preparation of NNN systems, such as the species presented in Figure 1.12a. This NNN complex was demonstrated to be active for C-H activation by performing H/D exchange, which occurred faster in basic solvents[80].

A further example of phosphine free catalysis is reported by Hong in 2010 (Figure 1.12b). The observed ONO is an unusual zwitterionic nitrone ligand which was advantageously formed in a single step synthesis. The resultant complex was active for the transfer hydrogenation of ketones[81].

The use of phosphine-free ligands continues to grow, especially with increased interest in NHC and sulfur-containing ligands. However, due to their stability, modifiable R substituents, and repeatedly demonstrated activity in catalysis, the phosphine binding group remains of substantial interest in ruthenium catalysis.

1.3.4   Asymmetrical PN pincer complexes

Thus far all species discussed have featured symmetrical pincer ligands. A perhaps more catalytically interesting subset of complexes are complexes of asymmetrical PN-containing ligands due to the increased electronic and steric diversity of this class of complexes – and therefore, increased tunability of a system[42]. These are particularly of interest due to the designed incorporation of a hemilabile donor arm. Milstein and coworkers have undertaken substantial work in this area, and to date have reported several complexes in the family of asymmetrical PNN and PNS ligands.

a) **Milstein, 2005**   b) **Clarke, 2007**   c) **Huang, 2012**
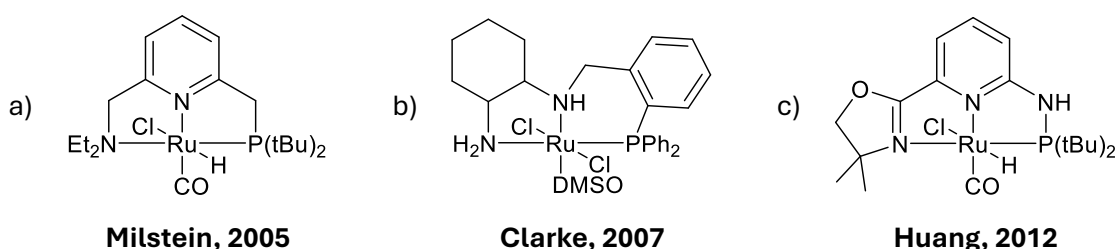
Figure 1.13 - Ruthenium PNN and PNNN complexes.

The Milstein PNN system (Figure 1.13a) was the first known pincer of this PNN category, and was an early example of complexes found to be effective for hydrogenative cleavage of esters with hydrogen gas[82]. Later work also demonstrated excellent efficacy in direct hydrogenative cleavage for amides and polymers[83,84]. In 2007, Clarke and coworkers also reported a series of aliphatic

PNN (and some PNO) complexes effective in hydrogenative ester cleavage[85]. Later work demonstrated the Clarke catalysts' efficacy for hydrogenative breakdown of polyesters[86].

Several investigations into the mechanism of Milstein's PNN systems have been performed [70,87,88], with a consensus demonstrating a de-aromatized active species, either preformed as an isolatable species or produced *in situ* using a strong alkoxide base, as shown with PNP ligands in Scheme 1.5 – though it is noted in asymmetric species this deprotonation occurs on the phosphine arm selectively. Activity is frequently reported as improved in PNN systems compared with symmetrical systems. A direct comparison of behaviour between hydrido borohydride species featuring either the PNN or PNP ligands showed that the PNN species had higher activity in dehydrogenation and hydrogenation reactions[89], which has been attributed to the hemilability of the amine arm[43] (Scheme 1.6).
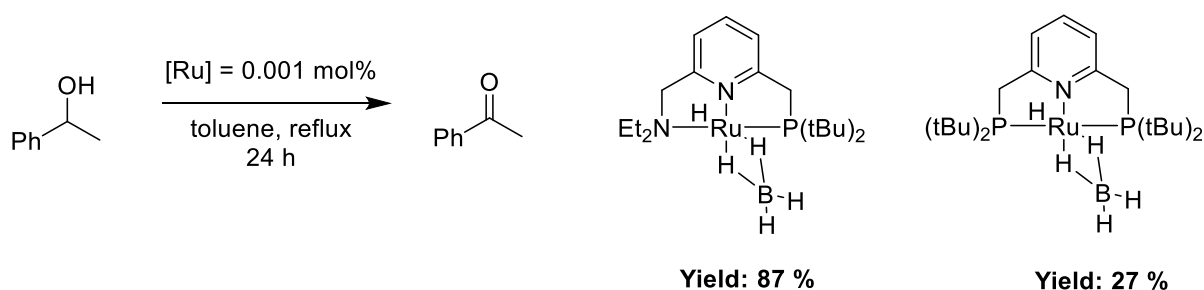
Scheme 1.6 - Direct comparison between PNN and PNP ligands in dehydrogenation of secondary alcohols[89].

The class of PNN complexes may also be expanded to consider PNNN species (Figure 1.13c). Huang and coworkers in 2012 reported a novel PNNN pincer complex[75] which demonstrated enhanced reactivity towards dehydrogenative alcohol coupling to esters relative to the symmetrical PN^{3}P complex, and similar excellent reactivity towards the dehydrogenative homocoupling of amines to form imines[90]. Activity towards amine coupling was significantly greater than the also studied Milstein PNN pincer complex. It is noted that catalysts were pre-activated by de-aromatisation with base to give the pseudo imine containing pincers and proposed to operate *via* a hydrogen-borrowing metal-ligand cooperative (MLC) mechanism.
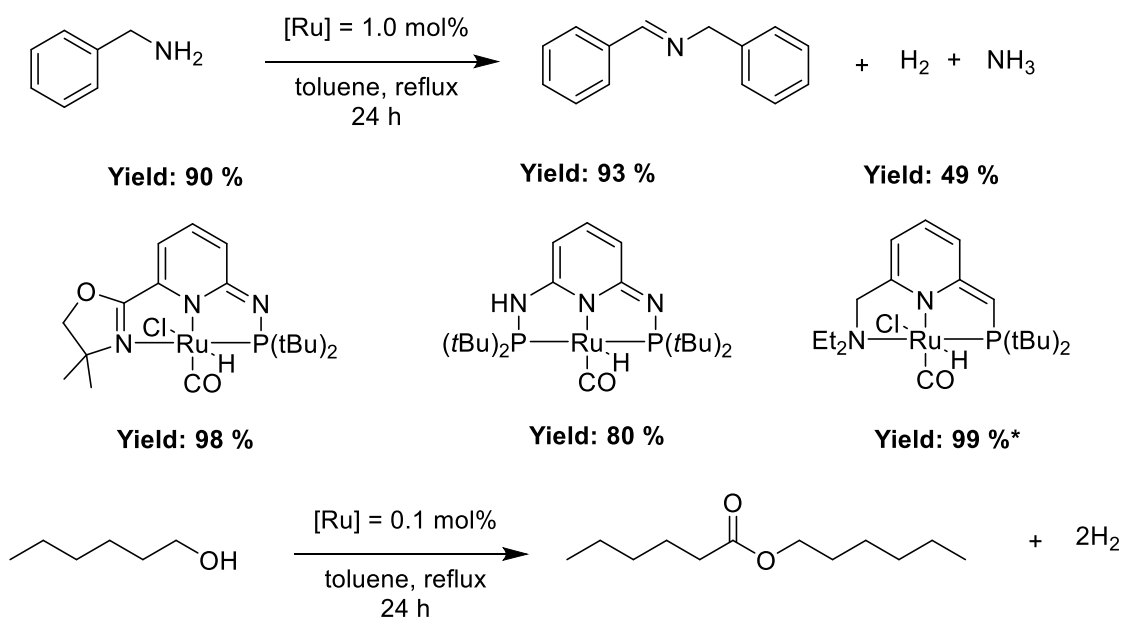
Scheme 1.7 - *Comparison of base-free dehydrogenative reactions of pre-activated PNN complexes[90]. *6h*

More recent developments by Milstein in asymmetric PN complexes include a novel PNS system also based around a pyridine ring. The hemilability of the PNS asymmetric system was noted as inducing selectivity towards amides in the coupling of alcohols and amines[91]; the PNN complex Figure 1.13a also selectively produced amides, but the symmetrical PNP system produced imines under the same conditions[92].
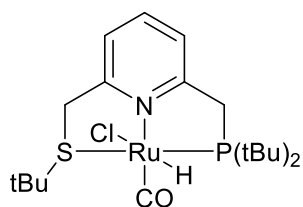
Milstein, 2012

Figure 1.14 - Ruthenium PNS complex.

1.4   Limitations of Ruthenium Pincer Complexes

It is important to mention that the classic challenges of homogeneous catalysis – primarily related to recovery and separation – apply to ruthenium pincer complexes as well. In industrial application, heterogeneous catalysts have the advantage of being easily removed by filtration, whereas homogeneous catalysts require additional steps for separation, increasing process complexity and costs. However, interesting work on heterogenization of homogeneous ligands has been reported, including the polymer-mounting of the MACHO ligand[93] and the similar supporting of the pyridine-backbone PNP complex shown in Figure 1.10a[94], both of which have been shown to retain catalytic activity. Recent work from the Wass group has focused on incorporation of pincer ligands into metal-organic frameworks[95].

Another major consideration is the cost of preparation. The majority of transition metal complexes may be formed by simple direct metalation of ligands. However, ligands themselves are frequently energy and time intensive to produce, with long-winded syntheses increasing to a cost greater than the metal constituent.

A final key factor which has only briefly been considered in this overview is the impact of co-ligands on reactivity. Given that pincer ligands are maximally tridentate, the ancillary ligands of a complex system account for 50 % of the coordination sphere in a classic octahedral ruthenium species. However, limited work in the literature is available on the specific impacts of these co-ligands, and more research is necessary.

1.5 Conclusions

The range in structure and utility of ruthenium pincer complexes for catalysis has been shown to be very broad, with recent interest focusing on designed-in functionality, including hemilability. Although there is focus in the literature on more abundant metal systems, the high activity of ruthenium systems demonstrates its continued relevance in catalysis, particularly towards small molecule activation and in hydrogen transfer mechanisms.

Metal-ligand cooperativity is commonly found in pincer complex mechanisms, so careful consideration of the structure of ligands allows production of catalysts with increased or diversified activities. Milstein's work, in particular has clearly demonstrated the functional utility of an asymmetrical ligand system, but these systems frequently require multistep, air sensitive chemical syntheses. Hence, further research into catalytically active and synthetically facile targets is of continued academic and industrial relevance.

1.6 Project Aims

The work in this thesis aims to expand upon the existing literature by developing novel ruthenium pincer complexes featuring ligands which are relatively simple to prepare and handle, yet display useful catalytic activity in direct and transfer hydrogenation reactions. Targeted species will feature asymmetric structures with a phosphorus-nitrogen component inspired by the highly catalytically active PN based species already discussed in section 1.3.4, with readily modifiable donor arms for tunability. Ligands will be applied to Ru(II) precursors and characterised. Target properties of particular interest are complexes which are easily soluble and stable in solution, as well as in the presence of alkoxide base, due to the prevalence of these conditions in homogeneous catalysis.

The catalytic activity of novel compounds in C-H and H_2 activation will be explored. In order to do this, the Guerbet reaction for alcohol coupling and direct hydrogenative cleavage of esters and amides will be investigated. Both of these reactions are known to proceed through transfer of hydrogen atoms to and from ruthenium-based homogeneous catalysts, and have sustainable applications, so are interesting useful reactions to investigate catalytic activity towards hydrogen transfer chemistry using multiple hydrogen sources. In these studies, novel species will be compared for activity against current state-of-the-art systems, with investigation into catalyst activation and kinetic behaviour discussed.

1.7 References

1   J. Wisniak, *Educación Química*, 2010, **21**, 60–69.

2   J. A. Moulijn, P. W. N. M. van Leeuwen and R. A. van Santen, in *Studies in Surface Science and Catalysis*, Elsevier, 1993, vol. 79, pp. 3–21.

3   S. Bhaduri and D. Mukesh, in *Homogeneous Catalysis: Mechanisms and Industrial Applications*, John Wiley & Sons, Ltd, 2nd edn., 2014, pp. 1–21.

4   G. B. Kauffman, *Platin Met Rev*, 1999, **43**, 122–128.

5   Döbereiner, *Ann Phys*, 1823, **74**, 269–273.

6   P. Sabatier and J.-B. Senderens, *C R Hebd Seances Acad Sci*, 1902, 514–516.

7   P. Sabatier and J.-B. Senderens, *C R Hebd Seances Acad Sci*, 1902, 689–691.

8   The Nobel Prize in Chemistry 1912, https://www.nobelprize.org/prizes/chemistry/1912/summary/, (accessed 13 March 2025).

9   K. Ziegler, E. Holzkamp, H. Breil and H. Martin, *Angewandte Chemie*, 1955, **67**, 541–547.

10   L. L. Böhm, *Angewandte Chemie International Edition*, 2003, **42**, 5010–5030.

11   D. J. Cole-Hamilton and R. P. Tooze, 2006, 1–8.

12   J. A. Moulijn, P. W. N. M. van Leeuwen and R. A. van Santen, in *Studies in Surface Science and Catalysis*, eds. J. A. Moulijn, P. W. N. M. van Leeuwen and R. A. van Santen, Elsevier, 1993, vol. 79, pp. 199–248.

13   T. Tanase, in *Coordination Chemistry: Molecular Science of Organic–Inorganic Complexes*, Royal Society of Chemistry, 2024, pp. 1–12.

14   V. Bhatt, in *Essentials of Coordination Chemistry*, Academic Press, 2016, pp. 1–35.

15   H. M. Smith, *Torchbearers of Chemistry*, 1949, 253.

16   G. A. Lawrance, *Introduction to Coordination Chemistry*, Wiley, Chichester, 1st edn., 2010.

17   J. E. House and K. A. House, in *Descriptive Inorganic Chemistry*, Academic Press, 2nd edn., 2010, pp. 441–478.

18   United States Patent and Trad0mark Office, US4981995A, 1990.

19   European Patent Organization, EP1153908, 2001.

20   G. Schwach, J. Coudane, R. Engel and M. Vert, *J Polym Sci A Polym Chem*, 1997, **35**, 3431–3440.

21   J. F. Young, J. A. Osborn, F. H. Jardine and G. Wilkinson, *Chemical Communications (London)*, 1965, **295**, 131–132.

22   J. A. Osborn, F. H. Jardine, J. F. Young and G. Wilkinson, *Journal of the Chemical Society A: Inorganic, Physical, Theoretical* , 1966, **I**, 1711–1732.

23   N. Koga, C. Daniel, J. Han, X. Y. Fu and K. Morokuma, *J Am Chem Soc*, 1987, **109**, 3455–3456.

24   B. Cornils, W. A. Herrmann and M. Rasch, *Angewandte Chemie International Edition in English*, 1994, **33**, 2144–2163.

25   D. Evans, J. A. Osborn and G. Wilkinson, *Journal of the Chemical Society A: Inorganic, Physical, Theoretical* , 1968, 3133–3142.

26   G. J. Sunley and D. J. Watson, *Catal Today*, 2000, **58**, 293–307.

27   E. Peris and R. H. Crabtree, *Chem Soc Rev*, 2018, **47**, 1959–1968.

28   M. A. W. Lawrence, K. A. Green, P. N. Nelson and S. C. Lorraine, *Polyhedron*, 2018, **143**, 11–27.

29   W. V Dahlhoff, S. M. Nelson, S. J. Kelly and G. H. Ford, *Journal of the Chemical Society A: Inorganic, Physical, Theoretical* , 1971, 2184–2190.

30   J. C. S. Dalton, C. J. Moulton, B. L. Shaw, H. D. Empsall, E. M. Hyde and B. L. Shaw, *Journal of the Chemical Society, Dalton Transactions*, 1976, 1020–1024.

31   C. S. Creaser and W. C. Kaska, *Inorganica Chim Acta*, 1978, **30**, L325–L326.

32   G. van Koten, J. T. B. H. Jastrzebski, J. G. Noltes, A. L. Spek and J. C. Schoone, *J Organomet Chem*, 1978, **148**, 233–245.

33   G. Van Kotex, K. Timmer, J. G. Noltes and A. L. Spek, *J Chem Soc Chem Commun*, 1978, 250–252.

34   G. van Koten, *Pure and Applied Chemistry*, 1989, **61**, 1681–1694.

35   J. C. Jeffrey and T. B. Rauchfuss, *Inorg Chem*, 1979, **18**, 2658–2666.

36 R. Lindner, B. Van Den Bosch, M. Lutz, J. N. H. Reek and J. I. Van Der Vlugt, *Organometallics*, 2011, **30**, 499–510.

37 P. M. Pérez García, P. Ren, R. Scopelliti and X. Hu, *ACS Catal*, 2015, **5**, 1164–1171.

38 H. A. Younus, N. Ahmad, W. Su and F. Verpoort, *Coord Chem Rev*, 2014, **276**, 112–152.

39 H. Li, T. P. Gonçalves, D. Lupp and K. W. Huang, *ACS Catal*, 2019, **9**, 1619–1629.

40 N. Selander and K. J. Szabó, *Chem Rev*, 2011, **111**, 2048–2076.

41 K. K. Manar, J. Cheng, Y. Yang, X. Yang and P. Ren, *ChemCatChem*, 2023, **15**, e202300004.

42 M. Asay and D. Morales-Morales, *Dalton Transactions*, 2015, **44**, 17432–17447.

43 H. Valdés, M. A. García-Eleno, D. Canseco-Gonzalez and D. Morales-Morales, *ChemCatChem*, 2018, **10**, 3136–3172.

44 K. Inamoto, J.-I. Kuroda, K. Hiroya, Y. Noda, M. Watanabe and T. Sakamoto, DOI:10.1021/OM060043.

45 I. Göttker-Schnetmann, P. White and M. Brookhart, *J Am Chem Soc*, 2004, **126**, 1804–1811.

46 W. H. Bernskoetter and M. Brookhart, *Organometallics*, 2008, **27**, 2036–2045.

47 W. Kuriyama, T. Matsumoto, O. Ogata, Y. Ino, K. Aoki, S. Tanaka, K. Ishida, T. Kobayashi, N. Sayo and T. Saito, *Org Process Res Dev*, 2012, **16**, 166–171.

48 S. Elangovan, C. Topf, S. Fischer, H. Jiao, A. Spannenberg, W. Baumann, R. Ludwig, K. Junge and M. Beller, *J Am Chem Soc*, 2016, **138**, 8809–8814.

49 M. Andérez-Fernández, L. K. Vogt, S. Fischer, W. Zhou, H. Jiao, M. Garbe, S. Elangovan, K. Junge, H. Junge, R. Ludwig and M. Beller, *Angewandte Chemie International Edition*, 2017, **56**, 559–562.

50 S. Elangovan, J. Neumann, J. B. Sortais, K. Junge, C. Darcel and M. Beller, *Nature Communications 2016 7:1*, 2016, **7**, 1–8.

51 M. Albrecht and G. van Koten, *Angewandte Chemie International Edition*, 2001, **40**, 3750–3781.

52 K. Junge, V. Papa and M. Beller, *Chemistry – A European Journal*, 2019, **25**, 122–143.

53 S. Z. Tasker, E. A. Standley and T. F. Jamison, *Nature 2014 509:7500*, 2014, **509**, 299–309.

54   H. Nagashima, *Bull Chem Soc Jpn*, 2017, **90**, 761–775.

55   M. J. Clarke, *Coord Chem Rev*, 2002, **232**, 69–93.

56   A. Jabłońska-Wawrzycka, P. Rogala, S. Michałkiewicz, M. Hodorowicz and B. Barszcz, *Dalton Transactions*, 2013, **42**, 6092–6101.

57   A. K. Sahu, D. K. Dash, K. Mishra, S. P. Mishra, R. Yadav, P. Kashyap, A. K. Sahu, D. K. Dash, K. Mishra, S. P. Mishra, R. Yadav and P. Kashyap, *Noble and Precious Metals - Properties, Nanoscale Effects and Applications*, DOI:10.5772/INTECHOPEN.76393.

58   K. Grela, *Wiley Blackwell 6*, 2014, **9781118207949**, 1–592.

59   S. Kundu, M. Layek, S. M. Rahaman, P. Karmakar and B. Saha, in *Homogeneous Hydrogenation and Metathesis Reactions*, Elsevier, 2025, vol. 5, pp. 3–27.

60   J. Hafeez, M. Bilal, N. Rasool, U. Hafeez, S. Adnan Ali Shah, S. Imran and Z. Amiruddin Zakaria, *Arabian Journal of Chemistry*, 2022, **15**, 104165.

61   C. Gunanathan and D. Milstein, *Chem Rev*, 2014, **114**, 12024–12087.

62   H. A. Younus, W. Su, N. Ahmad, S. Chen and F. Verpoort, *Adv Synth Catal*, 2015, **357**, 283–330.

63   T. Liu, L. Wang, K. Wu, Q. Wang and Z. Yu, *Inorganica Chim Acta*, 2023, **551**, 121458.

64   P. Dani, T. Karlen, R. A. Gossage, S. Gladiali and G. van Koten, *Angewandte Chemie International Edition*, 2000, **39**, 743–745.

65   M. Gagliardo, P. A. Chase, S. Brouwer, G. P. M. Van Klink and G. Van Koten, *Organometallics*, 2007, **26**, 2219–2227.

66   R. B. Bedford, M. Betham, M. E. Blake, S. J. Coles, S. M. Draper, M. B. Hursthouse and P. N. Scully, *Inorganica Chim Acta*, 2006, **359**, 1870–1878.

67   H. Fang, L. Guo, Y. Zhang, W. Yao and Z. Huang, *Org Lett*, 2016, **18**, 5624–5627.

68   Y. Zhang, H. Fang, W. Yao, X. Leng and Z. Huang, *Organometallics*, 2016, **35**, 181–188.

69   J. O. Bauer, G. Leitus, Y. Ben-David and D. Milstein, *ACS Catal*, 2016, **6**, 8415–8419.

70   A. Mukherjee, D. Srimani, Y. Ben-David and D. Milstein, *ChemCatChem*, 2017, **9**, 559–563.

71   G. A. Filonenko, E. J. M. Hensen and E. A. Pidko, *Catal Sci Technol*, 2014, **4**, 3474–3485.

72   M. Montag, J. Zhang and D. Milstein, *J Am Chem Soc*, 2012, **134**, 10325–10328.

73   C. Gunanathan, M. Hölscher, F. Pan and W. Leitner, *J Am Chem Soc*, 2012, **134**, 14349–14352.

74   C. Gunanathan, M. Hölscher and W. Leitner, *Eur J Inorg Chem*, 2011, **2011**, 3381–3386.

75   L. P. He, T. Chen, D. X. Xue, M. Eddaoudi and K. W. Huang, *J Organomet Chem*, 2012, **700**, 202–206.

76   D. Spasyuk, S. Smith, D. G. Gusev, D. Spasyuk, S. Smith and D. G. Gusev, *Angewandte Chemie International Edition*, 2013, **52**, 2538–2542.

77   M. J. Page, J. Wagler and B. A. Messerle, *Organometallics*, 2010, **29**, 3790–3798.

78   J. Schörgenhumer, A. Zimmermann and M. Waser, *Org Process Res Dev*, 2018, **22**, 862–870.

79   D. N. Chirdon, S. P. Kelley, N. Hazari and W. H. Bernskoetter, *Organometallics*, 2021, **40**, 4066–4076.

80   B. G. Hashiguchi, K. J. H. Young, M. Yousufuddin, W. A. Goddard and R. A. Periana, *J Am Chem Soc*, 2010, **132**, 12542–12545.

81   Y. Zhang, X. Li and S. H. Hong, *Adv Synth Catal*, 2010, **352**, 1779–1783.

82   J. Zhang, G. Leitus, Y. Ben-David and D. Milstein, *Angewandte Chemie International Edition*, 2006, **45**, 1113–1115.

83   E. Balaraman, B. Gnanaprakasam, L. J. W. Shimon and D. Milstein, *J Am Chem Soc*, 2010, **132**, 16756–16758.

84   A. Kumar, N. Von Wolff, M. Rauch, Y. Q. Zou, G. Shmul, Y. Ben-David, G. Leitus, L. Avram and D. Milstein, *J Am Chem Soc*, 2020, **142**, 14267–14275.

85   M. L. Clarke, M. B. Díaz-Valenzuela and A. M. Z. Slawin, *Organometallics*, 2007, **26**, 16–19.

86   J. A. Fuentes, S. M. Smith, M. T. Scharbert, I. Carpenter, D. B. Cordes, A. M. Z. Slawin and M. L. Clarke, *Chemistry – A European Journal*, 2015, **21**, 10851–10860.

87   D. G. Gusev, *Organometallics*, 2020, **39**, 258–270.

88   S. Kar, M. Rauch, A. Kumar, G. Leitus, Y. Ben-David and D. Milstein, *ACS Catal*, 2020, **10**, 5511–5515.

89   J. Zhang, E. Balaraman, G. Leitus and D. Milstein, *Organometallics*, 2011, **30**, 5716–5724.

90   L. P. He, T. Chen, D. Gong, Z. Lai and K. W. Huang, *Organometallics*, 2012, **31**, 5208–5211.

91   M. Gargir, Y. Ben-David, G. Leitus, Y. Diskin-Posner, L. J. W. Shimon and D. Milstein, *Organometallics*, 2012, **31**, 6207–6214.

92   B. Gnanaprakasam, J. Zhang and D. Milstein, *Angewandte Chemie International Edition*, 2010, **49**, 1468–1471.

93   S. Padmanaban, G. H. Gunasekar and S. Yoon, *Inorg Chem*, 2021, **60**, 6881–6888.

94   R. Konrath, A. Spannenberg and P. C. J. Kamer, *Chemistry – A European Journal*, 2019, **25**, 15341–15350.

95   H. Jepson, PhD Thesis, Cardiff University, 2023.

2 Design, synthesis and characterisation of mixed donor Ru(II) complexes

2.1 Design of PNX (X = O,N,S) ligands for hydrogen transfer catalysis

The potential structural and electronic variation available in a pincer complex featuring asymmetrical pincer ligands has already been demonstrated as highly valuable in catalyst design[1]. In the application of hydrogen transfer type catalysis, especially Noyori asymmetric hydrogenations, the ability of a ligand to participate in a catalytic cycle in tandem with the metal centre is well-established far beyond just ruthenium-centred systems[2,3]. Hence, the potential means of involvement of a ligand must be considered in the design of novel complexes for application in similar mechanisms.

Meridional coordination   Facial coordination
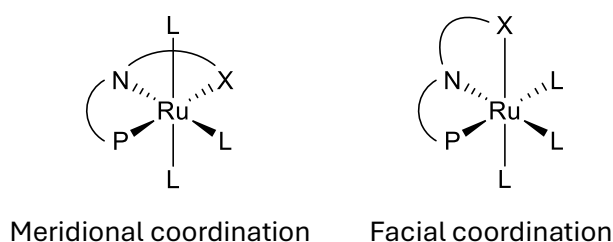
Figure 2.1 - Potential binding modes of novel PNX ligand system when coordinated to Ru(II) centre.

This work focuses on the application of novel ligands to Ru(II) centres, and initial ligand targets were assumed to adopt an octahedral binding geometry with standard tridentate pincer coordination and employment of three monodentate ancillary ligands (Figure 2.1). Typically meridional coordination would be anticipated, though facial is also possible. The high activity for various hydrogenations and dehydrogenations of asymmetric ligands containing PN moieties has already been discussed (section 1.3.4), so this binding mode is selected for further exploration. Additionally, this bidentate segment has been shown to support a hemilabile tertiary donor arm in PNN and PNS systems by Milstein and coworkers[4,5], considered to facilitate reactivity through access to the metal centre, so such tertiary arm donors are desirable to investigate further. The investigation of PNO type ligands is less common in recent work, but inclusion of an oxygen donor as a potential hemilabile donor is considered relevant due to established hemilabile behaviour in some of the earliest examples of ligand hemilability[6]. The harder oxygen donor would be expected to demonstrate poorer binding to ruthenium than nitrogen or sulfur due to poorer orbital

overlap with the large soft ruthenium centre, so initial focus on PNO species was selected for investigation of an anticipated highly labile species.

Ligand structure was selected to minimise reliance on multi-step air-intolerant processes and products. Though phosphines are reactive with oxygen, the use of bulky substituents tempers this reactivity. Tertiary aromatic substituents in particular are frequently air stable solids and readily commercially available, so were appropriate targets for use in tolerant and reusable catalytic systems.
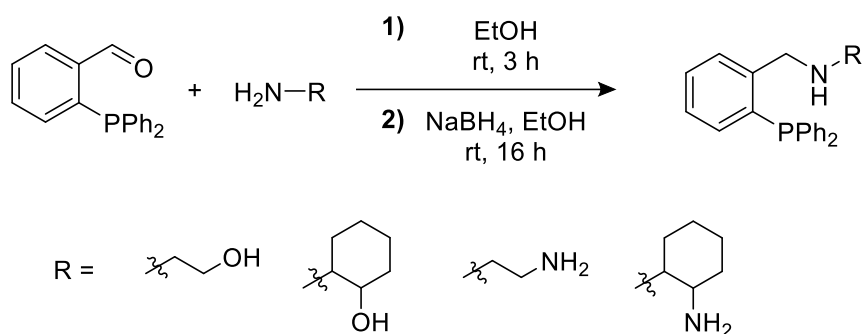
Scheme 2.1 - Preparation of Clarke family of PNO and PNN ligands[7,8].

The previously reported ligands prepared by Clarke and coworkers[7,8] are notable as straightforward synthetic targets, prepared in the literature by aldehyde and amine coupling to form an imine, followed by reduction under mild conditions using $NaBH_4$ (Scheme 2.1). However, the direct application of Schiff bases as ligands in catalytically active ruthenium complexes has also been long reported[9,10], with some recent work demonstrating increased activity of a complex with the introduction of an imine moiety to the ligand backbone[11]. Hence, structures similar to Clarke's work, but without reduction, were selected as initial targets in this work.

X = O, N, S
R = H, Me
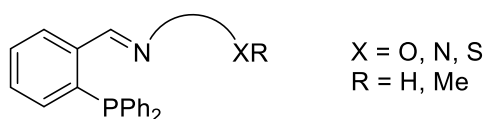
Figure 2.2 - General structure of asymmetric mixed-donor ligands selected to study in this work.

2.2 PNO ligands for novel Ru(II) complexes

2.2.1 Preparation of PNO ligands

A series of imine-based, potentially tridentate, PNO ligands featuring alcohol terminal groups were prepared by a simple condensation reaction between 2-(diphenylphosphino)benzaldehyde and various primary amino alcohols (Scheme 2.2) performed under N_2 atmosphere with basic Schlenk line techniques using modified literature conditions[8].
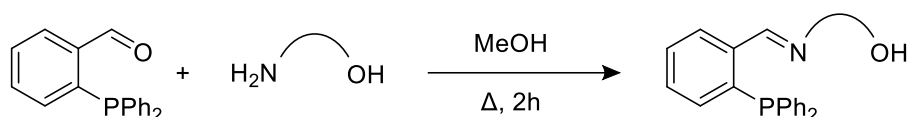
Scheme 2.2 - General synthetic route for imine-based alcoholic PNO ligands.

The choice of solvent was not found to influence reaction rate when heated to 60 °C, so methanol was primarily used due to ease of removal and efficacy as a recrystallisation solvent. Generally, products were not sensitive to the presence of water in reaction mixtures, so no additional *in situ* drying agent was required to drive reaction. It was noted that use of liquid amino alcohols stored in air frequently resulted in partial oxidation of the phosphine, so starting materials were degassed by freeze-pump-thaw prior to use. Due to low cost and relatively low boiling point, amines were used in slight excess to ensure complete reaction. Removal of solvent and any excess starting materials under high vacuum was sufficient to purify in most cases to give yields of >95 %, though recrystallisation from cold methanol was found useful if large excess of amine had been used.

A series of mixed donor PNO target ligands (summarised in Figure 2.3) were selected to vary the binding behaviour of the alcohol donor through a modification of steric bulk, chain length and rigidity. The previously reported **L1**[12] and **L3**[13] alcohol ligands were expanded upon with the novel **L2, L4** and **L5**. Additionally, inclusion of the previously reported **L6**, formed from 2-(methoxy)ethylamine allowed the further comparison of alcohol and ether behaviour as ligand components.

The isolated ligands were characterised using a range of spectroscopic and analytical techniques, primarily the use of ^1H and $^{31}P\{^1H\}$ NMR spectroscopy and IR spectroscopy. Novel ligands were additionally characterised with mass confirmation by HRMS.

L1 — 83 % — δ: -10.7 ppm

L2 — 87 % — δ: -10.9 ppm

L3 — 88 % — δ: -10.0 ppm

L4 — 96 % — δ: -13.7 ppm

L5 — 99 % — δ: -14.3 ppm

L6 — 98 % — δ: -13.8 ppm
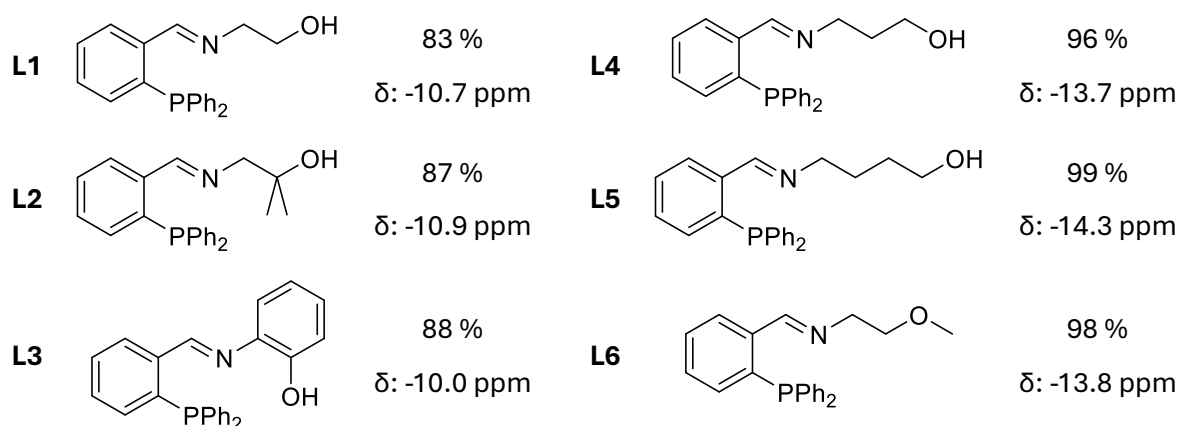
Figure 2.3 - Summary of PNO ligands prepared in this work. Synthetic yield and $^{31}P\{^{1}H\}$ NMR chemical shift shown.

2.2.2   Complexation of PNO ligands with Ruthenium(II)

2.2.2.1   Preparation and analysis of Ru(II) complexes of **L1**

Due to the well-established use of PNX (X = P,N,O,S) ligands in ruthenium(II) complexes, ligands **L1**-**L6** were expected to coordinate readily with common ruthenium precursors in stoichiometric fashion. Indeed, when reacted in a 1:1 molar equivalence to the common precursor [RuCl$_2$(PPh$_3$)$_3$] in toluene, **L1** successfully gave the previously reported[12] [RuCl$_2$(**L1**)PPh$_3$] in good yield as a red-brown solid isolated by induced precipitation with diethyl ether as counter solvent.
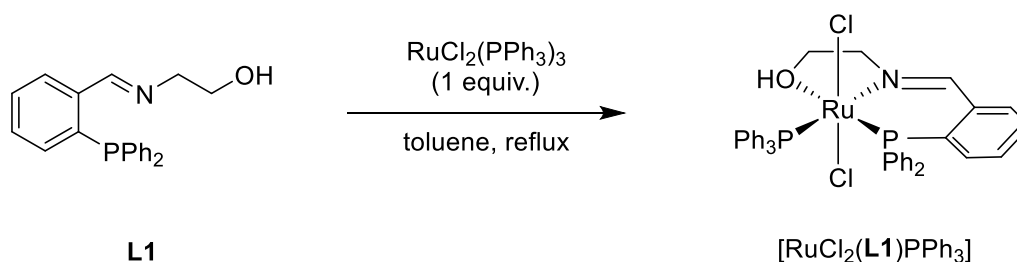
*Scheme 2.3 - Preparation of the complex [RuCl₂(**L1**)PPh₃]*

Examination of the $^{31}P\{^{1}H\}$ NMR data for [RuCl$_2$(**L1**)PPh$_3$] showed the expected pair of doublets (δ: +66.5, +34.5 ppm) indicative of bound **L1** and ancillary PPh$_3$ (Figure 2.5). Comparison with free ligand **L1** (δ: -10.7 ppm) demonstrates a substantial downfield shift caused by the deshielding effects of strong σ donation, with the **L1** phosphorus occupying the *trans* position to oxygen giving the more positive chemical shift.

However, use of superstoichiometric ligand resulted in an additional minor singlet in the downfield complex region of the spectrum (δ: +61.3 ppm), suggesting a second complex formed,

proposed to be a symmetrical bis-ligated impurity. Examination of the literature identified previously reported bis-ligated PNO complexes using similar Schiff base ligands reported by Kwong and coworkers[14] and Parr and coworkers[13], supporting this notion. Both complexes were reported in 1999, with each group showing a substituted aliphatic alcoholic ligand coordinating twice in a meridional coordination mode (Figure 2.4). The only other example identified in the literature of species of this structure was reported by Dilworth and coworkers in 2007, employing the ligand **L3**, among other aromatic PNO and PNS ligands, to give an unstable complex which isomerised in solution (discussed further in section 2.2.3.1).

a) **Kwong, 1999** b) **Parr, 1999** c) **Dilworth, 2007**
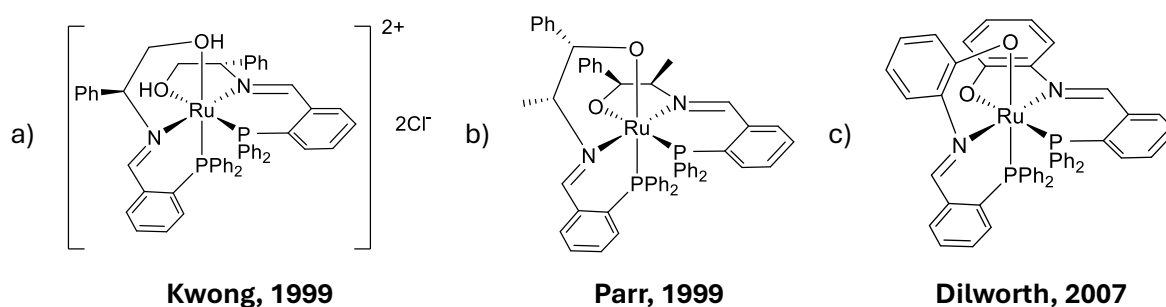
Figure 2.4 - Previously reported bis-ligated Ru(II) PNO complexes.

An attempt to prepare the bis-ligated **L1** complex directly from excess **L1** and alternative ruthenium precursor [RuCl$_2$(p-cymene)]$_2$ was successful, and [Ru(**L1**)$_2$]Cl$_2$ was isolated as a precipitate from toluene as a yellow solid (Scheme 2.4). HRMS confirmed [Ru(**L1**)$_2$]Cl$_2$ as a bisligated species featuring at least one chloride ((ES+/Q-TOF) m/z: [M-Cl]$^+$ Calcd for C$_{42}$H$_{40}$N$_2$O$_2$P$_2$ClRu 803.1297; Found 803.1311), suggesting a protonated complex featuring outer sphere chlorides like Kwong's complex (Figure 2.4) is what has been formed in this work.
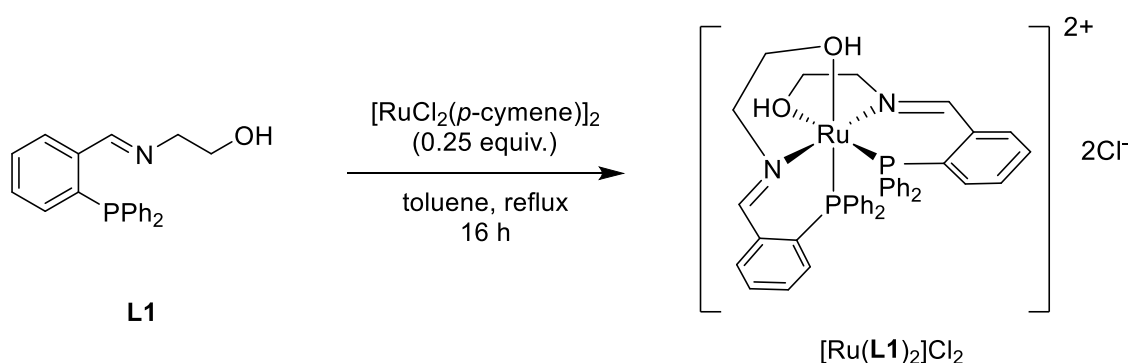
*Scheme 2.4 - Preparation of the novel complex [Ru(**L1**)$_2$]Cl$_2$*

^{31}P{^{1}H} NMR spectrum taken in CDCl$_3$ of [Ru(**L1**)$_2$]Cl$_2$ shows a singlet at δ: +61.3 ppm indicative of a symmetrical species, which confirms the identity of the impurity in [RuCl$_2$(**L1**)PPh$_3$] preparation as the bisligated species [Ru(**L1**)$_2$]Cl$_2$. A comparison of these spectra is shown in Figure 2.5.
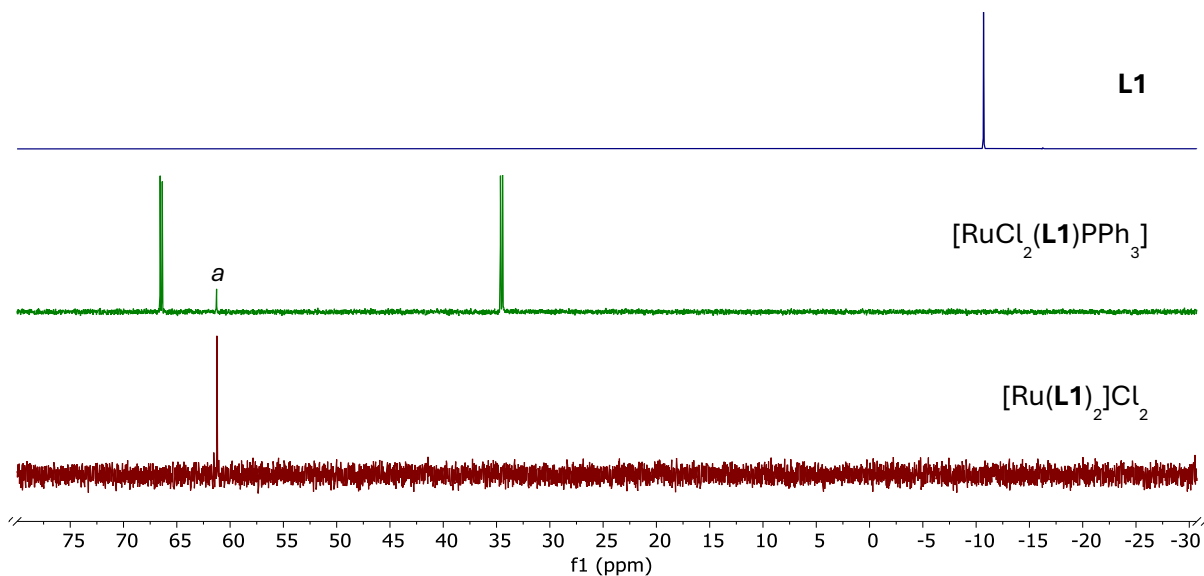
*Figure 2.5 - $^{31}P\{^1H\}$ NMR spectra recorded in CDCl$_3$ of **L1** (top), [RuCl$_2$(**L1**)PPh$_3$] (middle), [Ru(**L1**)$_2$]Cl$_2$ (bottom).*

*[a] Visible impurity of bis-ligated species [Ru(**L1**)$_2$]Cl$_2$.*

*Table 2.1 - Comparison of key analytical data between free **L1** and complexes of **L1**.*

	L1	[RuCl$_2$(**L1**)PPh$_3$]	[Ru(**L1**)$_2$]Cl$_2$
$^{31}P\{^1H\}$ δ / ppm	-10.7	+66.5, +34.5	+61.3
^1H δ *HC*=N / ppm	8.74	8.89	9.28
v(C=N) / cm^{-1}	1634	1631	1618

The coordinated imine results in a downfield shift in the ^1H NMR signal of the C-H imine proton, summarised in Table 2.1. Comparison of the imine proton in the ^1H NMR spectra between the two complexes shows increased deshielding effects of coordination of the imine nitrogen in [Ru(**L1**)$_2$]Cl$_2$ vs [RuCl$_2$(**L1**)PPh$_3$], suggesting greater σ donation from the imine in the bis-ligated complex. An increase in imine bond length upon coordination is expected due to this observed reduction in electron density, with larger increase in bond length in [Ru(**L1**)$_2$]Cl$_2$. FTIR supports this observation, showing a greater reduction in C=N stretching frequency in [Ru(**L1**)$_2$]Cl$_2$ when compared to free ligand, indicating larger increase in bond length in the bis-ligated species.

Evidence of tridentate ligand behaviour in [Ru(**L1**)$_2$]Cl$_2$ is seen in the aliphatic region of ^1H NMR, where four separate slightly broadened signals are observed in CDCl$_3$ (δ: 4.28, 4.12, 3.43 and 3.31 ppm). Given the single phosphorus environment, it is determined that the ligands are bound symmetrically, so four separate aliphatic environments must be observed on a single ligand. These are therefore attributed to the inequivalent proton environments introduced by the

metallacycle structure formed by both nitrogen and oxygen binding to the ruthenium centre. The existence of this chemical inequivalence in solution indicates stable oxygen-ruthenium binding in non-coordinating solvent.

The FTIR spectrum of [RuCl$_2$(**L1**)PPh$_3$] also shows an O-H stretching frequency at approximately 3329 cm^{-1}, though this proton could not be observed in ^{1}H NMR spectroscopy, possibly due to signal overlap in the aromatic region. This represents a shorter O-H bond than observed in free **L1** which shows this stretch at 3254 cm^{-1}, as is expected due to σ donation from coordinated oxygen. However, no such signal was seen in the O-H region of [Ru(**L1**)$_2$]Cl$_2$, suggesting spontaneous deprotonation of the alcohol upon coordination and ligand behaviour as a tridentate alkoxide. This is concordant with the spontaneous deprotonation upon coordination reported by Parr and coworkers[13]. However, the presence of both protons and chlorine in high resolution mass spectrometry also seen by Kwong and coworkers[14] shows that HCl does not exist in complete dissociation from the central ruthenium species. Indeed it could not be removed from the product by recrystallisation, which is indicative of a charged species – in this instance, only possible if the oxygens are not deprotonated.

2.2.2.2 Reaction of [Ru(**L1**)$_2$]Cl$_2$ with DMSO-d6
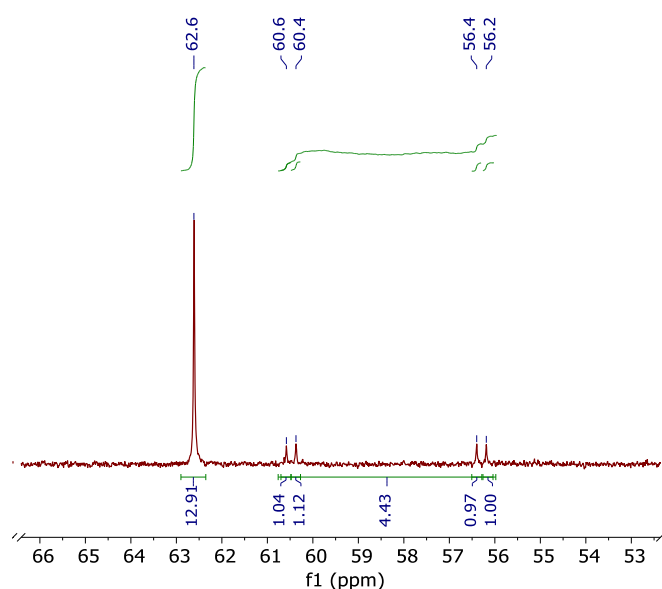
*Figure 2.6 - ^{31}P{^{1}H} NMR of [Ru(**L1**)$_2$]Cl$_2$ in DMSO-d6*

Due to only moderate solubility in CDCl$_3$, ^{13}C NMR of [Ru(**L1**)$_2$]Cl$_2$ was sought using DMSO-d6 as NMR solvent. When the ^{31}P{^{1}H} spectrum was analysed in DMSO-d6, a new pair of doublets indicating an asymmetric species appeared in minor quantity. Accordingly, two new singlets appeared in the ^{1}H spectrum at +9.29 ppm and +8.55 ppm with relative intensity matching the

33

new species and suggesting only one proton each. These were attributed to two new imine environments. It is also noted that the major imine signal of the original species showed a slight solvent upfield shift to +9.67 ppm, with the appearance of an OH signal at 9.06 ppm, suggesting retention of alcohol protons upon coordination, despite the absence of O-H stretching observed in FTIR analysis. Due to DMSO's ability to coordinate as a ligand, particularly with soft metal centres such as Ru(II), it is presumed that DMSO acts to displace a hemilabile coordination site, giving rise to a mixture. This evidence of hemilability was not demonstrated in previous work, and is gratifying as hemilability in an otherwise coordinatively saturated species is likely necessary for catalytic activity.
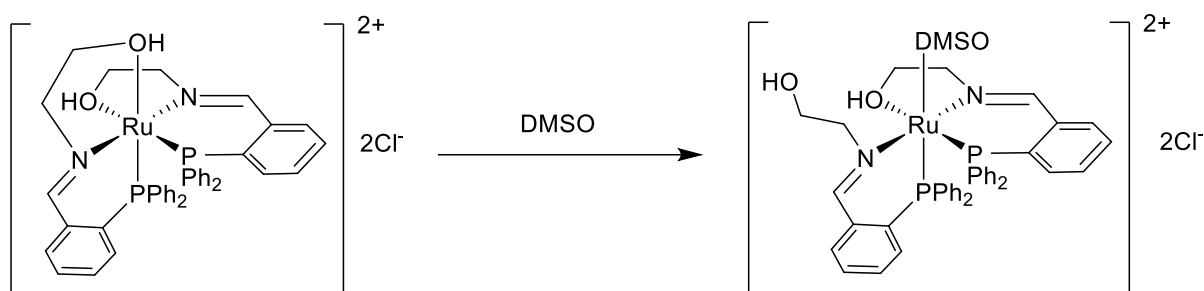
*Scheme 2.5 - Proposed production of [Ru(**L1**)$_2$DMSO]Cl$_2$*

2.2.2.3   Solid state structures of [RuCl$_2$(**L1**)PPh$_3$] and [Ru(**L1**)$_2$]Cl$_2$

Crystals of [RuCl$_2$(**L1**)PPh$_3$] suitable for single crystal X-ray diffraction were obtained by vapour diffusion of diethyl ether into concentrated solution of the complex in DCM to give dark red block-like crystals. Crystals of [Ru(**L1**)$_2$]Cl$_2$ suitable for single crystal X-ray diffraction were obtained as yellow needle-like crystals by slow evaporation of a concentrated solution in DCM. The crystal structures revealed the expected tridentate ligand behaviour in both species, with distorted octahedral structures around the ruthenium centre.
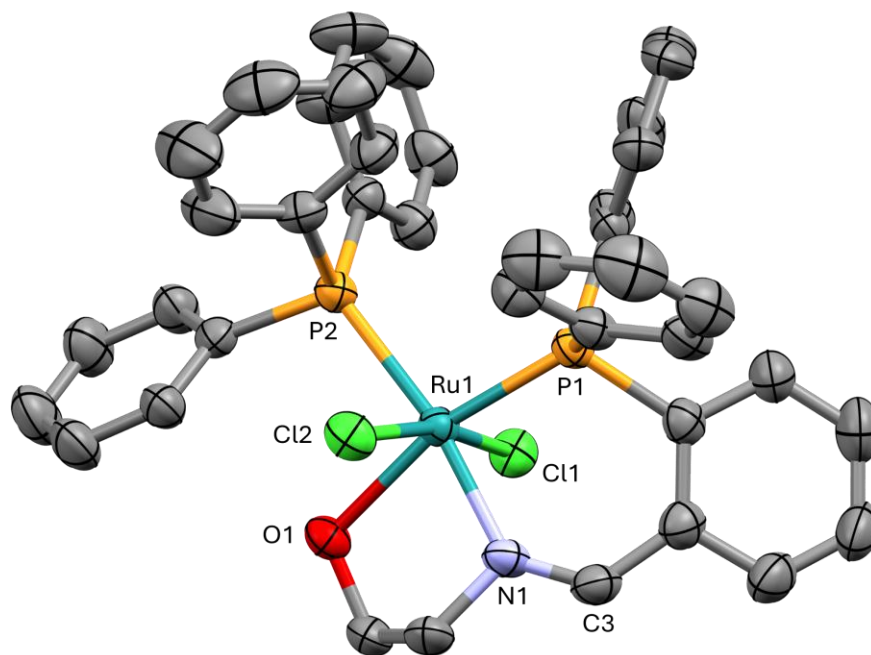
*Figure 2.7 – Single crystal structure obtained of [RuCl₂(**L1**)PPh₃] with 50 % thermal ellipsoids and hydrogen atoms removed for clarity. Asymmetric unit contained one molecule of complex and one solvent molecule (Et₂O) which has been removed for clarity.*

*Table 2.2 - Bond length data for [RuCl₂(**L1**)PPh₃].*

Complex	Bond lengths (Å)		Bond angles (°)			
[RuCl₂(**L1**)PPh₃]	Ru1-O1	2.241(3)	N1-Ru1-P1	87.91(11)	O1-Ru1-Cl1	84.34(9)
	Ru1-N1	2.083(3)	N1-Ru1-O1	78.45(13)	O1-Ru1-Cl2	84.41(9)
	Ru1-P1	2.2298(12)	N1-Ru1-Cl1	85.52(11)	O1-Ru1-P2	93.04(8)
	Ru1-P2	2.3587(11)	N1-Ru1-Cl2	87.01(11)	P2-Ru1-Cl1	99.13(4)
	Ru1-Cl1	2.4241(12)	P1-Ru1-P2	100.86(4)	P2-Ru1-Cl2	86.79(4)
	Ru2-Cl2	2.4089(12)	P1-Ru1-Cl2	98.46(4)	N1-Ru1-P2	169.92(12)
	N1-C3	1.272(6)	P1-Ru1-Cl1	91.22(4)	P1-Ru1-O1	165.93(8)
			Cl2-Ru1-Cl1	167.54(4)		
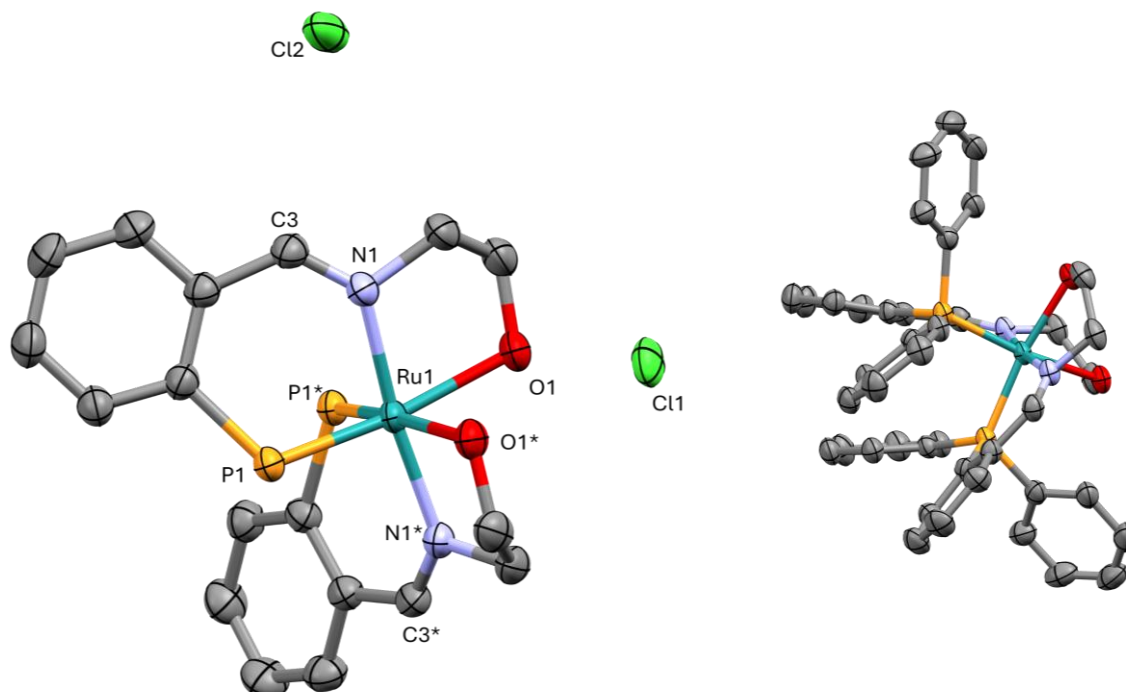
*Figure 2.8 – Single crystal structure obtained of [Ru(**L1**)$_2$]Cl$_2$ with 50 % thermal ellipsoids. The asymmetric unit bisected the crystal structure molecule of the complex, creating a plane of crystallographic symmetry through the structure, and included two DCM molecules which have been removed. Left: Hydrogen atoms and phosphine phenyl groups have been removed for clarity. Right: Paddle wheel stacking of phenyl rings shown with hydrogen atoms and outer sphere chlorine atoms removed for clarity.*

*Table 2.3 - Bond length data for [Ru(**L1**)$_2$]Cl$_2$.*

Complex	Bond lengths (Å)		Bond angles (°)			
[Ru(**L1**)$_2$]Cl$_2$	Ru1-O1	2.209(3)	N1-Ru1-P1	90.27(9)	N1*-Ru1-O1	93.82(11)
	Ru1-N1	2.047(3)	N1-Ru1-P1*	94.44(9)	N1*-Ru1-O1*	80.95(11)
	Ru1-P1	2.2556(9)	N1-Ru1-O1	80.95(11)	N1*-Ru1-P1	94.44(9)
	N1-C3	1.282(5)	N1-Ru1-O1*	93.82(11)	N1*-Ru1-P1*	90.27(9)
	Ru1-O1*	2.209(3)	N1-Ru1-N1*	173.04(16)	O1-Ru1-O1*	83.43(14)
	Ru1-N1*	2.047(3)	P1-Ru1-P1*	94.73(5)	O1-Ru1-P1*	91.59(8)
	Ru1-P1*	2.2556(9)	P1-Ru1-O1*	91.59(8)	P1*-Ru1-O1*	169.57(8)
	N1*-C3*	1.282(5)	P1-Ru1-O1	169.57(8)		

The obtained crystal structure of [RuCl$_2$(**L1**)PPh$_3$] shows the two bound phosphines coordinated *cis* to one another with two chloride ligands adopting a *trans* coordination. Significant distortion

away from octahedral is seen due to the steric bulk of the phenyl groups and the restriction of the chelate rings; the P-Ru-P bond angle is expanded by almost 11° from ideal. The ligand coordinates with the **L1** phosphorus and oxygen *trans* to one another, as predicted. The resultant two chelate rings are not planar. The 5-membered metallacycle shows distinct envelope conformation with C2 existing out of plane with the rest of the chelate ring. The larger 6-membered ring shows a distorted half-chair type conformation, with the extended aromatic ring system well aligned in one plane, and the ruthenium slightly out of plane, likely to accommodate the steric effects of the PPh$_3$ ancillary ligand.

The obtained structure of [Ru(**L1**)$_2$]Cl$_2$ shows crystallographic symmetry, such that a plane of symmetry exists within the centre of the structure: hence, both ligands and their bond lengths surrounding the Ru centre were observed as equivalent. Both ligands are bound in expected pincer type coordination, with phosphine and oxygen coordinated *trans* to each other. The distortion away from ideal octahedral is significantly less than that observed in [RuCl$_2$(**L1**)PPh$_3$]; the P-Ru-P bond is only expanded by 5° from ideal, with the phenyl rings in a paddle wheel formation, stabilised by the stacking of two phenyl rings in each ligand in a co-planar arrangement between ligands to accommodate steric effects (Figure 2.8, right). Similar envelope and half-chair conformation is observed in all four chelate rings to that described in [RuCl$_2$(**L1**)PPh$_3$].

In the ^{31}P{^{1}H} NMR spectrum of [RuCl$_2$(**L1**)PPh$_3$], the more deshielded signal is attributed to **L1** and the less deshielded signal is PPh$_3$ due to the increased trans influence of the alcohol ligand. In the crystal structure, the Ru-P1 bond length is accordingly shorter than the Ru-P2 bond length. Ru-P bonds in [Ru(**L1**)$_2$]Cl$_2$ are longer than seen between **L1** phosphorus and Ru in [RuCl$_2$(**L1**)PPh$_3$], but shorter than Ru-PPh$_3$. Accordingly, the observed ^{31}P{^{1}H} NMR signal of [Ru(**L1**)$_2$]Cl$_2$ is between the two signals in [RuCl$_2$(**L1**)PPh$_3$]. Examining the imine bonding, there is no statistically significantly difference between imine bond lengths between [RuCl$_2$(**L1**)PPh$_3$] and [Ru(**L1**)$_2$]Cl$_2$, despite the larger deshielding effect of complexation upon the imine proton observed in the ^{1}H NMR spectrum of [Ru(**L1**)$_2$]Cl$_2$ (see Table 2.1). Unfortunately, crystal data could not be obtained for the free ligand so a direct comparison cannot be made with the C=N bonding observed in free **L1**.

It is noted that there is slight reduction in Ru-O bond length in the bis-ligated species could support a shorter alkoxide type binding, but as protons cannot be observed in X-ray crystallography this cannot be confirmed. It is noted that the Ru-O bond length of 2.209(3) Å is slightly longer than that observed in Kwong's reported alcoholic complex (Figure 2.4a, 2.158(7) Å and 2.160(5) Å)[14], and markedly longer than the bond lengths reported by Parr and coworkers

(Figure 2.4b) who proposed an alkoxide binding type (2.092(2) Å)[13]. However, the presence of outer sphere chloride ions – with one held close to the oxygen atoms – confirms the close association of chloride in the system, supporting a charged species with outer sphere chloride counterions.

2.2.3 Expansion of RuCl$_2$(PNO)$_2$ series of compounds

The class of bis-ligated complexes was expanded through the attempted complexation of ligands **L2**-**L6** using at least two molar equivalents of ligand with respect to the Ru starting material; relevant reaction conditions are reported in Scheme 2.4. **L2**, **L3** and **L6** each gave a single species in good yield, while **L4** gave a mixture of two isomers. These complexes (shown in Figure 2.9) are discussed below and organised according to the coordination mode of the PNO ligands (bidentate versus tridentate). The only previously reported bis-ligated complex of this set is [Ru(**L3**)$_2$]Cl$_2$, though this work demonstrated a solution- and air-stable complex was formed, and is proposed to adopt an alternative facial binding mode to the similar complex reported by Dilworth and coworkers[15].
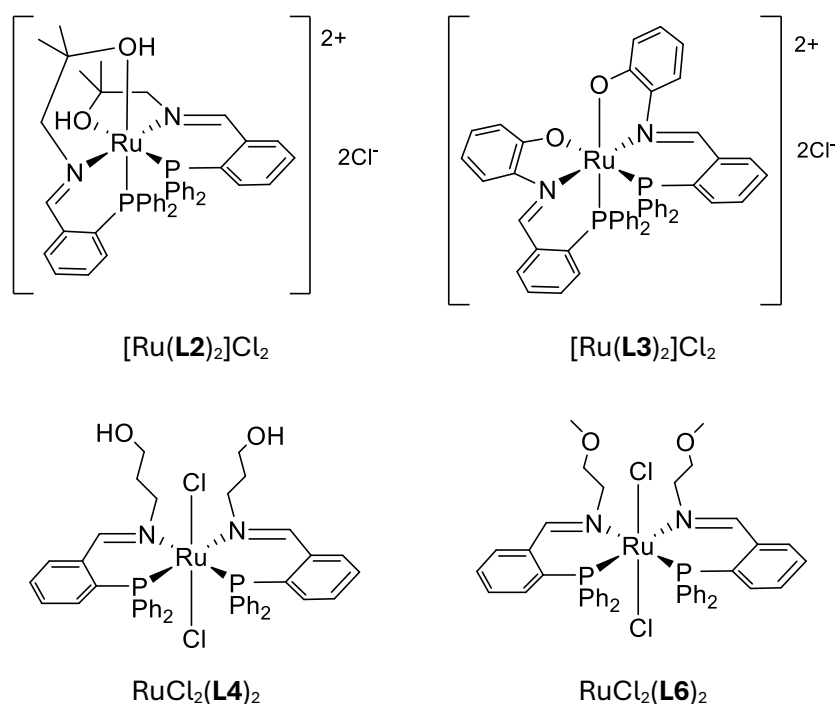
*Figure 2.9 - Summary of [RuCl$_2$(PNO)$_2$] complexes successfully isolated. Structures confirmed with single crystal X-ray diffraction of [Ru(**L2**)$_2$]Cl$_2$ and [RuCl$_2$(**L6**)$_2$].*

2.2.3.1   Bis-Tridentate PNO Complexes

[Ru(**L2**)$_2$]Cl$_2$ directly precipitated from toluene to give a bright yellow solid whose identity was confirmed with HRMS as containing two coordinated **L2** molecules and two chloride counterions.

Despite only moderate solubility in $CDCl_3$, NMR spectroscopic analysis gave data similar to that of [Ru(**L1**)$_2$]Cl$_2$, notably showing a strongly deshielded singlet in the $^{31}P\{^1H\}$ NMR spectrum at +58.9 ppm in $CDCl_3$ (shifted from free **L2** which shows a signal at -10.9 ppm), which implies only one ligand environment within the complex. A downfield shift of the **L2** imine proton from 8.73 ppm to 9.18 ppm was noted upon complexation. Furthermore, the FTIR spectrum showed a shift in the C=N vibrational frequency from 1631 cm^{-1} to 1616 cm^{-1} in [Ru(**L2**)$_2$]Cl$_2$. This analysis is all concordant with [Ru(**L1**)$_2$]Cl$_2$, suggesting an analogous tridentate coordination mode with outer sphere chlorides. Similar appearance of aliphatic C-H protons as two doublets showing geminal coupling (δ: 4.78, 3.68 ppm, J = 13.6 Hz) demonstrates the expected proton inequivalence created by fixed chelate rings. This coordination sphere which was confirmed through X-ray crystallography (Figure 2.10). Suitable crystals were obtained using vapour diffusion of Et$_2$O into concentrated DCM solution, giving yellow block-like crystals.

As with [Ru(**L1**)$_2$]Cl$_2$, the obtained crystal structure shows crystallographic symmetry, so both ligands and their bond lengths surrounding the Ru centre were observed as equivalent. The observed structures are very similar; [Ru(**L2**)$_2$]Cl$_2$ also shows two **L2** ligands coordinated in pincer type coordination with phosphorus positioned *trans* to the oxygen of the same ligand. The system shows distorted octahedral geometry with some expansion of the P-Ru-P bond angle by approximately 3.5° due to steric hindrance of the bulky phosphine groups: as seen previously this is substantially limited by the stabilising stacking of phenyl rings. Again, two chelate rings are observed per ligand, the 5-membered aliphatic ring showing envelope conformation with the C2 carbon out of plane, and the 6-membered ring adopting half-chair conformation with ruthenium out of plane. Chloride ions were again found in an outer sphere position, aligned near the oxygen atoms. When compared with [Ru(**L1**)$_2$]Cl$_2$, the increased compression of the P-Ru-O bond angle of a single ligand from 180° to 166.13(4)° (as opposed to 169.57(8)° in [Ru(**L1**)$_2$]Cl$_2$) is attributed to the steric effects of aliphatic methyl groups.
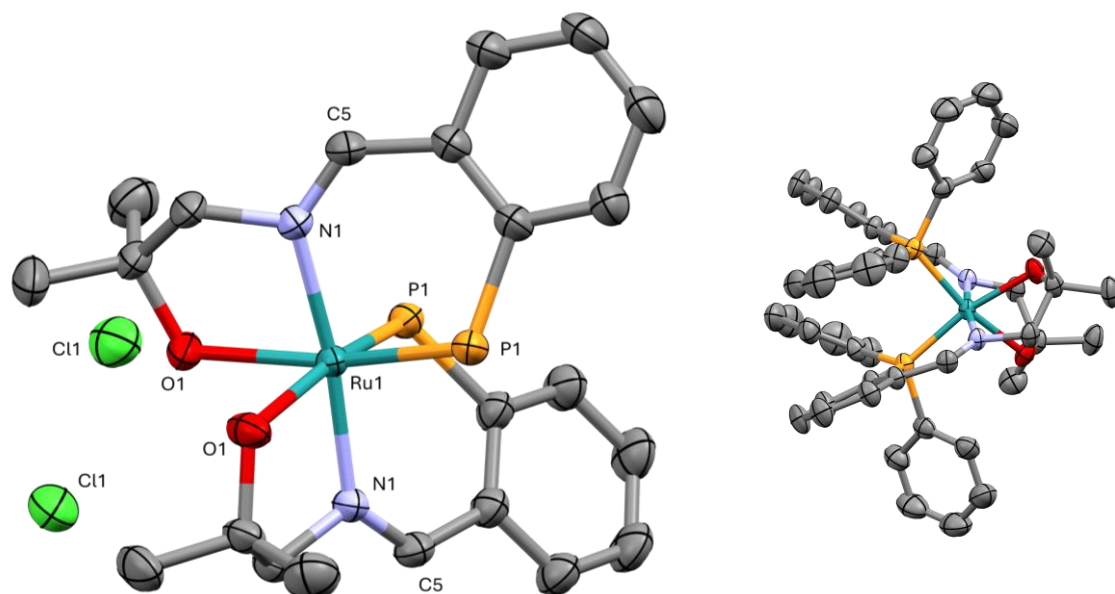
*Figure 2.10 - Single crystal structure obtained of [Ru(**L2**)₂]Cl₂ with 50 % thermal ellipsoids. Hydrogen atoms and phosphine phenyl groups have been removed for clarity. The asymmetric unit bisected the crystal structure molecule of the complex, creating a plane of crystallographic symmetry through the structure, and included two hexane molecules which have been removed.*

*Table 2.4 - Bond length data for [Ru(**L2**)₂]Cl₂*

Complex	Bond lengths (Å)		Bond angles (°)			
[Ru(**L2**)₂]Cl₂	Ru1-O1	2.1869(15)	N1-Ru1-P1	90.21(5)	N1*-Ru1-O1	95.79(6)
	Ru1-N1	2.0444(17)	N1-Ru1-P1*	95.12(5)	N1*-Ru1-O1*	78.14(6)
	Ru1-P1	2.2622(6)	N1-Ru1-O1	78.14(6)	N1*-Ru1-P1	95.12(5)
	N1-C5	1.283(3)	N1-Ru1-O1*	95.79(6)	N1*-Ru1-P1*	90.21(5)
	Ru1-O1*	2.1869(15)	N1-Ru1-N1*	172.23(9)	O1-Ru1-O1*	78.88(10)
	Ru1-N1*	2.0444(17)	P1-Ru1-P1*	93.45(3)	O1-Ru1-P1*	95.05(5)
	Ru1-P1*	2.2622(6)	P1-Ru1-O1*	95.05(5)	P1*-Ru1-O1*	166.13(4)
	N1*-C5*	1.283(3)	P1-Ru1-O1	166.13(4)		

As noted in section 2.2.2.1, Dilworth and coworkers previously reported the complexation of ligand **L3** by treatment of [RuCl₂(PPh₃)₃] with excess **L3** in methanol (Scheme 2.6, complex **I**). They reported a highly air-sensitive species which decomposed rapidly in air in either solid or solution state, and was soluble in methanol and chlorinated solvents. They found that attempts to prepare **I** from treatment of [RuCl₂(*p*-cymene)]₂ with **L3** required the addition of base. In the absence of base, they identified a partially oxidised dimeric species **II** which, when left to stand, reduced further to form two equivalents of Ru(III) species **III** (Scheme 2.6). Structures of these species

were confirmed with X-ray crystallography, but the paramagnetic nature of Ru(III) and the reported instability of their bis-ligated complex in solution precluded NMR analysis.
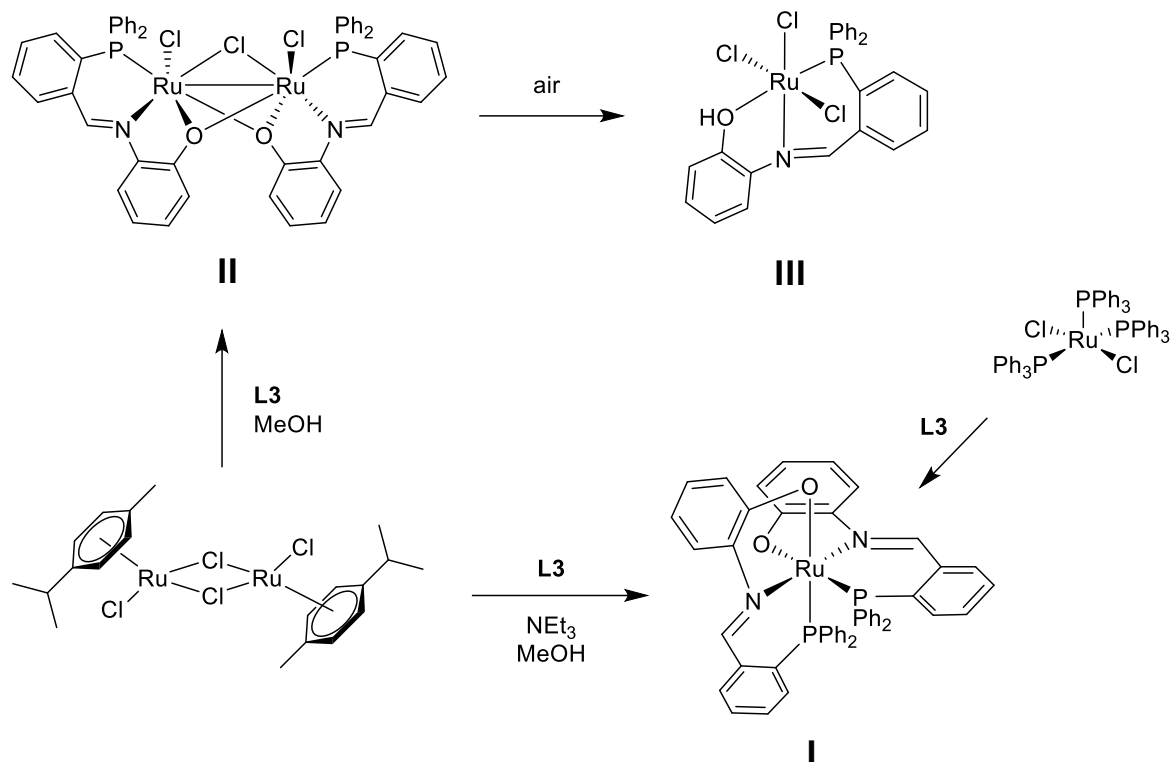
*Scheme 2.6 - Production of unstable complexes of **L3** reported by Dilworth and coworkers.*

Conversely, in this work, [Ru(**L3**)$_2$]Cl$_2$ was isolated readily as a dark brown solid which precipitated directly from toluene in 83 % yield, and was able to be stored as a solid in air over the course of several weeks with no observed decomposition. Unlike Dilworth's complex, this species was only very sparingly soluble in CDCl$_3$ so NMR spectral analyses were performed in DMSO-d6. This supports the production of a Ru(II) species, further demonstrating a different complex was formed in this work. The use in the literature of a protic solvent could have resulted in some kind of reaction to oxidise the complex, but a mechanism is unclear. Further analysis of the apparently novel complex [Ru(**L3**)$_2$]Cl$_2$ was performed with comparison to the previously confirmed complexes [Ru(**L1**)$_2$]Cl$_2$ and [Ru(**L2**)$_2$]Cl$_2$.

A singlet was observed in the ^{31}P{^{1}H} NMR spectrum at +58.7 ppm, again showing a similar complexation shift to that observed in both [Ru(**L1**)$_2$]Cl$_2$ and [Ru(**L2**)$_2$]Cl$_2$. This deshielded phosphorus signal is consistent with the other PNO tridentate ligands where the phosphorus is *trans* to a coordinated oxygen donor and therefore also assumed to be the case in this complex. It is noteworthy that no secondary product was observed in DMSO, as was the case when [Ru(**L1**)$_2$]Cl$_2$ was dissolved in DMSO-d6. This may be attributed to the increased rigidity of the

extended aromatic structure of **L3** and/or the bulk of the phenyl groups which prevents substitution with a coordinated DMSO molecule. The absence of any significant O-H stretch also supports the alkoxide type binding of oxygen considered for [Ru(**L1**)$_2$]Cl$_2$ and [Ru(**L2**)$_2$]Cl$_2$.

*Table 2.5 - Comparison of analytical data between ligands **L1, L2** and **L3** and their bis-ligated complexes.*

	^{31}P{^{1}H} δ / ppm			Ru-P length / Å	^{1}H δ HC=N / ppm			ν(C=N) / cm^{-1}			C=N length / Å
	L[a]	C[b]	Δ		L	C	Δ	L	C	Δ	
L1	-10.7	61.2	+71.9	2.2556(9)	8.74	9.18	+0.44	1634	1618	-16	1.282(5)
L2	-10.9	58.9	+69.8	2.2622(6)	8.73	9.18	+0.45	1631	1616	-15	1.283(3)
L3[c]	-10.0	58.7	+68.7	-	9.02	9.60	+0.58	1633	1560	-73	-
[a]L = free ligand. [b]C = bis-ligated complex. [c][Ru(**L3**)$_2$]Cl$_2$ dissolved in DMSO-d6. Bond lengths as observed in bis-ligated complexes.											

Closer comparison of analytical data between these three analogous complexes is summarised in Table 2.5. The larger downfield shift of ^{31}P{^{1}H} NMR signal upon complexation of **L1** indicates the most deshielding of phosphine; this is consistent with the shorter Ru-P bond seen in [Ru(**L1**)$_2$]Cl$_2$ than [Ru(**L2**)$_2$]Cl$_2$. Conversely, direct comparison of Ru-O bond lengths in [Ru(**L1**)$_2$]Cl$_2$ and [Ru(**L2**)$_2$]Cl$_2$ show a slightly shorter Ru-O bond in [Ru(**L2**)$_2$]Cl$_2$, suggesting greater σ donor behaviour of the **L2** oxygen (see Table 2.3, Table 2.4). However it is noted that these bond lengths are very similar, so may be insignificantly different when bond vibration is accounted for. ^{31}P{^{1}H} NMR spectral data for **L3** shows the smallest change in chemical shift upon complexation, but given the lack of crystallographic data it is impossible to determine a link to bond length and exclude the impact of potential solvent effects, given the insolubility of [Ru(**L3**)$_2$]Cl$_2$ in CDCl$_3$.

Comparison of imine data shows very similar C=N bonding in [Ru(**L1**)$_2$]Cl$_2$ and [Ru(**L2**)$_2$]Cl$_2$. This suggests very similar Ru-N bonding between the two species. The presence of an additional phenyl group in **L3** however extends the aromatic structure of the ligand, clearly impacting the Ru-N binding: the imine proton deshielding and C=N lengthening observed upon complexation is substantially greater than that observed for either **L1** or **L2**. Accordingly, Ru-N is expected to be noticeably shorter in [Ru(**L3**)$_2$]Cl$_2$ than in either [Ru(**L1**)$_2$]Cl$_2$ or [Ru(**L2**)$_2$]Cl$_2$ (statistically the same at 2.047(3) Å and 2.0444(17) Å respectively). This suggests the **L3** ligand experiences much greater structural distortion upon complexation than either **L1** or **L2**, likely due to the inability of the phenolic pendant arm to distort into an envelope conformation as seen in the aliphatic alcohols in [Ru(**L1**)$_2$]Cl$_2$ and [Ru(**L2**)$_2$]Cl$_2$. Indeed, distortion may be such that **L3** binds as a bent facial tridentate ligand, with the binding phosphorus and oxygen of the same ligand positioned

cis to one another (Figure 2.11). This potential alternative structure could explain the stability of the species produced in this work relative to that previously reported.
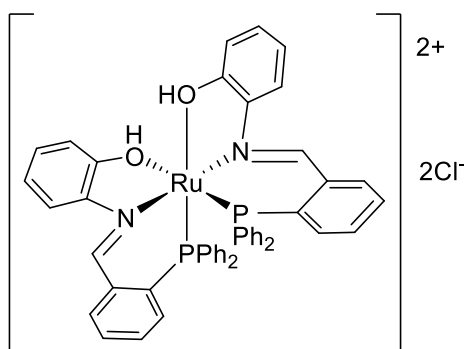
*Figure 2.11 - Potential alternative binding modes of **L3** in [Ru(**L3**)₂]Cl₂.*

2.2.3.2   Bis-Bidentate PNO Complexes

Complexation of **L6** with [RuCl$_2$(*p*-cymene)]$_2$ was straightforward under the conditions shown in Scheme 2.4, giving [RuCl$_2$(**L6**)$_2$] as a single dark red product which precipitated directly from toluene. HRMS confirmed bis-ligated structure with retained chlorines (HRMS (ES+/Q-TOF) m/z: [M]$^+$ Calcd for C$_{44}$H$_{44}$N$_2$O$_2$P$_2$Cl$_2$Ru 866.1299; Found 866.1320). Unlike the bis-tridentate species explored in Section 2.2.3.1, the complex was readily soluble in CDCl$_3$ allowing NMR spectral analysis. The ^{31}P{^{1}H} NMR data of [RuCl$_2$(**L6**)$_2$] showed a singlet at +49.2 ppm, consistent with formation of a single isomer with symmetrical environment. This shows a downfield shift of the phosphorus signal of +63.0 ppm upon chelation (Table 2.6), giving a complexed phosphorus signal significantly upfield of those observed in the tridentate PNO complexes discussed previously (see Table 2.5). This is proposed to indicate a change in binding mode.

*Table 2.6 - Comparison of key ^{1}H and ^{31}P{^{1}H} NMR shifts in free **L6** and [RuCl$_2$(**L6**)$_2$], taken in CDCl$_3$*

	L6	[RuCl$_2$(**L6**)$_2$]	Δ
^{1}H δ *H*C=N / ppm	+8.84	+8.75	-0.09
{^{1}H}^{31}P δ / ppm	-13.8	+49.2	+63.0

FTIR analysis showed changes to the C=N stretching frequency which are in line with the changes observed in previous complexes (**L6**: 1636 cm^{-1}, [RuCl$_2$(**L6**)$_2$]: 1616 cm^{-1}), showing the expected bond lengthening of C=N upon coordination of nitrogen. Interestingly, the ^{1}H NMR chemical shift of the imine proton shows an upfield shift relative to the free ligand, not previously observed in this family of complexes. This is proposed to be due to back-donation into the C=N π* orbital,

increasing electron density around the imine proton whilst still reducing C=N double bond character.
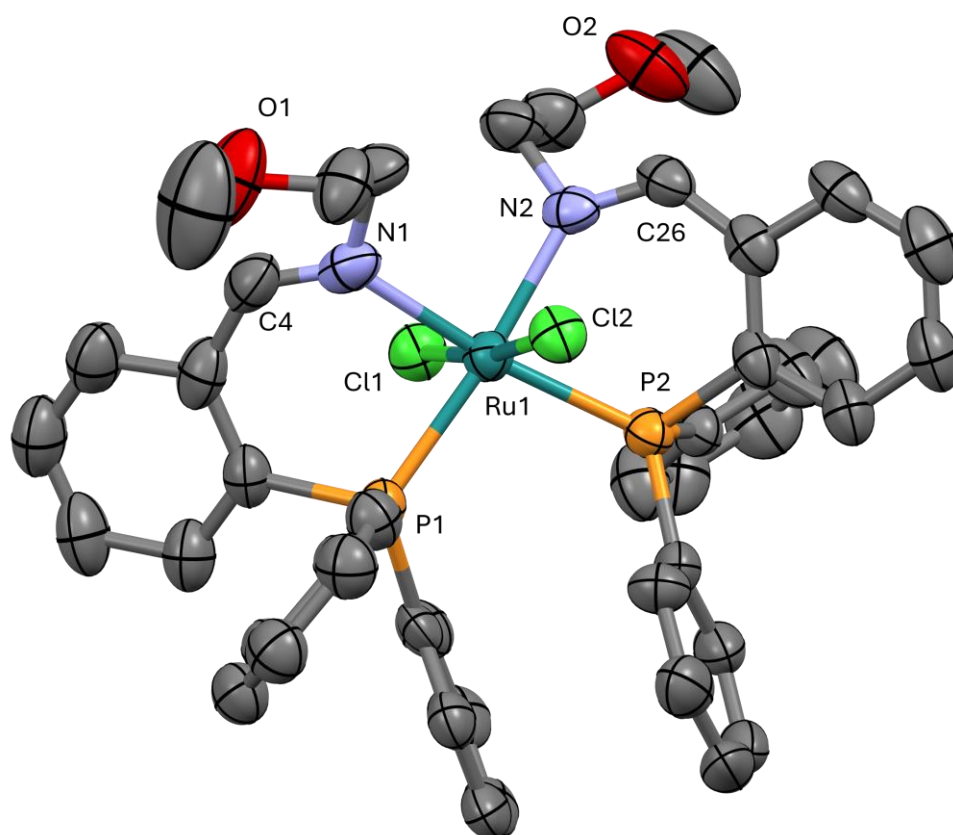
*Figure 2.12 - Single crystal structure obtained of [RuCl$_2$(**L6**)$_2$] with 50 % thermal ellipsoids and hydrogen atoms removed for clarity. Asymmetric unit contained two molecules of complex, one of which (Ru1) has been selected for bond length presentation, and two solvent molecules (DCM) which have been removed for clarity.*

*Table 2.7 – Key bond lengths and angles for [RuCl$_2$(**L6**)$_2$].*

Complex	Bond lengths (Å)		Bond angles (°)			
[RuCl$_2$(**L6**)$_2$]	Ru1-P1	2.3022(17)	Cl1-Ru1-P1	84.28(6)	Cl2-Ru1-P1	101.77(6)
	Ru1-P2	2.2789(17)	Cl1-Ru1-P2	96.90(6)	Cl2-Ru1-P2	86.81(6)
	Ru1-N1	2.176(5)	Cl1-Ru1-N1	89.08(16)	Cl2-Ru1-N1	86.56(16)
	Ru1-N2	2.147(5)	Cl1-Ru1-N2	88.30(14)	Cl2-Ru1-N2	85.33(14)
	Ru1-Cl1	2.4243(15)	Cl1-Ru1-Cl2	172.22(6)	P2-Ru1-P1	101.06(6)
	Ru1-Cl2	2.4399(15)	N1-Ru1-N2	90.8(2)	P2-Ru1-N2	83.48(14)
	N1-C4	1.258(9)	N1-Ru1-P1	85.42(17)	P1-Ru1-N2	171.70(14)
	N2-C26	1.284(8)	N1-Ru1-P2	171.55(18)		

To determine the absolute details of the coordination sphere, crystals suitable for single crystal X-ray diffraction were obtained by vapour diffusion of Et_2O into a concentrated solution of [RuCl$_2$(**L6**)$_2$] in DCM. The resultant structure (Figure 2.12) showed a distorted octahedral coordination sphere, with bidentate PN ligand behaviour resulting in a *trans* arrangement of two coordinated chloride ligands. The two phosphorus donors are mutually *cis* to one another and therefore each is *trans* to a nitrogen donor. The pendant oxygen atoms of the ligands are clearly non-coordinating and are positioned away from the coordination sphere. It is interesting to note that in the aliphatic region of the ^1H NMR spectrum, the CH_2 protons appear to exhibit chemical inequivalence, producing four separate multiplet signals which couple to each other (δ: 4.35, 3.81, 3.27, 2.94 ppm). This indicates that even with uncoordinated oxygen in solution, these pendant arms do not have free movement. This is proposed to be due to hydrogen bonding between the oxygen and the iminic proton. The CH_3 protons are equivalent, showing free rotation beyond the oxygen.
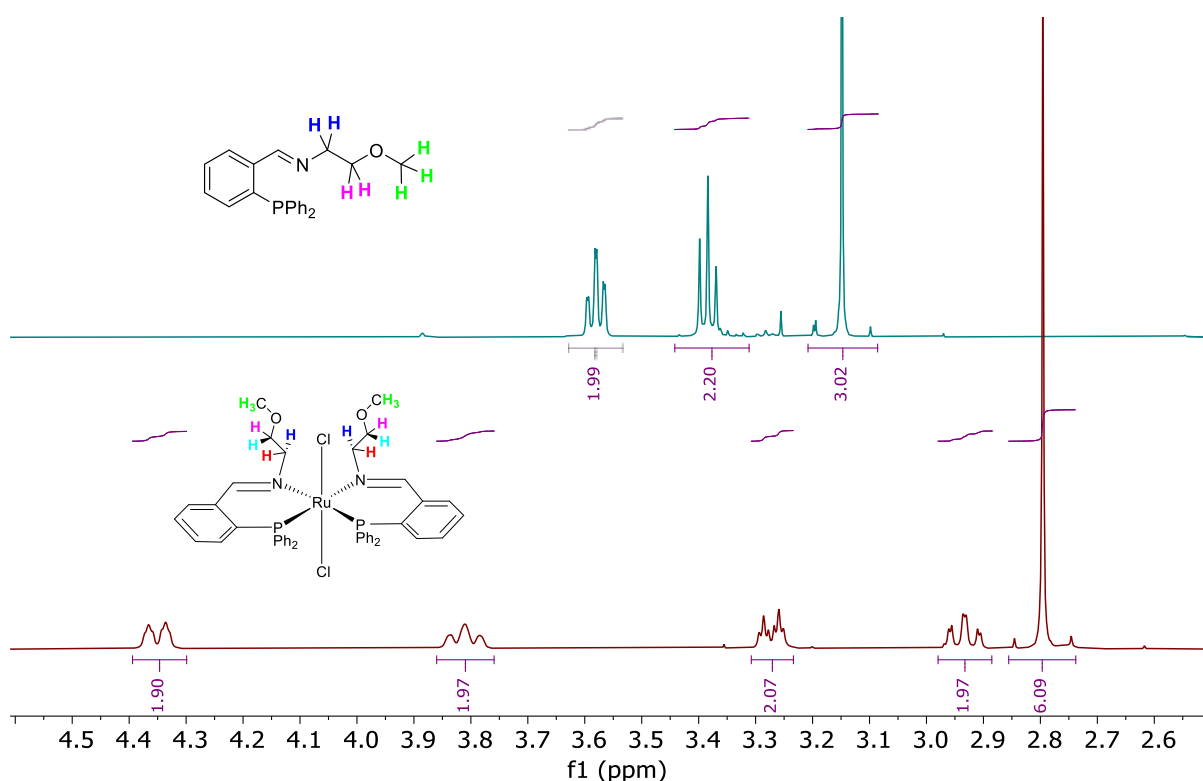
Figure 2.13 - Demonstration of inequivalent protons in aliphatic region of ^1H NMR spectrum, with inequivalent protons highlighted with different colours. Top: **L6**. *Bottom:* [RuCl$_2$(**L6**)$_2$].

The bidentate coordination mode of **L6** produces two 6-membered chelate rings, which demonstrate the same envelope type conformation as other crystal structures have shown, with the PN aromatic system existing on one plane with the ruthenium central atom out of plane. Interestingly, this chelate ring shows a notably smaller bond angle about the ruthenium centre

than in all systems exhibiting tridentate binding; the P-Ru-N bond angles for tridentate systems were fixed very close to 90°, whereas [RuCl$_2$(**L6**)$_2$] shows compression of this bond angle by almost 5°. The phenyl groups, as previously seen, adopt a paddle wheel conformation to minimise steric effects, though only one phenyl group in each ligand stacks in an off-set co-planar arrangement to each other. Given the bidentate system is less sterically restricted, the P-Ru-P bond angle is expanded to [RuCl$_2$(**L1**)PPh$_3$] at more than 11° distortion from ideal octahedral, which appears to result in the previously mentioned distortion of the chelate rings. The chloride ligands are similarly distorted away from the bulky phosphorus groups.

Examination of the bond length data that describe the coordination sphere shows that there are two slightly different Ru-N bond lengths depending on the nitrogen which can be attributed to crystal packing effects. However, Ru-N bonds were significantly lengthened in [RuCl$_2$(**L6**)$_2$] when compared with [RuCl$_2$(**L1**)PPh$_3$], [Ru(**L1**)$_2$]Cl$_2$ and [Ru(**L2**)$_2$]Cl$_2$, all of which were in the order of 0.1 Å shorter. This indicates poorer σ donation from the nitrogen in a bidentate system and is concordant with the relative lack of deshielding of the imine proton observed in the ^{1}H NMR spectrum upon complexation. There is no statistically significant difference in the C=N bond lengths between the two ligands, nor is there significant difference to the C=N bond lengths in previously reported complexes, which aligns with the FTIR data collected for other bis-ligated complexes. Ru-P bonds were slightly longer in [RuCl$_2$(**L6**)$_2$] than in tridentate systems, consistent with the smaller deshielding effect of complexation observed in ^{31}P NMR (Δδ = +63). The greater shielding of the phosphorus donor atoms may also be related to their position *trans* to nitrogen atoms instead of the more electronegative oxygen, or the presence of adjacent chlorine atoms altering the electron density surrounding the ruthenium centre.

The preparation of [RuCl$_2$(**L4**)$_2$] was achieved in high yield by reaction of excess **L4** with [RuCl$_2$(*p*-cymene)]$_2$ in toluene yielding a precipitation which when filtered gave a dark red solid. However, NMR analysis gave rise to two separate singlets in the ^{31}P{^{1}H} NMR spectrum, implying a mixture of two products which could not be separated using traditional approaches. LRMS analysis indicated that only bis-ligated complex species featuring chloride ions were present. The ^{31}P{^{1}H} NMR signals were recorded shifting from -13.7 ppm (free **L4**) to +47.8 ppm and +30.8 ppm in the complex mixture; therefore, both complexes contain a coordinated phosphorus unit. The complex at +30.8 ppm was the major product, and is designated [RuCl$_2$(**L4**)$_2$]-A, and the minor product [RuCl$_2$(**L4**)$_2$]-B. The two species were formed in approximately 2:1 molar ratio of [RuCl$_2$(**L4**)$_2$]-A: [RuCl$_2$(**L4**)$_2$]-B.

	L4	[RuCl$_2$(**L4**)$_2$]-A	Δ	[RuCl$_2$(**L4**)$_2$]-B	Δ
^1H δ HC=N / ppm	+8.79	+8.19	-0.60	+8.73	-0.06
$\{^1H\}^{31}P$ δ / ppm	-13.7	+30.8	+44.5	+47.8	+61.5

This ratio allowed assignment of the two species' imine signals, both of which revealed an upfield shift compared to free **L4** (Table 2.8). Given than an analogous upfield shift was only observed in the bidentate [RuCl$_2$(**L4**)$_2$], a similar bidentate behaviour is proposed for both [RuCl$_2$(**L4**)$_2$] complexes. Due to the similar chemical shifts between [RuCl$_2$(**L6**)$_2$] and [RuCl$_2$(**L4**)$_2$]-B, it is theorised that [RuCl$_2$(**L4**)$_2$]-B has the same *cis* bidentate arrangement of ligands with both chlorides positioned *trans* to one another. Other potential isomeric forms of [RuCl$_2$(**L4**)$_2$]-A are proposed in Figure 2.14 and future work should consider X-ray crystallographic studies to define the species. It is again noted that inequivalence of the aliphatic CH$_2$ protons was seen in both isomers of [RuCl$_2$(**L4**)$_2$] in the ^1H NMR spectrum, as seen with [RuCl$_2$(**L6**)$_2$]. Hence, it is evident that regardless of which product isomers are obtained, the aliphatic arms are not truly experiencing free motion in solution. This is again tentatively attributed to internal hydrogen bonding between oxygen and the iminic proton.

[RuCl$_2$(**L4**)$_2$]-A   [RuCl$_2$(**L4**)$_2$]-B
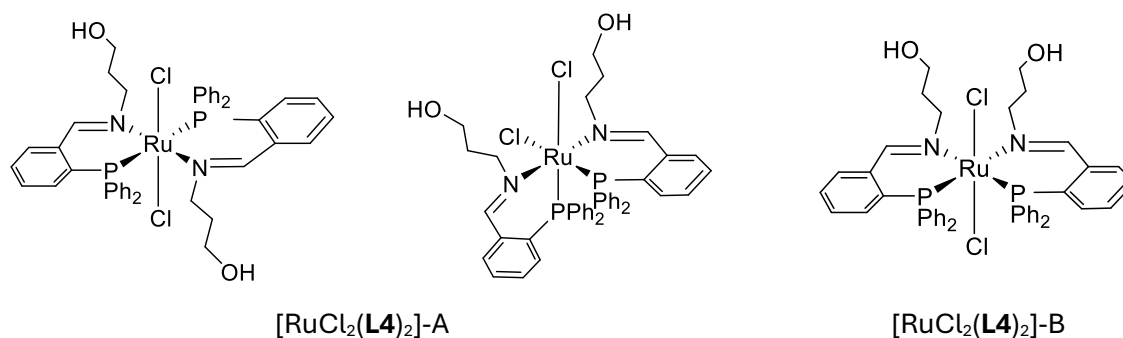
Figure 2.14 - Left: proposed structures of [RuCl$_2$(**L4**)$_2$]-A. Right: proposed structure of [RuCl$_2$(**L4**)$_2$]-B.

2.2.3.3   Unsuccessful Complexation
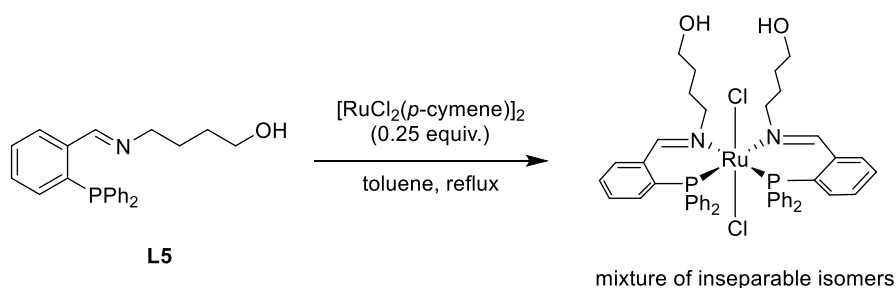
Scheme 2.7 - Attempted complexation of **L5**.

Unfortunately, the attempted complexation of **L5** was not as straightforward as previous examples, leading to a poor yield of an impure dark brown powder. LRMS indicated the presence of bis-ligated Ru(II) complexes (HRMS (ES+/Q-TOF) m/z: [M-Cl]$^+$ Calcd for $C_{46}H_{48}N_2O_2P_2ClRu$ 859.19; Found 859.19), but analysis by $^{31}P\{^1H\}$ NMR spectroscopy showed at least 5 separate complexes, two of which appeared as sets of doublets (showing multiple phosphorus environments within the same molecule). This may be due to the increased flexibility afforded by the n-butyl aliphatic arm. Repeated attempts to recrystallise the crude product to isolate a single major product were unsuccessful, and due to the poor yield (< 20 %) no further investigation was attempted with this ligand.

2.2.4 Conclusions

In this section, six ligands were prepared as part of the imine-based PNO ligand family, five of which were successfully coordinated to ruthenium to form a selection of novel bis-ligated species. The binding modes of PNO ligands varied, with alcoholic ligands featuring a 2C chain between nitrogen and oxygen binding as tridentate species; notably, [Ru(**L1**)$_2$]Cl$_2$ exhibited hemilabile behaviour in coordinating solvent. Extension of the carbon chain or substitution of the alcohol moiety with a methoxy group changed binding mode to bidentate. However, extension of the alcohol arm to a four-carbon chain yielded a complex mixture of isomers, attributed to the increased flexibility of the alcoholic pendant arm.

In future work, it would be useful if crystallographic data could be obtained from the full set of compounds, especially [Ru(**L3**)$_2$]Cl$_2$, given its proposed facial tridentate binding mode. Additional expansion of the set by modification of the phosphine R groups could also provide interesting information on the effects of steric and electronic bulk on the prevalence of bidentate *vs* tridentate coordination.

2.3 Synthesis of PO acetal ligand

During an early attempt to prepare **L1**, 2-(diphenylphosphino)benzaldehyde was heated in ethanol with 2.0 equivalents ethanolamine for 24 h. When monitoring by crude $^{31}P\{^1H\}$ NMR, an unexpected signal was observed in the spectrum at -17.0 ppm, further upfield than the reported signal in ethanol and for **L1** of -13.7 ppm[8]. Further analysis showed no imine proton in the ^1H NMR spectrum, instead showing a doublet at +6.12 ppm, and an absence of any C=N stretching in FTIR. The unknown material was isolated through recrystallisation from cold methanol as an off-white solid and identified through FTIR and NMR spectroscopy as a diethyl acetal, ligand **L7**, with an isolated yield of 71 %. Attempts to confirm via HRMS were unsuccessful, as the ligand appeared to be highly sensitive to the ionisation environment and fragmented extensively.
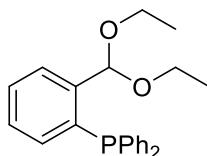
*Figure 2.15 – **L7***

Ligand **L7**, having three potential σ donor atoms, was reacted with [RuCl$_2$(*p*-cymene)]$_2$ in the same conditions shown in Scheme 2.4, giving [RuCl$_2$(**L7**)$_2$] as a bright red solid. HRMS confirmed a bis-ligated Ru(II) complex ((ES+/Q-TOF) m/z: [M-Cl]$^+$ Calcd for C$_{46}$H$_{50}$O$_4$P$_2$ClRu 865.1916; Found 865.1926). $^{31}P\{^1H\}$ NMR spectroscopy in CDCl$_3$ allowed identification as a single complex, showing a singlet at 47.0 ppm, suggesting a single phosphorus environment with similar chemical shift observed in bis-ligated species [RuCl$_2$(**L6**)$_2$]. Fortunately, crystals suitable for X-ray crystallography could be obtained through slow evaporation of a concentrated solution of [RuCl$_2$(**L7**)$_2$] in DCM. The obtained solid-state structure (Figure 2.16) demonstrates bidentate ligand behaviour in a distorted octahedral coordination sphere. This coordination mode results in the C7 and C30 carbons becoming stereocentres. The chloride ions coordinate *trans* to one another and phosphines occupy *cis* coordination, directly analogous to the structure of [RuCl$_2$(**L6**)$_2$]. Key bond lengths and angles are summarised in Table 2.9.
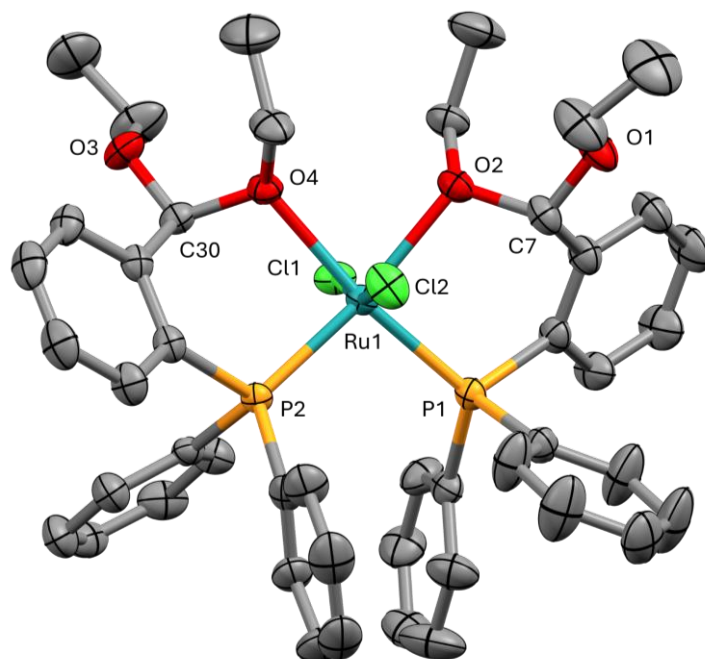
*Figure 2.16 - Single crystal structure obtained of [RuCl₂(**L7**)₂] with 50 % thermal ellipsoids and hydrogen atoms removed for clarity. Asymmetric unit contained one molecule of complex.*

*Table 2.9 - Key bond lengths and angles in solid-state crystal structure of RuCl₂(**L7**)₂*

Complex	Bond lengths (Å)		Bond angles (°)			
[RuCl₂(**L7**)₂]	Ru1-P1	2.2708(6)	Cl1-Ru1-P1	88.98(2)	Cl2-Ru1-P1	99.91(2)
	Ru1-P2	2.2632(5)	Cl1-Ru1-P2	100.48(2)	Cl2-Ru1-P2	87.86(2)
	Ru1-O2	2.2772(15)	Cl1-Ru1-O2	87.60(4)	Cl2-Ru1-O2	82.60(4)
	Ru1-O4	2.2730(15)	Cl1-Ru1-O4	81.74(4)	Cl2-Ru1-O4	87.97(4)
	Ru1-Cl1	2.4021(5)	Cl1-Ru1-Cl2	166.81(2)	P2-Ru1-P1	98.77(2)
	Ru1-Cl2	2.4003(6)	O2-Ru1-O4	80.75(5)	P2-Ru1-O4	90.97(4)
	C7-O1	1.383(3)	O2-Ru1-P1	90.77(4)	P1-Ru1-O4	167.64(4)
	C7-O2	1.459(3)	O2-Ru1-P2	167.55(4)		
	C30-O3	1.388(3)				
	C30-O4	1.454(3)				

Notably, the P-Ru-P bond is expanded by almost 9° to 98.77° to accommodate bulky phenyl rings which exist, as in other species, in a paddle wheel conformation, though the two co-planar rings are fully off-set from one another in [RuCl₂(**L7**)₂] instead of stacking as in previous complexes. The observed P-Ru-P distortion from ideal octahedral coordination is less pronounced than the 101.06° analogous bond angle in [RuCl₂(**L6**)₂]. Ru-P bond lengths in [RuCl₂(**L7**)₂] are also slightly

shorter than in [RuCl$_2$(**L6**)$_2$] (> 2.276 Å). However, the O2-Ru-O4 bond is significantly compressed to 80.75°, whereas the N-Ru-N bond seen in [RuCl$_2$(**L6**)$_2$] sees statistically no distortion away from ideal.

Upon complexation, the acetal proton in ^{1}H NMR shifted significantly downfield from +6.12 ppm in free **L7** to +7.04 ppm in [RuCl$_2$(**L7**)$_2$], signifying a loss of electron density. This is different behaviour from previous bidentate complex [RuCl$_2$(**L6**)$_2$], likely due to the lack of availability of a π system to receive back-donation from the metal centre, so all bonding through oxygen must be σ donation and lead to loss of electron density across the C-O bond. Similarly, the methylene -CH$_2$- and terminal -CH$_3$ groups also demonstrated a downfield shift upon complexation, but also significant broadening and total loss of fine structure in ^{1}H NMR: the clear ABX$_3$ splitting pattern seen at 3.45 ppm in free **L7** is shifted to a broad signal at 4.58 - 3.56 ppm in [RuCl$_2$(**L7**)$_2$] (Figure 2.17). This suggests moderate exchange between states in solution, alternating which oxygen is bound to the ruthenium centre continuously. Exchange appears not fast enough to provide a single average signal but fast enough to separate and broaden, suggesting moderate hemilability of the oxygen ligand arm. It is no great surprise that in the solid state, the binding oxygen expresses a longer C-O acetal bond than the adjacent non-complexing C-O (e.g. C7-O2 > C7-O1, Table 2.9). However, it is expected that these bonds average in solution given the exchange observed in NMR spectroscopy. Although not directly comparable structures, the Ru-O bond is markedly longer than in either [RuCl$_2$(**L1**)PPh$_3$] (2.241(3) Å) or [Ru(**L1**)$_2$]Cl$_2$ (2.209(3) Å).
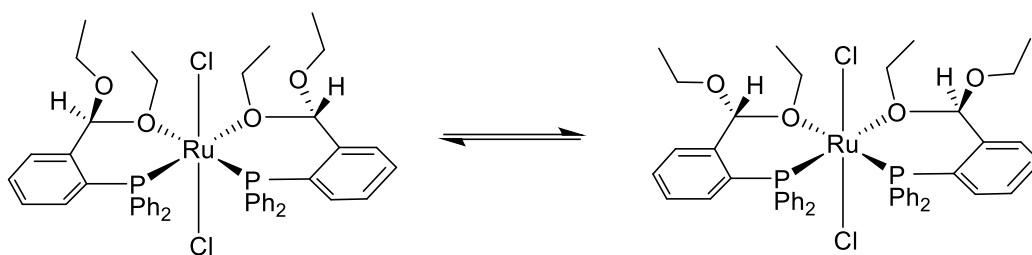
*Scheme 2.8 - Exchange of binding oxygen in [RuCl$_2$(**L7**)$_2$].*
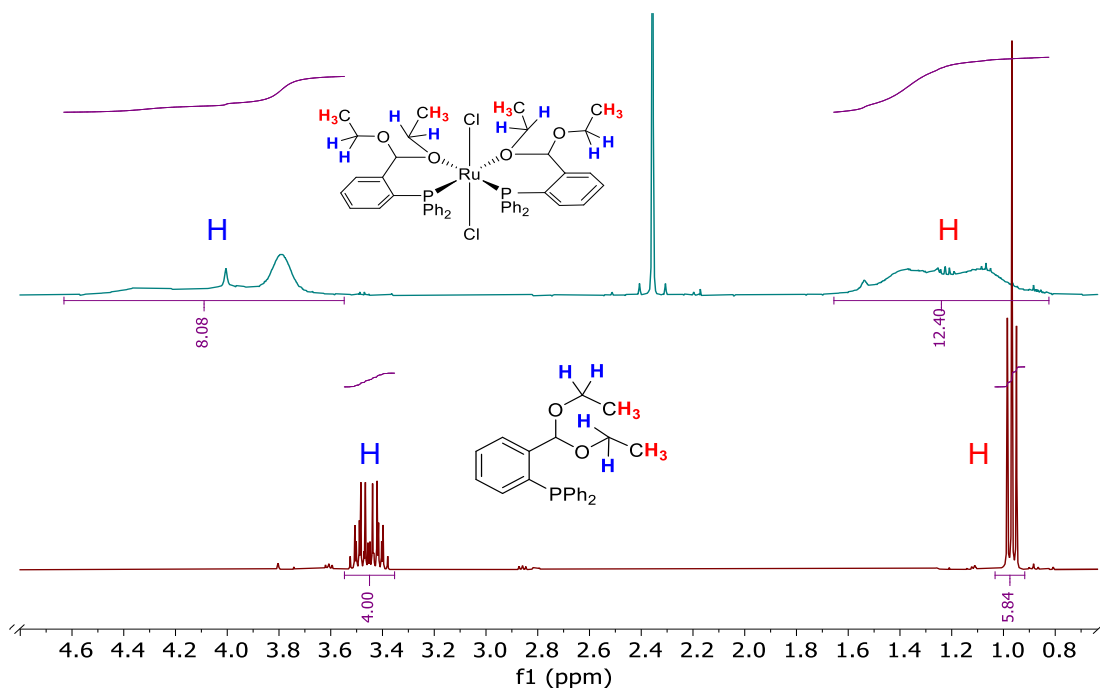
*Figure 2.17 - Comparison of aliphatic region of ^1H NMR spectrum of **L7** (bottom) and [RuCl$_2$(**L7**)$_2$] (top).*

2.3.1   Synthetic route of acetal **L7**

Due to the unexpected formation of **L7**, a reaction mechanism was sought. Only two incidences of this specific compound were found in the literature: Grotjahn and Lo reported modification of a known preparation of 2-(diphenylphosphino)benzaldehyde without deprotection of the aldehyde (Scheme 2.9a), wherein the acetal was formed prior to addition of the phosphine using a strong acid catalyst in lieu of a traditional aldehyde protection using ethylene glycol[16]. Interestingly, the only other reported preparation of this ligand was described by Elsegood *et al.* as an unexpected product during an attempt to prepare a Schiff base from 2-(diphenylphosphino)benzaldehyde in ethanol[17] (Scheme 2.9b), as in the work conducted here.
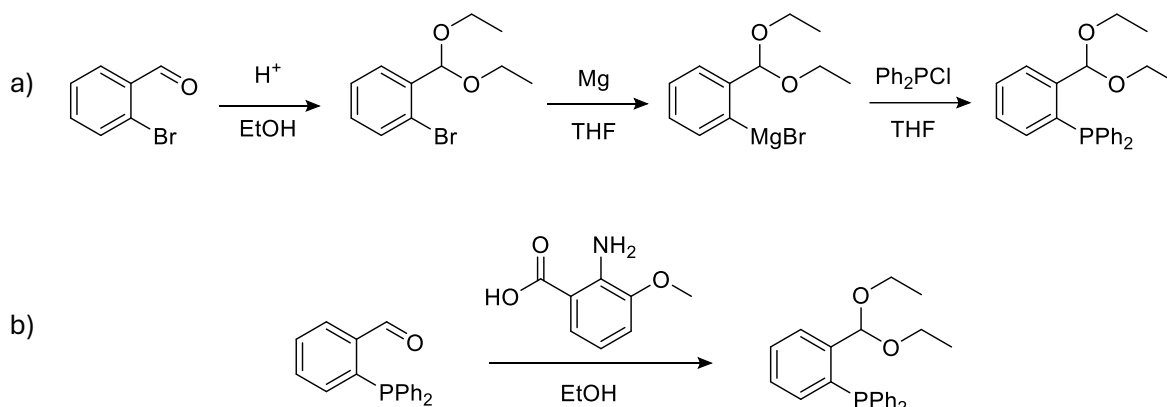
*Scheme 2.9 a) Previously reported preparation of **L7** by Grotjahn and Lo[16]. b) Previously reported unexpected preparation of **L7** by Elsegood* et al.[17]*.*

52

It is apparent that at some stage of this failed imine synthesis, solvent ethanol was able to behave unexpectedly as a nucleophile without an obvious catalyst for this transformation. Given the absence of any strong acid used in the system, potential alternative catalytic processes were considered. As the length of reaction was significantly greater than that later established as necessary for synthesis of **L1**, the potential catalytic behaviour of the mildly basic ethanolamine at these longer timescales was explored. 2-(diphenylphosphino)benzaldehyde was refluxed with varying quantities of ethanolamine in ethanol and monitored by $^{31}P\{^{1}H\}$ NMR spectroscopy (Table 2.10).

Table 2.10 - Reaction conditions of investigative reactions performed in attempted **L7** synthesis.

Entry	2-aminoethanol / mmol	[RuCl$_2$(*p*-cymene)]$_2$ / mol%	Time / h	Spectrum
1)	2	-	24	*a*
2)	0.25	-	24	*b*
3)	-	-	24	*c*
4)	-	-	7 days	*d*
5)	-	0.5	24	*e*
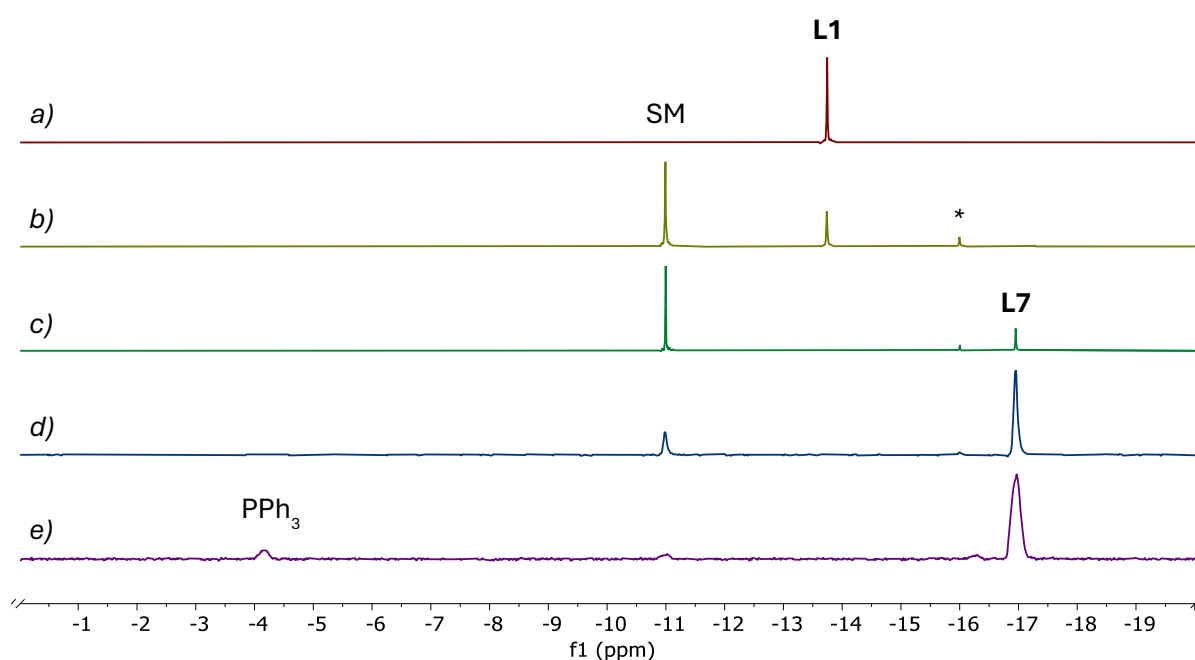
Figure 2.18 - ^{1}H NMR spectra of crude reaction mixtures described in Table 2.10. SM = Starting material 2-(diphenylphosphino)benzaldehyde. * = Unknown intermediate.

The direct repeat of the originally attempted preparation (Table 2.10, Entry 1) was not successful in reproducing **L7**, instead producing the expected **L1** as the sole product after 24 h, seen as a signal at -13.8 ppm (Figure 2.18a). Similarly, use of a sub-stoichiometric quantity of ethanolamine resulted in partial reaction to produce imine, with substantial remaining starting aldehyde (-11.0 ppm), though an unknown impurity was noted in low quantity at -16.0 ppm. Hence, standard imine preparation conditions do not appear to typically result in an acetal side product even after 24 h reflux. When the aldehyde alone was refluxed in absolute ethanol, however, a peak at -17.0 ppm became visible, showing partial conversion to **L7**, albeit in only 25 % conversion (NMR yield, Figure 2.18c). The unknown peak at -16.0 ppm was once again visible, so is tentatively assigned as an intermediate in synthesis of **L7**.

As Elsegood *et al*. reported an NMR yield of approximately 60 % after reflux for 7 days[17], reflux was continued, and crude NMR after 7 days showed an NMR yield of 79 % **L7** (Figure 2.18d). It is concluded that this acetal formation will occur spontaneously with heating, though gives much poorer yield than observed in initial reaction; the mild basicity of the imine formation conditions even seemed to inhibit acetal formation. Therefore, an alternative contaminant was suspected as the catalyst in this case.

It was proposed that potential glassware contamination with catalytic quantities of transition metal could have catalytically activated the carbonyl. A further experiment was performed using a catalytic quantity (0.5 mol%) of our most commonly used Ru(II) precursor, [RuCl$_2$(*p*-cymene)]$_2$ (Table 2.10, Entry 5). After only 16 h, crude ^{31}P{^{1}H} NMR spectroscopy showed >95 % conversion of aldehyde, giving two products: **L7**, in 87 % yield, and triphenylphosphine in 8 % yield as a decarbonylation byproduct. No further purification was performed.
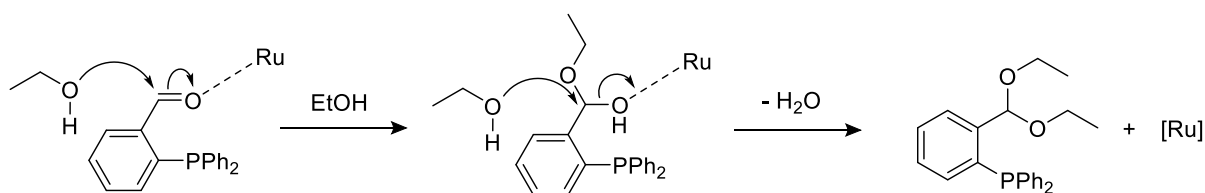
*Scheme 2.10 - Proposed catalytic activation of 2-(diphenylphosphino)benzaldehyde by [Ru] and formation of **L7**.*

2.3.2 Reactions of Ru(II) with 2-(diphenylphosphino)benzaldehyde

To investigate this aldehyde activation, direct reactions were performed between [RuCl$_2$(*p*-cymene)]$_2$ and 2-(diphenylphosphino)benzaldehyde. Initially, conditions shown in Scheme 2.4 were repeated, using excess aldehyde and performing reflux overnight in toluene. This gave a single product as a beige solid in high yield: examination of ^{31}P{^{1}H} and ^{1}H NMR spectra

allowed assignment as the known complex [Ru(CO)$_2$Cl$_2$(PPh$_3$)$_2$], with identity supported by LRMS ((ES+/Q-TOF) m/z: [M+Na]+ Calcd for C$_{38}$H$_{30}$Cl$_2$NaO$_2$P$_2$Ru 775.00; Found 775.00). Fortunately, crystals suitable for X-ray diffraction were grown from vapour diffusion of diethyl ether into a concentrated solution of [Ru(CO)$_2$Cl$_2$(PPh$_3$)$_2$] in DCM, confirming the reaction led to complete decarbonylation of aldehyde by transfer of the carbonyl to ruthenium with the aldehyde proton undergoing transfer to the phenyl ring.
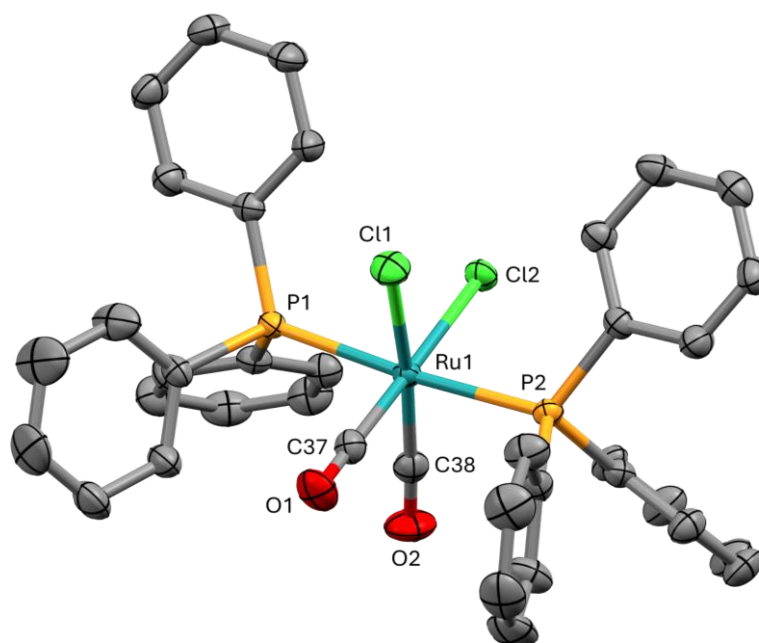
Figure 2.19 - Crystal structure obtained of Ru(CO)$_2$Cl$_2$(PPh$_3$)$_2$ with 50 % thermal ellipsoids and hydrogen atoms removed for clarity. Asymmetric unit contained one molecule of complex.

Complex	Bond lengths (Å)		Bond angles (°)			
Ru(CO)$_2$Cl$_2$(PPh$_3$)$_2$	Ru1-P1	2.4221(4)	P1-Ru1-Cl1	90.556(17)	P2-Ru1-Cl1	88.744(17)
	Ru1-P2	2.4198(4)	P1-Ru1-Cl2	87.037(15)	P2-Ru1-Cl2	88.057(15)
	Ru1-Cl1	2.4563(5)	P1-Ru1-C37	93.51(6)	P2-Ru1-C37	91.34(6)
	Ru1-Cl2	2.4331(4)	P1-Ru1-C38	89.82(6)	P2-Ru1-C38	91.62(6)
	Ru1-C37	1.877(2)	P1-Ru1-P2	174.948(16)	C38-Ru1-C37	89.82(9)
	Ru1-C38	1.869(2)	Cl1-Ru1-Cl2	95.835(17)	C38-Ru1-Cl2	92.76(6)
	C37-O1	1.136(3)	Cl1-Ru1-C37	81.59(6)	Cl1-Ru1-C38	171.40(6)
	C38-O2	1.134(3)	Ru1-C37-O1	178.74(19)	Cl2-Ru1-C37	177.37(6)
			Ru1-C38-O2	175.62(19)		

The obtained crystal structure is in accordance with data obtained from literature, showing *cis* coordination of both carbonyl and chloride ligands to each other, with the bulky PPh$_3$ ligands coordinated *trans* to each other[18]. All bond lengths and angles were found concordant with those previously reported, and the two expected v_{CO} bands were observed at 2061 cm^{-1} and 1998 cm^{-1}. To the best of our understanding, this specific method of preparation of [Ru(CO)$_2$Cl$_2$(PPh$_3$)$_2$] has not been previously reported although the preparation of transition metal carbonyl species by decarbonylation of amides is known.

Given the observed behaviour of Ru(II) species as catalysts for the preparation of **L7**, complexation of 2-(diphenylphosphino)benzaldehyde was also attempted in absolute ethanol under nitrogen atmosphere (Scheme 2.11), to investigate the possibility of direct formation of [RuCl$_2$(**L7**)$_2$] from the aldehyde as starting material.
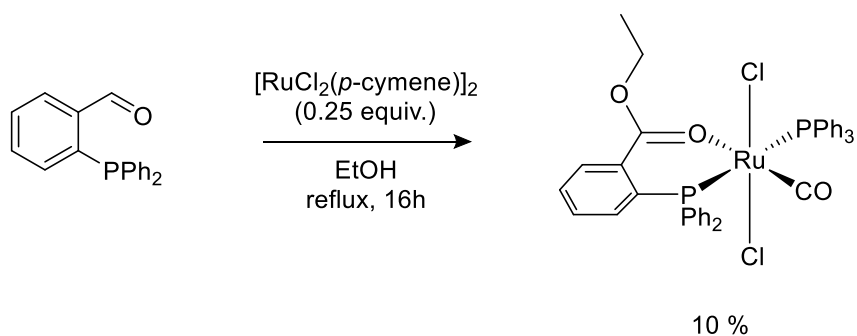
*Scheme 2.11 - Preparation of Ru(CO)Cl$_2$(**L7***)PPh$_3$.*

After 18 h, a small quantity of yellow precipitate formed and was isolated by filtration under nitrogen. NMR analysis showed two doublets in the ^{31}P{^{1}H} spectrum at 34.1 ppm and 31.5 ppm with a very large coupling of J_{PP} = 356.4 Hz. Indeed, the resultant roofing effect was so large that initial assessment of the NMR spectrum appeared to only show two singlets at 33.0 ppm and 32.6 ppm, with the outer peak of each doublet far smaller than the inside peak. In the ^{1}H NMR spectrum, a triplet and quartet in the aliphatic region suggested an ethyl arm, though neither the signal broadening observed in [RuCl$_2$(**L7**)$_2$] nor any sign of diastereomeric behaviour was seen. In LRMS the typical isotope pattern for only one ruthenium-containing species was observed, confirming the precipitate was a Ru(II) coordinate species. To identify the complex, crystals suitable for X-ray crystallography were successfully grown by vapour diffusion of Et$_2$O into concentrated solution in DCM to give fine yellow block-like crystals, allowing assignment of structure as the novel [Ru(CO)Cl$_2$(**L7***)PPh$_3$] in 10 % yield (Figure 2.20).

56
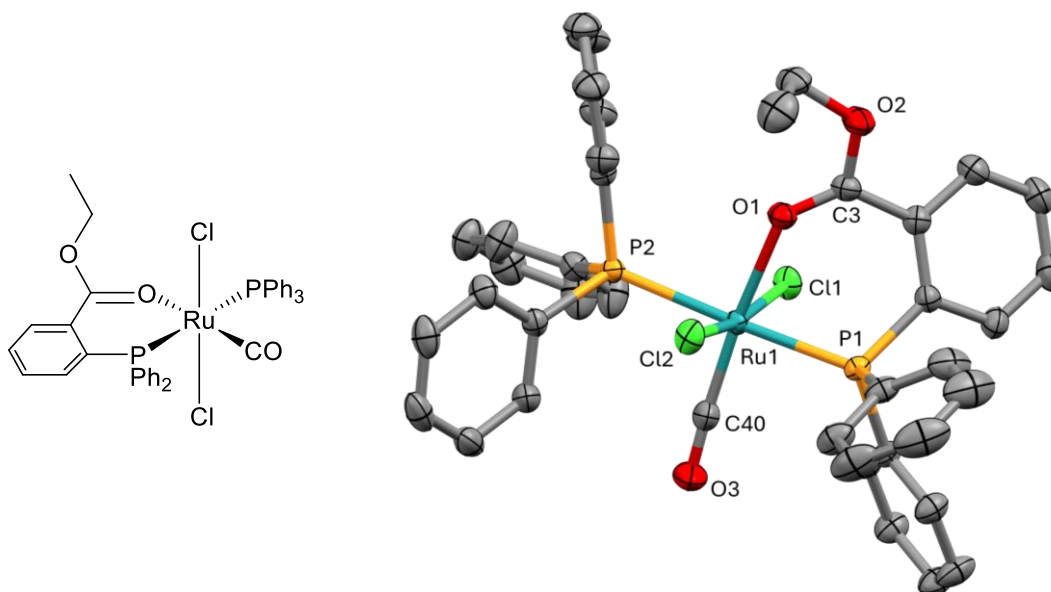
*Figure 2.20 – Left: Ru(CO)Cl₂(**L7***)PPh₃. Right: Single crystal structure obtained of [Ru(CO)Cl₂(**L7***)PPh₃] with 50 % thermal ellipsoids and hydrogen atoms removed for clarity. Asymmetric unit contained one molecule of complex.*

Complex	Bond lengths (Å)		Bond angles (°)		
[Ru(CO)Cl₂(**L7***)PPh₃]	Ru1-P1	2.3469(5)	P1-Ru1-Cl1	87.107(17)	P2-Ru1-Cl1	93.489(17)
	Ru1-P2	2.4181(5)	P1-Ru1-Cl2	94.245(17)	P2-Ru1-Cl2	84.628(17)
	Ru1-Cl1	2.4021(5)	P1-Ru1-O1	83.37(4)	P2-Ru1-O1	93.91(4)
	Ru1-Cl2	2.3802(5)	P1-Ru1-C40	91.17(7)	P2-Ru1-C40	91.53(7)
	Ru1-O1	2.1864(13)	P1-Ru1-P2	177.151(17)	Cl2-Ru1-O1	84.55(4)
	Ru1-C40	1.810(2)	Cl1-Ru1-O1	84.44(4)	Cl2-Ru1-C40	94.34(7)
	C3-O1	1.234(2)	Cl1-Ru1-C40	96.87(7)	Cl1-Ru1-Cl2	168.672(18)
	C3-O2	1.319(2)	Ru1-C40-O3	176.7(2)	O1-Ru1-C40	174.32(8)
	C40-O3	1.153(3)				

The observed species appears to be the product of decarbonylation of one equivalent of 2-(diphenylphosphino)benzaldehyde, as seen in the preparation of [Ru(CO)₂Cl₂(PPh₃)₂], with a second aldehyde molecule undergoing initial aldehyde C-H activation to create an intermediate hydride species and organometallic chelate ring susceptible to back-side attack by ethanol solvent, giving the second ligand as a variation of **L7**, assigned **L7***.

The observed crystal structure is supported by LRMS ((ES+/Q-TOF) m/z: [M-Cl]⁺ Calcd for C₄₀H₃₄O₃P₂ClRu 761.07; Found 761.07). FTIR also showed a single stretching frequency at 1938 cm⁻¹ in the region typical for C≡O. Additionally, a signal at 1646 cm⁻¹ is assigned to C=O stretching, further informing **L7*** exists as a coordinated ethyl ester in the solid state.
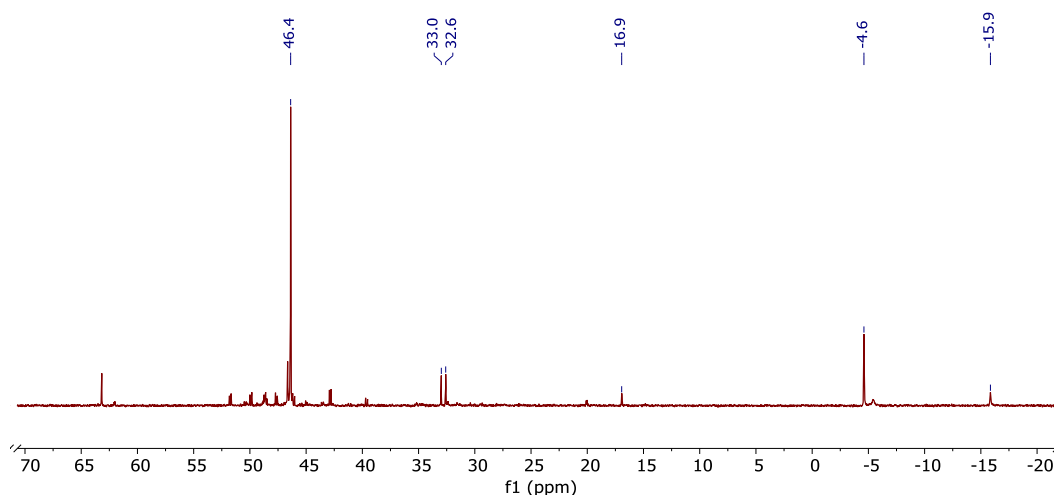
*Figure 2.21 – $^{31}P\{^1H\}$ NMR spectrum of reduced filtrate remaining after isolation of [Ru(CO)Cl$_2$(**L7***)PPh$_3$].*

To further investigate the chemistry occurring in this reaction between [RuCl$_2$(*p*-cymene)]$_2$, 2-(diphenylphosphino)benzaldehyde and ethanol, the reaction filtrate was reduced to give a brown solid. NMR analysis of the solid showed many signals in the $^{31}P\{^1H\}$ NMR spectrum, including free PPh$_3$ and a small quantity of free **L7**. Also visible were a small quantity of dissolved [Ru(CO)Cl$_2$(**L7***)PPh$_3$] (only the larger of the doublet peaks shown at δ: 33.0, 32.6 ppm) and an even smaller yield of [Ru(CO)$_2$Cl$_2$(PPh$_3$)$_2$] (δ: 16.9 ppm), suggesting decarbonylation is a minor side reaction. The notable major signal in the spectrum was visible at +46.4 ppm in CDCl$_3$. Initially, it was theorised that this species was [RuCl$_2$(**L7**)$_2$], but the characteristic broad signals in the aliphatic region of the ^1H NMR spectroscopy were not present. However, the major aliphatic signals did include a quartet and triplet at 3.63 ppm and 1.14 ppm respectively, showing a slightly more deshielded ethyl terminal group than seen in [Ru(CO)Cl$_2$(**L7***)PPh$_3$], with integration indicating two ethyl groups present. Given the Ru-catalysed activation of aldehydes to ethanol has been established, and the $^{31}P\{^1H\}$ NMR signal is in the same region as those observed in other symmetrical bis-bidentate species, a tentative structure is proposed (Figure 2.22), though the only available literature data for this compound proved inconsistent as Das *et al*. reported multiple phosphorus environments[19]. However, no solid conclusion may be drawn as the obtained data is not conclusive. In future work this compound would need to be isolated and further analysis attempted, including using MS and crystallographic techniques to properly assign it.
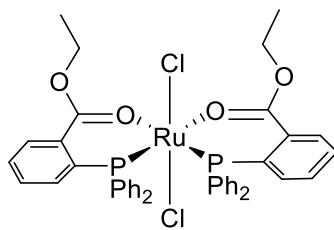
Figure 2.22 - Proposed second major product of reaction of 2-(diphenylphosphino)benzaldehyde with

[RuCl₂(p-cymene)]₂.

2.4 Exploration of PNN and PNS ligand systems

As previously noted, PNN complexes are frequently highly active, particularly in hydrogen transfer type reactions, and recent work has also shown expansion into PNS systems[5,20] with particular note of the hemilability of the sulfur group made[19]. Hence, a series of PNN and PNS ligands were targeted for further investigation in this series.

2.4.1   Preparation of PNN and PNNP ligands

Due to significant difference in bonding behaviour observed between [Ru(**L1**)$_2$]Cl$_2$ and [RuCl$_2$(**L6**)$_2$], the basic structures of **L1** and **L6** were modified in design of PNN ligands selected to investigate. The targeted ligands are summarised in Figure 2.23.
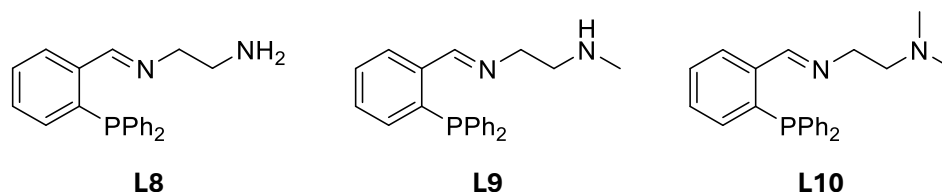
Figure 2.23 - Targeted PNN ligands

Attempts to use ethylenediamine as an ethanolamine substitute were unfortunately largely unsuccessful, as the aldehyde was prone to reacting at both ends of the ethylenediamine even in large excess of amine, giving mixtures which could not be easily separated. Use of a modified literature procedure[8] did successfully give the monoimine **L8** as a red oil by slow addition of aldehyde at room temperature (Scheme 2.12), but attempts to purify resulted in internal reaction once again giving the known diimine product **L11** shown in Scheme 2.13. Further attempts to isolate the imine **L8** were not pursued.
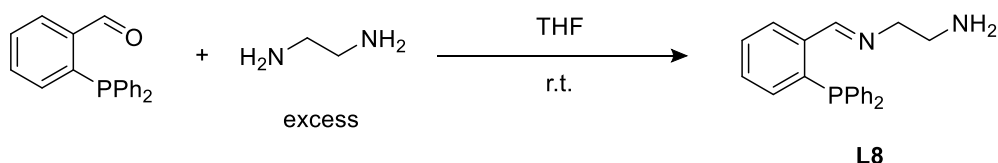
Scheme 2.12 - Attempted preparation of monoimine L8 by dropwise addition of solvated aldehyde over 4 h.
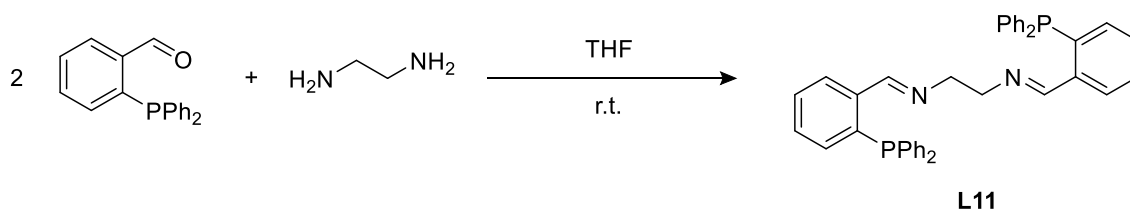
Scheme 2.13 - Preparation of diimine ligand L11.

Instead, the methylated and dimethylated analogues **L9** and **L10** were investigated, using the same preparation method as used in Scheme 2.2. **L10** was produced readily in high yield and purity. However, attempts to prepare **L9** produced a crude mixture which could not be separated by traditional methods, also reported in literature[21]. Yang *et al.* reported that the mixture was a result of a rehydration of the imine produced to give an amino alcohol as the major product (Figure 2.24).
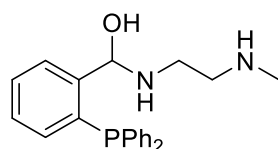
*Figure 2.24 - Previously reported structure of the major form of **L9**.[21]*

^{1}H NMR data in this work also demonstrated a mixture of major amine and minor imine compounds, though MS data did not support the existence of a hydrated form. Furthermore, three separate multiplets in the ^{1}H NMR aliphatic region of the major product suggested a non-linear system was present. As it is known that imidazolidines may be prepared from the reaction of aldehyde with 1,2-diamines where both amino groups are secondary[22], it stands to reason that the two products produced are an imidazolidine primary product and a linear imine minor product. This type of tautomeric equilibrium has also been reported in a reaction of N-methylethylenediamine with various benzaldehydes by Witek *et al.*, whereby the nature of substitution on the benzaldehyde influences the degree to which the heterocycle is favoured[23]. Hence, it is concluded that the ligand **L9** exists as a tautomeric mixture of linear imine **L9a** as the minor product and imidazolidine **L9b** as the major product.
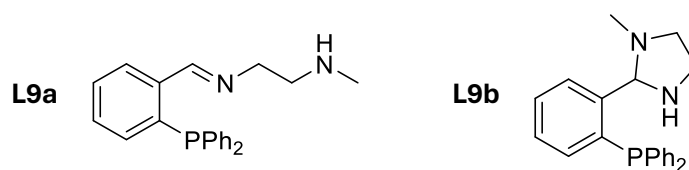
*Figure 2.25 – Proposed structure of **L9a**, minor component, and **L9b**, major component, of **L9**.*

2.4.2   Complexation of PNN & PNNP ligands with Ru(II)

Preparation of the previously reported [RuCl$_2$(**L11**)] was achieved readily *via* literature methods, with **L11** binding in tetradentate fashion to give a red solid (Scheme 2.14). Based on ^{1}H NMR data, the ligand remains planar and symmetrical, with no distortion of the middle chelate ring; only one singlet attributed to the aliphatic CH$_2$ protons is visible in the spectrum.
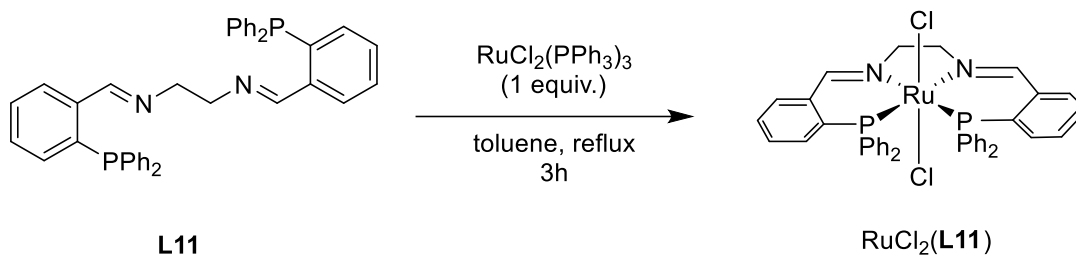
*Scheme 2.14 - Preparation of RuCl$_2$(**L11**).*

Complexation of the two ligands **L9** and **L10** was attempted by reaction with [RuCl$_2$(*p*-cymene)]$_2$ according to the conditions in Scheme 2.4, as has been successful for the preparation of the [RuCl$_2$(PNO)$_2$] set.

L9 has been reported in literature to complex with Pt and Pd as an imine regardless of its existence as a tautomeric mixture[21]. Here, the mixture was applied in excess to a solution of [RuCl$_2$(*p*-cymene)]$_2$ in toluene and gave a major product which could be isolated in moderate yield following filtration and precipitation induced with counter-solvent as a yellow-orange powder. This complex was confirmed to have a bis-ligated structure of [RuCl$_2$(**L9**)$_2$] by HRMS ((ES+/Q-TOF) m/z: [M-Cl]$^+$ Calcd for C$_{44}$H$_{46}$N$_4$P$_2$ClRu 829.1930; Found 829.1939). According to ^{31}P{^{1}H} NMR spectroscopy the species contained two distinct phosphorus environments in the downfield complex region of the spectrum (δ: +50.8 and +35.7 ppm) which coupled together, indicating two different binding modes of **L9**. The ^{1}H NMR spectrum supports this, as two signals in the imine region suggest that two different imine proton signals exist in the complex. A notable absence of amine proton signals in the complex supports the notion that only the imine tautomer **L9a** coordinates to a metal centre. In FTIR, a slight increase in intensity of the C=N stretch absorbance and a wavenumber shift from 1655 cm^{-1} to 1633 cm^{-1} upon complexation support the bond lengthening associated with an imine bound to Ru(II) observed in previous PNO complexes. Binding of two imine nitrogens in an inequivalent fashion is corroborated by a shift of the imine carbon in the ^{13}C NMR spectrum to give two separate signals, both downfield of the free ligand **L9a** (Table 2.11), demonstrating the expected loss of electron density due to coordination of nitrogen.

*Table 2.11 - Key NMR signals of **L9a** and [RuCl(**L9**)$_2$]Cl.*

	L9a	[RuCl(**L9**)$_2$]Cl	
^{1}H δ H*C*=N / ppm	8.82	9.18	8.79
^{13}C{^{1}H} δ H*C*=N / ppm	161.0	169.7	169.3
^{31}P{^{1}H} δ / ppm	-12.2	50.8	35.7

Examination of key NMR signals (Table 2.11) suggests a mixture of tridentate and bidentate binding, so the complex is accordingly labelled [RuCl(**L9**)$_2$]Cl. One of the imine proton signals demonstrates a downfield shift previously observed in tridentate binding ligands, whilst the other shows the slight upfield shift associated with bidentate behaviour in previous complexes. Similarly, the upfield shift of +63 ppm of one phosphorus signal is indicative of the tridentate binding observed in tridentate complexes of **L1**, but the smaller shift of +47.9 ppm of the other is more akin to the more shielded ^{31}P{^{1}H} NMR signal observed in bidentate species [RuCl$_2$(**L6**)$_2$]. Most notably, the aliphatic region showed eight different signals attributed to -CH$_2$- protons, as well as two separate singlets for the aminomethyl protons. This demonstrates that, as in other bis-ligated species explored in this work, the pendant arms demonstrate steric constraints preventing free motion in solution, and in this instance, are certainly asymmetrically bound.

Crystals suitable for single crystal X-ray crystallography were able to be grown by vapour diffusion of Et$_2$O into DCM. The crystal quality was too poor to provide accurate bond lengths or angles, but coordination sphere was able to be determined and is shown in Figure 2.26. Gratifyingly, this observed structure confirms the bis-ligated system, and additionally shows the two different binding modes predicted. One ligand adopts a tridentate binding mode, featuring two envelope-shaped chelate rings. The other ligand binds in a bidentate fashion, with the pendant amine arm positioned away from the bulky phenyl groups. In this conformation, all three binding nitrogens are *cis* to each other. One chlorine is directly bound to the ruthenium centre as a chloride ligand, with the other existing near the unbound amine in an outer sphere position. It is noted that this is the only isomer observed of this species.
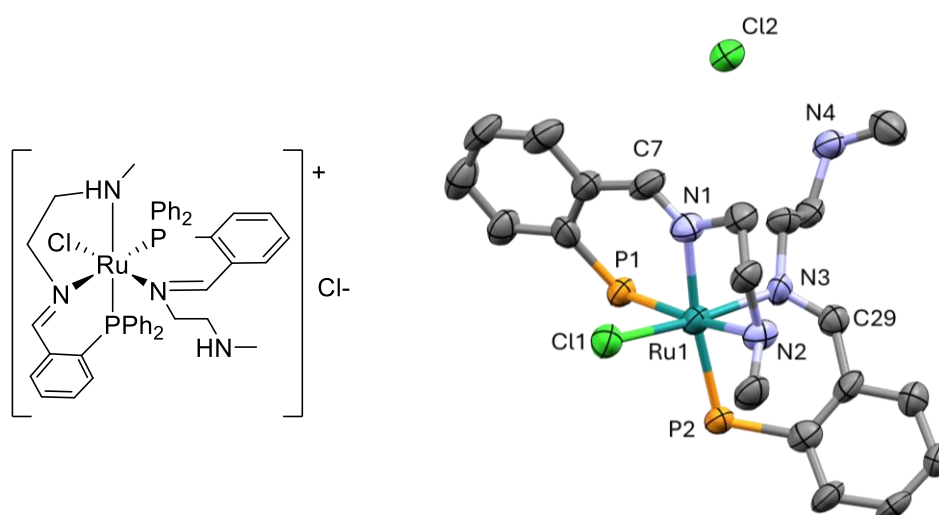
*Figure 2.26 - Crystal structure obtained of [RuCl(**L9**)$_2$]Cl with 50 % thermal ellipsoids and hydrogen atoms and phenyl groups removed for clarity. Asymmetric unit contained one molecule of complex and two molecules of crystal growth solvent (DCM) which have been removed for clarity.*

Attempted complexation of **L10** was less straightforward. Reflux of **L10** with [RuCl$_2$(*p*-cymene)]$_2$ did not initially give the anticipated bis-ligated product in any significant yield. A small amount of dark brown solid directly precipitated from the reaction mixture and gave the expected mass of a bis-ligated species by LRMS ((ES+/Q-TOF) m/z: [M-Cl]$^+$ Calcd for C$_{46}$H$_{50}$N$_4$P$_2$ClRu 857.22; Found 857.22) but the extremely poor yield (< 20 mg) prevented full analysis. Addition of hexane induced precipitation of a second complex in poor yield featuring two mutually coupled phosphorus environments in ^{31}P{^{1}H} NMR. Crystals suitable for X-ray crystallography were grown by vapour diffusion of Et$_2$O into DCM and surprisingly showed one coordinated molecule of **L10**, with a molecule of 2-(diphenylphosphino)benzaldehyde directly coordinated as the second ligand (Figure 2.27). This complex was assigned [RuCl(**L10**)(PPh$_3$^{CO})].
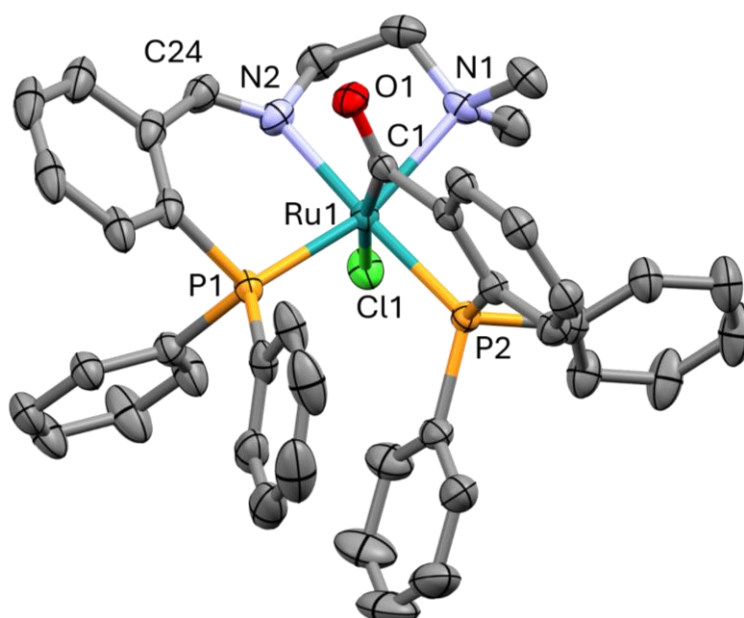
*Figure 2.27 – Single crystal structure obtained of [RuCl(**L10**)(PPh$_3$^{CO})] with 50 % thermal ellipsoids and hydrogen atoms removed for clarity. Asymmetric unit contained one molecule of complex and one molecule of Et$_2$O solvent.*

Complex	Bond lengths (Å)		Bond angles (°)			
[RuCl(**L10**)(PPh$_3$^{CO})]	Ru1-P1	2.2818(5)	P1-Ru1-Cl1	103.257(19)	N1-Ru1-Cl1	85.69(5)
	Ru1-P2	2.2737(5)	P1-Ru1-P2	95.92(2)	N1-Ru1-P2	97.59(5)
	Ru1-N1	2.3524(18)	P1-Ru1-N2	87.13(6)	N1-Ru1-N2	79.28(7)
	Ru1-N2	2.1063(18)	P1-Ru1-C1	85.71(6)	N1-Ru1-C1	86.06(7)
	Ru1-Cl1	2.5762(5)	P1-Ru1-N1	163.54(5)	C1-Ru1-N2	94.18(8)
	Ru1-C1	2.006(2)	Cl1-Ru1-P2	91.804(19)	C1-Ru1-P2	85.34(6)
	C24-N2	1.283(3)	Cl1-Ru1-N2	88.19(5)	C1-Ru1-Cl1	170.85(6)
	C1-O1	1.224(3)	Ru1-C1-O1	126.27(16)	N2-Ru1-P2	176.86(6)

This system was also confirmed by HRMS ((ES+/Q-TOF) m/z: [M-Cl]$^+$ Calcd for $C_{42}H_{39}N_2OP_2Ru$ 751.1581; Found 751.1602). The crystal structure shows a distorted octahedral structure with one chloride ligand, distorted away from the bulky phenyl groups. One single ligand of **L10** bound in a tridentate coordination mode with the expected two chelate rings adopting distorted envelope conformation. The asymmetry of the CH_2 protons is demonstrated by the existence of four signals in the aliphatic region; the two separate singlet signals for the methyl groups further demonstrate the fixed conformation due to binding of the amino nitrogen. The aldehyde ligand PPh$_3^{CO}$ binds in a bidentate fashion, forming a planar 5-membered metallacycle with observed Ru-P2 bond length typical for this type of σ donation. However, the Ru-C1 bond length is the shortest of all Ru-L bonds; the absence of an aldehyde proton suggests covalent-type binding of the aldehyde carbon. This is also seen with the absence of an aldehyde proton in the ^{1}H NMR spectrum. Examination of the ^{13}C{^{1}H} NMR spectrum however shows an absence of the typically highly deshielded aldehyde carbon, with a signal at 161.0 ppm, much more shielded than free 2-(diphenylphosphino)benzaldehyde (191.7 ppm). The observed chemical shift of the C=O carbon is more typical of the coordinated imine carbons, suggesting substantial back-donation from the ruthenium centre to the carbonyl carbon. This donation does not seem to significantly lengthen the carbonyl bond, which is reported as similar to aldehyde C=O bond lengths in uncoordinated aldehydes.

The unexpected formation of this species was initially suspected to be due to growth of crystals in an aerated environment over the course of several weeks permitting hydrative cleavage of the imine bond during crystal growth. However, agreement of both mass spectrometry and NMR spectroscopic analysis of the solid product with the reported structure demonstrated that the crystal structure obtained is indeed representative of the solid product obtained. Therefore, the imine hydration must have occurred due to the incidental presence of water in some stage of the complex synthesis. Given that in the initial preparation of ligand **L10**, no *in situ* drying agent was used, it is assumed that not all water was successfully removed from the ligand in purification, and this is the water source. Hydrative cleavage is proposed to occur after complexation of **L10** (Scheme 2.15).
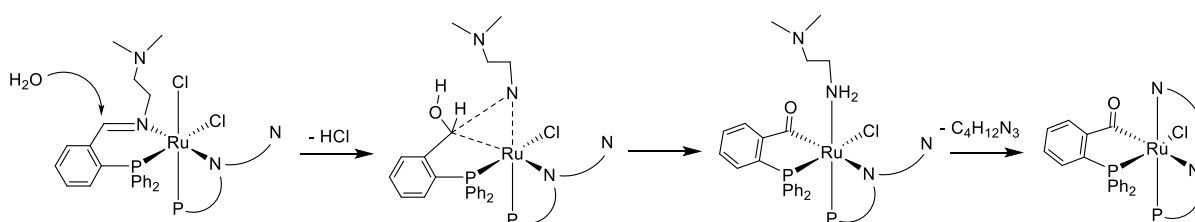
*Scheme 2.15 – Potential pathway to [RuCl(**L10**)(PPh$_3^{CO}$)] from [RuCl$_2$(**L10**)$_2$].*

Complexation with **L10** was repeated, this time using a sample of **L10** which was prepared over Na_2SO_4 and then stirred in toluene over 3 Å molecular sieves overnight. Identical conditions were used for complexation with [RuCl$_2$(p-cymene)]$_2$ were used as previously. A low yield (23 %) of [RuCl$_2$(**L10**)$_2$] was successfully prepared as an induced precipitate, with identity confirmed by HRMS (HRMS (ES+/Q-TOF) m/z: [M-Cl]$^+$ Calcd for $C_{46}H_{50}N_4P_2ClRu$ 857.2243; Found 857.2269.). Examination of the NMR spectroscopic data suggested a bis-ligated symmetrical bidentate structure akin to [RuCl$_2$(**L6**)$_2$]: a single singlet in the $^{31}P\{^1H\}$ NMR spectrum at 48.8 ppm, a single imine proton signal slightly upfield of free ligand (complex: 8.71 ppm, **L10**: 8.90 ppm), and the appearance of four separate CH$_2$ environments in the ^1H NMR spectrum all are analogous to [RuCl$_2$(**L6**)$_2$]. Additionally, the non-coordination of the amine nitrogens is indicated by the appearance of all methyl protons in the ^1H NMR spectrum as a single singlet integrating to 12 protons at 1.76 ppm.
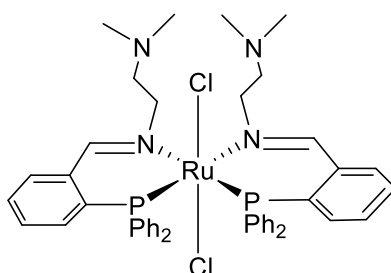
*Figure 2.28 - Proposed structure of RuCl$_2$(**L10**)$_2$.*

No other synthesis required such stringent exclusion of water for isolation of a single product in good yield. It is apparent this ligand system is particularly sensitive to cleavage. Given the low yield of both [RuCl(**L10**)(PPh$_3$^{CO})] (15 %) and [RuCl$_2$(**L10**)$_2$] (23 %), it is proposed that the increased bulk created by use of a tertiary amine pendant arm inhibits stable formation of a bis-ligated species, such that hydration of an imine pre-activated through complexation with ruthenium is particularly favourable.

2.4.3 Preparation of PNS ligands

Preparation of a range of similar imine-based PNS ligands was attempted by the same method as the PNO series (Scheme 2.16).
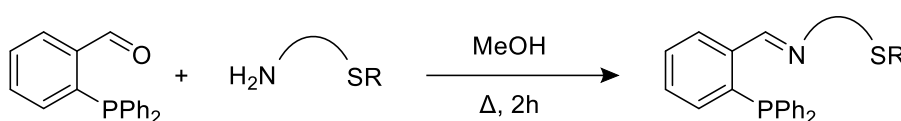
Scheme 2.16 - Standard conditions used for preparation of targeted PNS ligands.

L12   67 %   δ: -17.3 ppm

L13   67 %   δ: -17.2 ppm

L14   93 %   δ: -13.6 ppm

L15   99 %   δ: -13.4 ppm

L16   64 %   δ: -14.6 ppm

L17   89 %   δ: -19.3 ppm

L18   91 %   δ: -16.0 ppm
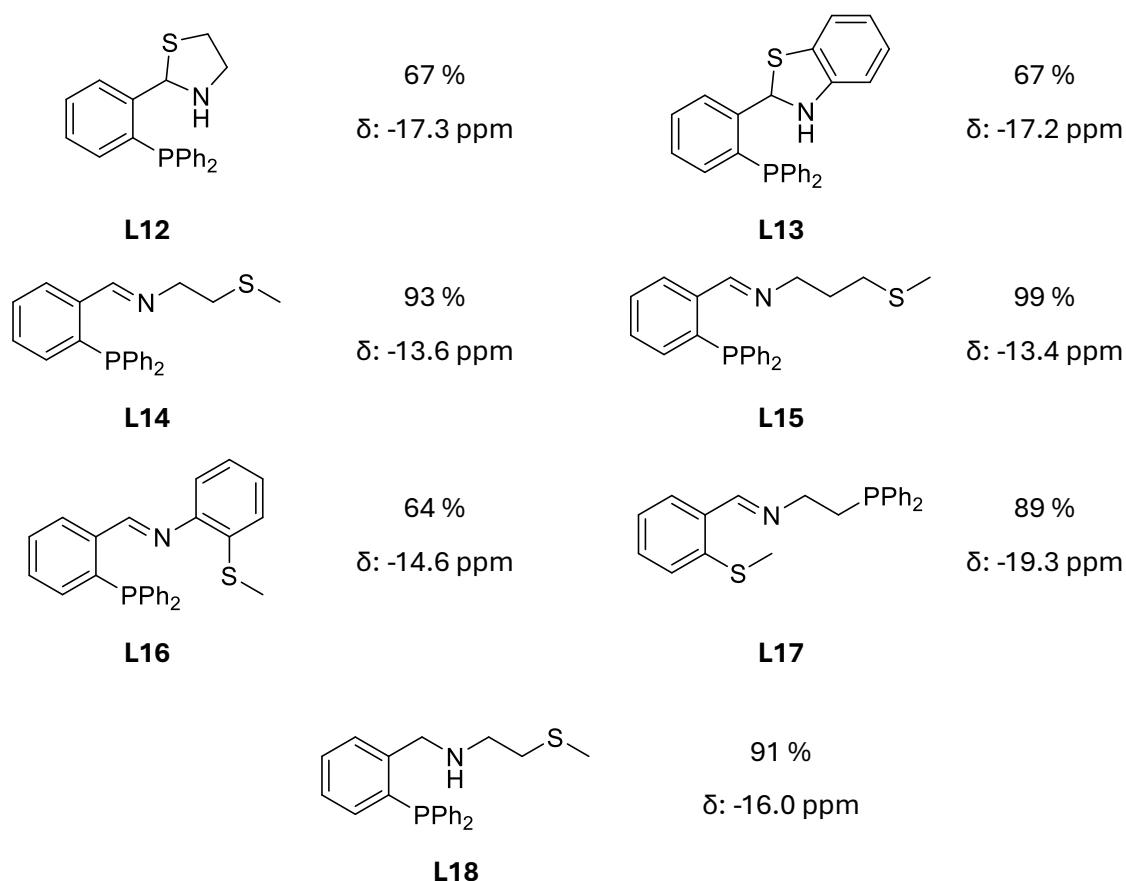
Figure 2.29 - Summary of PNS ligands prepared in this work. Synthetic yield and $^{31}P\{^{1}H\}$ NMR chemical shift shown.

Initial PNS targets were selected to mimic the structures of the PNO series where possible, and a range of imines and cyclised ligands were obtained (Figure 2.29). Attempts to obtain a free SH terminal arm through reaction of cysteamine with 2-(diphenylphosphino)benzaldehyde were unsuccessful, instead giving a thiazolidine ring structure (**L12**). Whilst ligand **L12** is unreported previously, similar cyclised compounds have been obtained through reaction of an aldehyde with a primary 1,2-aminothiol, including thiazolidine itself[24]. The cyclisation was evidenced by complete loss of the imine proton in ^{1}H NMR spectroscopy, with appearance of a moderately deshielded single proton signal at 6.21 ppm, indicating a single sp^{3} C-H adjacent to two heteroatoms. Four protons in the aliphatic heterocycle were, as expected, inequivalent, showing multiplet signals consistent with those observed in 2-phenylthiazolidine[25]. Hence it is presumed the adopted structure is an analogous envelope conformation with axial N-H and equatorial substitution at the 2 position. The previously reported cyclised ligand **L13** was also able to be produced readily per the method in Scheme 2.2.

Ligands **L14** and **L15** were obtained readily from their respective aminothioethers. Similar attempts to prepare **L16** required more forcing conditions: complete reaction required reflux in toluene using continuous removal of water, either through the use of Dean-Stark apparatus or

simply *in situ* inclusion of pre-activated 3 Å molecular sieves. Difficulty in synthesis is presumed due to increased steric bulk of product.
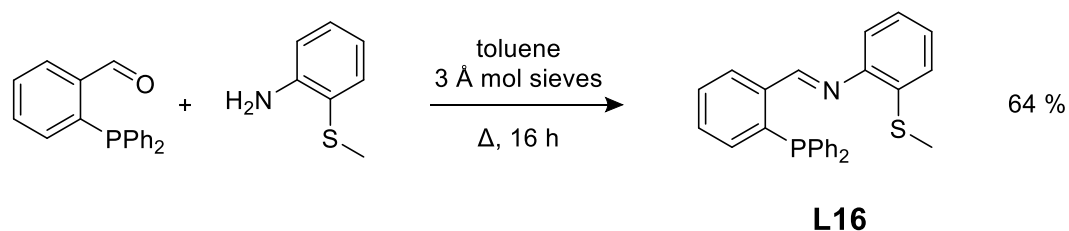
*Scheme 2.17 - Synthesis of **L16**.*

In order to further investigate the binding modes in the PNS ligand family, the ligands **L17** and **L18** were prepared. The previously reported[26] **L17** was obtained in high yield from 2-(diphenylphosphino)ethylamine and 2-(methylthio)benzaldehyde. **L18** could be prepared from treatment of **L14** with NaBH₄.
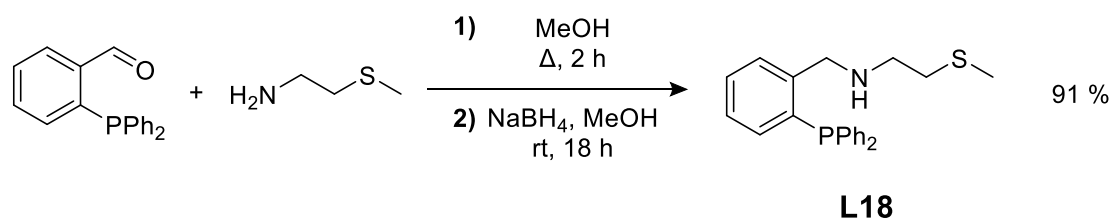
*Scheme 2.18 - Synthesis of **L18**.*

2.4.4 Complexation of PNS ligands

2.4.4.1 Complexation of **L12**

Initially upon addition of a large excess of **L12** to a solution of [RuCl₂(*p*-cymene)]₂ dissolved in room temperature toluene, a red precipitate immediately formed. This was then isolated by filtration and identified by LRMS (m/z: [M-Cl]⁺ Calcd for $C_{31}H_{34}NPClRuS$ 620.09; Found 620.08) as a complex featuring only a single equivalent of ligand **L12**, labelled complex [RuCl(**L12**)(*p*-cymene)]Cl. In the $^{31}P\{^{1}H\}$ NMR spectrum, a single species at 36.2 ppm is visible, showing a downfield shift of the ligand signal by +54.5 ppm upon complexation. Poor solubility in CDCl₃ made fine detail in the ^{1}H NMR spectrum difficult to determine, but a set of two proton signals at 5.32 and 5.62 ppm were attributed the coordinated *p*-cymene ligand. The binding mode is presumed to be η⁶ with rotation restricted by steric constraints of other ligands, as in precursor [RuCl(**L12**)(*p*-cymene)]Cl. A series of four broad multiplet signals at 3.83, 3.71, 3.56 and

68

3.13 ppm each integrating to one hydrogen were attributed to the single **L12** ligand and its four inequivalent protons. The absence of an imine proton and the presence of a signal at 6.28 ppm demonstrate a slightly deshielded amine proton, indicating the heterocycle coordinates with retained cyclisation, unlike the PNN heterocyclic ligand **L9b**. This is supported by the absence of a C=N stretching frequency in FTIR. Coordination is proposed as PN-type based on the existence of similar PN coordinate species[27], but in the absence of crystallographic data it is impossible to determine with certainty.
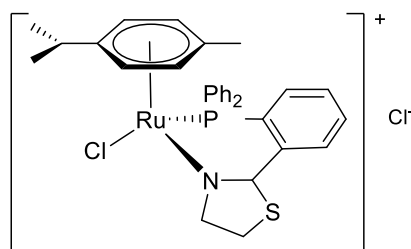
*Figure 2.30 - Proposed structure of [RuCl(**L12**)(p-cymene)]Cl.*

An attempt to prepare the bis-ligated analogue of [RuCl(**L12**)(p-cymene)]Cl was performed by adding solvated ligand **L12** directly to a pre-heated solution of [RuCl$_2$(p-cymene)]$_2$ to minimise competitive precipitation of [RuCl(**L12**)(p-cymene)]Cl. This led to the production of a yellow-brown solid, identified by LRMS as a bis-ligated analogue ([M-Cl]$^+$ Calcd for $C_{42}H_{40}N_2P_2S_2ClRu$ 835.08; Found 835.08). Interestingly, FTIR analysis of the solid crude solid mixture of isomers of [RuCl$_2$(**L12**)$_2$] showed absorbance at 1620 cm^{-1}, demonstrating the existence of a coordinated C=N bond. This suggests **L12** underwent ring-opening upon complexation when heated to reform an imine-containing ligand with a free thiol arm.
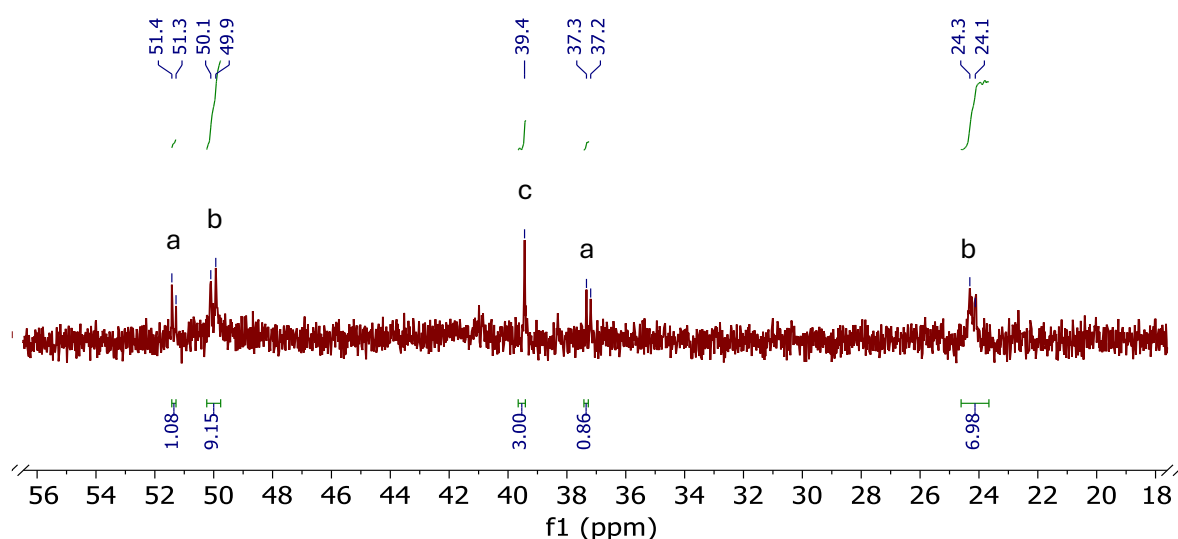
*Figure 2.31 - ^{31}P{^{1}H} NMR spectrum of crude mixture of [RuCl$_2$(**L12**)$_2$] showing three isomers formed, A B and C. No other signals were observed in the spectrum.*

NMR analysis was non-trivial due to poor solubility and multiple isomers observed, but appeared to support this potential ring-opening. $^{31}P\{^1H\}$ NMR analysis showed a mixture of three species which were not readily separable by recrystallisation in a ratio A:B:C of approximately 1:8:3. The major product [RuCl$_2$(**L12**)$_2$]-B showed a pair of doublets coupled together at 50.0 ppm and 24.2 ppm and accounted for approximately 65 % of product. The major product is therefore proposed to be an asymmetric species similar to [RuCl(**L9**)$_2$]Cl, so labelled [RuCl(**L12**)$_2$]Cl. Minor product [RuCl$_2$(**L12**)$_2$]-A was a second set of doublets coupled together at 51.4 and 37.3 ppm, tentatively assigned as an isomer of [RuCl(**L12**)$_2$]Cl. The final product [RuCl$_2$(**L12**)$_2$]-C appeared as a singlet, so was identified as a symmetrical species – the initial assumption was this species was a slightly shifted signal of [RuCl(**L12**)(*p*-cymene)]Cl, but no visible protons attributable to the *p*-cymene ligand and no appropriate signals in the mass spectrum preclude this as a possibility.

The ring-opening to reform an imine is supported by the presence of a pair of overlapping peaks at 8.78 and 8.76 ppm in the ^1H NMR spectrum, similar chemical shift to those signals reported for imines in bis-ligated species previously discussed. Unfortunately, due to the number of isomers and resultant overlapping signals in the 1H NMR spectrum, further detail about the structure was difficult to elucidate. However, broad multiplets in the aliphatic region show more than four aliphatic proton environments, with 7 overlapping broad multiplets between 4.15 and 2.60 ppm integrating to give 8 proton environments relative to the two imine proton signals. Hence, it is tentatively proposed that the binding mode of the primary obtained isomer in this system involves one tridentate coordinated imine tautomer of **L12** and one bidentate imine form of **L12** (Figure 2.32).
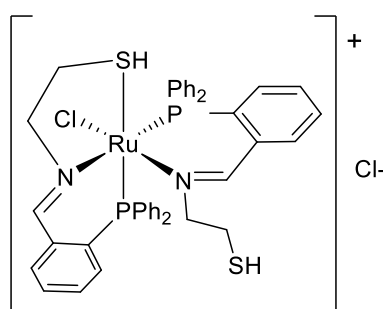
*Figure 2.32 - Proposed structure of [RuCl(**L12**)$_2$]Cl.*

Without successful isolation of a single isomer and crystallographic data to support this proposed structure, the structures of these species remain unconfirmed. Further work could explore synthesis with alternative ruthenium precursors attempt to bypass competitive production of [RuCl(**L12**)(*p*-cymene)]Cl and investigate control of the ring-opening of ligand **L12**. However, it is demonstrated that altering conditions alters the ligand structure in the complex.

*Table 2.12 - Key NMR data for **L12** and its complexes.*

	L12	[RuCl(**L12**)(*p*-cymene)]Cl	[RuCl(**L12**)$_2$]Cl	
^{1}H δ *H*CN / ppm	6.21	6.28	8.78	8.76
^{31}P{^{1}H} δ / ppm	17.3	36.2	50.0	24.4
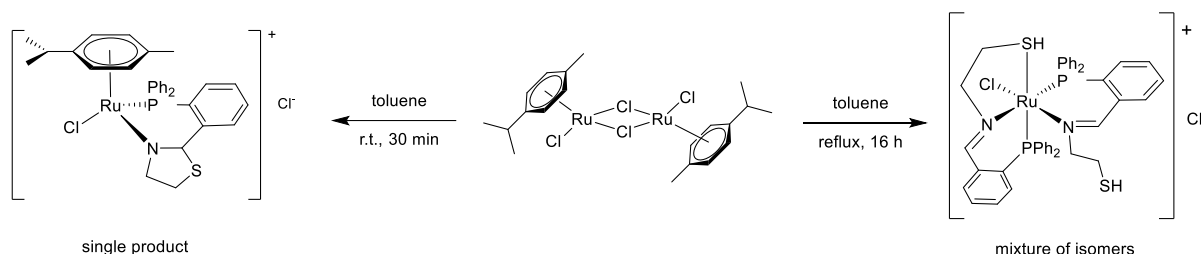
*Scheme 2.19 - Conditions used to prepare different complexes of **L12**.*

2.4.4.2   Complexation of linear aliphatic PNS ligands

The remaining aliphatic systems were also investigated. When reacted with [RuCl$_2$(*p*-cymene)]$_2$, ligand **L14** coordinated readily in a bis-ligated form, giving a single asymmetric product in excellent yield as yellow solid. The presence of two coordinated molecules of **L14** and chlorine was confirmed by HRMS (HRMS (ES+/Q-TOF) m/z: [M-Cl]$^+$ Calcd for C$_{44}$H$_{44}$N$_2$P$_2$S$_2$ClRu 863.1153; Found 863.1160), with two doublets in the ^{31}P{^{1}H} NMR spectrum coupling together (44.4, 41.1 ppm) confirming an asymmetric binding mode. Hence, the complex was labelled [RuCl(**L14**)$_2$]Cl and proposed to have the same bidentate/tridentate binding structure as seen in [RuCl(**L9**)$_2$]Cl. Key NMR signals are summarised in Table 2.13. As with [RuCl(**L9**)$_2$]Cl, two imine signals in the ^{1}H NMR spectrum were visible, as were two imine carbons in the ^{13}C spectrum. Again, eight separate aliphatic proton environments are also visible, demonstrating not only ligand inequivalence but steric restriction on free rotation, even when pendant arm is uncoordinated. Crystals suitable for X-ray crystallography were obtained from slow evaporation of a concentrated solution of [RuCl(**L14**)$_2$]Cl in DCM to give yellow needle-like crystals. The obtained structure is shown in Figure 2.33.

*Table 2.13 - Key NMR signals of **L14** and [RuCl(**L14**)$_2$]Cl.*

	L14	[RuCl(**L14**)$_2$]Cl	
^{1}H δ *H*C=N / ppm	8.89	9.15	9.11
^{13}{^{1}H}C δ H*C*=N / ppm	160.8	172.3	169.3
^{31}P{^{1}H} δ / ppm	-13.6	44.4	41.1
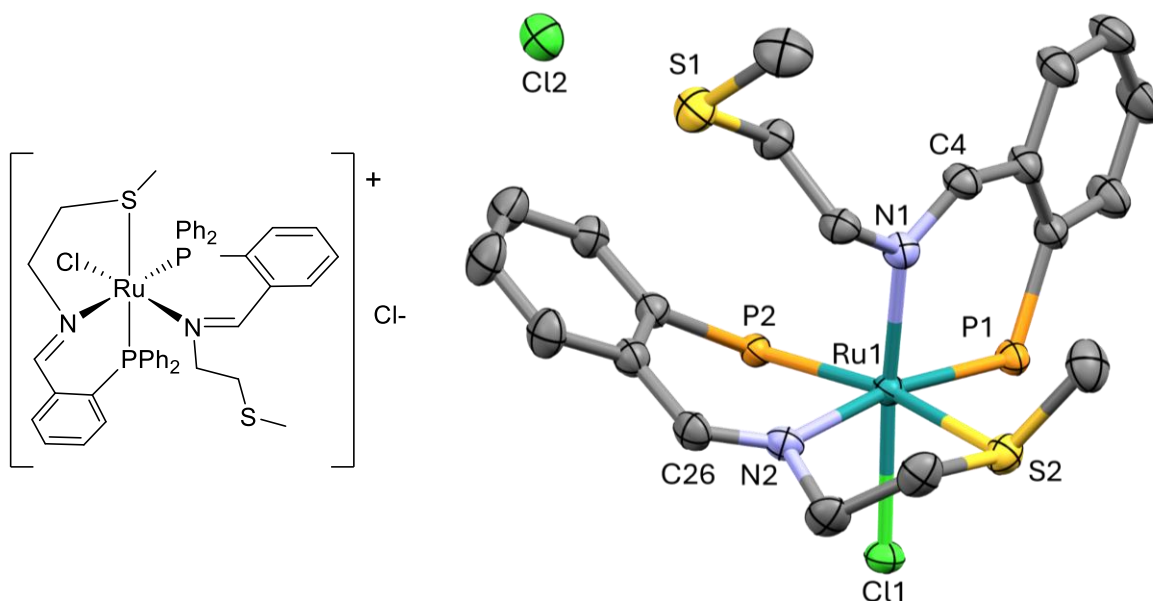
*Figure 2.33 - Crystal structure obtained of [RuCl(**L14**)₂]Cl with 50 % thermal ellipsoids and hydrogen atoms and phenyl groups removed for clarity. Asymmetric unit contained one molecule of complex and two molecules of crystal growth solvent (DCM) which have been removed for clarity.*

Complex	Bond lengths (Å)		Bond angles (°)			
[RuCl(**L14**)₂]Cl	Ru1-P1	2.3030(7)	P1-Ru1-Cl1	89.12(2)	N2-Ru1-Cl1	83.18(6)
	Ru1-P2	2.3185(7)	P1-Ru1-P2	99.23(3)	N2-Ru1-P2	95.38(6)
	Ru1-N1	2.099(2)	P1-Ru1-N1	92.15(7)	N2-Ru1-S2	82.38(7)
	Ru1-N2	2.160(2)	P1-Ru1-S2	90.91(3)	N2-Ru1-N1	94.84(9)
	Ru1-Cl1	2.4149(6)	P1-Ru1-N2	170.29(6)	N1-Ru1-P2	95.38(6)
	Ru1-S2	2.4123(7)	Cl1-Ru1-P2	90.78(2)	N1-Ru1-S2	90.07(6)
	C4-N1	1.289(4)	Cl1-Ru1-S2	83.46(2)	P2-Ru1-S2	168.27(3)
	C26-N2	1.274(4)	Cl1-Ru1-N1	173.42(6)		

The obtained structure showed a distorted octahedral structure featuring two molecules of **L14** and one coordinated chloride ligand. A second chloride was observed as an outer sphere counterion. The two phosphine groups are positioned *cis* to one another, with an expanded P-Ru-P bond angle of 99°. The phosphine rings are positioned in a fixed paddlewheel conformation but show no co-planar positioning or stacking of p orbitals. The tridentate ligand forms two chelate rings, each adopting analogous conformation to that seen previously, with an envelope 5-membered N-S ring and a 6-membered half-chair P-N ring. The coordinated sulfur is chiral. The bidentate ligand forms a planar 6-membered chelate ring, binding by the phosphorus and nitrogen donor atoms, with the aliphatic methylthio arm positioned away from the bulky phenyl ring systems.

The reduced form of **L14**, **L18**, also complexed readily according to the conditions in Scheme 2.4 to give a yellow solid product. However, this complex was unfortunately very difficult to analyse due to its insolubility in chloroform, DCM, DMSO, methanol and acetonitrile. HRMS was able to confirm a bis-ligated structure featuring two chlorides, $[RuCl_2(\mathbf{L18})_2]$ ((ES+/Q-TOF) m/z: [M+H]$^+$ Calcd for $C_{44}H_{49}N_2P_2S_2Cl_2Ru$ 903.1233; Found 903.1245). Potential oligomerisation of the complex could be the cause for such insolubility, but no evidence of heavier fragments was seen in the mass spectrum. Very sparing solubility in toluene permitted identification of a singlet at 48.9 ppm in toluene in the $^{31}P\{^1H\}$ NMR spectrum. This represents a downfield shift of +65.0 ppm upon complexation, consistent with the shifts observed in preparation of tridentate species $[Ru(\mathbf{L1\text{-}3})_2]Cl_2$. However, without any significant ^1H NMR or crystallographic data, any coordination of sulfur cannot be confirmed.
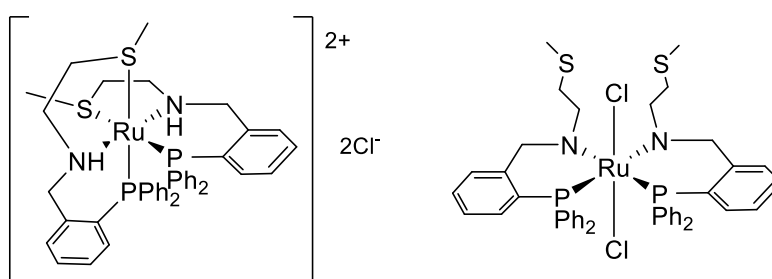
*Figure 2.34 - Possible structures of [RuCl$_2$(**L18**)$_2$].*

Complexation of ligand **L15** (again using complexation conditions described in Scheme 2.4) successfully produced the single isomer species $[RuCl_2(\mathbf{L15})_2]$ as a red solid by induced precipitation with dry pentane. When analysed by HRMS, it showed a bis-ligated species featuring two chlorides. NMR analysis of the species shows a single singlet at 48.9 ppm in the $^{31}P\{^1H\}$ NMR spectrum, a downfield shift of +62.3 ppm from free **L15** (δ: -13.4 ppm). The symmetry is further confirmed with ^1H NMR analysis. The key imine proton also shows a slight upfield shift in the ^1H NMR spectrum, from 8.87 ppm (free **L15**) to 8.75 ppm ($[RuCl_2(\mathbf{L15})_2]$). These shifts are very similar to those observed in the bidentate complex $[RuCl_2(\mathbf{L4})_2]$, which crystallographic data determined showed a *cis* bidentate structure. Hence, it is proposed that $[RuCl_2(\mathbf{L15})_2]$ also shows this binding mode (Figure 2.35). Interestingly, as with all other species, distinct aliphatic signals were observed for the six CH_2 protons in the ^1H NMR spectrum, again demonstrating restricted motion of pendant arms in solution. However, as with $[RuCl_2(\mathbf{L4})_2]$, $[RuCl_2(\mathbf{L15})_2]$ also demonstrates free rotation of the methyl protons, which appear as one singlet at 1.84 ppm.
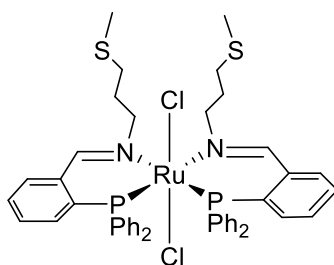
*Figure 2.35 - Proposed structure of [RuCl$_2$(**L15**)$_2$].*

The final complexation attempted was of **L17**. When complexed with [RuCl$_2$(*p*-cymene)]$_2$, an initial precipitate was obtained and isolated by filtration, labelled [RuCl$_2$(**L17**)$_2$]-A, at 17 % yield. Subsequent addition of dry pentane to the filtrate resulted in isolation of a second product, [RuCl$_2$(**L17**)$_2$]-B, in 40 % yield. HRMS analysis of both products demonstrated both species were bis-ligated and featured chlorides. However, both systems showed distinct NMR signals; key signals are summarised in Table 2.14.

*Table 2.14 - Key NMR data for L17 and the two produced isomers of [RuCl$_2$(**L17**)$_2$].*

	L17	[RuCl$_2$(**L17**)$_2$]-A				[RuCl$_2$(**L17**)$_2$]-B			
		δ	Δ	δ	Δ	δ	Δ	δ	Δ
^{1}H δ *H*C=N / ppm	8.64	9.68	+1.04	8.77	+0.13	8.76	+0.12	8.25	-0.39
{^{1}H}^{31}P δ / ppm	-19.1	38.0	+57.1	33.7	+52.8	44.6	+63.7	30.0	+49.1

It is immediately obvious that both obtained isomers show ligand asymmetry and are additionally distinct from one another. The large downfield shifts of the phosphorus signals are indicative of binding of the phosphorus atom in all cases, so it is presumed binding modes are at least bidentate and there is a PN binding moiety in each species. This is supported by a shift in C=N stretch in the FTIR from 1627 cm^{-1} (free **L17**) to 1584 cm^{-1} (observed in both isomers of [RuCl$_2$(**L17**)$_2$]). Given the anticipated PN binding region of each ligand is substantially different from the other systems explored in this work (5-membered aliphatic chelate ring, as opposed to the 6-membered planar or half-chair shaped rings discussed previously), it is difficult to infer structural information between species by comparison with their data.

It is notable in the aliphatic region of the ^{1}H NMR spectrum of both isomers that the CH$_2$ protons experience substantial downfield shifts due the deshielding effects of coordination. In both cases, there are also more than two CH$_2$ signals, further supporting ligand inequivalence. In the minor product [RuCl$_2$(**L17**)$_2$]-A, the sample was rather impure and the NMR data is poor, but the aliphatic region of the ^{1}H spectrum shows a region of broad deshielded signals between

74

approximately 5.35 ppm and 3.45 ppm, integrating to account for eight distinct CH_2 protons, and suggesting significant inequivalence between the two **L17** ligands. This typically indicates chelate ring distortion, so a structure similar to that of [RuCl(**L14**)$_2$]Cl is considered most likely (Figure 2.36a) for this species. Unfortunately, the relatively poor solubility and purity of [RuCl$_2$(**L17**)$_2$]-A makes further detail impossible to obtain from NMR. Interestingly, in the purer and more soluble major product [RuCl$_2$(**L17**)$_2$]-B, there are only three signals attributable to the four CH_2 protons, but the methyl proton signals are inequivalent. Hence, there must be increased symmetry in the aliphatic region, either through planar chelate rings (and therefore geminal chemical equivalence), or symmetrical PN moiety binding. Symmetrical PN chelate rings would likely result in a single $^{31}P\{^1H\}$ NMR signal instead of the observed pair of doublets, so this binding mode is unlikely. The lack of chelate ring distortion could be possible by an inequivalent bidentate structure, which is proposed in Figure 2.36b, though this does not effectively explain the differences in methyl group ^1H NMR chemical shift. However, multiple possible other ligand coordination modes are available so without additional structural data, these proposals remain tentative.
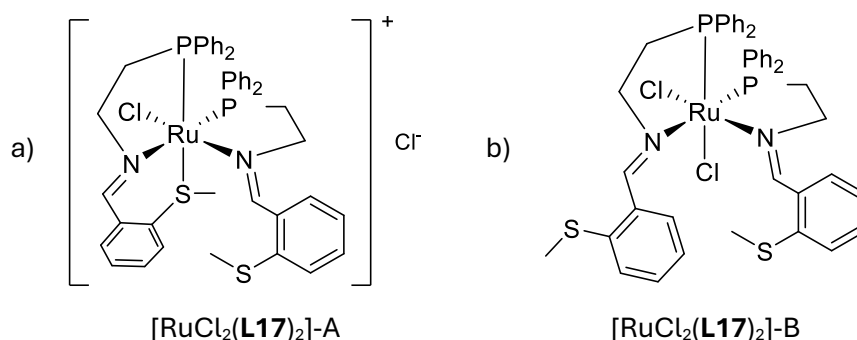
*Figure 2.36 - Proposed structures for isomers of [RuCl$_2$(**L17**)$_2$].*

2.4.4.3   Unsuccessful complexations

Complexation of the ligands **L13** and **L16** was attempted unsuccessfully. When complexation of the second thiazolidine ligand **L13** was attempted according to the same procedure using excess **L13**, a dark green crude mixture of several singlets appeared in the $^{31}P\{^1H\}$ NMR spectrum which could not be separated by traditional techniques. When sat in solution for several hours, black solid appeared suspended and free ligand became visible in the NMR spectrum, suggesting an unstable species, and notably degrading in the same way described by Dilworth in their work with similar aromatic PNO and PNS ligands[15]. Therefore, this complex was not investigated further. Similarly, attempted complexation of **L16** produced a very insoluble dark black solid which

showed no significant signals in either $^{31}P\{^1H\}$ or ^1H NMR, suggesting decomposition of starting material with no successful complexation. The failure of either of these ligands to produce complexes where phenolic ligand **L3** was successful is attributed to the proposed alkoxide bonding in [Ru(**L3**)$_2$]Cl$_2$ stabilising the extended aromatic backbone as it undergoes the necessary distortion to coordinate in a tridentate conformation.
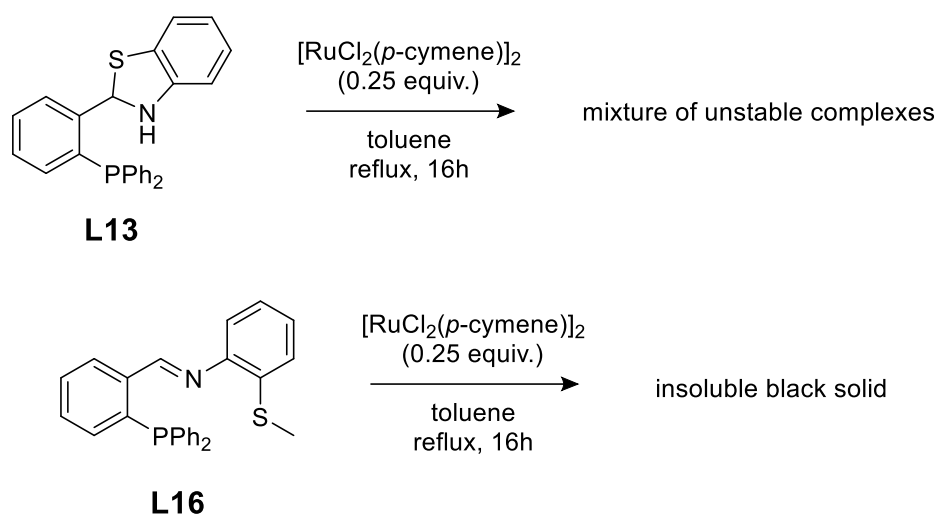
Scheme 2.20 - Unsuccessful complexations of *L13* and *L16*.

2.4.5   Conclusions

The series of novel [RuCl$_2$(PNX)$_2$] (X = N,S) complexes prepared in this set appeared to demonstrate more variation in stable binding mode than the previous [Ru$_2$(PNO)$_2$] set. The use of R substituted amines and thiols was necessary to prevent internal reaction, either by further imine rearrangement (as seen in the failure of isolation of primary amine terminated **L8**) or cyclisation (see **L12** and **L13**). The tautomeric cyclic structure of **L9** was found to not affect the binding modes observed upon complexation due to spontaneous ring-opening, but the thiazolidine ring structure of **L12** was apparently more stable, only showing partial ring-opening upon coordination, and leading to a more complex product mixture. Notably, this ring-opening did not occur at all in the absence of heat; exploration of room-temperature complexation of **L9** could further establish the preference towards an imine ligand over an imidazolidine ligand.

Unlike in the PNO set, substitution at the pendant arm heteroatom did not preclude tridentate coordination, as confirmed by crystal structures obtained of both [RuCl(**L9**)$_2$]Cl and [RuCl(**L14**)$_2$]Cl. It is interesting that for these two species, isomeric mixtures were not obtained, demonstrating clear stability of these mixed bidentate-tridentate species. This evidence of stable

binding in both coordination modes is promising for potential applications to homogeneous catalysis, where pincer ligand hemilability is frequently proposed in catalytic cycles.

Extension of the aliphatic pendant arm did however result in loss of pincer-type tridentate coordination (seen in both PNO complex [RuCl(**L4**)$_2$] and PNS complex [RuCl$_2$(**L15**)$_2$]), showing the formation of two adjacent 6-membered chelate rings in this type of pincer ligand is disfavoured. An exploration of the reduced forms of these species in future work would be an interesting way to determine if the increased flexibility of the backbone would permit tridentate coordination, though it is noted that reduced solubility may be an issue, given the problem of analysis of [RuCl$_2$(**L18**)$_2$]. It is noted that introduction of flexibility in the PN binding moiety resulted in multiple stable isomers of [RuCl$_2$(**L17**)$_2$], so this is presumed to be a likely outcome in more flexible reduced PNX complexes. However, reduction would allow fuller comparison of PNN species without the risk of internal formation of PNNP complexes, as well as potentially provide more stable pincer-type binding modes of thiazolidine ligands. Given that, when applied to catalysis for hydrogen transfer mechanisms Ru-N containing species are frequently proposed to undergo reduction/oxidation at the binding nitrogen site, a more direct comparison with analogous reduced ligand species could provide interesting data on potential catalytic cycles in such reactions.

2.5 References

1 M. Asay and D. Morales-Morales, *Dalton Transactions*, 2015, **44**, 17432–17447.

2 J. R. Khusnutdinova, D. Milstein, D. Milstein and J. R. Khusnutdinova, *Angewandte Chemie International Edition*, 2015, **54**, 12236–12273.

3 P. A. Dub and J. C. Gordon, *ACS Catal*, 2017, **7**, 6635–6655.

4 C. Gunanathan, Y. Ben-David and D. Milstein, *Science (1979)*, 2007, **317**, 790–792.

5 M. Gargir, Y. Ben-David, G. Leitus, Y. Diskin-Posner, L. J. W. Shimon and D. Milstein, *Organometallics*, 2012, **31**, 6207–6214.

6 J. C. Jeffrey and T. B. Rauchfuss, *Inorg Chem*, 1979, **18**, 2658–2666.

7 M. L. Clarke, M. B. Díaz-Valenzuela and A. M. Z. Slawin, *Organometallics*, 2007, **26**, 16–19.

8 J. A. Fuentes, S. M. Smith, M. T. Scharbert, I. Carpenter, D. B. Cordes, A. M. Z. Slawin and M. L. Clarke, *Chemistry – A European Journal*, 2015, **21**, 10851–10860.

9 J. C. S. Dalton, J. R. Thornback, G. Wilkinson, M. D. Hobday, T. D. Smith, F. Calderazzo, C. Floriani, R. Henzi and F. L'eplattenier, *Journal of the Chemical Society, Dalton Transactions*, 1978, **9**, 110–115.

10 A. Singh and P. Barman, *Topics in Current Chemistry 2021 379:4*, 2021, **379**, 1–71.

11 L. P. He, T. Chen, D. Gong, Z. Lai and K. W. Huang, *Organometallics*, 2012, **31**, 5208–5211.

12 K. Nakajima, S. Ishibashi and M. Kojima, *Chem Lett*, 1998, **27**, 997–998.

13 P. Bhattacharyya, M. L. Loza, J. Parr and A. M. Z. Slawin, *Journal of the Chemical Society, Dalton Transactions*, 1999, 2917–2921.

14 H. L. Kwong, W. S. Lee, T. S. Lai and W. T. Wong, *Inorg Chem Commun*, 1999, **2**, 66–69.

15 S. R. Bayly, A. R. Cowley, J. R. Dilworth and C. V. Ward, *Dalton Transactions*, 2008, 2190–2198.

16 D. B. Grotjahn and H. C. Lo, *Organometallics*, 1996, **15**, 2860–2862.

17 M. R. J. Elsegood, M. B. Smith and S. H. Dale, *Acta Crystallogr C*, 2007, **63**, m7–m9.

18 A. A. Batista, J. Zukerman-Schpector, O. M. Porcu, S. L. Queiroz, M. P. Araujo, G. Oliva and D. H. F. Souza, *Polyhedron*, 1994, **13**, 689–693.

19 P. Das, M. Sharma, N. Kumari, D. Konwar and D. K. Dutta, *IJC-A Vol.41A(03) [March 2002]*.

20 P. A. Dub, R. J. Batrice, J. C. Gordon, B. L. Scott, Y. Minko, J. G. Schmidt and R. F. Williams, *Org Process Res Dev*, 2020, **24**, 415–442.

21 C. Yang, Y. K. Cheung, J. Yao, Y. T. Wong and G. Jia, *Organometallics*, 2001, **20**, 424–429.

22 J. L. Riebsomer and R. J. Ferm, *Chem Rev*, 1954, **54**, 593–613.

23 S. Witek, A. Bielawska and J. Bielawski, *Heterocycles*, 1980, **14**, 1313.

24 S. Rather and H. T. Clarke, *J Am Chem Soc*, 1937, **59**, 200–206.

25 D. Barbry, G. Ricart and D. Couturier, *Journal of the Chemical Society, Perkin Transactions 2*, 1990, 133–140.

26 M. E. Bluhm, O. Walter and M. Döring, *J Organomet Chem*, 2005, **690**, 713–721.

27 R. L. Wingad, P. J. Gates, S. T. G. Street and D. F. Wass, *ACS Catal*, 2015, **5**, 5822–5826.

3 Application of Ru(II) Complexes to the Upgrading of Ethanol for Advanced Biofuels

This chapter discusses the application of catalysis in the upgrading of ethanol for production of butanol as an advanced biofuel. The application of novel species presented in Chapter 2 to this transformation is investigated and compared to state-of-the-art systems.

3.1 Background

3.1.1 Fossil Fuels

It is well established that the modern human lifestyle is unsustainable. This is particularly true with respect to ongoing enthusiastic consumption of non-renewable resources. Fossil fuels are the obvious case of this: formed over the course of millions of years from the anaerobic decomposition of prehistoric organic matter[1], they are not possible to reproduce in anywhere close to the required rate to sustain supply. Significant consumption began in the British Industrial Revolution in the mid-1700s, predominantly coal, with rapid expansion to Europe and the rest of the world by the early 1800s[2]. An explosion in use of fossil fuels in the mid-twentieth century included crude oil (also referred to as petroleum) and natural gas at increasing rates. Despite international scientific and political acknowledgement of the major contribution of their use to the uncontrolled global heating now known as the climate emergency[3,4], both production and consumption rates of fossil fuels have increased every year since 1982 (excluding only 2009 and 2020)[1,5]. This is inherently unsustainable, both in the production of greenhouse emissions, and in the use of a finite resource. Indeed, current global reserves are estimated to be unable to sustain current demand within this century, with the Millennium Alliance for Humanity and the Biosphere (MAHB) estimating petroleum reserves unable to meet demand by 2060[6]. This uncontrolled consumption, and the resultant emissions, is one of the major markers of the current geological epoch: the Anthropocene[2].

Petroleum is currently the most consumed fossil fuel by energy, and has been since the 1960s[1,7]. In 2023, global consumption of petroleum exceeded 100 million barrels of petroleum consumed per day for the first time ever[7], with the US being the largest producer and consumer, using around 20 million barrels daily[8]. Most petroleum is used as a transformed fuel, with the transportation sector the primary user: over 80 % by volume of petroleum is directly converted to liquid fuel

products in the US[8]. These include light distillates such as gasoline and naphtha, middle distillates like diesel and kerosine, and heavy fractions referred to as fuel oil.

Gasoline, or petrol, is a C_4-C_{12} petroleum fraction used primarily as liquid fuel in private vehicles and is by far the most consumed petroleum product by volume[8]. In 2023, finished motor gasoline accounted for 42 % of petroleum consumption in the US, exceeding pre-COVID levels of 2019 for the first time[7,8]. Despite increasing interest amongst consumers and corporations in western markets for alternative low-emission options like electric vehicles (EVs), there has been no loss of demand for liquid fuel sources compatible with current engine technology. This is understandable: electric vehicles are expensive, use large quantities of critical materials, require ready access to a robust electrical infrastructure so are frequently unsuitable for long distance use, and depending on location, the primary source of electrical power is not guaranteed to be renewable anyway[9]. Despite limited adoption in some markets (1 in 3 new cars purchased in China were electric in 2023), it is incredibly localised and slow; China, Europe and the US account for 95 % of all sales[9], and of these regions only China has EVs make up more than 5 % of cars in use[10]. There is currently no projected timeline for EVs becoming the majority stock share of personal vehicles[10], and long-haul travel remains an inappropriate application. Hence, reliance on liquid fuel remains.

3.1.2 Biofuels

A biofuel is defined by the Intergovernmental Panel on Climate Change (IPCC) as a fuel produced from any form of biomass or its metabolic byproducts[4]. Sustainability advantages as a material are clear: their feedstock materials can be produced in timescales ranging from years to months, making them renewable sources. Production is not geographically restricted by fossil fuel reserve locations, which has substantial geopolitical benefits for regions dependent on a small number of fossil fuel producers. Feedstocks may be grown for purpose, or make use of industrial bio waste. Although biofuels are still greenhouse gas emitters when burned, there is cyclical carbon capture and release in the growth of the source biological material, so biofuels may be considered low emission or carbon neutral[11].

Given projected loss of access to petroleum within the next 40 years, and a lack of alternative vehicle options reaching majority of users in this timeframe, alternative options suitable for existing infrastructure are imminently necessary. Liquid biofuels are widely considered as promising improvements to the current fuel consumption model and are almost exclusively used in the transportation sector[12]. However, by nature of their production using biomass, a limitation of biofuels is the competitive use of land and resources which could be used for food production

to instead produce fuel-source biomass. Additionally, associated concerns with the impact of monocultures, loss of diverse habitat for farming, and carbon release from cleared land are common criticisms of commercial starch- and sugar-sourced biofuels, especially when expanded to account for increasing demand[11,13]. Hence biofuels are categorised according to their source and related environmental cost, and therefore their sustainable profile with respect to the UN Sustainable Development Goals[14] and the 12 Principles & Criteria of Sustainability as set out by the Roundtable on Sustainable Biofuels[15]. These category definitions vary somewhat in the literature but are approximately summarised as follows[16,17]:

- First generation (conventional): biofuels produced from starch- or sugar-based sources, edible biomass, or biomass grown on arable land otherwise possible to be used for food farming.
- Second generation (advanced): biofuels produced from lignocellulosic biomass, non-edible crop matter including industrial waste.
- Third generation: biofuels produced from algal biomass, not using land-grown crops.
- Fourth generation: biofuels produced using genetically engineered microorganisms to enhance efficiency of fermentation.

3.1.3   Bioethanol

Bioethanol is the most well-known liquid biofuel and is mostly commercially produced by fermentation as a first generation (or conventional) biofuel[18], though lignocellulosic and algal feedstock development for commercial use is ongoing[17]. Bioethanol is distinct from ethanol in the production process and in the use. Whilst the hydration of ethene sourced from fossil fuels is a traditional petrochemical transformation to produce ethanol, bioethanol is manufactured from fermentation of crop biomass, typically sugarcane or corn[5]. Additionally, bioethanol specifically refers to fuel ethanol, and does not refer to ethanol used in food or chemical industry, even if the ethanol in this context is also sourced from biomass.

Interest in ethanol as a vehicle fuel has been established for decades, with Brazil particularly leading the industry. The combination of a centuries-long history of ethanol production from sugarcane and the 1973 oil crisis led to legislative inclusion of ethanol in gasoline from 1975 to combat exorbitant fuel prices and increase availability[19]. The current standard ethanol blend in Brazil is E25 (25 % ethanol by volume). Legislation has since driven the regular use of bioethanol as an additive to gasoline in many other regions including the UK, in response to both commitments to climate targets and fluctuations in petroleum price and availability. In the UK,

E10 (10 % ethanol by volume) is the standard petrol available for sale as of 2021[20]. The US – now the largest producer of bioethanol[12,21] – has long required the use of ethanol blends in light vehicles and introduced further legislation in 2022 temporarily allowing the sale of E15 (15 % ethanol by volume) gasoline blends in response to oil supply issues due to the Russian invasion of Ukraine. This legislation has been renewed annually as of 2024[22].

Use of ethanol as a vehicle fuel is limited by its incompatibility with gasoline engines. Specialty vehicles are available and are particularly popular in Brazil: the first car designed to run on ethanol alone was the Fiat 147 introduced in Brazil in 1979[19,23], and flex-fuel vehicles suitable for 100 % ethanol fuel remain in widespread use[24]. However, in petrol engines (which made up almost 60 % of the UK light vehicles on the road in 2019), ethanol is an unsuitable replacement and can only be used as a low-level additive without substantial engine modification. It is hygroscopic, and hydrated ethanol is corrosive so blends must be made with anhydrous ethanol; it has low heat value, making cold starts difficult; and it has low energy density, so approximately 50 % more fuel is required to provide the same power[25]. Therefore, to permit a green fuel transition while retaining reasonable access to existing engines, alternative biofuels must be considered.

3.1.4   Biobutanol

To obtain a closer alternative to gasoline, other chemicals featuring closer properties to gasoline are investigated. Butanol is identified as an option: the increased carbon chain length relative to oxygen content increases energy density compared to ethanol, and decreases the solubility of water in it, reducing the corrosive effects. A comparison of physiochemical properties is given in Table 3.1. Branching is also noted to affect the physical properties of even short chain chemicals which can drastically affect its suitability as a fuel, so *n*-butanol, *sec*-butanol and isobutanol are included. *tert*-Butanol was excluded as it is solid at room temperature[26].

Table 3.1 - Properties of gasoline compared to ethanol and three isomers of butanol. Values from literature[26–29].

	Gasoline	Ethanol	*n*-Butanol	Isobutanol	*sec*-Butanol
Density[a] / g/mL	0.74	0.79	0.810	0.802	0.808
Solubility in water[a] / wt%	Negligible	Miscible	7.7	8.7	12.5
Solubility of water in compound[a] / wt%	Negligible	Miscible	20.1	20.2	60
Boiling point / °C	27–225	78	117.7	107.9	99.6
Energy density / MJ/L	30-33	21.4	26.9	26.6	26.7
Latent heat of vaporisation / kJ/kg	352	919.6	707.9	686.4	671.1
Autoignition temperature / °C	257	363	343	415	405
Flash point / °C	-43	13	29	28	24
AKI[b]	88	100	93	98	99

[a]At 20 °C. [b]AKI – anti-knock index – the mean of research octane number and motor octane number which represent combustion ability of a fuel under idling conditions and full engine throttle conditions respectively.

Higher AKI indicates lower air/fuel ratio required for combustion; the high relative oxygen content in short chain alcohols decreases the required air for combustion, but the resultant miscibility with water and significantly reduced energy density of ethanol make longer chain butanol more appropriate alternative fuels. The energy density (combustion energy per unit volume) is still reduced in butanol relative to gasoline due to the relatively short chain length, but much more comparable given the increased density. Fuel efficiency by volume would be expected at 80-90 % of gasoline[30]. Additionally, cold starts are heavily impacted by high latent heat of vaporisation, further making butanol a preferential alternative fuel for general use[29]. With comparison of isomers, notably the solubility of water is much higher in *sec*-butanol than *n*-butanol and isobutanol, demonstrating the benefit of some isomers over others.

This overlapping of properties permits the use of especially *n*-butanol and isobutanol as direct drop-in replacements for gasoline and in mixtures with gasoline without engine modification[27,30]. Butanol has also been investigated for its ability to operate as a blend with diesel, a longer chain fraction of petroleum which is the second most popular liquid fuel in use and frequently used for cars, vans and HGVs[7]. The heavier nature of diesel requires a different engine structure so biobutanol could not be a drop-in alternative, but has been assessed to function much as bioethanol currently does in blends of 20-40 % whilst maintaining suitable performance in existing diesel engines[27].

n-Butanol and isobutanol are produced traditionally from fossil fuels in the hydroformylation of propene over cobalt or rhodium catalysts to produce a mixture of butyraldehyde and

isobutyraldehyde. The hydrogenation of this mixture produces *n*-butanol and isobutanol, which can then be separated[31]. However, sustainable production methods to produce biobutanol as a first generation biofuel are available, most commonly the ABE (acetone-butanol-ethanol) fermentation process, whereby butanol is produced by fermentation of biomass using various *Clostridium* species of bacteria[32,33].

Initially developed as a method of mass-producing acetone during the first World War[33], the ABE process lost popularity at the end of the 20th century with the growth of the petroleum industry[34]. It has since seen a resurgence for *n*-butanol production in China especially, but faces many major limitations: cost of feedstocks, low yield relative to feedstock, poor productivity rate due to toxicity of butanol to *Clostridium*, and complex product mixture requiring energy intensive downstream processing to isolate and dry the desired butanol[32]. The type of feedstock provides the same limitation bioethanol faces: waste biomass is a preferential feedstock for sustainability and food security but requires expensive pretreatment due to poor availability of fermentable sugar in lignocellulosic biomass[34]. It is noted that due to the nature of biobutanol as a potential complete replacement for gasoline, it is sometimes referred to in the literature as an "advanced biofuel". However, due to the definitions discussed in section 3.1.1 relying on feedstock type, the term "drop-in biofuel" is perhaps more accurate as a catch-all term. Currently the ABE process is limited industrially to categorisation as first generation.

Recent developments in the process focus on modifying strains of bacteria to tolerate increased butanol concentrations, increase process selectivity and more efficiently use wider ranges of feedstocks, including algae[35]. Despite significant progress on the research scale using genetic modification of bacteria to access a wider range of feedstocks, lignocellulosic and algal feedstocks (which would turn biobutanol into a second or third generation biofuel) still require substantial pretreatment and make the process prohibitively expensive[35]. Additional post-reaction processing leaves the current system unable to compete economically with petrochemical feedstocks[34].

3.2 Interest in Guerbet for biofuels

3.2.1 The Guerbet Reaction
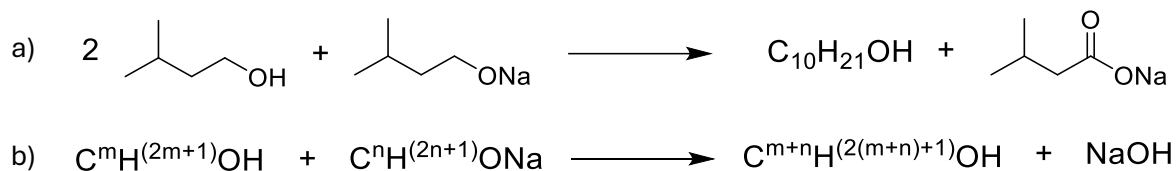
Scheme 3.1 – a) First reported Guerbet coupling reaction. b) General reaction for alcohol coupling reported by Guerbet in 1909.

The Guerbet reaction has long been established as a means of coupling alcohols, first reported by its inventor and namesake Marcel Guerbet in 1899[36]. Initially performed with 3-methyl-1-butanol and its sodium alkoxide to produce an unexpected 10-carbon coupling product (Scheme 3.1a), the work was expanded to investigate other alcohols and it was later demonstrated that ready reaction of several primary alcohols with their sodium alkoxides produced a single long-chain alcohol with NaOH byproduct[37]. Subsequently, the reaction has developed to employ transition metal catalysts and remained highly industrially relevant, frequently in use to produce long chain branching fatty alcohols known as Guerbet alcohols which are employed as surfactants and lubricants[38,39].
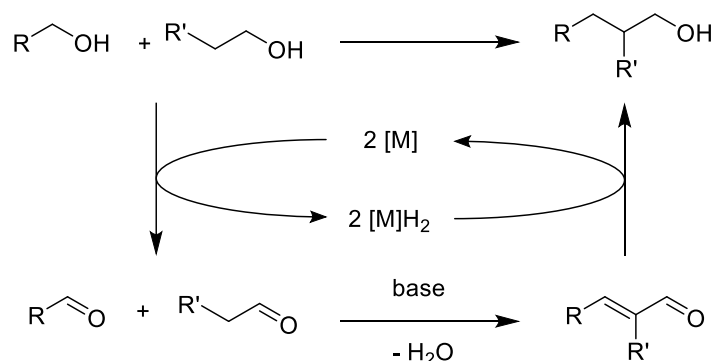
Scheme 3.2 - General scheme for the modern Guerbet coupling of alcohols, with a metal catalyst to facilitate dehydrogenation and rehydrogenation steps.

The commonly accepted pathway of the Guerbet reaction, shown in Scheme 3.2, was first proposed in 1967 by Veibel and Nielsen[40]. An initial metal-catalysed dehydrogenation produces the corresponding aldehydes, followed by base-catalysed aldol condensation to form the α,β-unsaturated carbonyl compound. Finally, rehydrogenation produces the saturated alcohol product, with one molecule of water lost. This type of transfer hydrogenation reactivity is known as a "borrowing hydrogen" type mechanism, as the hydrogen removed from the substrate is later returned to the unsaturated intermediate product[41].

The only requirement for an alcohol to react in this way is it be primary or secondary with a methylene group at the β position. Hence, this cycle may repeat after an initial coupling to produce long chain or branching alcohols, should the product also fulfil this requirement. Furthermore, whilst it is possible for the dehydrogenation/hydrogenation steps to occur without a catalyst, hydrogen transfer catalysts significantly improve rate and yield, with initial popular choices being Raney nickel or palladium[40].

3.2.2   The Guerbet Homocoupling of Ethanol to n-Butanol

In the system described above, it is obvious that the application to two ethanol molecules would produce *n*-butanol. Should the source be bioethanol, the product is therefore biobutanol. Hence, the Guerbet reaction is proposed as an alternative means of production of biobutanol.

Interestingly, Guerbet's initial attempt to couple ethanol with its sodium derivative failed to result in anything except ethene, sodium acetate and hydrogen gas[36]. The use of hydrogen transfer catalysts however has vastly expanded reaction scope, permitting production of butanol from ethanol coupling. Early research focused predominantly on heterogeneous catalysts, but particularly when applied in the homocoupling of ethanol these systems often required very high temperatures of over 400 °C, where degradative reactions have been reported to become dominant at temperatures exceeding 180 °C[42], with systems resulting in only moderate n-butanol yields of up to 20 % and generally poor selectivity[43–45].

Homogeneous systems have recently provided much more promising results. Although the first use of homogeneous catalysis for Guerbet coupling of alcohols was in 1972[46], the first reported example of successful homocoupling of ethanol to produce n-butanol wasn't until 2009 when Ishii and coworkers demonstrated the use of an iridium complex with a phosphine co-catalyst and 1,7-octadiene additive in neat ethanol (Scheme 3.3)[47].
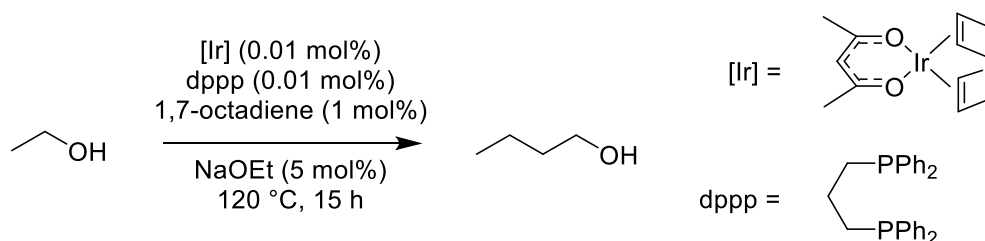
Scheme 3.3 – Iridium-catalysed ethanol homocoupling to produce n-butanol, reported by Ishii and coworkers[47].

This system performed just as well in a batch reactor as previously reported heterogeneous systems, producing 21 % yield of n-butanol, with 55 % selectivity based on an ethanol conversion of 41 %, using the far lower temperature of 120 °C. Poor selectivity was largely due to further

reaction to produce higher alcohols. Interestingly, a "preactivation" of the catalyst by stirring the system at room temperature for 2 h, and only then heating to 120 °C, was required to obtain such high yields; removal of this step resulted in halved conversion and yield. The incorporation of hydrogen acceptor additive was necessary for any reaction to occur, and only trace product was produced in the absence of the diphosphine cocatalyst. Therefore, it is presumed that an active catalyst species incorporating these components was pre-formed during this preactivation step.

3.2.3   Precedent for Ru(II) Complexes in Guerbet Catalysis

Ru(II) species have been noted as effective catalysts in hydrogenation and dehydrogenation mechanisms (section 1.3) and the hydrogen borrowing strategy employed by the Guerbet reaction uses such hydrogen transfer inherently in the cycle[41]. This has made such species attractive prospects for investigation for this coupling. Indeed, several ruthenium catalyst systems have been successfully applied to the homocoupling of ethanol to produce n-butanol with moderate yield but excellent selectivity.
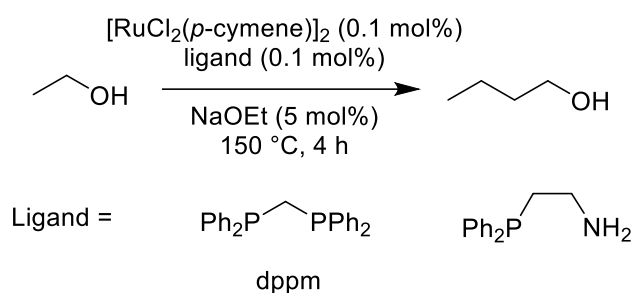
Scheme 3.4 – Ruthenium-catalysed ethanol homocoupling to n-butanol, reported by Wass and coworkers [48,49].

In 2013, Wass and co-workers reported a system where ruthenium complex [RuCl$_2$(p-cymene)]$_2$ and a diphosphine ligand were applied with no additional hydrogen acceptor (Scheme 3.4)[48]. The ligand featuring the smallest bite angle, 1,1-bis(diphenylphosphino)methane (dppm), gave the best yield of 18 % n-butanol at 90 % selectivity. Increase in size of ligand decreased yield. When pre-formed complexes of ruthenium and the respective pincer ligands were formed, yield increased further using the dppm complex [RuCl(dppm)(p-cymene)]Cl to produce 20 % n-butanol yield at an excellent 94 % selectivity. Yield was not improved when reaction time was increased, and using the preformed complexes of larger ligands reduced yield relative to their *in situ* application. Interestingly, use of the bis-ligated complex [RuCl$_2$(dppm)$_2$] provided poorer yield at 4 h but continued to react, showing the highest yield to date of 36 % n-butanol - albeit at reduced selectivity of 52 % - when run time was increased to 24 h.
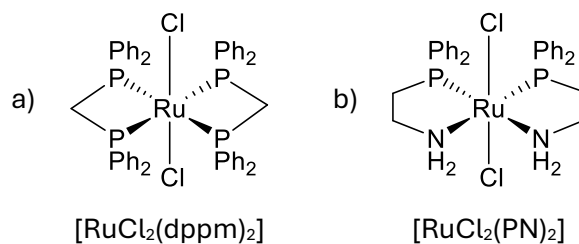
Figure 3.1 - Bis-ligated complexes reported by Wass and coworkers for n-butanol production.

Subsequent work by Wass and co-workers employed [RuCl$_2$(*p*-cymene)]$_2$ with mixed donor PN ligand additives[49]. The use of 2-(diphenylphosphino)ethylamine produced similar yields of n-butanol to the dppm analogues, when applied *in situ* or in either mono- or bis-ligated preformed complexes. Additionally, the PN ligands demonstrated increased water tolerance relative to PP complexes. Substitution of the ligand nitrogen with methyl groups reduced yields, indicating the relevance of an N-H moiety.
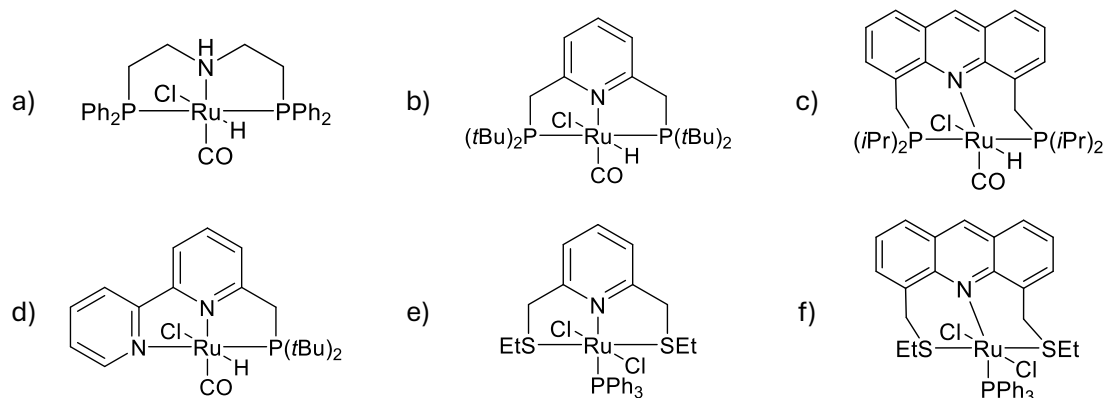
Figure 3.2 - Ruthenium pincer complexes tested in the Guerbet homocoupling of ethanol.

Table 3.2 - Summary of ruthenium pincer catalysts applied to the Guerbet homocoupling of ethanol.

Author	Catalyst (mol%)	Base (mol%)	Time / h	T / °C	*n*-Butanol yield / %	*n*-Butanol selectivity / %
Wass[49]	3.2a (0.1)	NaOEt (5)	4	150	2	12
Milstein[50]	3.2b (0.02)	NaOEt (4)	16	110	4	63
Milstein[50]	3.2c (0.02)	NaOEt (4)	16	110	21	93
Milstein[50]	3.2d (0.02)	NaOEt (4)	16	110	2	57
Whitelegge[51]	3.2e (0.1)	NaOEt (5)	20	150	26	74
Srimani[52]	3.2f (0.045)	NaOH (4.5)	24	140	10	-

Interestingly, application of ruthenium pincer complexes in the literature has provided mixed results. RuMACHO® was found by Wass and coworkers to be functionally inactive towards n-butanol production[49]. Milstein reported in 2016 the activity of various other mixed donor pincer complexes over 16 h at the lower temperature of 110 °C (Figure 3.2b-d)[50]. Their acridine-based system (Figure 3.2c) was highly active at a catalyst loading of 0.02 mol%, producing 21 % n-butanol at a selectivity of 93 %. All other tested systems produced less than 4 % n-butanol yield after 16 h.

More recently, exploration of SNS type pincer ligands by Srimani and coworkers demonstrated in 2023 the use of an analogous acridine-based system effective for ethanol coupling, producing a moderate 10 % yield of n-butanol after 24 h using commercially favourable base NaOH, though selectivity was not reported[51]. Last year, novel application of pyridine-based SNS complexes from the Wass group showed surprisingly good activity, producing up to 26 % n-butanol yield at 73 % selectivity after 20 h using the same conditions used by Dowson *et al*. in 2013 (Scheme 3.4)[52].

3.2.4   Ru(II) Catalysed Production of Butanol Isomers

The Guerbet reaction has also been demonstrated as effective in a cross-coupling reaction between ethanol and methanol to selectively produce isobutanol, wherein the same basic mechanism is followed, with the intermediate *n*-propanol product re-entering the cycle and reacting with a second methanol molecule (Scheme 3.5)[39]. Given methanol is widely available by renewable methods, either as biomethanol from gasification of biomass[53] or produced by hydrogenation of captured CO_2[54], when coupled with bioethanol the butanol produced is considered renewable.
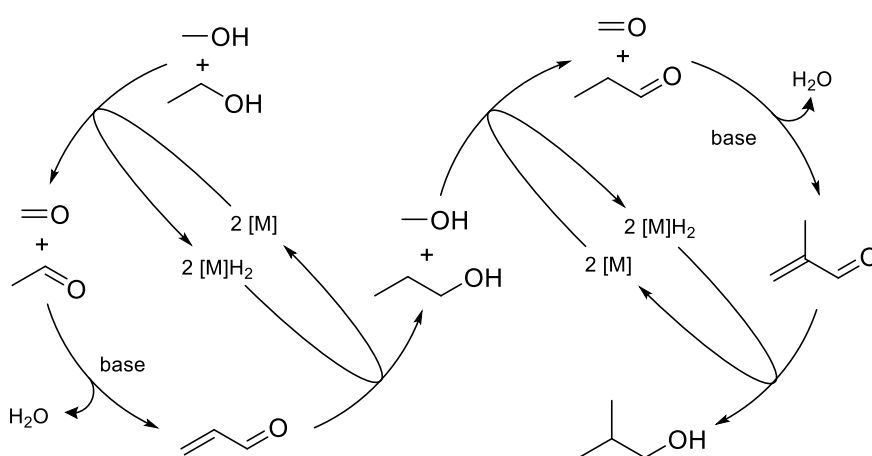
Scheme 3.5 - Production of isobutanol by the Guerbet cross-coupling of ethanol and methanol.

In 2016, Wass and coworkers explored the use of the highly effective PP and PN ligand systems in the homocoupling of ethanol and methanol and reported excellent results with their previously reported preformed bis-ligated catalysts[55]. Under the standard conditions tested, the performance of [RuCl$_2$(dppm)$_2$] was by far the best, giving 66 % yield at a remarkable 98 % selectivity. Increase of reaction time to 20 h increased yield to 75 % with 99.8 % selectivity reported. Interestingly, investigation into water tolerance demonstrated the opposite effect observed with *n*-butanol production; [RuCl$_2$(dppm)$_2$] saw no significant decrease in activity in the presence of water, but activity of the PN complex (Figure 3.3b) was depressed[56]. Newland *et al*. identified an bulky asymmetric PP ligated system for isobutanol production under the same conditions, demonstrating similar results to the Wass PN system[57] (Table 3.3). Last year, Wass and coworkers reported further PP variants with pendant arms, designed for enhanced solubility and functionality, with an excellent 62 % yield at 100 % selectivity after 2 h from a thiol-terminated complex (Figure 3.3d). This increased to an industry-best 79 % yield after 20 h.
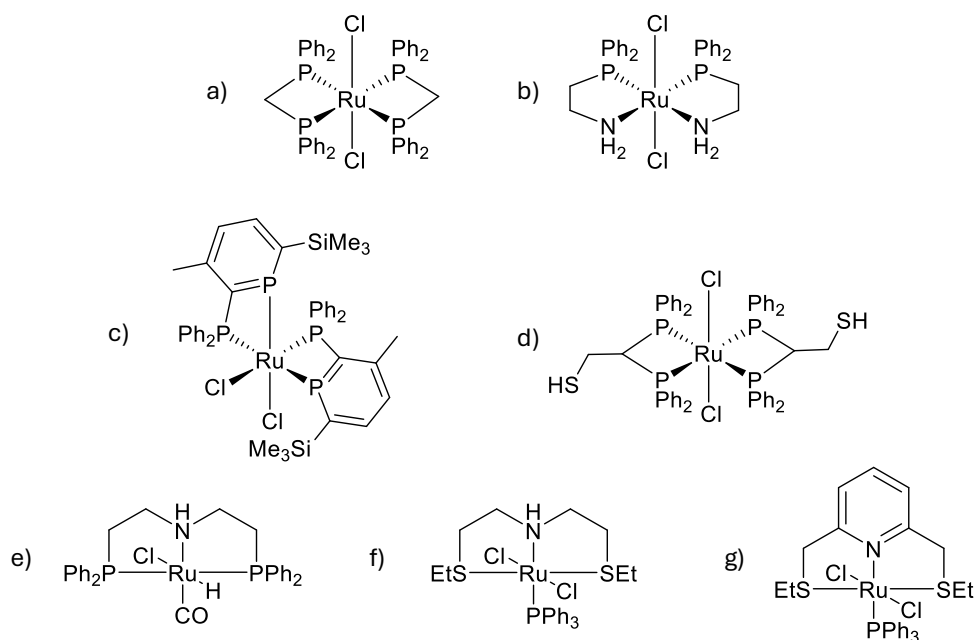
Figure 3.3 - Selection of ruthenium complexes tested for isobutanol production.

Table 3.3 – Summary of state-of-the-art catalysts reported for isobutanol production by Guerbet coupling of ethanol and methanol.

Author	Catalyst	Time / h	Isobutanol yield / %	Isobutanol selectivity / %
Wass[55]	3.3a	2	66	98
Wass[55]	3.3a	20	75	99.8
Wass[55]	3.3b	2	38	92
Mansell[57]	3.3c	2	38	88
Wass[58]	3.3d	2	62	100
Wass[58]	3.3d	2	79	100
Wass[56]	3.3e	20	44	89
Whitelegge[52]	3.3f	20	31	93
Whitelegge[52]	3.3g	20	50	96

Again, expansion into pincer complexes shows varied results. RuMACHO® was moderately active towards isobutanol production, giving 36 % yield after 2 h, but extension to 20 h only slightly increased yield to 44 %[56]. SNS complexes are less studied, but investigation of the aliphatic

Gusev complex (Figure 3.3f) and its pyridine-based analogue (Figure 3.3g) show improved yield using the pyridine complex, with moderate 50 % yield after 20 h.
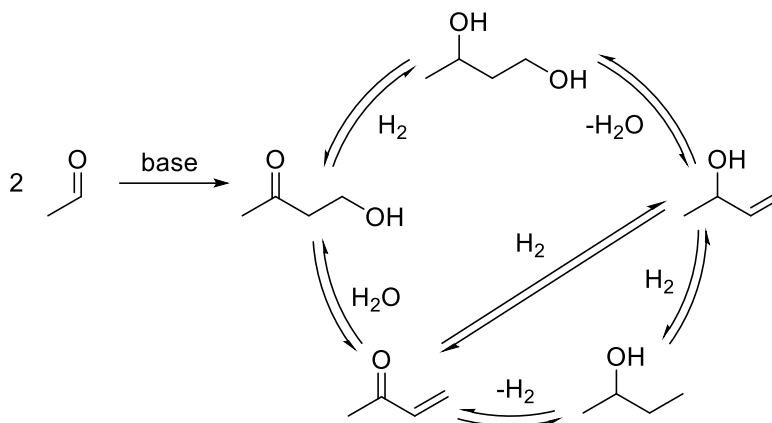
Scheme 3.6 - Proposed mechanism for sec-butanol production by rearrangement of products in the Guerbet ethanol homocoupling reaction.

In 2023, the Wass group also reported the use of pincer type mixed donor complexes has also been noted to result in the unexpected production of *sec*-butanol under standard ethanol homocoupling conditions (shown in Scheme 3.6)[59]. In particular, use of the tetradentate PNNP complex prepared in Chapter 2, [RuCl₂(**L11**)], gave overall low yields but similar selectivities towards *n*-butanol and *sec*-butanol (17 % and 14 % respectively). With modified conditions of 120 °C and 20 mol% base, RuMACHO® remarkably produced a moderate 13 % yield of *sec*-butanol at an unprecedented 68 % selectivity, demonstrating pincer donor modification has substantial impacts on selectivity.

[RuCl₂(**L11**)]
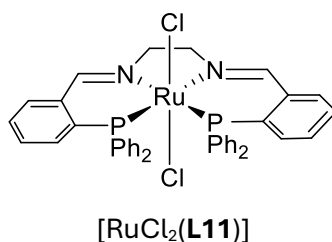
Figure 3.4 - Catalyst found to selectively produce sec-butanol in ethanol homocoupling.

3.2.5   Limitations of the Guerbet reaction

As is demonstrated in the literature, selectivities in Guerbet alcohol coupling are difficult to control. Further reaction of products is liable to produce heavier and more branched alcohols. Ethyl acetate may also be produced by Tishchenko type pathways[60], especially at lower temperatures. At low operating temperatures (140-160 °C), initial alcohol dehydrogenation has been found to be the rate-limiting step, but when temperature is increased (160-180 °C), the aldol

coupling step of the reaction becomes rate-limiting[40]. Therefore, large quantities of alkoxide base are typically used to encourage this transformation and limit ethyl acetate production.

Additionally, the production of water is frequently poorly tolerated by reaction systems; its reaction with excess alkoxide base in standard conditions produces NaOH, which may react by Cannizzaro type chemistry to produce sodium acetate[61], or result in dehydrogenative production of sodium carbonate[62,63]. Consequently, large excesses of base are also beneficial in minimising the impact of this.
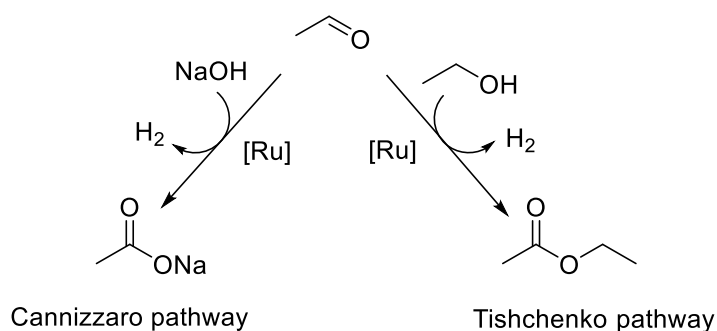
Scheme 3.7 - Cannizzaro and Tishchenko pathways in the Guerbet reaction system.

It is clear that there is opportunity for improved catalyst performance. Ruthenium pincer complexes have already been demonstrated as effective systems for alcohol coupling, with varying selectivity depending on structure; it stands to reason that designed-in modifications may provide further improved performance.

3.3 Aims

The range of Ru(II) PNX (X = O, N, S) complexes introduced in Chapter 2 are based upon ligand systems with established precedent for hydrogen transfer catalysis, so are promising candidates for efficacy in the Guerbet upgrading of ethanol. Additionally, they are considered to have practical and structural qualities with the potential to improve upon some key limitations of current state-of-the-art catalysts:

- **Low cost of production**: the simple preparation and remarkable long-term air stability in solid form of the series provide the potential for reduced costs in production, handling and large-scale application.

- **Solubility in alcohols**: polar pendant arms have recently been explored by the Wass group due to their improved alcohol solubility to some success[58]; this family of complexes shares the property of enhanced solubility at low temperatures, potentially enabling milder reaction conditions.

- **Internal base behaviour**: the hemilabile alcohol ligand functionality was discussed previously as having potential alkoxide binding behaviour (see section 2.2). This in-built alkoxide type structure is theorised to be able to behave in a catalytic system similarly to alkoxide co-catalysts in the Guerbet system, and could operate in sequence as catalyst for hydrogen borrowing and aldol condensation steps. This could provide the benefit of reducing the reliance of the system on large quantities of added alkoxide base.

This chapter aims to explore the application of a selection of these complexes to the Guerbet reaction for the production of both *n*-butanol and isobutanol. Only complexes which were isolated in good yield are investigated for these transformations.

3.4 Novel Ru(II) PNX (X = O,N,S) complexes in the Guerbet synthesis of isobutanol

3.4.1 Screen of novel Ru(II) PNO catalysts

A selection of the PNO-ligated complexes prepared in Chapter 2 (shown in Figure 3.5) were screened for catalytic activity in the Guerbet-type preparation of isobutanol (Scheme 3.8). In this section, the results of these screening experiments are presented. Standard conditions for the cross-coupling of methanol and ethanol developed by the Wass group[56,58,59] were employed, with a benchmark comparative experiment performed against the previously reported $RuCl_2(dppm)_2$ catalyst. Additional complexes $[Ru(CO)_2Cl_2(PPh_3)_2]$ and $[RuCl_2(L7)_2]$ were also included.
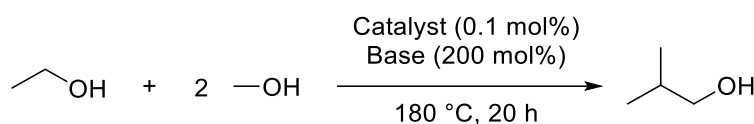
Scheme 3.8 - General reaction conditions for the cross-coupling of ethanol and methanol to produce isobutanol.

$[Ru(CO)_2Cl_2(PPh_3)_2]$ $[RuCl_2(L1)PPh_3]$

$[Ru(L1)_2]Cl_2$ $[Ru(L2)_2]Cl_2$ $[Ru(L3)_2]Cl_2$

$[RuCl_2(L4)_2]$ $[RuCl_2(L6)_2]$ $[RuCl_2(L7)_2]$

Figure 3.5 - Series of PNO/PO ligated Ru(II) complexes initially screened in the Guerbet ethanol/methanol cross-coupling to form isobutanol.
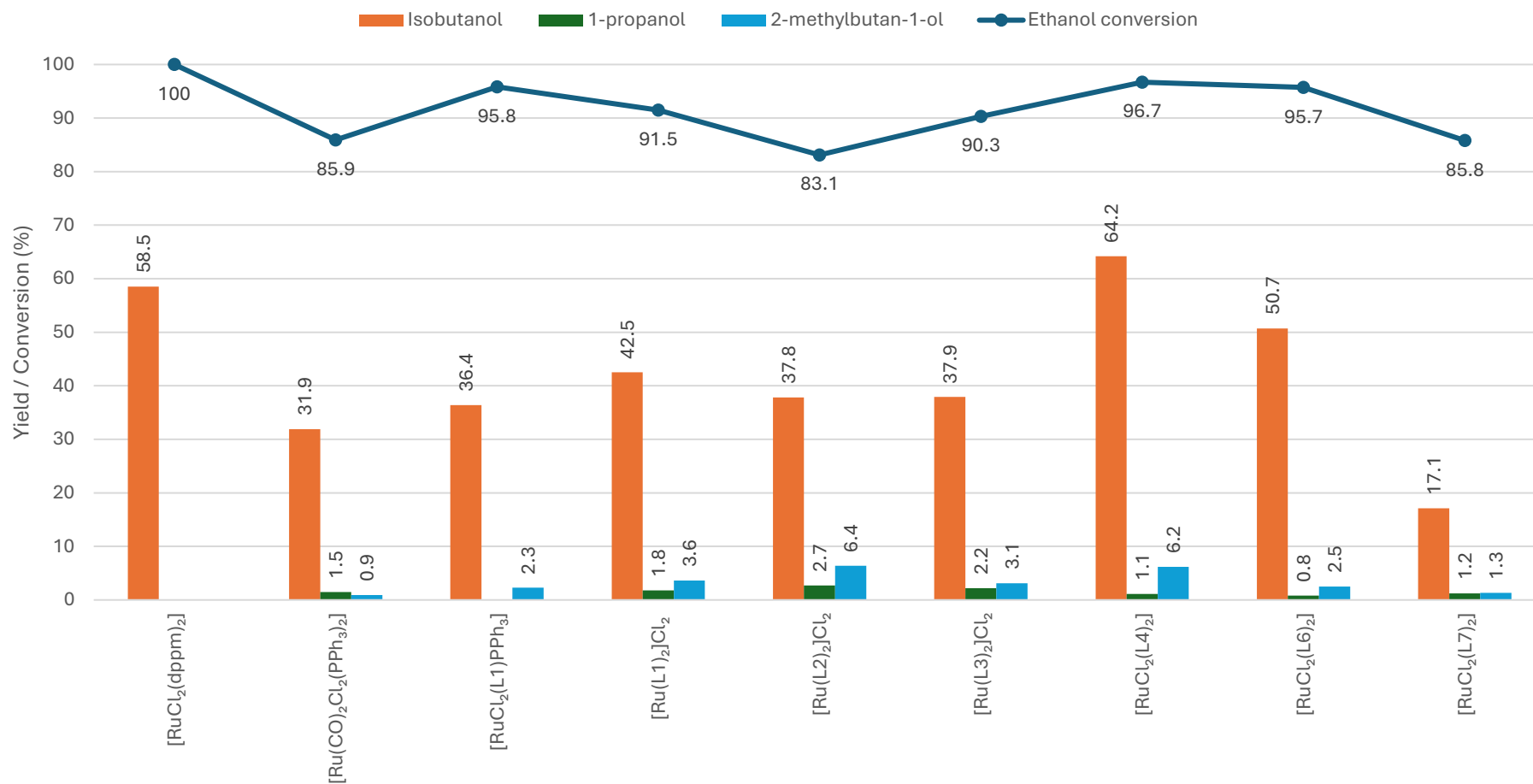
Figure 3.6 - Yield of liquid products and ethanol conversion obtained in the ethanol/methanol cross-coupling with $RuCl_2(PNO)_2$ catalyst series. Conditions: ethanol (1 mL, 17.1 mmol), methanol (10 mL, 247.1 mmol), NaOMe (200 mol%, 1.851 g, 34.16 mmol) and catalyst (0.1 mol% [Ru] basis) were reacted under an inert N_2 atmosphere in a 100 mL Parr reactor at 180 °C for 20 h. Total conversion of ethanol determined by GC-FID using hexadecane as internal standard.
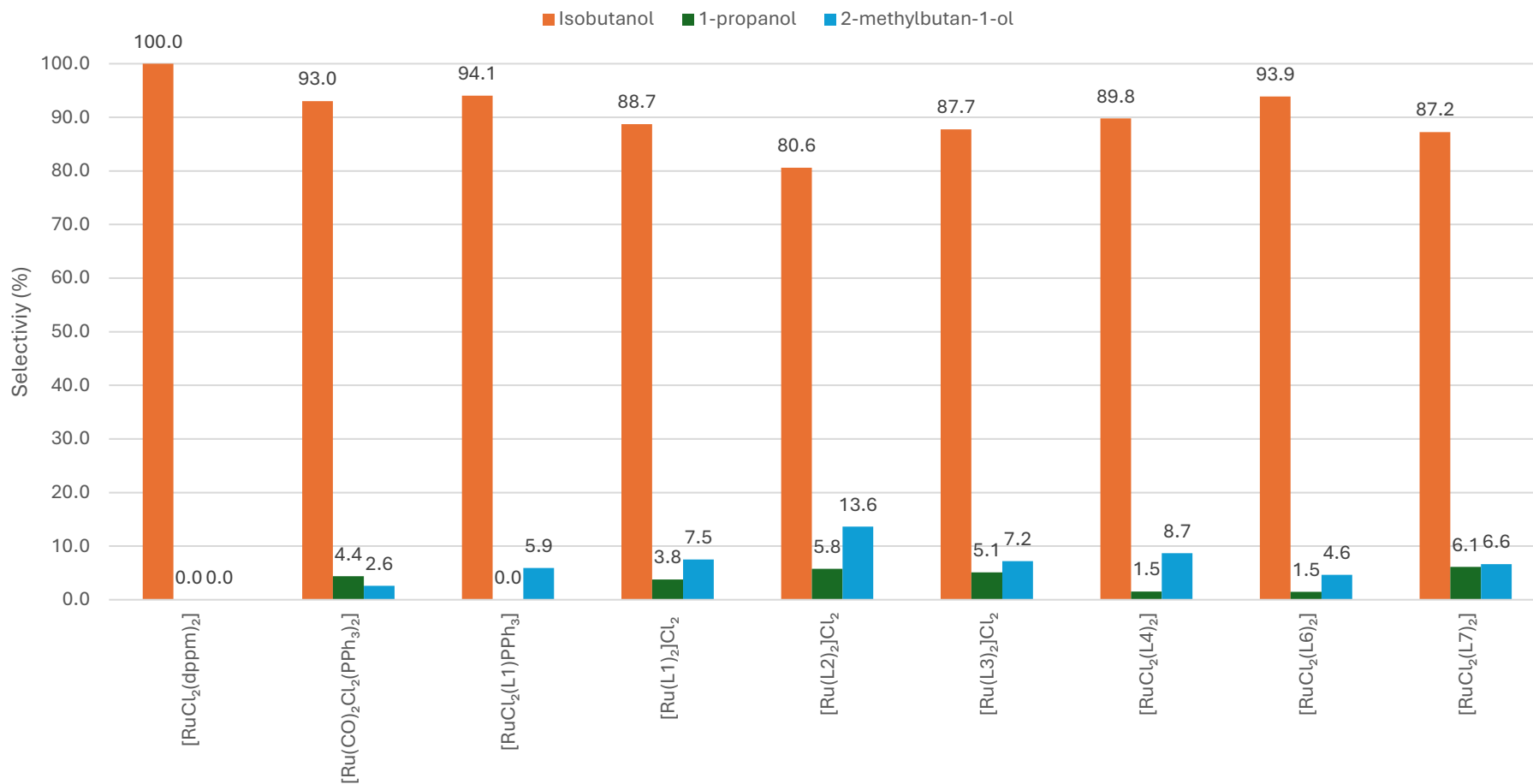
Figure 3.7 – Selectivity of liquid products obtained in the ethanol/methanol cross-coupling with RuCl$_2$(PNO)$_2$ catalyst series. Conditions: ethanol (1 mL, 17.1 mmol), methanol (10 mL, 247.1 mmol), NaOMe (200 mol%, 1.851 g, 34.16 mmol) and catalyst (0.1 mol% [Ru] basis) were reacted under an inert N$_2$ atmosphere in a 100 mL Parr reactor at 180 °C for 20 h. Total conversion of ethanol determined by GC-FID using hexadecane as internal standard.

Despite previous group publications showing [RuCl$_2$(dppm)$_2$] routinely gave isobutanol yields of approx. 70 % under these conditions[58], in this case yield was slightly reduced despite complete conversion of ethanol and 100 % selectivity of liquid phase products. This is attributed to slightly different head space of reaction vessel used, as previous work has found this a significant contributing factor to alternative pathways, and therefore butanol yield, when investigating Guerbet coupling reactions[64].

Across the series, ethanol conversion was high, greater than 80 % in all cases. Yield of isobutanol was generally higher where ethanol conversion was higher and vice versa, with selectivities also moderately high, typically > 85 %. The only observed products in the liquid phase in all cases were intermediate 1-propanol and side product 2-methylbutan-1-ol. There was no production of other butanol isomers observed.

It is clear that the monodentate phosphine complex [Ru(CO)$_2$Cl$_2$(PPh$_3$)$_2$] provides the poorest conversion of ethanol and lowest isobutanol yield at the given conditions; this is consistent with established literature for such systems, as monodentate ligands offer poor stability benefits at elevated temperatures. However, conversely, none of the pincer systems where tridentate ligand binding is observed (complexes of ligands **L1**-**L3**) performed particularly well either, producing similar isobutanol yields to commercially available P-N-P complex RuMACHO[56]. High selectivities towards 1-propanol production in the coordinatively saturated series ([Ru(**L1**)$_2$]Cl$_2$, [Ru(**L2**)$_2$]Cl$_2$, [Ru(**L3**)$_2$]Cl$_2$) suggest reduced reaction rate of the second catalytic cycle with these catalysts. The mono-ligated and bis-ligated **L1** complexes [RuCl$_2$(**L1**)PPh$_3$] and [Ru(**L1**)$_2$]Cl$_2$ performed very similarly, with marginal improvement in yield with the bis-ligated complex. Selectivity in the liquid phase was reduced however, due to greater yields of intermediate 1-propanol and alternative Guerbet alcohol 2-methylbutan-1-ol. Monoligated [RuCl$_2$(**L1**)PPh$_3$] appears to show greater conversion and lower sum of products however, indicating a greater selectivity towards alternative reaction pathways and non-liquid products. Generally speaking, this series of ligands carrying a C2 pendant alcohol arm only showed moderate catalytic activity with no obvious distinctions in isobutanol yield with increased bulk (**L2**) or rigidity (**L3**) of this arm. It may be noted that selectivity towards side product 2-methylbutan-1-ol is greatest in the complex with the greatest steric bulk around this pendant alcohol, [Ru(**L2**)$_2$]Cl$_2$.

The two bis-ligated complexes exhibiting bidentate binding behaviour [RuCl$_2$(**L4**)$_2$] and [RuCl$_2$(**L6**)$_2$] both showed significantly improved isobutanol yields compared to the tridentate PNO complexes. [RuCl$_2$(**L4**)$_2$] showed excellent isobutanol yield of 64 %, better than that obtained from our state-of-the-art catalyst [RuCl$_2$(dppm)$_2$] in these conditions. Indeed,

compared with the structurally similar complexes [RuCl$_2$(PN)$_2$] and [RuCl$_2$(PN^{Me})$_2$] (Figure 3.8), where only 51 % and 46 % isobutanol yields were reported[55], this system is a marked improvement. Selectivity was good at 90%, with competitive production of 2-methylbutan-1-ol was the primary limitation. [RuCl$_2$(**L6**)$_2$] gave reasonably good isobutanol yield of 51 %, with excellent selectivity towards isobutanol.

a) [RuCl$_2$(PN)$_2$]	b) [RuCl$_2$(PN^{Me})$_2$]	c) [RuCl$_2$(PN^{Me2})$_2$]

Yield (selectivity) / % = 51 (90) 46 (96) 29 (93)
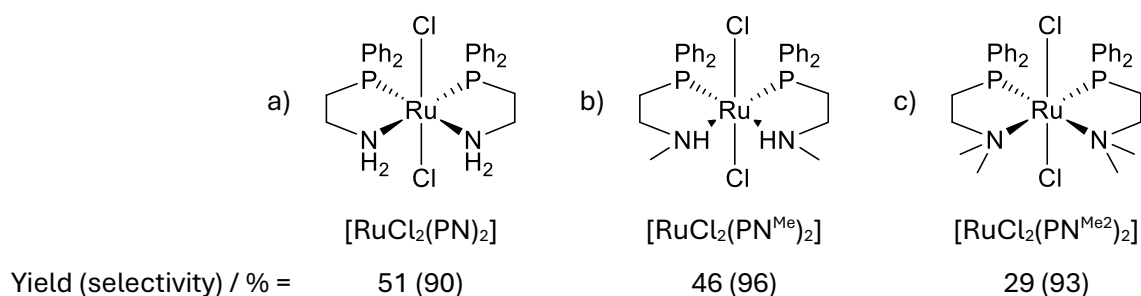
Figure 3.8 - PN complexes and their respective isobutanol yields after 20 h[55]. Yields given with selectivities in brackets. a) [RuCl$_2$(PN)$_2$] b) [RuCl$_2$(PN^{Me})$_2$] c) [RuCl$_2$(PN^{Me2})$_2$]

Interestingly, the PO ligated complex [RuCl$_2$(**L7**)$_2$] performed particularly poorly. Selectivity towards isobutanol is good, but an extremely poor isobutanol yield of 17 % was obtained, despite high ethanol conversions.

3.4.2   Screen of novel Ru(II) PNS catalysts

A selection of the PNS-ligated complexes prepared in Chapter 2 (shown in Figure 3.9) were screened for catalytic activity in the Guerbet-type preparation of isobutanol (Scheme 3.8). In this section, the results of these screening experiments are presented. The same standard conditions were used as in section 3.4.1. In order to investigate the impact of isomers, the two isolated isomers of [RuCl$_2$(**L17**)$_2$] were both included in the catalyst screen.

$[RuCl_2(\textbf{L12})_2]$ $[RuCl(\textbf{L12})(p\text{-cymene})]Cl$ $[RuCl(\textbf{L14})_2]Cl$

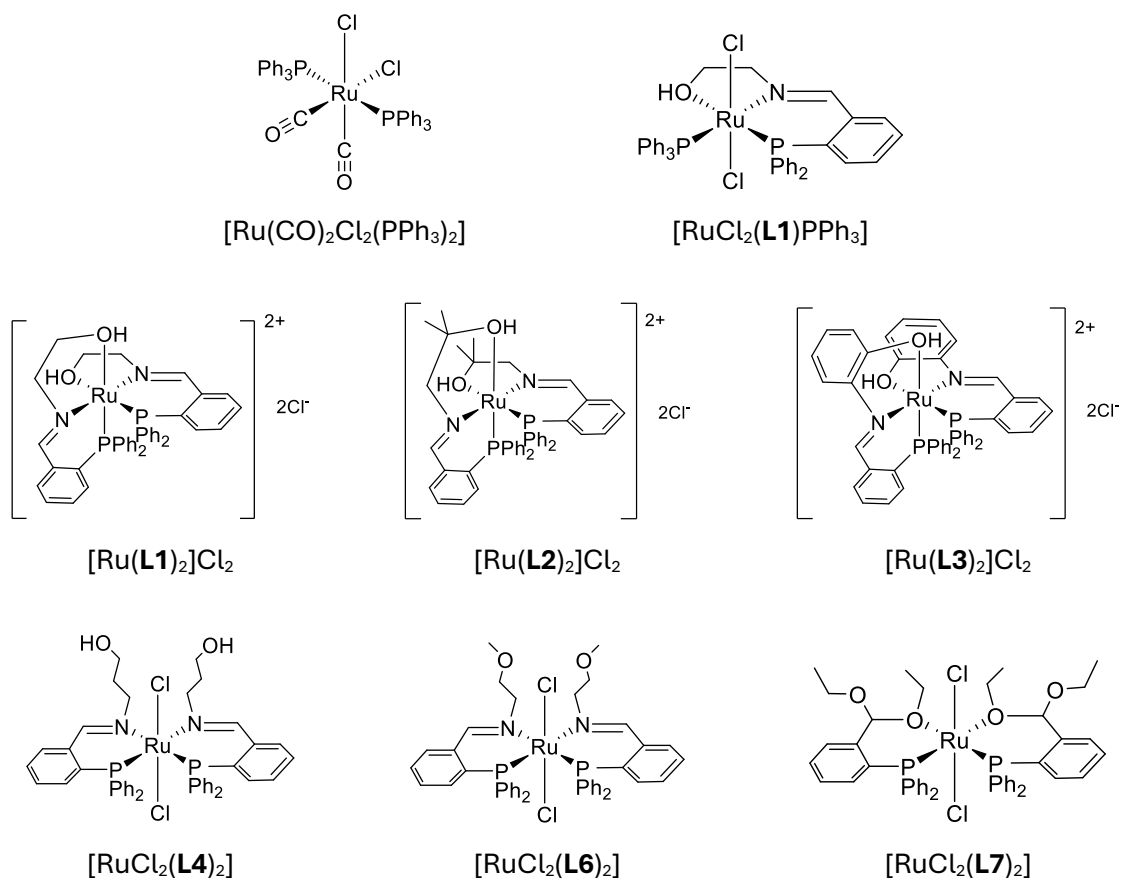$[RuCl_2(\textbf{L15})_2]$ $[RuCl_2(\textbf{L17})_2]$ $[RuCl_2(\textbf{L18})_2]$
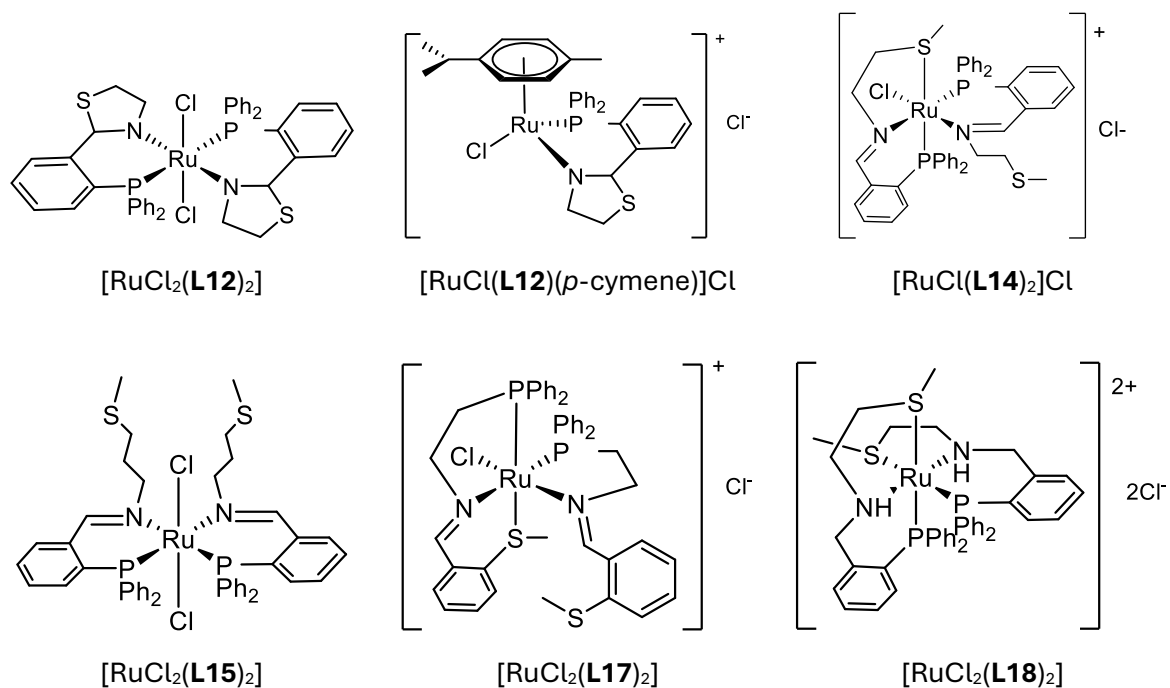
Figure 3.9 - Series of PNS ligated Ru(II) complexes initially screened in the Guerbet ethanol/methanol cross-coupling to form isobutanol.
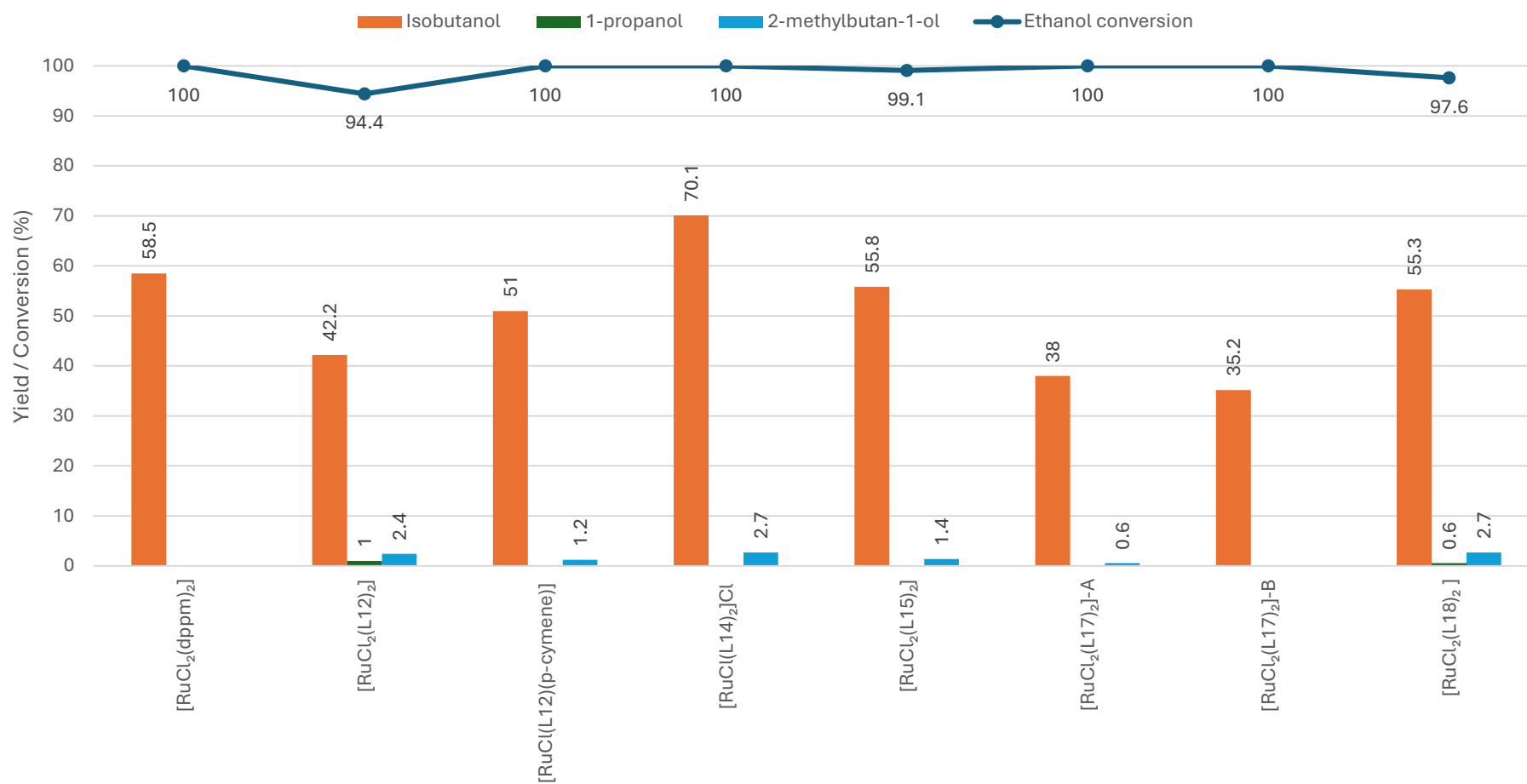
Figure 3.10 – Yield of liquid products and ethanol conversion obtained in the ethanol/methanol cross-coupling with RuCl$_2$(PNS)$_2$ catalyst series. Conditions: ethanol (1 mL, 17.1 mmol), methanol (10 mL, 247.1 mmol), NaOMe (200 mol%, 1.851 g, 34.16 mmol) and catalyst (0.1 mol% [Ru] basis) were reacted under an inert N$_2$ atmosphere in a 100 mL Parr reactor at 180 °C for 20 h. Total conversion of ethanol determined by GC-FID using hexadecane as internal standard.
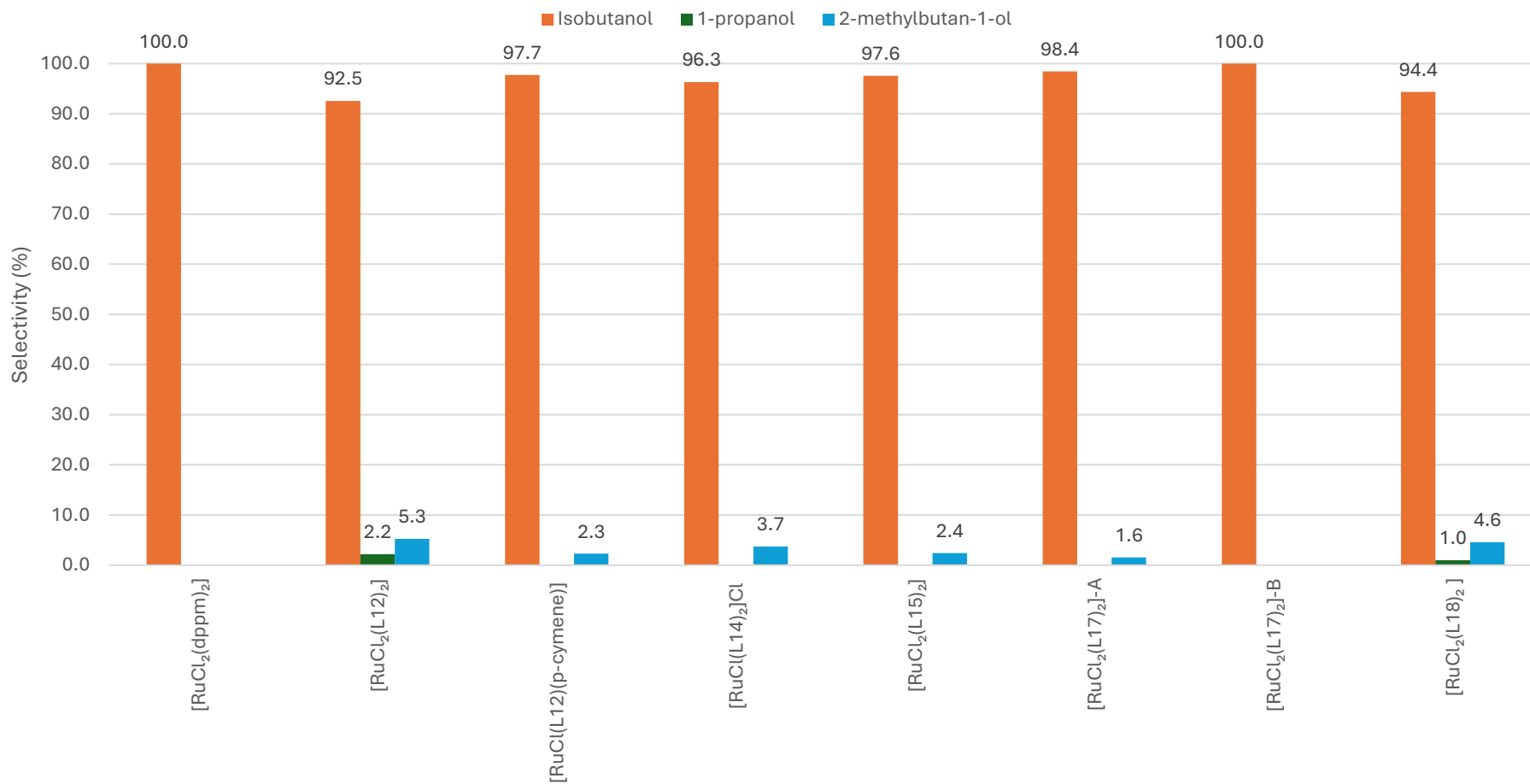
Figure 3.11 - Selectivity of liquid products obtained in the ethanol/methanol cross-coupling with RuCl$_2$(PNS)$_2$ catalyst series. Conditions: ethanol (1 mL, 17.1 mmol), methanol (10 mL, 247.1 mmol), NaOMe (200 mol%, 1.851 g, 34.16 mmol) and catalyst (0.1 mol% [Ru] basis) were reacted under an inert N$_2$ atmosphere in a 100 mL Parr reactor at 180 °C for 20 h. Total conversion of ethanol determined by GC-FID using hexadecane as internal standard.

The sulfur-containing catalysts were, on the whole, found to give higher conversions and yields of isobutanol than the oxygen-containing catalysts, with very high selectivities. This is a promising development in sulfur-catalysed Guerbet, with other recent work within the group giving excellent yields from phosphine free catalysts[52]. The cyclised aminothiol ligand **L12** was assessed for efficacy in both mono- and bis-ligated species [RuCl$_2$(**L12**)$_2$] and [RuCl(**L12**)(*p*-cymene)]Cl. Results were similar, with moderate yield isobutanol, but slightly greater yield and selectivity observed by [RuCl(**L12**)(*p*-cymene)]Cl. This is particularly interesting as previously reported *in situ* ESI-MS and NMR spectroscopy experiments noted analogous structures formed when ruthenium precursor [RuCl$_2$(*p*-cymene)]$_2$ was used in conjunction with two equivalents of a PN ligand in the coupling of ethanol to form *n*-butanol (Figure 3.12)[49]. This work also reported slower reaction times for pre-formed bis-ligated systems, which could be an effect seen in the incomplete conversion by [RuCl$_2$(**L12**)$_2$] and the presence of intermediate 1-propanol in the product mixture.
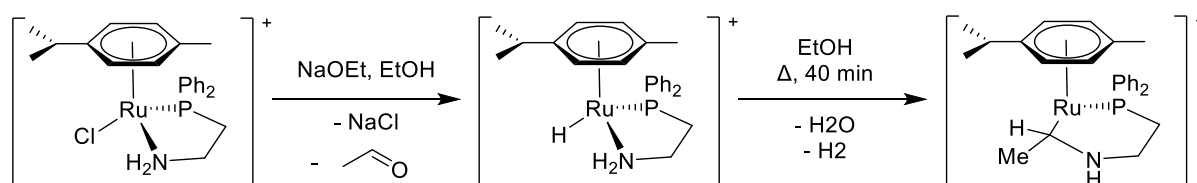
Figure 3.12 - Intermediate fragments observed by Wingad et al. with addition of base & heat [49]. Structures identified by NMR spectroscopy studies and mass spectrometry samples taken from crude reaction mixture.

The catalyst showing the highest yield of isobutanol was [RuCl(**L14**)$_2$]Cl, which exhibits an unusual asymmetric structure with tridentate and bidentate ligand behaviour. This structure strongly suggests hemilability of the sulfur arm (discussed in section 2.4.4.2), potentially enabling improved access to the ruthenium core to increase reactivity – a comparison also made between the more catalytically efficient bidentate PNO-type catalysts [RuCl$_2$(**L4**)$_2$] and [RuCl$_2$(**L6**)$_2$] and their tridentate counterparts. The isobutanol yield recorded using [RuCl(**L14**)$_2$]Cl is comparable to the highest reported yields, with complete conversion of ethanol, albeit some production of 2-methylbutan-1-ol side product – though isobutanol selectivity remains high at over 95 %.

When compared with [RuCl(**L14**)$_2$]Cl, extension of the pendant arm chain length to three carbons in [RuCl$_2$(**L15**)$_2$] also gives a reduced yield of 56 % despite extremely high conversion - however, excellent selectivity is retained. Hence production of non-liquid side products appears slightly favoured. This is in contrast with the trend observed with PNO complexes [Ru(**L1**)$_2$]Cl$_2$ and [RuCl$_2$(**L4**)$_2$] (see Figure 3.6). Extension of the PNO pendant arm increased activity: the longer

chain C3 complex almost doubled isobutanol yield to give comparable yield to the best PNS system.

When using the reduced amine complex [RuCl$_2$(**L18**)$_2$], the results also surprisingly show somewhat reduced yield of isobutanol, giving only 55 % yield. The presence of 1-propanol and incomplete ethanol conversion indicate a reduced reactivity when starting with the amine ligand. It was noted that this complex, unlike [RuCl(**L14**)$_2$]Cl, was extremely insoluble at room temperature, which perhaps contributed to reduced reactivity, though with low concentration of catalyst used, post-reaction or *in situ* analysis of the two complexes was not possible directly. Further attempts to investigate the behaviour of the two catalysts in model conditions are discussed in section 0.

Given the production of [RuCl$_2$(**L17**)$_2$] in two isolated isomers (see section 2.4.4.2), when investigated for catalytic activity, both isomers of each complex were investigated for catalytic behaviour, despite incomplete understanding of ligand binding modes of each. [RuCl$_2$(**L17**)$_2$]-**A** and [RuCl$_2$(**L17**)$_2$]-**B** performed statistically no differently from one another, producing extremely high selectivities to isobutanol in the liquid phase, though only 38 % and 35 % yield respectively. Similar data obtained concerning *cis* and *trans* isomers of [RuCl$_2$(dppm)$_2$] was used to suggest interchange between isomers in solution[48]; this effect is plausible under the high operating temperatures and base loadings for this family of catalysts too. Yield from both [RuCl$_2$(**L17**)$_2$] isomers is lower than that obtained from the structurally similar [RuCl$_2$(PN^{Me})$_2$] but greater than the [RuCl$_2$(PN^{2Me})$_2$] analogue (Figure 3.8). This could indicate the involvement of heteroatoms with vacancy able to carry hydrogen atoms (in this case, ruthenium-bound nitrogen) in the mechanism, lending support to a previously proposed mechanism involving insertion of alcohol into the Ru-N bond[49] (Figure 3.12) though further investigation would be necessary to understand any intermediate complexes formed when using imine-based ligand structures. It has also already been established that Ru-N is not necessary for efficient catalytic activity given the excellent activity and selectivity seen from [RuCl$_2$(dppm)$_2$], so multiple potential catalysis operations are plausible. It does appear that the rigidity of an aromatic pendant arm, whilst not strictly disadvantageous in PNO complexes (see [Ru(**L3**)$_2$]Cl$_2$), does not improve catalytic activity in this family of hemilabile species.

3.4.3 Effect of choice of pendant arm donor atom

To investigate the impact of free arm electronics and resultant structure-activity relationship, a direct comparison of the complexes containing analogous methylated ligands **L6**, **L9** and **L14** (Figure 3.13) was performed.
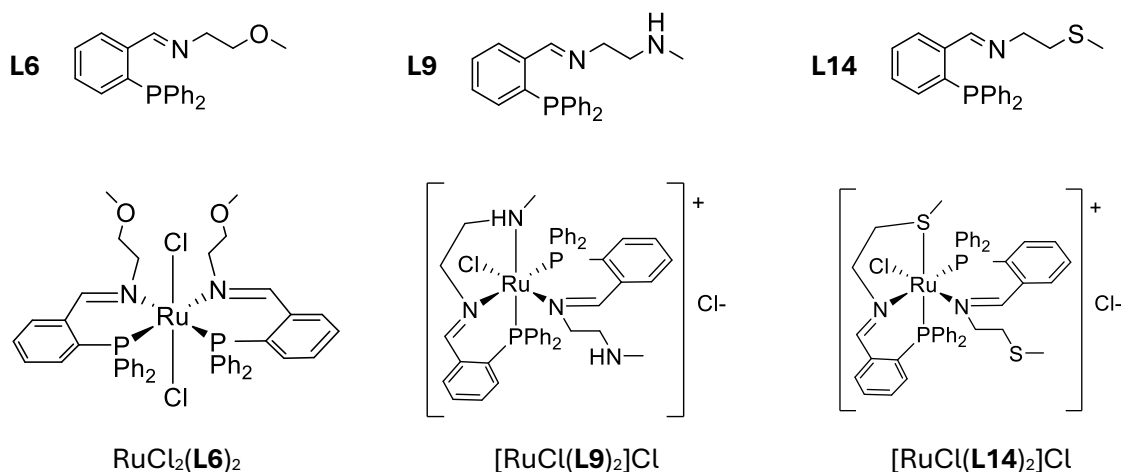
Figure 3.13 - Methylated ligands and complexes compared for Guerbet methanol/ethanol cross-coupling.
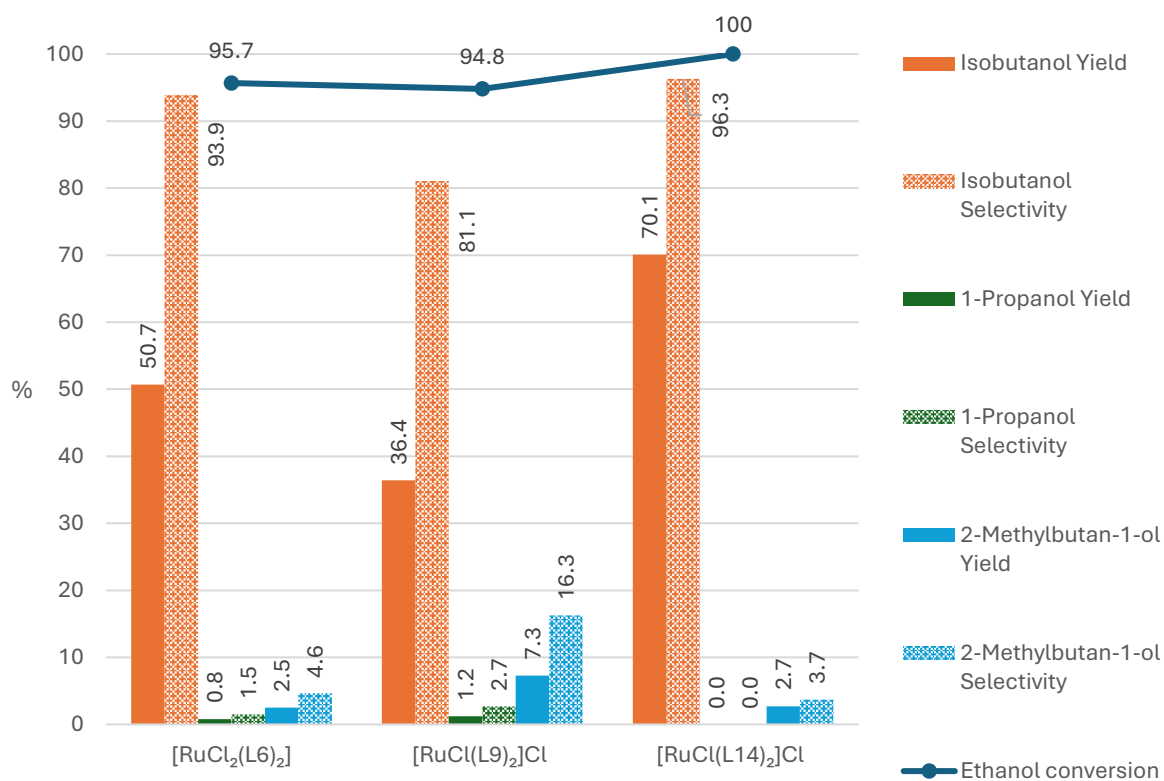
Figure 3.14 - Results of isobutanol production using methylated catalysts listed in Figure 3.13.

A direct comparison between the analogous PNO, PNN and PNS methylated complexes shows that all were active for isobutanol production, though a clear improvement in activity and yield was seen in the group 8 elements. Reaction for both [RuCl$_2$(**L6**)$_2$] and [RuCl(**L9**)$_2$]Cl was seen to be incomplete even after 20 h, with slightly depressed ethanol conversion and visible intermediate 1-propanol. Substantial loss of 40-50 % of ethanol is also seen to non-liquid products in both of these complexes, based on conversion. Conversely, as previously described, [RuCl(**L14**)$_2$]Cl gave the highest isobutanol yield of all tested catalysts with excellent selectivity.

Of the three methylated complexes [RuCl(**L9**)$_2$]Cl performed worst, giving only 36 % yield isobutanol and the highest yield and selectivity of all catalysts tested towards side product 2-methylbutan-1-ol, produced at 16 % selectivity. This switch of selectivity and increase production of 2-methylbutan-1-ol has also been observed in PNP pincer complex RuMACHO[56], potentially indicating the nitrogen-containing pincer complex system enables alternative reactivity. The inactivity of PNN pincer complexes in the Guerbet production of n-butanol has been reported by Milstein[50]; however, activity in the two alcohol coupling systems is not always correlated (see section 0) and there is insufficient data on PNN pincers under these conditions to draw such conclusions.

Given the proposed weak Ru-O interaction in [RuCl$_2$(**L6**)$_2$] and relatively strong Ru-N binding interactions, it is tentatively suggested that the larger, softer sulfur exhibits greater ability to donate into the ruthenium centre as a truly hemilabile arm, enabling ready access of reagents to the ruthenium core whilst maintaining electron density available for facilitating hydrogen transfer. However, it is unknown if this reaction proceeds *via* an inner- or outer-sphere type pathway, so the relevance of hemilability is difficult to ascertain.

3.4.4   Side Products

3.4.4.1   Liquid Side Products

The benefit of cross-coupling with methanol is the number of available alternative Guerbet pathways is limited by the intermediates available. Use of large excess of methanol in the system limits the possibility of co-condensation of ethanol to give 1-butanol or other such products; in none of the examples above were such co-condensation products observed. Additionally, the formaldehyde intermediate formed by dehydrogenation of methanol is highly reactive as an electrophile, making certain pathways considerably more likely. Indeed, consistently across the catalyst screen, the only observed side products in the liquid phase were alternative Guerbet products 1-propanol and 2-methylbutan-1-ol. Both products are consistent with previously

reported syntheses of isobutanol in this method[58,59]. 1-propanol is an intermediate of isobutanol production, so is consistent with the catalytic cycle occurring with only one cycle. Two proposed methods of production of 2-methylbutan-1-ol are considered feasible. One is the cross-coupling of methanol with 1-butanol, competitively produced from co-coupling of ethanol; given the lack of 1-butanol observed in any examples above, this pathway is not considered likely. The other potential pathway is reaction of intermediate 1-propanol with ethanol (Scheme 3.9). This pathway is particularly plausible as the production of 2-methylbutan-1-ol appears to correlate with the presence of 1-propanol. Interestingly, no products of the coupling of two molecules of 1-propanol are observed, and 2-methylbutan-1-ol is consistently observed in larger quantities than 1-propanol. This suggests no significant build-up of the intermediate, so no significant reduction in rate of the second cycle of the alcohol coupling relative to the first.
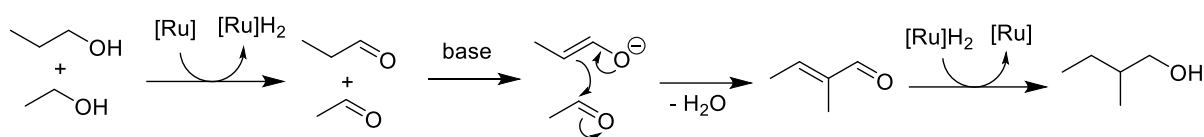
Scheme 3.9 - Proposed mechanism for the production of 2-methylbutan-1-ol side product from intermediate 1-propanol and ethanol.

3.4.4.2   Other side products

Examination of the catalyst screen shows a consistent gap between proportion of ethanol consumed and sum of liquid products yielded. Hence it must be concluded that ethanol is being transformed into solid or gaseous products. Early work in the Wass group involved investigation into the nature of these products[56,65].

It has been reported that large quantities of white solid were routinely produced in catalytic runs; this was also consistently observed in this work. The solid products from a routine catalytic run using the best-performing catalyst [RuCl(**L14**)$_2$]Cl were isolated and analysed quantitatively by FTIR spectroscopy, ^{1}H and ^{13}C{^{1}H} NMR spectroscopy. Identified solid product fragments were predominantly formate and carbonate, with a small quantity of acetate.

It is recognised that the *in situ* generation of water in the Guerbet reaction will result in the production of NaOH base. This is known to facilitate ruthenium-catalysed dehydrogenation of both ethanol and methanol in different pathways. Sodium acetate formation is possible by the competitive Cannizzaro-type formation of acetic acid from dehydrogenated ethanol and NaOH with two equivalents of hydrogen released (Scheme 3.10)[49,61]. It is plausible this is where ethanol is lost from the liquid phase products. The production of formate and carbonate as major solid

products is also consistent with the reported base-assisted dehydrogenation of methanol, also releasing hydrogen, in the presence of ruthenium pincer complexes (Scheme 3.11)[62,63].
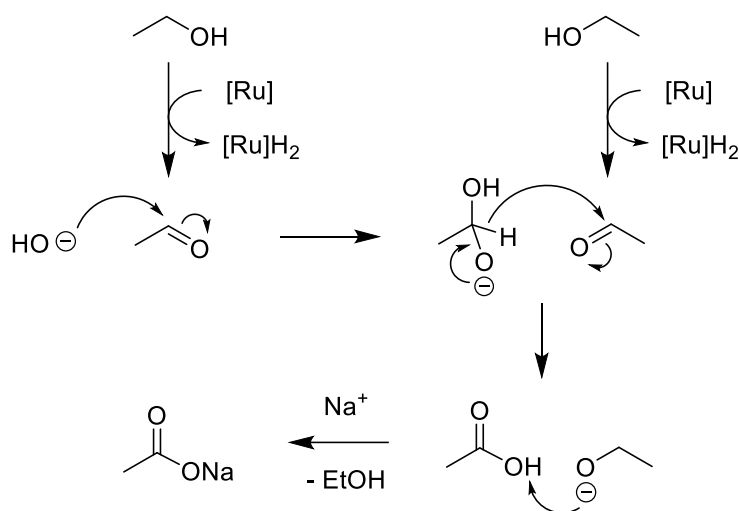
Scheme 3.10 - Cannizzaro reaction of ethanol to give sodium acetate.
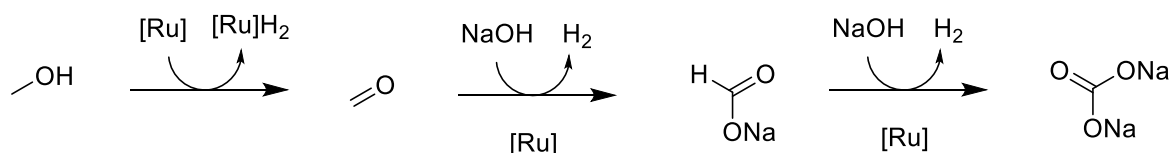
Scheme 3.11 – Proposed pathway for base-assisted production of formate and carbonate from methanol.

It is obvious gaseous products are produced during this catalysis as substantial pressure build up over the course of 20 h catalytic runs, with around 10-15 bar residual pressure typical after the reaction vessel was permitted to cool to room temperature. Previous Wass group work into isobutanol synthesis has shown the gaseous byproducts in this transformation are approximately 95 % hydrogen[65], which is unsurprising due to hydrogen release in the production of the identified solid products. No gas product analysis was performed in this work, but given the consistency of qualitative solid state and liquid phase analysis with reported results, it is presumed gas produced in this work is also predominantly hydrogen.

3.4.5   Base loading study

Desirable properties of Guerbet catalysts include an ability to operate at reduced base loading. This would be distinctly advantageous given the current use of superstoichiometric NaOMe required for high ethanol conversion and isobutanol yields, with two equivalents used per ethanol – amounting under current conditions to 1.85 g solid for 1 mL ethanol. An initial theory was that a hemilabile alcohol arm could operate as an internal base in the catalytic system, catalysing the

aldol condensation step of the Guerbet reaction. To investigate this possibility, base loading was reduced in three PNO complexes showing structural variation in their pendant arms ([Ru(L1)$_2$]Cl$_2$, [RuCl$_2$(L4)$_2$] and [RuCl$_2$(L6)$_2$]), and the most effective PNS complex [RuCl(L14)$_2$]Cl.
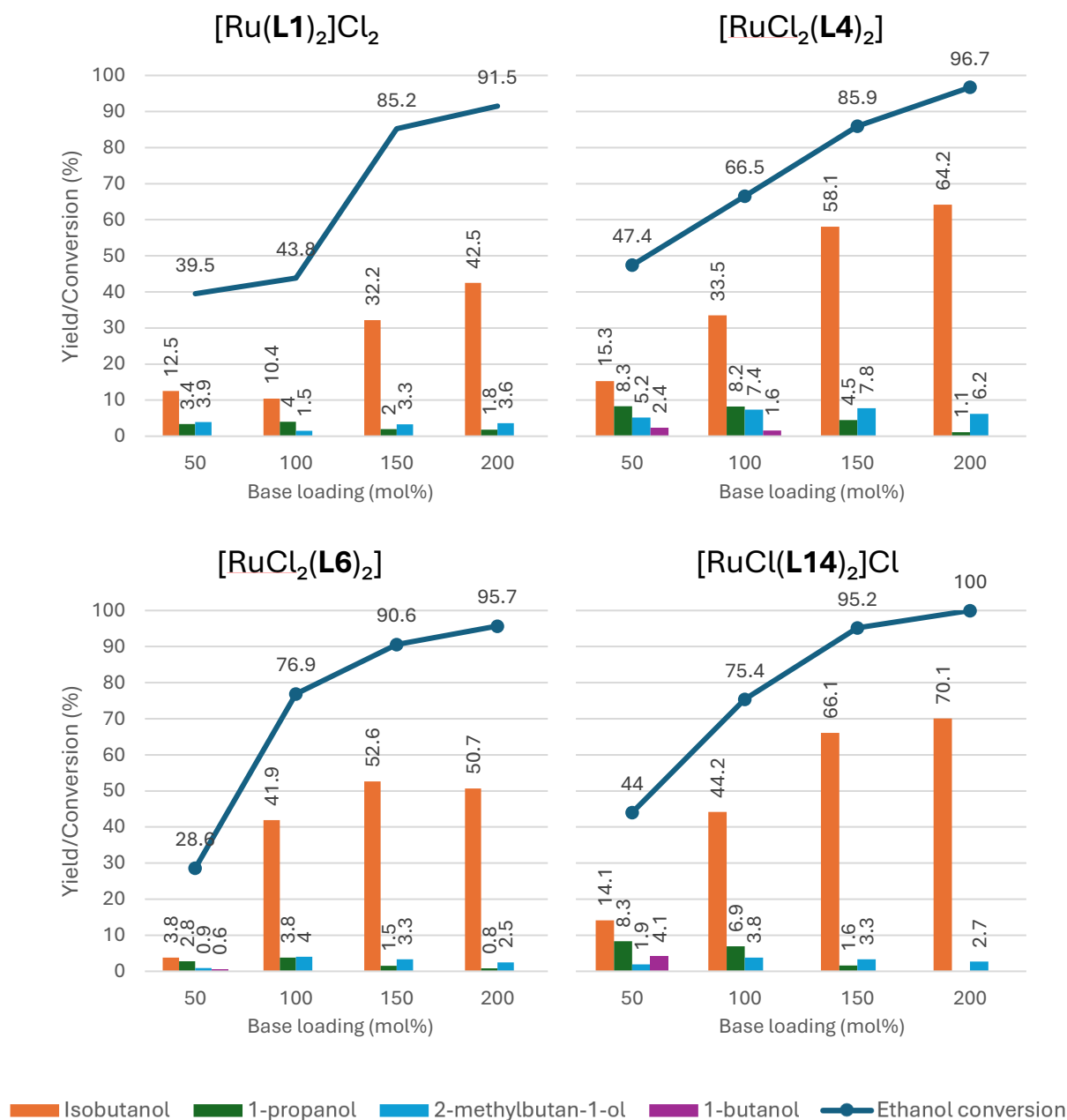
Figure 3.15 – Products produced in Guerbet ethanol/methanol coupling with varying NaOMe loading using catalysts [Ru(L1)$_2$]Cl$_2$, [RuCl$_2$(L4)$_2$], [RuCl$_2$(L6)$_2$] and [RuCl(L14)$_2$]Cl.

All catalysts showed a continuous drop in ethanol conversion with reduction in base loading. When considering the two catalysts featuring alcohol groups, there was no obvious retention in activity over the two methylated complexes, suggesting no catalytic benefit of an internal alcohol-based ligand.

Isobutanol yield was retained well with a reduction to 150 mol% base in all four systems, with the two methylated systems showing particularly excellent tolerance to reduction in loading, despite the slight reduction in ethanol conversion. Perhaps unsurprisingly, the poorest yielding catalyst investigated ([Ru(**L1**)$_2$]Cl$_2$) showed the largest drop in isobutanol yield when base loading was reduced to 150 mol%. A much greater negative effect was seen in all catalysts when base loading was reduced to 100 mol%. [Ru(**L1**)$_2$]Cl$_2$ showed a yield of only 10 % and saw a dramatic drop in conversion, as well as reduction in selectivity due to increased production of intermediate 1-propanol in the product mixture. However, this degree of activity was retained at even lower base loading of 50 mol%, instead of reducing further as might be expected – and was indeed observed in all other catalysts tested.

Reduction in selectivity was consistent across catalysts as base loading was decreased, largely due to increased recovery of intermediate 1-propanol. The C3 chain alcohol complex [RuCl$_2$(**L4**)$_2$] also showed unexpected production of *n*-butanol at 100 mol% base loading, which is produced from ethanol coupling. With both methylated complexes [RuCl$_2$(**L6**)$_2$] and [RuCl(**L14**)$_2$]Cl, *n*-butanol was also produced at the lowest tested base loading of 50 mol%. This could be an indicator of relative rate of dehydrogenation increasing relative to aldol condensation, leading to increased initial concentration of acetaldehyde when low base loadings are used. However, selectivity towards *n*-butanol over 2-methylbutan-1-ol is observed by [RuCl(**L14**)$_2$]Cl, suggesting increased selectivity towards coupling of acetaldehyde molecules, instead of cross-coupling acetaldehyde with the longer chain 1-propanol.

Generally, it is interesting that the methoxy complex [RuCl$_2$(**L6**)$_2$] suffered only minor losses in activity at 100 mol% base loading, showing greater isobutanol yield than [RuCl$_2$(**L4**)$_2$] and similar to [RuCl(**L14**)$_2$]Cl, both of which performed substantially better at 200 mol% base loadings. However, yield of isobutanol remains reasonable in both [RuCl$_2$(**L6**)$_2$] and [RuCl(**L14**)$_2$]Cl at 100 mol% base loading, suggesting that the methylated hemilabile arms are better ligands for this type of catalysis than alcohols at low base loading.

3.4.6   NaOH tolerance study

One of the potential reasons for high base loading being required is the intolerance of catalysts to alternative base NaOH. Given the production of water during the Guerbet reaction, interaction with NaOMe base will lead to the production of NaOH *in situ*. Hence, the complexes used must be compatible with NaOH for catalysis to be effective, else production of water will kill any activity as the reaction progresses. Use of NaOH would also have additional financial benefit as it is cheaper than NaOMe. This was investigated by replacement of NaOMe base with the molar

equivalent of NaOH in the same series of four catalysts, to imitate the effect of water production during reaction. The results of these experiments are summarised in Figure 3.16.
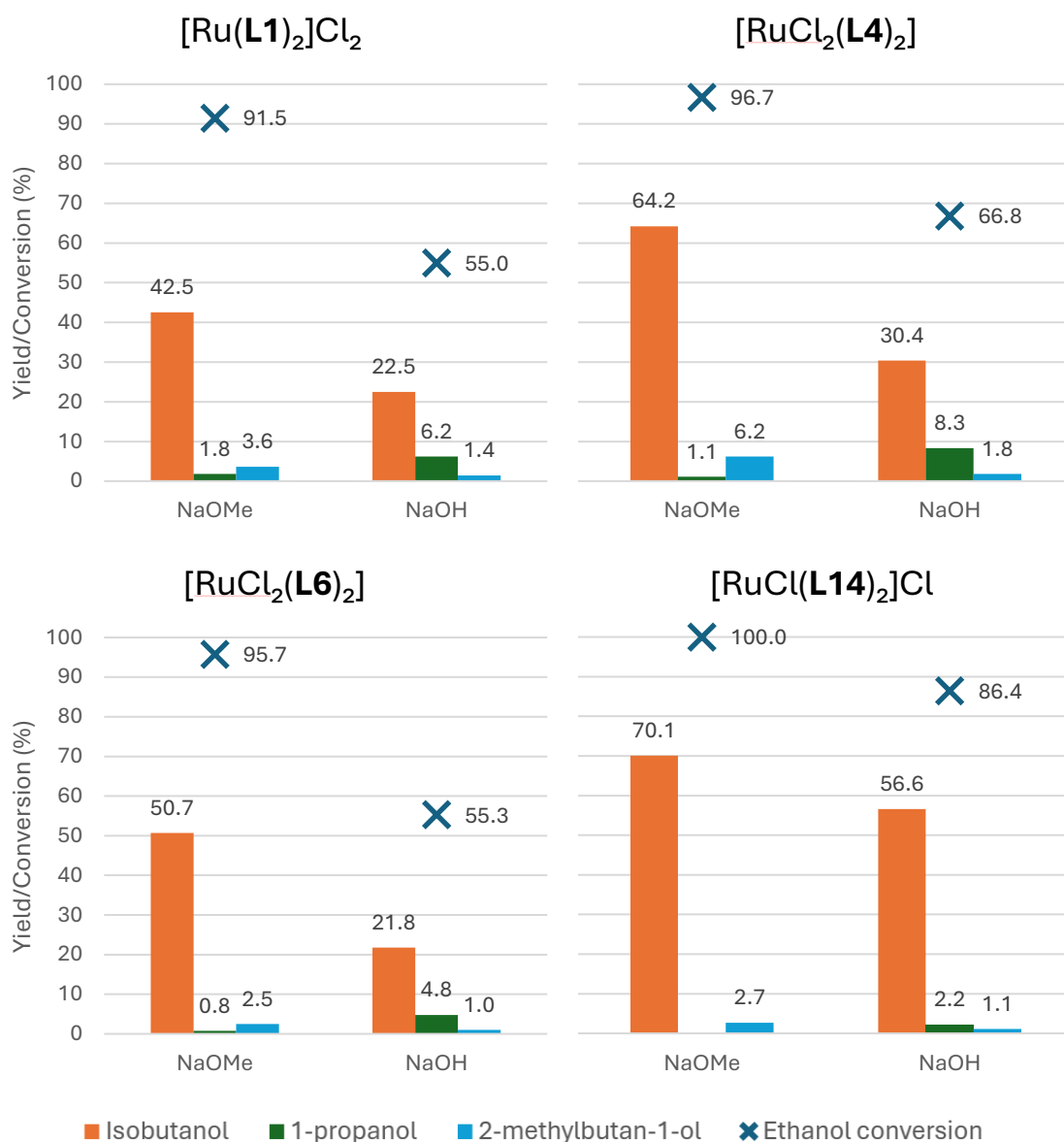
*Figure 3.16 - Products produced in Guerbet ethanol/methanol coupling with varying base, using catalysts [Ru(**L1**)$_2$]Cl$_2$, [RuCl$_2$(**L4**)$_2$], [RuCl$_2$(**L6**)$_2$] and [RuCl(**L14**)$_2$]Cl.*

It is obvious that all complexes tested are less efficient catalysts using NaOH base. Whilst production of side product 2-methylbutan-1-ol is reduced, all catalysts see decreased ethanol conversion, isobutanol yield and selectivity, clearly due to increased production of intermediate alcohol product 1-propanol. Interestingly, this effect is most pronounced in PNO type complexes, with a much more minor effect seen when [RuCl(**L14**)$_2$]Cl is used with NaOH. When comparing the PNO complexes, all saw a reduction in isobutanol yield of around 50 %, regardless of efficacy

with NaOMe. In this way, it appears that structural variation within ligands did not make as much of an impact as electronic impact of third atom.

What is interesting, based on comparison of ethanol consumption and sum of liquid product yields, is that there does not appear to be increased selectivity towards non-liquid side products with the use of NaOH, and instead just a general reduction in activity. In all catalysts, proportion of ethanol unaccounted for in the liquid phase products is almost identical whether NaOMe or NaOH were used. This could indicate some kind of general catalyst deactivation to all reactivity, including towards Cannizzaro or methanol dehydrogenation pathways – though it is gratifying no increased reactivity towards Cannizzaro-type side production of acetate was obvious when NaOH was initially applied. A full mass balance and solid product analysis would be required to confirm this, however.

Additionally, in all reactions with PNO type catalysts, solid produced was dark grey, which was an effect not observed when [RuCl(**L14**)$_2$]Cl was used; no solid analysis was performed in these reactions, but this observation has been previously linked to catalyst decomposition and deposition of ruthenium[49]. If [RuCl(**L14**)$_2$]Cl is able to remain homogeneous with NaOH this shows great promise for its tolerance to high water content reaction conditions. Unfortunately, low catalyst concentration prevented post-reaction catalyst analysis in this work.

3.4.7 [RuCl(**L14**)$_2$]Cl short run time experiments

Previous work from the Wass group has noted that pre-formed catalysts typically produce equivalent yields but over greater timespans when compared to the application of free ligand with ruthenium precursor complex for the Guerbet coupling of ethanol[48]. In this work, due to the practical concerns created by very low catalyst loadings used and the state of many ligands tested as viscous oils, this type of testing was not performed. However, the best performing system [RuCl(**L14**)$_2$]Cl was tested at reduced run times to compare to previously reported [RuCl$_2$(dppm)$_2$]. Results are summarised in Figure 3.17.
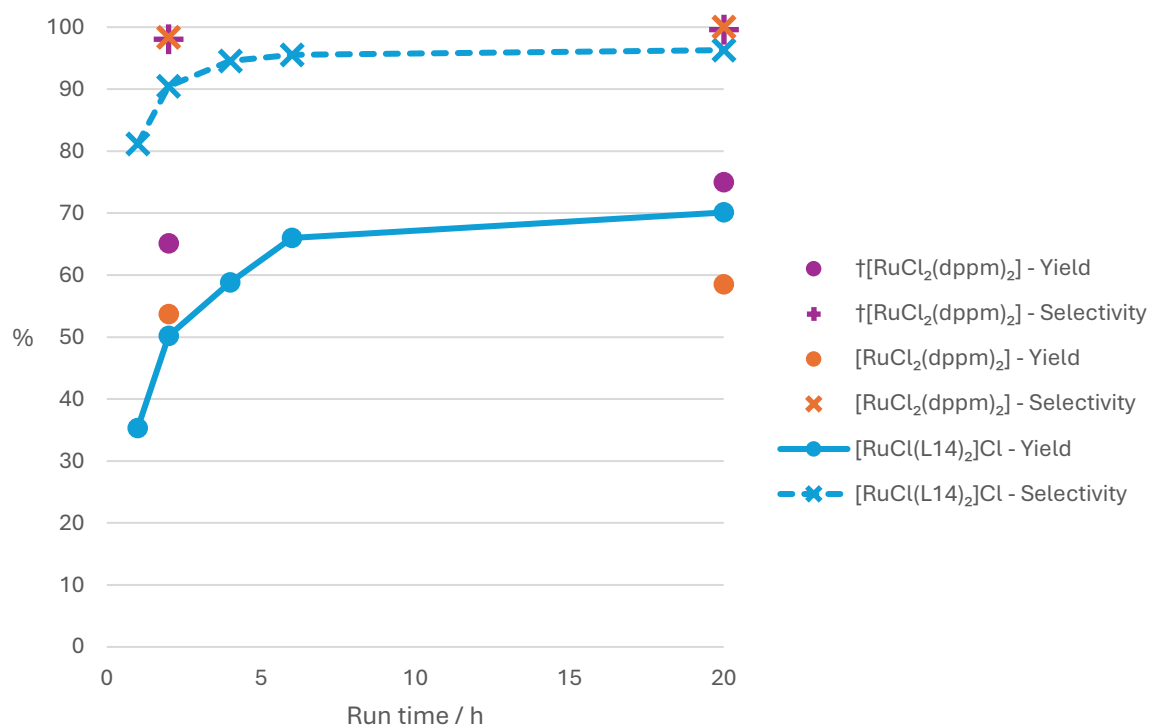
Figure 3.17 - Comparison of isobutanol yield and selectivity at different run times. † Data from literature[55].

Given the inability to directly reproduce reported data for $[RuCl_2(dppm)_2]$, comparative data points after 2 h and 20 h run times were obtained in this work; although isobutanol yields were reduced for this catalyst in this work, the trend observed was very similar, with the isobutanol yield after 2 h accounting for ~90 % of isobutanol yield after 20 h. Interestingly, $[RuCl(\textbf{L14})_2]Cl$ took much longer to produce comparative yields; 90 % of yield after 20 h was not reached until 6 h of reaction. However, isobutanol yield after 20 h is comparable between catalysts. This suggests either a slower-acting catalyst or a longer activation period. The similar increase in selectivity over time is due to initial production of intermediate propanol which undergoes further reaction to give product isobutanol. Given the increased solubility of $[RuCl(\textbf{L14})_2]Cl$ relative to $[RuCl_2(dppm)_2]$, and its rapid reaction with NaOMe at room temperature (see section 0), it is presumed that the catalyst activation by base of $[RuCl(\textbf{L14})_2]Cl$ is not the rate-limiting condition, unless the initially formed species requires further activation of some type to perform alcohol dehydrogenation.

3.5 NMR scale study of interactions with base

Given the low catalyst concentration in isobutanol synthesis, attempts to investigate crude reaction mixture by NMR spectroscopy after reaction were unsuccessful. Instead, preliminary attempts to study the behaviour of the PNS catalysts [RuCl($\textbf{L14}$)$_2$]Cl and [RuCl$_2$($\textbf{L18}$)$_2$] were made by monitoring interaction of complexes with NaOMe in methanol-d4, both at room temperature and after heating to 50 °C overnight.

Given its excellent performance, [RuCl($\textbf{L14}$)$_2$]Cl was selected as the primary target in this investigation. The complex fully dissolved in methanol-d4 at room temperature to give a yellow solution showing the expected pair of doublets in the ^{31}P{^{1}H} NMR spectrum at 44.2 and 40.5 ppm. After heating for 16 h in the absence of base, a second minor species appeared as a singlet at 40.1 ppm (Figure 3.18b, signal 2), proposed to be a symmetrical species featuring coordinated methanol-d4 with displacement of a hemilabile sulfur ligand (Scheme 3.12). It is noted ligand rearrangement must occur for this transformation to produce a symmetrical species. Concordantly, an additional singlet imine signal in the ^{1}H spectrum was visible at 9.29 ppm (Figure 3.19b, signal 2).
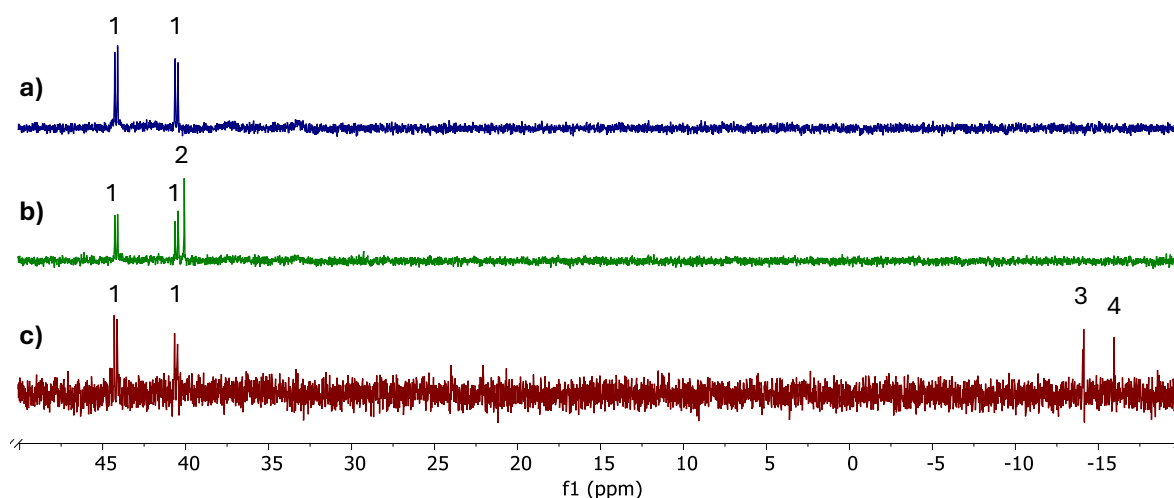
Figure 3.18 - ^{31}P{^{1}H} NMR NMR spectra of [RuCl($\textbf{L14}$)$_2$]Cl in methanol-d4. [a] Room temperature spectrum. [b] After heating in MeOD at 50 °C for 16 h. [c] [RuCl($\textbf{L14}$)$_2$]Cl and excess NaOMe in methanol-d4 after heating to 50 °C for 16 h.
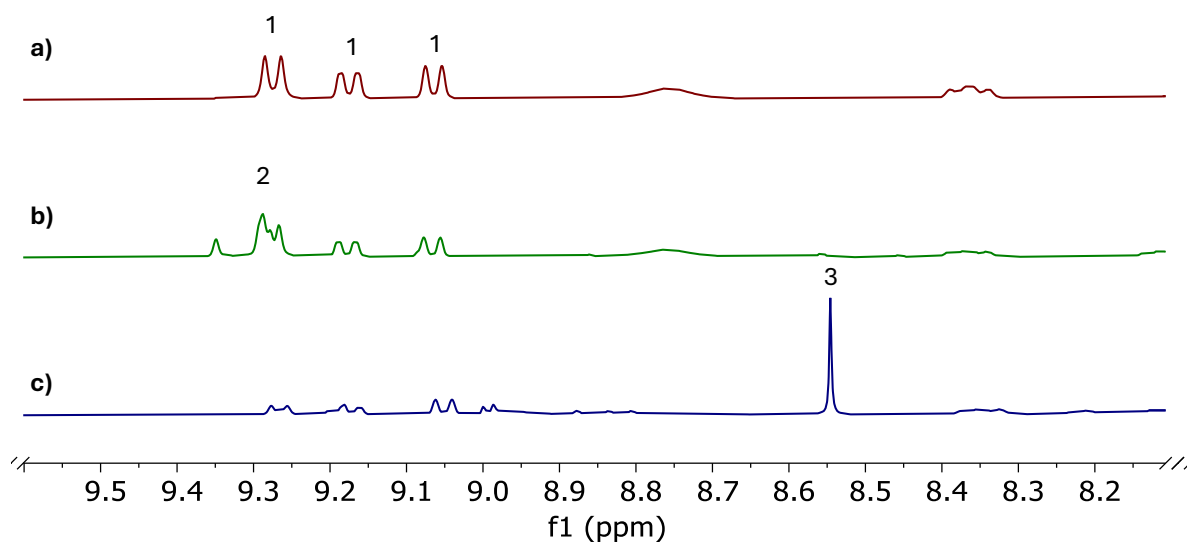
Figure 3.19 - ^1H NMR NMR spectra of [RuCl(**L14**)$_2$]Cl in methanol-d4. [a] Room temperature spectrum. [b] After heating in MeOD at 50 °C for 16 h. [c] [RuCl(**L14**)$_2$]Cl and excess NaOMe in methanol-d4 after heating to 50 °C for 16 h.
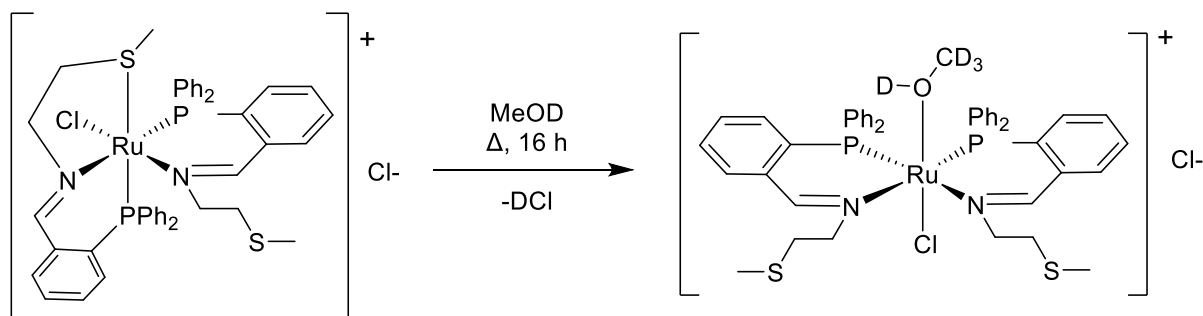
Scheme 3.12 - Proposed production of a symmetrical species upon heating of [RuCl(**L14**)$_2$]Cl in methanol-d4.

Upon addition of a superstoichiometric quantity of NaOMe to a second solution of [RuCl(**L14**)$_2$]Cl at room temperature, a colour change to dark green-brown was observed; however, no changes to the NMR data were observed, with the same pair of doublets observed in the ^{31}P{^{1}H} NMR spectrum. No evidence of formation of an anticipated hydride species as seen by Wingad *et al*. in their 2015 study of PN complexes[49] was observed (see section 3.4.2, Figure 3.12). The observed colour change is typically associated with formation of a Ru(III) species, suggesting partial formation of such a species. As Ru(III) is paramagnetic, analysis of such species by NMR spectroscopy is nontrivial due to signal broadening and large changes to chemical shifts, which were not observed in this work. However, the retention of clear [RuCl(**L14**)$_2$]Cl signals in this work suggests such a transformation was not complete.

After heating to 50 °C under N_2 for 16 h in the presence of base, the solution became dark brown. The starting material species was still visible in the $^{31}P\{^1H\}$ NMR spectrum, and two new singlets at -14.1 ppm and -16.0 ppm (Figure 3.18c, signals 3 and 4) were attributed to free **L14** (CDCl$_3$ δ: -13.6 ppm) and **L18** (CDCl$_3$ δ: -16.0 ppm) respectively. This suggests de-coordination both with and without reduction of ligand. The appearance of a singlet at 8.54 ppm ^1H NMR spectrum supports the generation of free imine ligand (Figure 3.19c, signal 3). No similar signal attributed to the amine proton of reduced ligand **L18** was obvious, presumed due to overlap with NaOMe and residual solvent signals. No second complex was observed, and the mixture remained fully dissolved, indicating the species which liberated ligand was an NMR invisible homogeneous species.

As discussed in section 2.2.3.2, Dilworth and coworkers[66] observed Ru(III) degradation products featuring single ligands in both a dimer and single centre species when synthesis was attempted in methanol. Hence, similar species are proposed to be produced in this system (Scheme 3.13). It would be interesting to pursue isolation of any of these species through crystallography in future work for structural analysis. Furthermore, it is unclear if such a species is catalytically active or this proposed oxidation is a deactivating pathway, as both [RuCl(**L14**)$_2$]Cl and the unknown proposed Ru(III) species are present after 16 h; a catalytically active species is clearly present as the production of **L18** indicates reductive catalysis occurring. If a Ru(III) species could be isolated at scale, and applied in catalysis, further mechanistic insight could be obtained for this species. Additionally, robust post-reaction analysis of an alcohol coupling reaction would be needed to understand whether this study is representative of species which may be formed *in situ*.
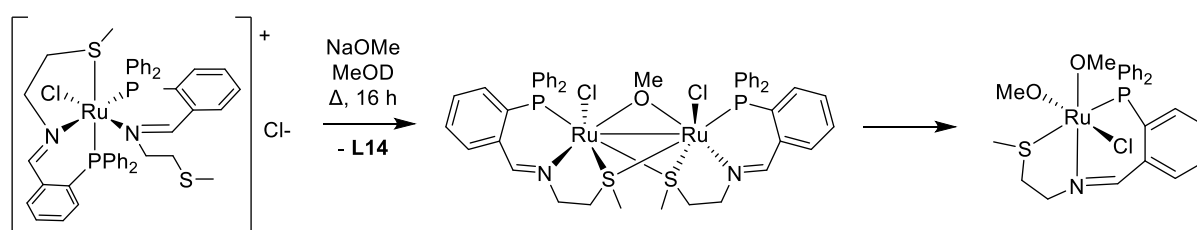
*Scheme 3.13 - Potential transformation of [RuCl(**L14**)$_2$]Cl when treated with MeOD and NaOMe.*

To understand the possible differences in behaviour created by a reduced ligand, especially given apparent release of **L18** by [RuCl(**L14**)$_2$]Cl, complex [RuCl$_2$(**L18**)$_2$] was also targeted for this study. However, its extremely poor solubility at room temperature and after heating at 50 °C for 16 h prevented any meaningful data collection. No visible reaction with base was observed to produce a soluble species either, even after heating. The appearance of a post-reaction mixture after its

use in the Guerbet cross-coupling of ethanol and methanol as a clear yellow solution demonstrates transformation into some kind of soluble active species under reaction conditions, but this could not be accessed under the tested conditions on an NMR scale. Further study of a high catalyst loading under reaction conditions would be necessary to better understand the active species of [RuCl$_2$(**L18**)$_2$], and would be interesting to compare with an analogous study of [RuCl(**L14**)$_2$]Cl.

3.6 Novel Ru(II) PNX (X = O,S) complexes in the Guerbet synthesis of n-butanol

3.6.1 Catalyst Screening Experiments

A selection of the complexes prepared in Chapter 2 (shown in Figure 3.20) were screened for catalytic activity in the Guerbet-type preparation of n-butanol (Scheme 3.14). In this section, the results of these screening experiments are presented.
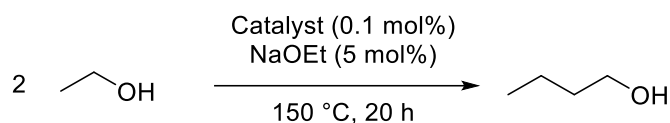
Scheme 3.14 - General conditions for the upgrading of ethanol to n-butanol.
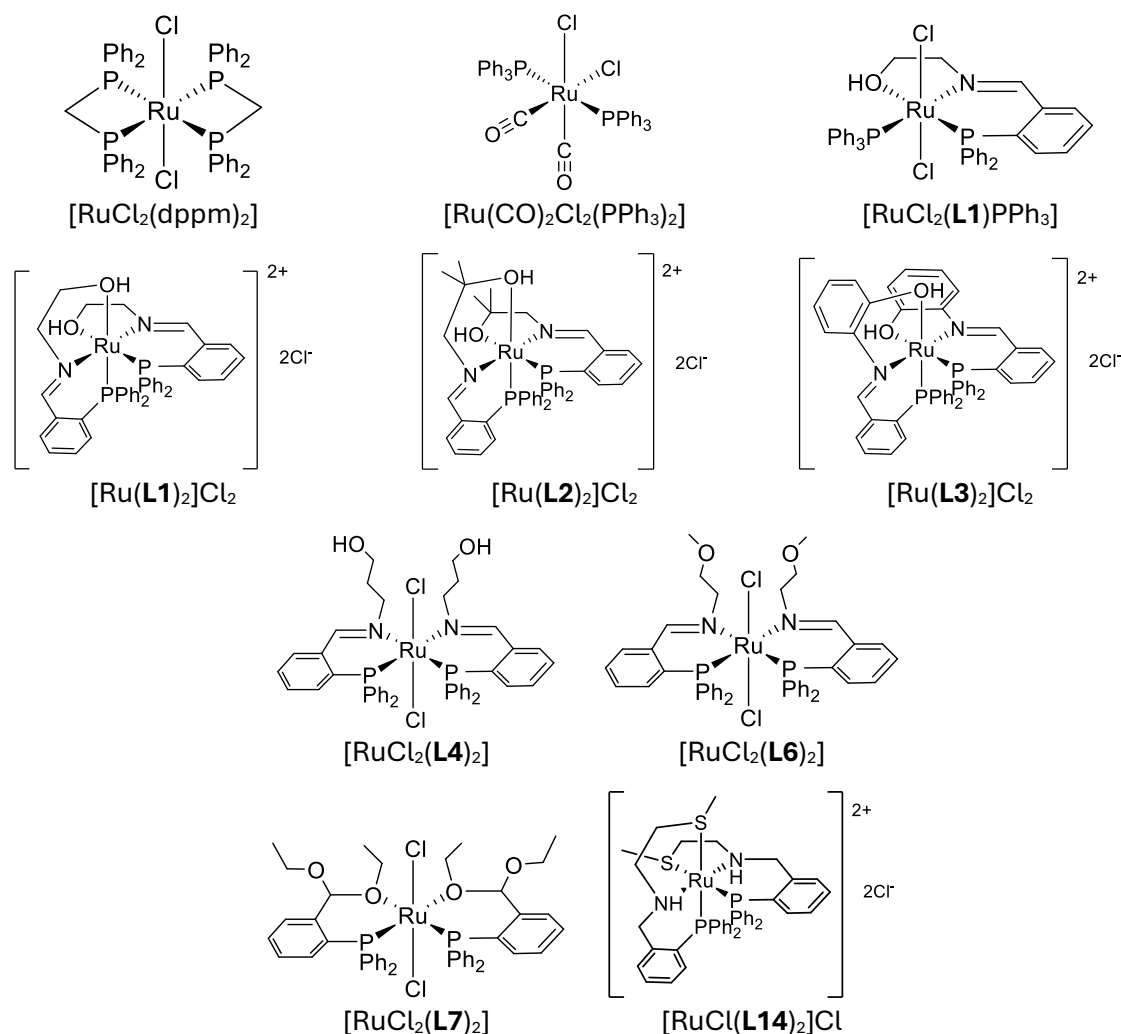
Figure 3.20 - Selection of Ru(II)Cl$_2$(PNX)$_2$ (X = O,S) complexes prepared and selected for screening in the catalytic upgrading of ethanol to n-butanol.
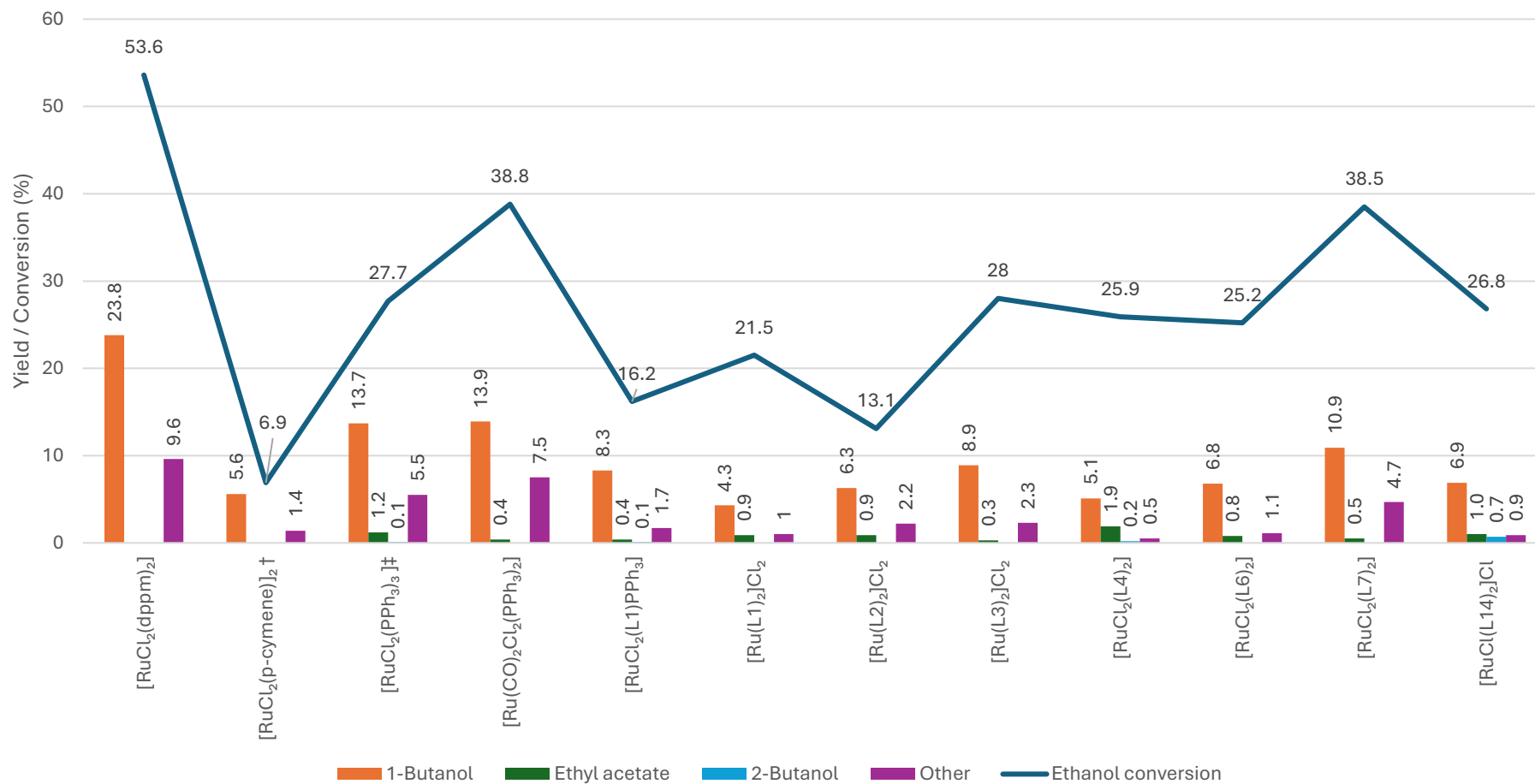
Figure 3.21 – Yield of liquid products and ethanol conversion obtained in ethanol coupling with RuCl$_2$(PNX)$_2$ catalyst series. Conditions: ethanol (10 mL, 171.3 mmol), NaOEt (5.0 mol%, 0.565 g, 8.565 mmol) and catalyst (0.1 mol% [Ru] basis) were reacted under an inert N$_2$ atmosphere in a 100 mL Parr reactor at 150 °C for 20 h. Other products are a mixture of: 2-ethyl-1-butanol, 1-hexanol, 2-ethyl-1-hexanol and 1-octanol (see section 5.3.3, Table 5.2). Total conversion of ethanol determined by GC-FID using hexadecane as internal standard. †Data obtained from literature[48]. ‡Data obtained from literature[52].
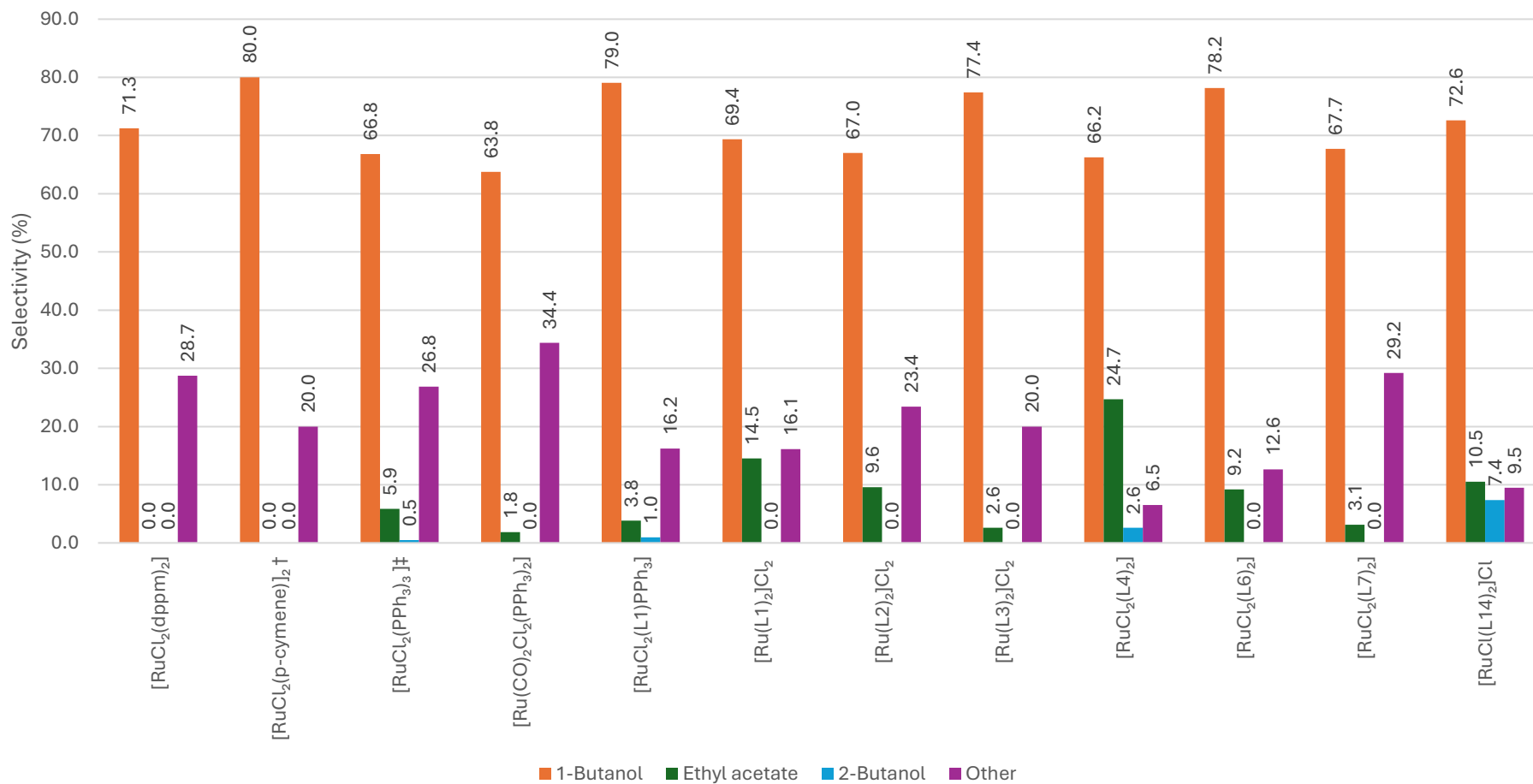
Figure 3.22 - Selectivity of liquid products obtained in ethanol coupling with RuCl$_2$(PNX)$_2$ catalyst series. Conditions: ethanol (10 mL, 171.3 mmol), NaOEt (5.0 mol%, 0.565 g, 8.565 mmol) and catalyst (0.1 mol% [Ru] basis) were reacted under an inert N$_2$ atmosphere in a 100 mL Parr reactor at 150 °C for 20 h. Other products are a mixture of: 2-ethyl-1-butanol, 1-hexanol, 2-ethyl-1-hexanol and 1-octanol (see section 5.3.3, Table 5.2). Total conversion of ethanol determined by GC-FID using hexadecane as internal standard. †Data obtained from literature[48]. ‡Data obtained from literature[52].

As in isobutanol synthesis experiments, included in the screen was [RuCl$_2$(dppm)$_2$], which under the given conditions was found to produce comparable results to those previously reported by the Wass group[48]. Also presented are previously reported results for ruthenium precursors [RuCl$_2$(*p*-cymene)]$_2$ and [RuCl$_2$(PPh$_3$)$_3$]. Unfortunately, due to the large quantity of catalyst required for this scale of reaction (equalling >100 mg per run), the catalyst screen was limited to only those complexes which were readily produced in very good yields; for this reason, only complexes containing oxygen ligands were able to be screened, with the exception of the sulfur-containing [RuCl(**L14**)$_2$]Cl. No investigation of the mixed donor PNN type ligand structure could be performed for this reaction.

The two monodentate phosphorus complexes [Ru(CO)$_2$Cl$_2$(PPh$_3$)$_2$] and [RuCl$_2$(PPh$_3$)$_3$] both produced extremely similar yields of *n*-butanol, as well as other side products, in very similar selectivities. Given the high temperature of the system, it is likely the CO ligand does not remain coordinated and is lost during reaction. Therefore, it is presumed that the active species of these two catalysts is structurally analogous. The lack of stability provided in the absence of multidentate ligands has been suggested in the literature to result in catalyst decomposition[48,49]; further post-reaction analysis would be necessary to confirm homogeneity is retained here, but black solid was produced in these reactions which does suggest reduction to ruthenium black. Additional gas-phase analysis could further be performed to identify any potential release of CO from [Ru(CO)$_2$Cl$_2$(PPh$_3$)$_2$], though it is noted that trace CO gas has been reported as a side product of ethanol coupling side reactions[65]. Interestingly, a disparity between ethanol conversions is observed between [RuCl$_2$(PPh$_3$)$_3$] and [Ru(CO)$_2$Cl$_2$(PPh$_3$)$_2$]; this work found higher ethanol conversion with no significantly increased liquid product yields with [Ru(CO)$_2$Cl$_2$(PPh$_3$)$_2$], which could show an increase in side reactions to produce non-liquid products (see section 3.6.2).

It is immediately clear that, when operating under the same conditions, none of the novel tridentate PNX complexes prepared in this work produce comparable yields of *n*-butanol to that produced by the two monodentate phosphine complexes, let alone the previously reported [RuCl$_2$(dppm)$_2$]. Indeed, yields from imine-containing catalysts were all < 9%, and therefore show no real improvement to the yields obtained from their ruthenium precursor [RuCl$_2$(*p*-cymene)]$_2$. This is consistent with the use of pincer complexes previously reported for this transformation: non-rigid mixed donor PNP and PNNP pincer ligands in particular have shown poor conversion to *n*-butanol when compared to their bidentate PN counterparts[59]. Even in the case of the sulfur-containing complex [RuCl(**L14**)$_2$]Cl, which was considered promising for this transformation due to its success in isobutanol synthesis (section 3.4.2) and recent work within the Wass group of

SNS-type pincer complexes giving *n*-butanol yields of up to 26 %[52] (section 0), it seems that the combination of a sulfur-containing arm with a PN moiety did not benefit reactivity.

It is, however, noted that the two complexes producing highest isobutanol yields [RuCl$_2$(**L4**)$_2$] and [RuCl(**L14**)$_2$]Cl (section 3.4.1, section 3.4.2), both showed some selectivity towards *sec*-butanol production, albeit at very low yields. Trace production was also seen with [RuCl$_2$(**L1**)$_2$] and precursor complex [RuCl$_2$(PPh$_3$)$_3$]. This is again similar to reports of other PN-containing pincer ligands, though Wingad *et al.* found tridentate PNP-type pincers were additionally found to produce ethyl acetate as the major product[59]. Further imine-based sulfur containing ligands could be interesting to investigate further to target this type of selectivity towards *sec*-butanol, especially given only moderate selectivity towards side product ethyl acetate observed.

Continuing examination of the imine-containing systems in this work, comparison between the mono- and bis-ligated species [RuCl$_2$(**L1**)PPh$_3$] and [Ru(**L1**)$_2$]Cl$_2$ shows a substantially lower yield in the bis-ligated species. However, the increased alcohol conversion of [Ru(**L1**)$_2$]Cl$_2$ relative to liquid product yield suggests activity remains moderate, with only selectivity towards liquid products substantially reduced. Additionally, moderate selectivity towards side product ethyl acetate was observed in almost all bis-ligated imine containing complexes, with only [Ru(**L3**)$_2$]Cl$_2$ not sharing this behaviour; this is consistent with increased reactivity towards non-liquid products (see section 3.6.2). This also does not appear to be an observation limited to bis-ligated tridentate species: poor activity is still seen in this work in bis-ligated systems even when P-N ligands have been demonstrated to bind in a bidentate fashion (e.g. [RuCl$_2$(**L6**)$_2$], see section 2.2.3.2). Hence, attribution to reduced access to the ruthenium centre is not reasonable. This trend is contrary to the trend observed when bidentate phosphine and phosphinoamine systems have been used previously: typically the bis-ligated species have shown greater yields of *n*-butanol due to longer-lived catalyst[67].

The most active catalyst by far in this series was [RuCl$_2$(**L7**)$_2$], which is the only multidentate system explored containing no nitrogen moiety. It produced *n*-butanol yields almost as good as those seen in monodentate phosphine systems [RuCl$_2$(PPh$_3$)$_3$] and [Ru(CO)$_2$Cl$_2$(PPh$_3$)$_2$], with similar selectivity towards higher alcohols seen. The only potential benefit considered of the acetal moiety (and subsequent bidentate ligand behaviour) is increased stability as a homogeneous catalyst: in reaction with [RuCl$_2$(**L7**)$_2$], initial observation of the crude product mixture showed the solid produced was not black in colour and the liquid phase was dark red-brown and clear. This suggests catalyst homogeneity may be better retained by the bidentate system, though further analysis of the post-reaction system would need to be performed to draw

any significant conclusions. Therefore, no benefit of the acetal moiety can be definitively noted under these conditions without further investigation.

Given the extremely poor results of the imine-containing systems in this work, particularly relative to the precursor complexes, it is tentatively proposed that the PN moiety is limiting activity towards *n*-butanol production, though it is unclear why. Unfortunately, because of the high catalyst loading needed and the poor results obtained, no further investigation could be conducted on this series of complexes for this reaction.

3.6.2   Side products

3.6.2.1   Liquid Side Products

In this series of experiments, a range of side products were observed in the liquid phase, which are fully reported in section 5.3.3 (Table 5.2). Unlike in the isobutanol production reaction, where excess methanol is limiting due to formaldehyde's extremely electrophilic behaviour, in the *n*-butanol production conditions higher alcohols are readily accessible by further reaction of ethanol with Guerbet products. An example of this further reactivity is shown in Figure 3.23.
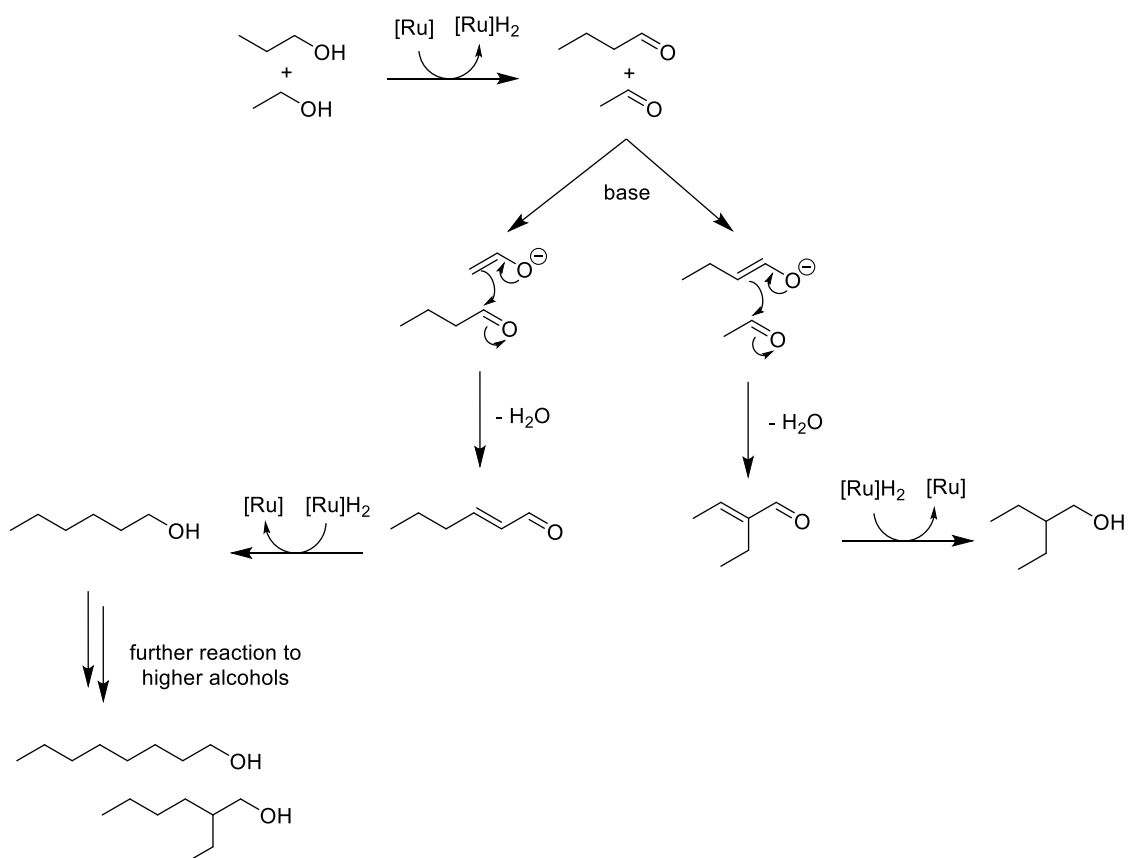
Figure 3.23 - Cross-coupling of ethanol with 1-butanol to produce linear and branched higher alcohol Guerbet products.

124

Low to moderate yields of linear and branched higher alcohols were produced in all cases, with a general trend seen of more higher alcohol production with increased n-butanol production. The following alcohols were typically present: 2-ethylbutan-1-ol, 1-hexanol, 2-ethylhexan-1-ol and 1-octanol. 1-hexanol made up the largest fraction of higher alcohol products in all cases. The selectivity of a system either towards or away from these higher alcohols is desirable due to the energy required in separation, and unfortunately such selectivity was not observed here.

A major side product seen in the liquid phase is ethyl acetate. This is accepted to be produced in the competitive Tishchenko coupling of two aldehydes to form an ester[60], and was not observed in isobutanol production due to the vast excess of methanol highly disfavouring the process. The unexpected production of 2-butanol has been previously observed, and proposed by the Wass group to proceed via a potential series of hydration and hydrogenation rearrangements of n-butanol (Figure 3.24). This selectivity to the best of our knowledge has only been reported by the Wass group.

Figure 3.24 - Potential mechanisms for production of liquid and solid byproducts of the ethanol coupling reaction to produce n-buatanol, as reported by Wingad et al. (2023)[59]. Figure reproduced from literature with permission.

3.6.2.2 Other Side Products

As with isobutanol production, large quantities of solid are produced in these systems. The solid products from a routine catalytic run using the catalyst [RuCl(**L14**)$_2$]Cl were isolated and analysed qualitatively by FTIR spectroscopy, ^{1}H and ^{13}C{^{1}H} NMR spectroscopy. As is consistent with previous Wass group reports, the solid produced was found to be acetate salt, presumed to be sodium acetate. This is formed by one of two routes, both of which are noted in Figure 3.24 and facilitated by the NaOH formed *in situ*: saponification of ethyl acetate to sodium acetate; or the Cannizzaro mechanism previously discussed whereby sodium acetate is formed directly from acetaldehyde coupling (see section 3.4.4.2). As in isobutanol production, gaseous byproduct led to a residual pressure at room temperature of approximately 4-8 bar in these reactions, which is consistent with the release of H$_2$ gas in the production of sodium acetate.

3.7 Conclusions and future work

A selection of novel Ru(II) complexes prepared in this work were applied to the Guerbet alcohol coupling for preparation of isomers of butanol from ethanol. In the ethanol/methanol cross-coupling to produce isobutanol, promising yields of isobutanol were obtained from multiple systems, with yields given by [RuCl$_2$(**L4**)$_2$] and [RuCl(**L14**)$_2$]Cl comparable to the best reported results from state of the art catalyst [RuCl$_2$(dppm)$_2$], though when tested the pincer complex [RuCl(**L14**)$_2$]Cl was found to take longer to reach high yields. It is noted that best two systems each featured at least one bidentate ligand, which may indicate the importance of access to the ruthenium centre for an inner-sphere mechanism. Calculations of the buried volume of these species may be possible to investigate further. The PNS complex [RuCl(**L14**)$_2$]Cl also showed good compatibility with NaOH, so is a good candidate to investigate further for its tolerance to water concentrations representative of industrially produced bioethanol. The excellent solubility of these catalysts may also be interesting for testing reaction efficiency at lower temperatures.

A smaller selection of catalysts were also applied to the homocoupling of ethanol to produce *n*-butanol. Unfortunately, none of the novel pincer complexes investigated were found to provide significant improvement relative to their ruthenium precursors. Further work was limited by practical considerations, and considering the poor yields obtained, no attempt to investigate lower catalyst loadings was made. However, expansion of investigation into acetal type complexes could be interesting: if a straightforward synthetic method for this family of complexes is established they may be tuneable to produce higher yields.

3.8 References

1   H. Ritchie and P. Rosado, *Our World in Data*.

2   S. Pirani, *Burning Up: A Global History of Fossil Fuel Consumption*, Pluto Press, London, UK, 2019.

3   W. J. Ripple, C. Wolf, T. M. Newsome, P. Barnard and W. R. Moomaw, *Bioscience*, 2020, **70**, 8–12.

4   The Core Writing Team, H. Lee and J. Romero, *Summary for Policymakers. In: Climate Change 2023: Synthesis Report. Contribution of Working Groups I, II and III to the Sixth Assessment Report of the Intergovernmental Panel on Climate Change*, Geneva, Switzerland, 2023.

5   V. Smil, *Energy Transitions: Global and National Perspectives*, Praeger, Santa Barbara, California, 2nd edition., 2017.

6   When Fossil Fuels Run Out, What Then? - MAHB, https://mahb.stanford.edu/library-item/fossil-fuels-run/, (accessed 26 January 2025).

7   *Energy Institute Statistical Review of World Energy*, 2024.

8   U. Energy Information Administration, *Monthly Energy Review - December 2024*, 2024.

9   IEA, *Global EV Outlook 2024*, Paris, France, 2024.

10   Global EV Data Explorer – Data Tools - IEA, https://www.iea.org/data-and-statistics/data-tools/global-ev-data-explorer, (accessed 26 January 2025).

11   *Sustainable biofuels: prospects and challenges*, London, UK, 2008.

12   Inernational Energy Agency, *Renewables 2024*, 2024.

13   J. Markard, F. W. Geels and R. Raven, *Environmental Research Letters*, 2020, **15**, 081001.

14   United Nations Department of Economic and Social Affairs, THE 17 GOALS | Sustainable Development, https://sdgs.un.org/goals, (accessed 29 January 2025).

15   RSB - Roundtable on Sustainable Biomaterials Association, *RSB Principles & Criteria (RSB-STD-01-001)*, Geneva, Switzerland, 2023.

16   P. Cavelius, S. Engelhart-Straub, N. Mehlmer, J. Lercher, D. Awad and T. Brück, *PLoS Biol*, 2023, **21**, e3002063.

17   T. J. Tse, D. J. Wiens and M. J. T. Reaney, *Fermentation 2021, Vol. 7, Page 268*, 2021, **7**, 268.

18   Alternative Fuels Data Center: Renewable Fuel Standard, https://afdc.energy.gov/laws/RFS, (accessed 26 January 2025).

19   M. Briguet Bastos, Brazil's Ethanol Program – An Insider's View, https://web.archive.org/web/20110710193215/http://www.energytribune.com/articles.cfm?aid=534, (accessed 26 January 2025).

20   E10 petrol explained - GOV.UK, https://www.gov.uk/guidance/e10-petrol-explained, (accessed 26 January 2025).

21   Annual Ethanol Production | Renewable Fuels Association, https://ethanolrfa.org/markets-and-statistics/annual-ethanol-production, (accessed 26 January 2025).

22   Fuel Waivers | US EPA, https://www.epa.gov/enforcement/fuel-waivers, (accessed 26 January 2025).

23   X. Navarro, A bit of history: Fiat 147, the first mass-produced ethanol car - AutoblogGreen, https://web.archive.org/web/20081219225354/http://www.autobloggreen.com/2008/12/17/a-bit-of-history-fiat-147-the-first-mass-produced-ethanol-car/, (accessed 27 January 2025).

24   M. Curcio, Carro flex chega aos 15 anos com 30,5 milhões de unidades, https://web.archive.org/web/20200925154218/http://www.automotivebusiness.com.br/inovacao/56/carro-flex-chega-aos-15-anos-com-305-milhoes-de-unidades, (accessed 26 January 2025).

25   A. C. T. Malaquias, N. A. D. Netto, F. A. R. Filho, R. B. R. da Costa, M. Langeani and J. G. C. Baêta, *Journal of the Brazilian Society of Mechanical Sciences and Engineering*, 2019, **41**, 1–23.

26   J. Yanowitz, E. Christensen and R. L. Mccormick, *Utilization of Renewable Oxygenates as Gasoline Blending Components (NREL/TP-5400-50791)*, 2011.

27   B. G. Harvey and H. A. Meylemans, *Journal of Chemical Technology & Biotechnology*, 2011, **86**, 2–9.

28   Y. C. Liu, F. E. Alam, Y. Xu, F. L. Dryer, C. T. Avedisian and T. I. Farouk, *Combust Flame*, 2016, **169**, 216–228.

29   M. Gautam and D. W. Martin, *Proceedings of the Institution of Mechanical Engineers, Part A: Journal of Power and Energy*, 2000, **214**, 497–511.

30   M. Fenkl, M. Pechout and M. Vojtisek, *EPJ Web Conf*, 2016, **114**, 02021.

31   H.-D. Hahn, G. Dämbkes, N. Rupprich, H. Bahl and G. D. Frey, *Ullmann's Encyclopedia of Industrial Chemistry*, DOI:10.1002/14356007.A04_463.PUB3.

32   J. Zhao, C. Lu, C.-C. Chen and S.-T. Yang, in *Bioprocessing Technologies in Biorefinery for Sustainable Production of Fuels, Chemicals, and Polymers*, John Wiley & Sons, Ltd, 2013, pp. 235–262.

33   P. Dürre, *Ann N Y Acad Sci*, 2008, **1125**, 353–362.

34   V. García, J. Päkkilä, H. Ojamo, E. Muurinen and R. L. Keiski, *Renewable and Sustainable Energy Reviews*, 2011, **15**, 964–980.

35   D. S. Nabila, R. Chan, R. R. P. Syamsuri, P. Nurlilasari, W. A. A. Q. I. Wan-Mohtar, A. B. Ozturk, N. Rossiana and F. Doni, *Curr Res Microb Sci*, 2024, **7**, 100250.

36   M. Guerbet, *C R Hebd Seances Acad Sci*, 1899, **128**, 1002–1004.

37   M. Guerbet, *C R Hebd Seances Acad Sci*, 1909, **149**, 129–132.

38   K. Noweck and W. Grafahrend, *Ullmann's Encyclopedia of Industrial Chemistry*, 2006.

39   D. Gabriëls, W. Yesid Hernández, B. Sels, P. Van Der Voort and A. Verberckmoes, *Catal Sci Technol*, 2015, **5**, 3876.

40   S. Veibel and J. I. Nielsen, *Tetrahedron*, 1967, **23**, 1723–1733.

41   A. Corma, J. Navas and M. J. Sabater, *Chem Rev*, 2018, **118**, 1410–1459.

42   A. J. O'Lenick, *J Surfactants Deterg*, 2001, **4**, 311–315.

43   C. Yang and Z. Y. Meng, *J Catal*, 1993, **142**, 37–44.

44   A. S. Ndou, N. Plint and N. J. Coville, *Appl Catal A Gen*, 2003, **251**, 337–345.

45   T. Tsuchida, S. Sakuma, T. Takeguchi and W. Ueda, *Ind Eng Chem Res*, 2006, **45**, 8634–8642.

46   G. Gregorio, G. F. Pregaglia and R. Ugo, *J Organomet Chem*, 1972, **37**, 385–387.

47   K. Koda, T. Matsu-ura, Y. Obora and Y. Ishii, *Chem Lett*, 2009, **38**, 838–839.

48 G. R. M. Dowson, M. F. Haddow, J. Lee, R. L. Wingad and D. F. Wass, *Angewandte Chemie International Edition*, 2013, **52**, 9005–9008.

49 R. L. Wingad, P. J. Gates, S. T. G. Street and D. F. Wass, *ACS Catal*, 2015, **5**, 5822–5826.

50 Y. Xie, Y. Ben-David, L. J. W. Shimon and D. Milstein, *J Am Chem Soc*, 2016, **138**, 9077–9080.

51 N. Biswas, R. Sharma, B. Sardar and D. Srimani, *Synlett*, 2023, **34**, 622–628.

52 J. Whitelegge, PhD Thesis, Cardiff University, 2024.

53 G. Iaquaniello, G. Centi, A. Salladini and E. Palo, in *Methanol: Science and Engineering*, Elsevier, 2018, pp. 95–111.

54 B. Dziejarski, R. Krzyżyńska and K. Andersson, *Fuel*, 2023, **342**, 127776.

55 R. L. Wingad, E. J. E. Bergström, M. Everett, K. J. Pellow and D. F. Wass, *Chemical Communications*, 2016, **52**, 5202–5204.

56 K. J. Pellow, R. L. Wingad and D. F. Wass, *Catal Sci Technol*, 2017, **7**, 5128–5134.

57 R. J. Newland, M. F. Wyatt, R. L. Wingad and S. M. Mansell, *Dalton Transactions*, 2017, **46**, 6172–6176.

58 F. J. Sama, R. A. Doyle, B. M. Kariuki, N. E. Pridmore, H. A. Sparkes, R. L. Wingad and D. F. Wass, *Dalton Transactions*, 2024, **53**, 8005–8010.

59 R. L. Wingad, L. Birch, J. Farndon, J. Lee, K. J. Pellow and D. F. Wass, *ChemCatChem*, 2023, **15**, e202201410.

60 T. Seki, T. Nakajo and M. Onaka, *Chem Lett*, 2006, **35**, 824–829.

61 J. Cook, J. E. Hamlin, A. Nutton and P. M. Maitlis, *Journal of the Chemical Society, Dalton Transactions*, 1981, 2342–2352.

62 M. Nielsen, E. Alberico, W. Baumann, H. J. Drexler, H. Junge, S. Gladiali and M. Beller, *Nature 2013 495:7439*, 2013, **495**, 85–89.

63 E. Alberico, A. J. J. Lennox, L. K. Vogt, H. Jiao, W. Baumann, H. J. Drexler, M. Nielsen, A. Spannenberg, M. P. Checinski, H. Junge and M. Beller, *J Am Chem Soc*, 2016, **138**, 14890–14904.

64 R. L. Wingad and D. F. Wass, [*Unpublished Results*].

65 K. Pellow, PhD Thesis, University of Bristol, 2018.

66   S. R. Bayly, A. R. Cowley, J. R. Dilworth and C. V. Ward, *Dalton Transactions*, 2008, 2190–2198.

67   H. Aitchison, R. L. Wingad and D. F. Wass, *ACS Catal*, 2016, **6**, 7125–7132.

4 Application of Ru(II) Complexes to the Direct Hydrogenation of Amides and Esters

This chapter discusses the potential of catalysis to provide alternative methods to tackle waste management and new material production through hydrogenative cleavage of polymers. The application of novel species presented in Chapter 2 to model systems is described and compared to previously reported systems.

4.1 Background

4.1.1 Plastics as a fossil fuel product

The term plastic refers to a material produced primarily from synthetic polymer. All significant plastic usage has occurred in the past century[1], with the early major boom in production occurring during the Second World War and much more widespread commercial use in the economic growth following thereafter[2–4]. Global annual plastic production had already reached two million tonnes by 1950, and according to the PlasticsEurope Market Research group, production has increased every year since then, excluding only the years of the two major oil crises (1975, 1980) and the global recession in 2008[2,5]. Global annual production volume exceeded 400 million tonnes for the first time in 2022[5].

The impact of the oil crises is relevant as the majority of current polymer production uses fossil fuel feedstocks. These are sometimes referred to as petroleum-based polymers, despite natural gas products also accounting for a major fraction of plastic production feedstocks[6]. Additionally, plastics are not just made of their polymeric component: additives, mostly plasticisers and flame retardants, are estimated to account for around 7 % by mass of plastic materials. These additives are specialty chemicals, frequently also from petrochemical sources[7].

The development of bioplastics – plastics produced from biomass sources – has gained momentum in recent years. The target products are often chemically identical to materials produced from fossil fuel sources: notably, the PlantBottle, released by Coca cola in 2009, was 100 % PET (polyethylene terephthalate), 30 % of which was sourced from plant sources[8]. More recently, advances in new polymer technology, such as PLA (polylactic acid) and starch blend polymers, have expanded the use of plastics made from 100 % biomass sources, particularly in

the packaging industry, and PLA has the advantage of being industrially compostable[9]. However, bioplastics only accounted for approximately 0.6 % of annual plastics production in 2022[10].

4.1.2 The fate of plastics

PLA, and its biodegradability, is a notable exception to the norm. None of the major fossil fuel-derived plastic products are biodegradable, defined by Geyer as having biodegradation timescales which far exceed the relevant timescales for their waste management[2]. This is a separate concern to non-renewable feedstocks, as currently around 50 % of biobased polymer also accounts for non-biodegradable products[10]. Even PLA, classified as a biodegradable polymer, is sometimes non-biodegradable by Geyer's definition, requiring elevated temperatures and microbial treatment to break down within relevant timescales. The British Plastics Federation excludes timescales from its definition of polymer biodegradability entirely to avoid such confusion, simply defining a biodegradable polymer as one which may be entirely converted to water, carbon dioxide, biomass and possibly methane through at least partially cell-mediated processes. If 90 % of a material is converted thus within 6 months in the environment, it is considered compostable[11].

However, for the vast majority of plastics currently in circulation, if released into the environment, they will fragment, accumulate and persist[12]. Indeed, the ubiquity of plastics since 1950 combined with their long lifetime has resulted in the recent proposed use of plastic as a stratigraphic indicator of the Anthropocene[13].

The lifetime of plastic products varies widely, from around a year in the packaging sector, to over 30 years in the construction sector[2]. However, it is estimated that waste generation is continuing to increase, with over 340 million tonnes of plastic waste generated in 2018, and an estimated total cumulative waste volume of 6.9 billion tonnes of plastic[3]. Due to plastic lifetime, landfill is an inappropriate waste management strategy; almost all of this plastic still exists.

4.2 Recycling

If plastic waste is instead considered as a resource, there are two primary means of use: energy recovery, and recycling. Energy recovery typically refers to incineration. Plastic-to-fuel technologies do exist however, such as pyrolysis or gasification, which are most suitably applied to polymers containing low oxygen content[14,15]. Energy recovery currently accounts for >40 % of plastics waste management in Europe[16].

Recycling overtook landfill as the next most common fate of plastics in Europe in 2016. It refers to the reprocessing of plastics into new products, ultimately delaying the end of life of the material. Recycling may be split into the following two types:

- Mechanical recycling: The physical reprocessing of a plastic into a new product, without significant changes to chemical structure.
- Chemical recycling: The chemical cleavage of bonds in a polymer to produce oligomers or monomers which are reintroduced into the production chain.

Recycling processes are inherently limiting. Mechanical methods rely on manual sorting methods, so require well-labelled starting products. No separation of constituent parts occurs, so any additives remain part of the product mixture. This is particularly problematic when considering older materials, as legislation on permitted additives has changed: many flame retardants are now banned, for example, preventing any recycling of these materials which would retain such additives[17]. Additionally, the products of mechanical recycling typically represent a reduction in economic value. If a polymer is thermoset (non-melting), it is only able to be physically shredded, limiting potential uses. If a polymer is thermoplastic, so able to be melted down and re-extruded, resultant changes in polymer packing lead to changes in physical properties. Hence, to retain desirable properties, products often use a mixture of recycled material and virgin polymer[18].
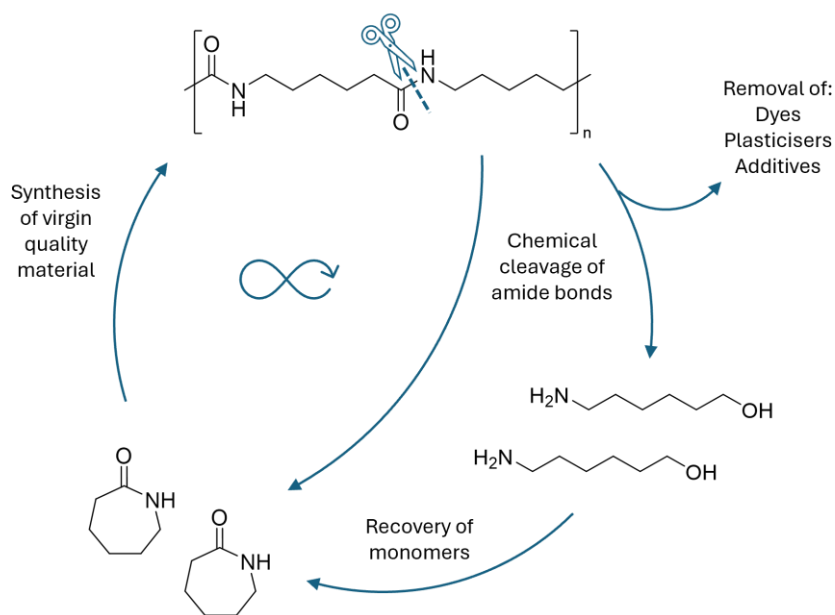
Figure 4.1 - Chemical recycling in a closed-loop system, demonstrated with Nylon-6.

Chemical recycling is much more promising for high value products. In closed-loop chemical recycling, the breaking of bonds leads to oligomeric or monomeric products, allowing the re-synthesis of long-chain polymers using the isolated monomers. This enables regeneration of plastic product of equivalent quality to virgin material. Usually this would include some chemical transformation of the oligomers/monomers produced to ensure they are appropriately functionalised for reinsertion into existing manufacture processes (demonstrated in Figure 4.1). In theory, this would allow removal of additives, such as colourants, plasticisers, and flame retardants, which make the physical recycling of many materials so difficult[19]. Despite a much higher energy cost than mechanical methods, this is the only method of recycling which would enable material to remain in circulation indefinitely and is frequently considered a key component of a circular plastics economy[16].

Unfortunately, plastics are designed to be robust, long-lasting, and chemically inert. Therefore the polymers which make up the bulk of the material are extremely difficult to break down into their constituent monomers. Hence, chemical recycling has not yet developed into widely economically viable processes for many polymers, as it remains cheaper to make new polymer from traditional feedstocks.

4.3 Chemical Recycling Methods

4.3.1 Condensation Polymers

Condensation polymers are attractive targets for chemical recycling. Whilst many polymers have a long carbon backbone, condensation polymers are so named due to their formation through condensation reactions, resulting in retained heteroatoms incorporated into their backbone. Common types of mass-produced condensation polymer are summarised in Figure 4.2, but the category also includes naturally occurring polymers such as proteins and polynucleotides.

Polylactic acid (PLA)   Polyurethane

Polyethylene terephthalate (PET)   Nylon-6
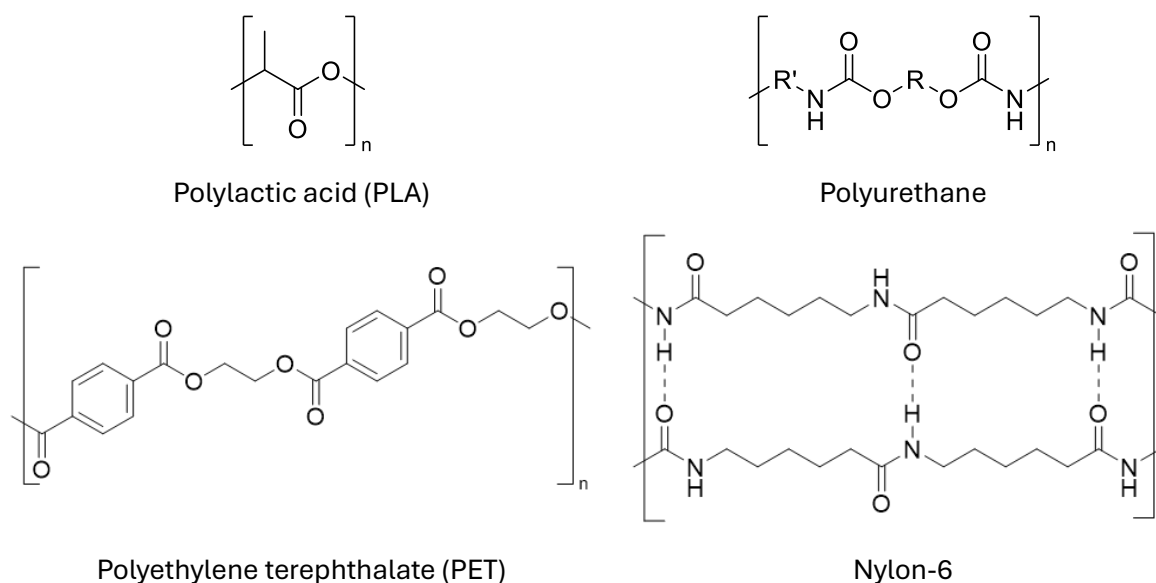
Figure 4.2 - Common commercially produced condensation polymers.

The backbone functionality of these polymers can be readily exploited for chemical cleavage. This is particularly appealing as polyesters are the majority polymer type used in both the packaging and textiles sectors, which are the two sectors producing the largest quantities of plastics waste annually[2]. Of these, the textile sector especially contributes very little to recycling. Fibrous polymer material is a common mechanical recycling product of PET[20], but is unsuitable for physical re-extrusion and typically is discarded as highly mixed waste which is notoriously difficult to recycle further by traditional means[21].

4.3.2 Existing Chemical Recycling Methods

Commercial chemical recycling is still in its infancy, and represents an estimated 2 % of current recycling methods in Europe, with most infrastructure currently accommodating either depolymerisation or pyrolysis techniques[16]. This proportion is estimated at <0.5 % globally[19]. As mentioned previously, thermochemical methods such as pyrolysis and gasification are best

suited to low oxygen content polymers. Techniques applied to condensation polymers are typically depolymerisation methods, and are briefly summarised below[22,23]. Although these technologies exist for all condensation polymers at some stage of research, the only polymer to which these techniques are applied at any significant scale is PET[18,19,23].
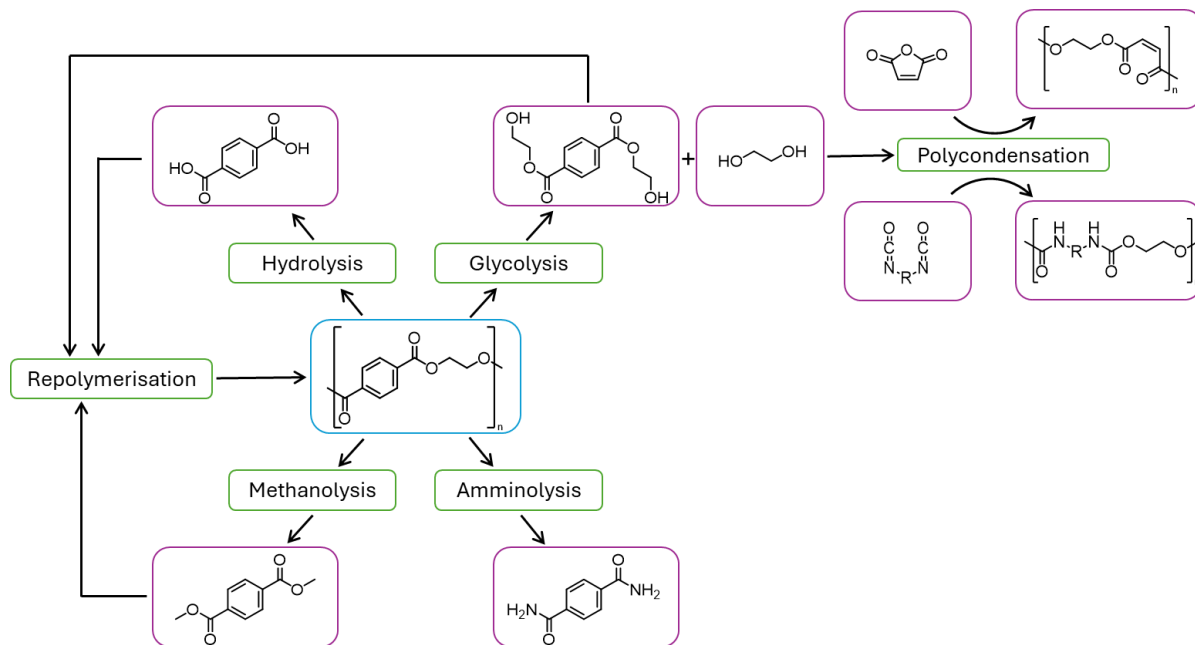
Figure 4.3 - Main PET chemical recycling products. Figure reproduced from Aguado & Serrano, 1999[24].

Solvolysis is the most common type of chemical recycling for PET. This is a blanket term which applies to the use of solvents to cleave chemical bonds in the backbone. This includes hydrolysis, alcoholysis and glycolysis. The primary products of different PET solvolysis products are summarised in Figure 4.3. All these processes employ catalysts (both heterogeneous and homogeneous) and operate at varying conditions, though historically high temperatures, pressures and large excesses of solvent have been applied[25].

Additional methods of chemical recycling are under investigation[19] for the processing of PET, such as selective dissolution, frequently using ionic liquids[25] (though there is dispute whether this is considered a chemical or a mechanical process), and enzymatic methods[26]. The latter is of particular interest; technically, the widespread industrial composting of PLA employs such biological methods on an industrial scale for catalysing hydrolytic depolymerisation, but in practice monomer recovery is not performed.

A final method of note is hydrogenolysis. This refers to the application of a source of hydrogen to break the sp^3 C-X bond in a condensation polymer to result in the amine or alcohol products, using hydrogen sources such as silanes, aminoboranes or H_2 gas[27]. The latter is especially

promising due to the limited required further processing of monomers and the accessibility of H_2 as a low carbon source, widely produced by either steam methane reforming with carbon capture or water splitting[28].

4.3.3   Hydrogenative Polymer Cleavage by Homogeneous Catalysts

As with other processes, this has been widely explored with some excellent reviews published in recent years providing detailed summaries of both heterogeneous and homogeneous methods[27,29]. Of particular interest in this work is the use of homogeneous pincer complexes, with interesting examples presented. The efficacy of such systems in direct hydrogenation has been briefly discussed in section 1.3.4, and unsurprisingly, the pioneers in this transformation on a molecular scale have also pioneered much of the exploration in polymer degradation. Most research in this area targets polyesters and polycarbonates.
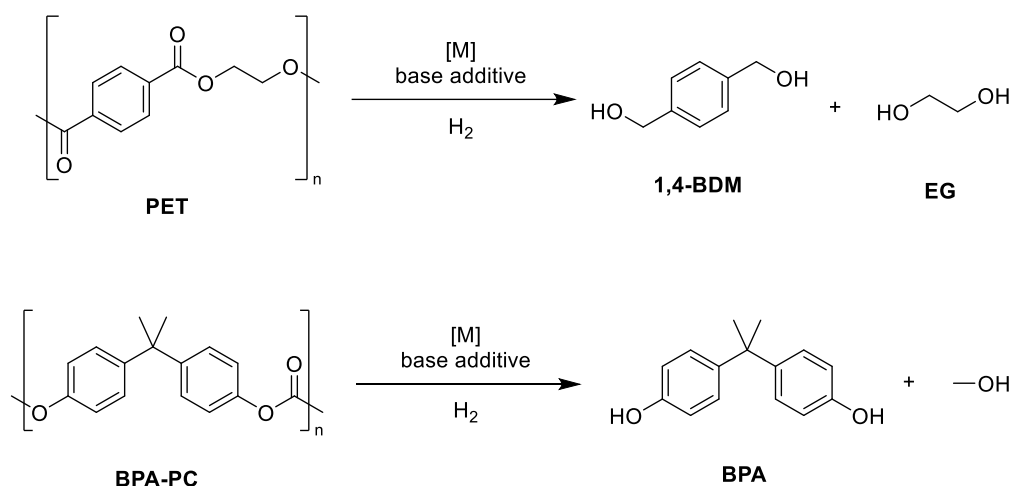
Scheme 4.1 - Direct hydrogenative cleavage of polymers using metal catalysts under basic conditions.
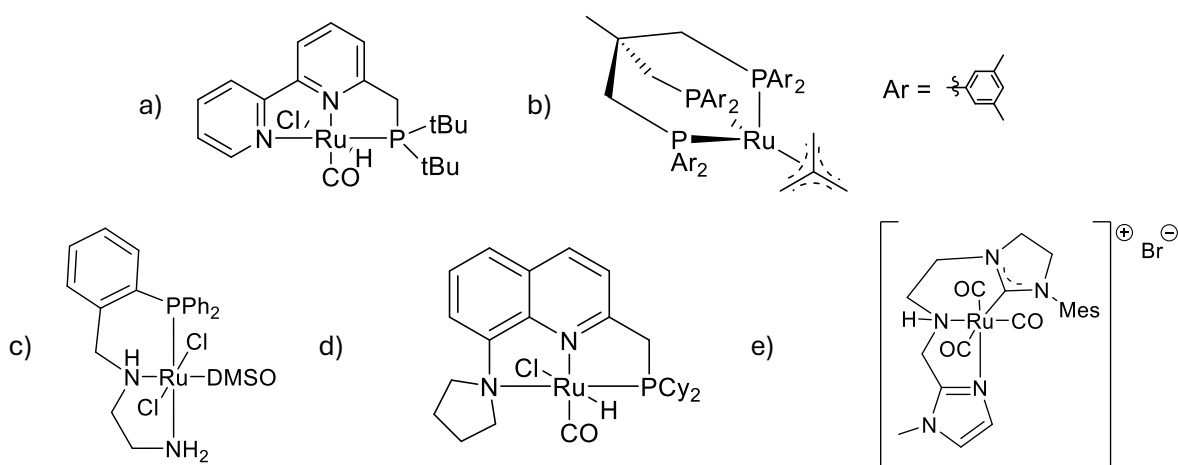
Figure 4.4 – Homogeneous pincer catalysts reported for hydrogenative depolymerisation of PET.

Table 4.1 - Summary of homogeneous pincer catalysts applied to the hydrogenative depolymerisation of PET.

Author	Catalyst (mol%)	Base (mol%)	H$_2$ / bar	Solvent	Time / h	T / °C	1,4-BDM yield[a] / %
Robertson[30]	4.4a (2)	tBuOK (4)	54.4	THF:anisole 50:50	4	160	>99
Klankermayer[31]	4.4b (1)	HNTf$_2$ (1)	100	1,4-dioxane	16	140	64
Clarke[32]	4.4c (2)	tBuOK (40)	50	THF:anisole 50:50	48	110	73 (53)
Xie[33]	4.4d (0.5)	tBuOK (3)	5	MeOH:toluene 90:10	24	80	61
Xie[33]	4.4d (0.5)	tBuOK (3)	5	MeOH:toluene 90:10	72	80	88 (86)
Liu[34]	4.4e (3)	tBuOK (30)	50	2-MeTHF	72	150	89

[a] Isolated yields given in brackets where specified.

The first reported example of homogeneous catalysis using pincer complexes for selective reduction of esters to alcohols was demonstrated by Milstein and coworkers in 2005 using a new family of Ru(II) PNN catalyst[35]. Their bipyridyl catalyst (Figure 4.4a) was later used by Robertson and coworkers to be active in polymer hydrogenative cleavage. Following pre-activation with base, the catalyst resulted in remarkable conversion of >99 % PET with only alcohol products observed after 48 h under 54.4 bar H$_2$ at 160 °C[30]. Expansion of scope demonstrated efficient conversions of several other polyesters and some polycarbonates. The following year, Clarke and coworkers also reported a series of Ru(II) PNO and PNN complexes which showed remarkable tolerance to multiple functional groups in hydrogenative cleavage of esters[36]. Their best PNN system (Figure 4.4c) later demonstrated efficient conversions of PET at the lower temperature of 110 °C, with NMR yields of 73 % NMR yield of 1,4-benzenedimethanol (53 % isolated yield)[32].

In 2018, Klankermayer and coworkers reported a Ru(II) triphos complex featuring a coordinatively unsaturated trimethylenemethane ligand (Figure 4.4b) as performing complete conversion of poly(bisphenol-A carbonate) to produce BPA and MeOH under alkoxide base free conditions with 100 bar H$_2$ in 16 h[31]. Under the same conditions, 42 % conversion of PET was achieved, with an increase to 64 % conversion at >99 % selectivity towards 1,4-BDM with substitution of phenyl groups on the triphos ligand with xylene groups. This complex was then successfully applied to

complete depolymerisation of a number of commercial samples of polymer, showing up to 87 % recovery of isolated monomer 1,4-benzenedimethanol from a PET bottle sample and 73 % bisphenol-A recovery from a CD.

A recent report from Xie and coworkers proposed an interesting solution to the initial insolubility of polymers through use of a tandem system, following initial transesterification with methanol to give oligomers with a direct hydrogenative reduction to produce isolated diol monomers[33]. This was particularly interesting due to the poor activation of H_2 of Milstein's systems when applied in protic solvents due to favourable coordination of methanol (Scheme 4.2)[37]. They proposed that a more stable delocalised species would be more stable to protic solvents, thus applicable to both transformations, and demonstrated a Ru(II) PNN pincer system featuring a quinoline backbone (Figure 4.4d). This complex was successfully applied under extremely mild conditions of 5 bar H_2 in a 9:1 MeOH:toluene solvent mixture to give 61 % recovery of monomer after only 24 h, increasing to 88 % after 72 h.
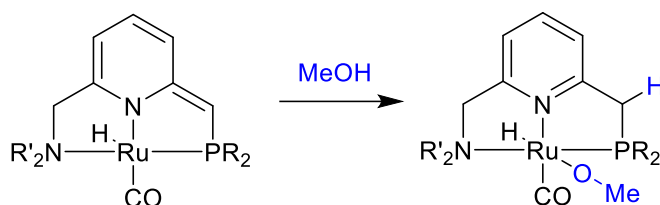
Scheme 4.2 - Quench of active Ru(PNN) Milstein complex by coordination of protic solvent.

Whilst the use of ruthenium phosphine complexes is almost ubiquitous in this literature, a report in 2023 from Liu and coworkers showed successful use of a manganese NHC complex (Figure 4.4e) in the hydrogenative depolymerisation of PET, though it is noted somewhat higher concentrations of catalyst (3 mol%) and base (30 mol%) were required for a comparable conversion of 89 % to be achieved[34].
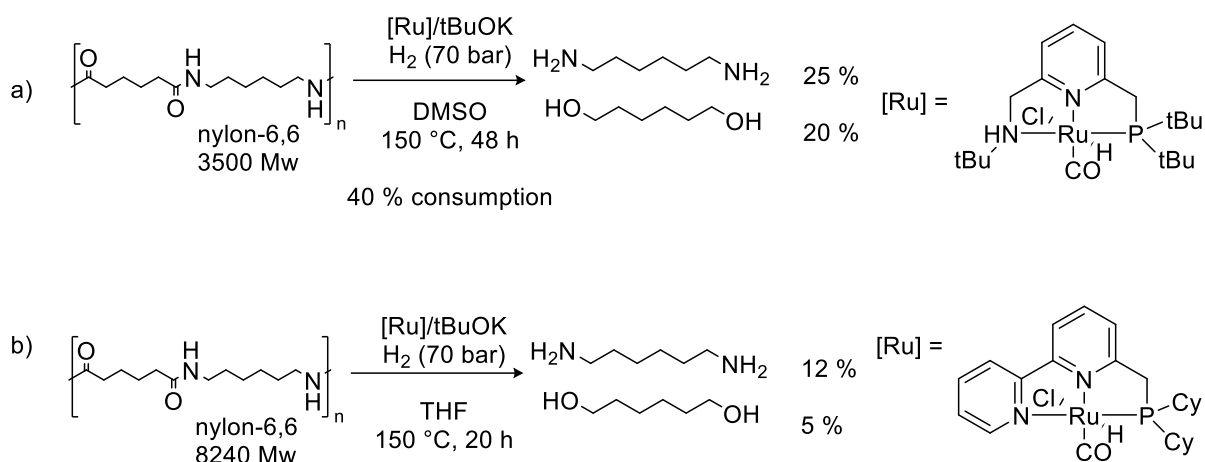
Scheme 4.3 - Catalytic hydrogenative depolymerisation of polyamides. a) Milstein and coworkers (2020). b) Schaub and coworkers (2021).

Despite broader investigation of polyesters, only two reported examples of polyamide depolymerisation through direct hydrogenation have been found, reported by Milstein *et al*[38] in 2020 and Schaub *et al*[39] the following year, and both using Milstein's category of highly effective Ru(II) PNN complexes. Both used high pressure hydrogen with homogeneous ruthenium pincer complexes and metal alkoxide co-catalysts to enable polymer degradation at relatively low temperatures (Scheme 4.3). Schaub's work was also notably extended to include investigation of polyurethanes, including commercial foam samples, and saw complete conversions of some commercial samples using 100 bar H_2 in as little as 30 h, though elevated temperatures of 200 °C were also employed.

It is clear the application of Ru(II) PN-containing pincer catalysts in the successful hydrogenolysis of several polymers, with PNN complexes produced by Milstein and coworkers the best in class. However, ligand systems such as Milstein's and Klankermayer's are frequently difficult to make and highly air sensitive, making them industrially impractical. Additional reliance on high pressures and long reaction times leaves the potential for improvements through further catalyst development.

4.4 Aims

The aim of the work performed in this chapter was to expand upon previously reported Ru(II) catalysts in the direct hydrogenative cleavage of esters and amides, with the intention of applying to polymeric systems.

Initial work aimed to prepare and apply a series of complexes to the previously reported hydrogenative cleavage of amides, based upon work reported by Milstein and coworkers using asymmetric PNN species[40], with an initial conditions screen and catalyst screen performed. Due to the difficulty replicating previously reported results, a second system was developed for further investigation for catalyst screening, featuring aromatic esters as a model substrate for PET.

The catalyst series introduced in Chapter 2 are very similar to Clarke's Ru(II) catalysts previously reported to be effective for direct hydrogenative cleavage of esters featuring a range of different functional groups[32]. The series of imine-based complexes in this work have already been demonstrated as highly effective catalysts in hydrogen transfer mechanisms in alcohol coupling (Chapter 3). Hence, they were also considered promising for application in direct hydrogenation, so were investigated for efficacy in direct hydrogenation of esters. Additionally, the use of the imine moiety was interesting due to reports suggesting aromaticity surrounding Ru-N binding sites is involved in the catalytic cycle of such systems. Further work included expansion of this catalyst series to include SNS and NNN phosphine-free complexes, with comparison to analogous PNP complexes. NMR scale experiments investigating reactivity with hydrogen of two systems were performed.

4.5 Direct Hydrogenation of Amides

Initial work in this chapter targets amide cleavage by direct hydrogenation through the use of a model system. This section discusses the selection and development of a model system, including the preparation of previously reported Ru(II) PNN complexes. Benchmarking, catalyst screen and subsequent run time experiments are discussed.

4.5.1 Preparation of Ru(II) PNN complexes
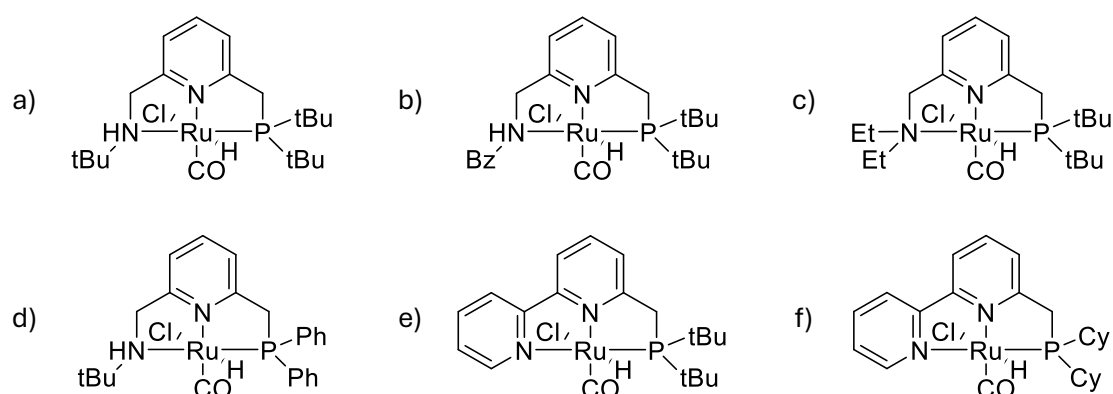
Figure 4.5 - Complexes reported as active for hydrogenative cleavage of polyamides by Milstein[38] and Schaub[39].

Initial targets for benchmark studies were selected from the six complexes reported as successful for the hydrogenative cleavage of polyamides (Figure 4.5). The asymmetric PNN complex [RuCO(Cl)H(**L19**)] (Figure 4.5b) was reported by Milstein and coworkers as the most effective catalyst for direct hydrogenative amide cleavage in a model system whereby single amides were reduced at up to 97 % isolated yield at room temperature under only 10 bar of hydrogen[41]. This catalyst was then also successfully to hydrogenative depolymerisation at almost identical activity to their best reported system[38]. Given their reports included a wide range of amide substrates under low base loadings, and their reported 77 % conversion of nylon-6 under the conditions shown in Scheme 4.3, this complex was initially selected for preparation and use as a benchmark in system development.

The ligand **L19** and complex [RuCO(Cl)H(**L19**)] were successfully prepared according to literature procedures, but difficulties in ligand purification led to very poor yields for both ligand and complex preparation (Scheme 4.4). Yields were insufficient to perform multiple repeats of a test system, and certainly insufficient to achieve loadings required for potential polymer cleavage experiments. Therefore this complex was not pursued further for model system studies.
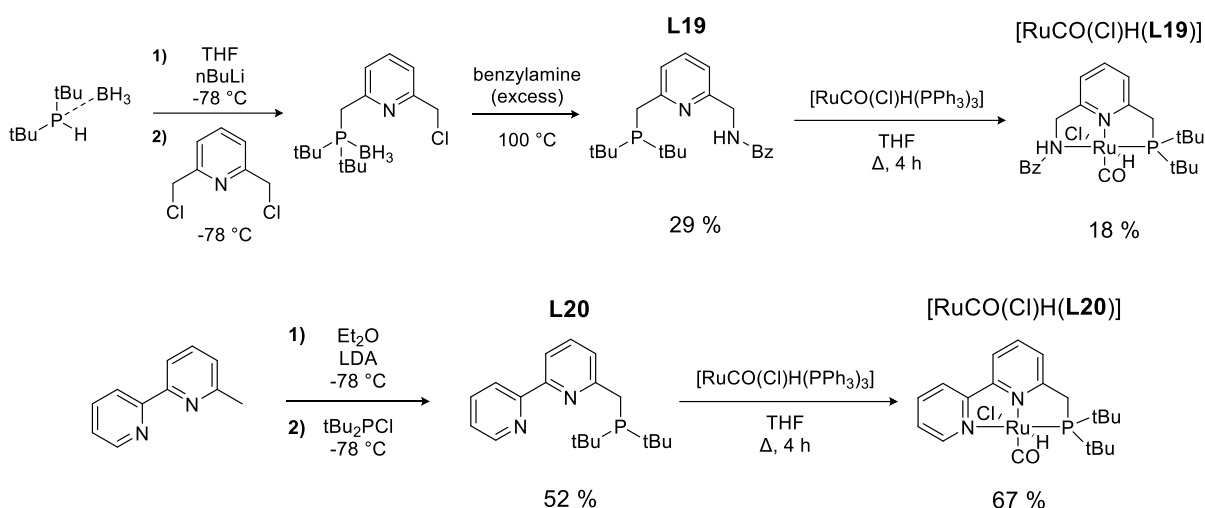
*Scheme 4.4 - Top: synthesis and yields of previously reported **L19** and [RuCO(Cl)H(**L19**)] as performed in this work. Bottom: synthesis and yields of previously reported **L20** and [RuCO(Cl)H(**L20**)] as performed in this work.*

The related complex [RuCO(Cl)H(**L20**)] (Figure 4.5e) was also reported. Milstein and coworkers did investigate this complex for catalytic hydrogenation of nylons, but under the conditions selected they reported only moderate conversion of starting material and no recovered amino alcohol monomer[42]. Better yields were consistently reported with ligands featuring various substituted secondary amines akin to **L19** (Figure 4.5a-d). However, when applied to polyamide and polyurethane degradation, Schaub and coworkers reported excellent yields with a bipyridyl complex featuring cyclohexane phosphine substituents (Scheme 4.3)[39]. The similar ligand **L20** featured *tert*-butyl phosphine substituents and provided very similar hydrogenation results.

Gratifyingly, whilst the literature preparation of **L20** involved ligand isolation by column chromatography under an inert atmosphere, it was found possible in this work to isolate the ligand by removal of liquid starting materials through distillation under continuous vacuum. Further purification was possible by recrystallisation from dry and degassed methanol. This ligand was readily able to be isolated in significantly greater yield and purity than **L19**, and complexation proved facile and high yielding according to literature procedures. Therefore, [RuCO(Cl)H(**L20**)] was selected for further investigation.

4.5.2   Model System Development

Due to the practical difficulties of quantitative polymer analysis, a model system was selected for this work based upon earlier work by the Milstein group using a linear diamide substrate (Scheme 4.5)[43].
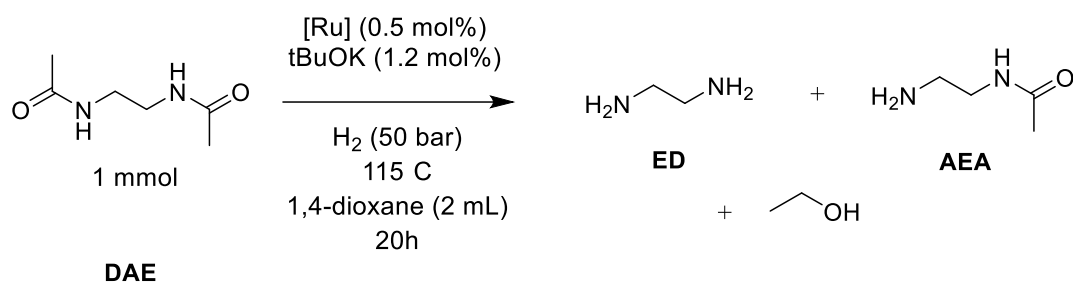
Scheme 4.5 – Selected model system developed in this work based upon reaction conditions reported by Milstein and coworkers[43].

Model substrate diamide N,N'-diacetylethylenediamine (DAE) was selected due to its linear structure, akin to commercial nylons, as well as the ease of analysis of cleavage products by ^{1}H NMR spectroscopy. Analysis of this system was performed in literature by ^{1}H NMR spectroscopy against an internal standard, which was also found to be a suitable analytical method in this work. THF was also tested as solvent and produced similar starting material conversions as those observed in 1,4-dioxane, but solvent signals overlapped with product signals in NMR spectra so precise product distribution could not be determined. Greater solvent quantity was found detrimental to yield, presumably due to limitations in the diffusion rate of H_2.

An initial conditions screen was performed, the results of which are summarised in Table 4.2.

*Table 4.2 – Summary of results of conditions screen of hydrogenative cleavage of N,N'-diacetylethylenediamine with catalyst [RuCO(Cl)H(**L20**)].*

Entry	Cat. Loading / mol%	Base Loading / mol%	H_2 pressure / bar	Conversion / %	AEA yield / %	Ethylene diamine yield / %	Ethanol yield / %
1	1	2.5	70	100	0	80	69
2	1	2.5	50	100	5	95	71
3	0.5	1.25	50	100	21	69	75
4	0.5	5	50	73	49	19	34
5[a]	0.5	1.25	40	87	48	26	37
6	0.5	1.25	40	89	55	30	43
7[b]	0.5	1.25	50	6	trace	-	-
8	0	0	50	2	-	-	-
Reaction conditions: 20 h, 115 °C, [Ru] = [RuCO(Cl)H(**L20**)]. [a]Reaction heating failed partway through the reaction, prompting further investigation into run time. [b]Reaction performed at room temperature							

Conversions obtained were comparable to literature reports[43]. It is unsurprising to observe increased conversions of amide to hydrogenative cleavage products with both catalyst loading and H_2 pressure, trends consistent with literature reports[41,43] for similar systems. Interestingly, increase in base loading relative to ruthenium catalyst did not aid reactivity, instead appearing to inhibit it. No conversion was observed in the absence of ruthenium complex and base.

4.5.3   Reaction time

In one experiment, mid-way through the 20 h run time, heating failed (Table 4.2, entry 5). It is not known precisely how long the reaction was heated, but for at least the final 4 hours of the run the reaction proceeded at room temperature. However, observed conversion of substrate DAE and recovery of all hydrogenative cleavage products was no different to that observed when heating was continued for the full timeframe. This was unexpected, and indicated that the reaction did not require sustained temperature of 115 °C. However, performing hydrogenation at room temperature resulted in negligible reaction (Table 4.2, entry 7), suggesting an initial heating period is required for reaction, but sustained heating is not. An attempt to better understand this was performed by investigating multiple reaction times (Figure 4.6). Given the nature of applied high pressure reactions, the reaction could not be continuously sampled for analysis, so multiple runs of different lengths were performed with direct NMR analysis of the product mixture. The results are summarised in Figure 4.6.
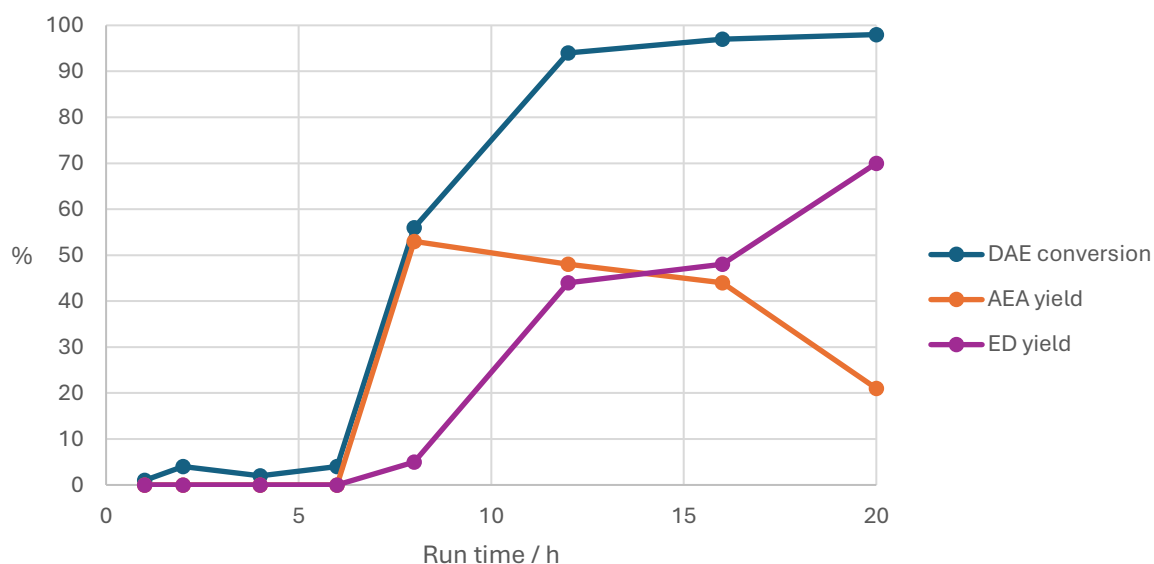
*Figure 4.6 - Change in product mixture composition with run time. Ethanol yields excluded. Reaction conditions: 0.5 mol% RuCO(Cl)H(**L20**), 1.25 % tBuOK, 2 mL 1,4-dioxane, 50 bar H$_2$, 115 °C.*

Very little reaction is observed for the first 6 hours, followed by rapid reaction of the diamine starting material to almost exclusively produce the monoamide intermediate N-actetylethylenediamine (AEA). Subsequent complete reduction occurs more slowly as ethylenediamine yield grows steadily after approximately 8 hours. Longer reactions were not performed, but it is presumed that over longer run times, yields of AEA would continue to decrease as hydrogenation continues, giving ethylenediamine as sole product.

Table 4.3 - Comparison of DAE conversion after 6 hours with and without 1 mmol ethylenediamine additive.

Entry	ED additive / mmol	Run time / h	Conversion / %	AEA yield / %	Ethylene diamine yield / %	Ethanol yield / %
1	0	6	4	0	0	0
2	0	8	56	53	5	18
3	1	6	51	44	100	24
Reaction conditions: 0.5 mol% [RuCO(Cl)H(**L20**)], 1.25 % tBuOK, 2 mL 1,4-dioxane, 50 bar H_2, 115 °C.						

An initial proposed explanation for the initial 6 hour induction period in reaction was an autocatalytic pathway, whereby amine products facilitated the hydrogenation of DAE, increasing reaction rate. To investigate, a 6 hour experiment was performed with 1 mmol ethylenediamine added at the start of the experiment and compared to regular conditions (Table 4.3). Interestingly, 51 % conversion of starting material was observed to produce exclusively the singly reduced compound AEA – the recovery of 1 mmol ethylenediamine in the crude product is assumed to entirely come from the spike, though error in quantitative analysis could disguise low percentage production of ethylenediamine as a reduction product. Notably, this result is extremely comparable to the yields obtained in an un-spiked 8 hour run, showing some benefit to rate of the inclusion of ethylenediamine. However, shorter spiked runs were not performed, so it is unknown whether this increase in rate also shows a similar pattern of large induction period followed by rapid selective reduction of one amide bond and gradual completion of reaction over time. Therefore, substantial further study would be needed to assess if the addition of ethylenediamine accessed an alternative reaction pathway, or aided in another way.
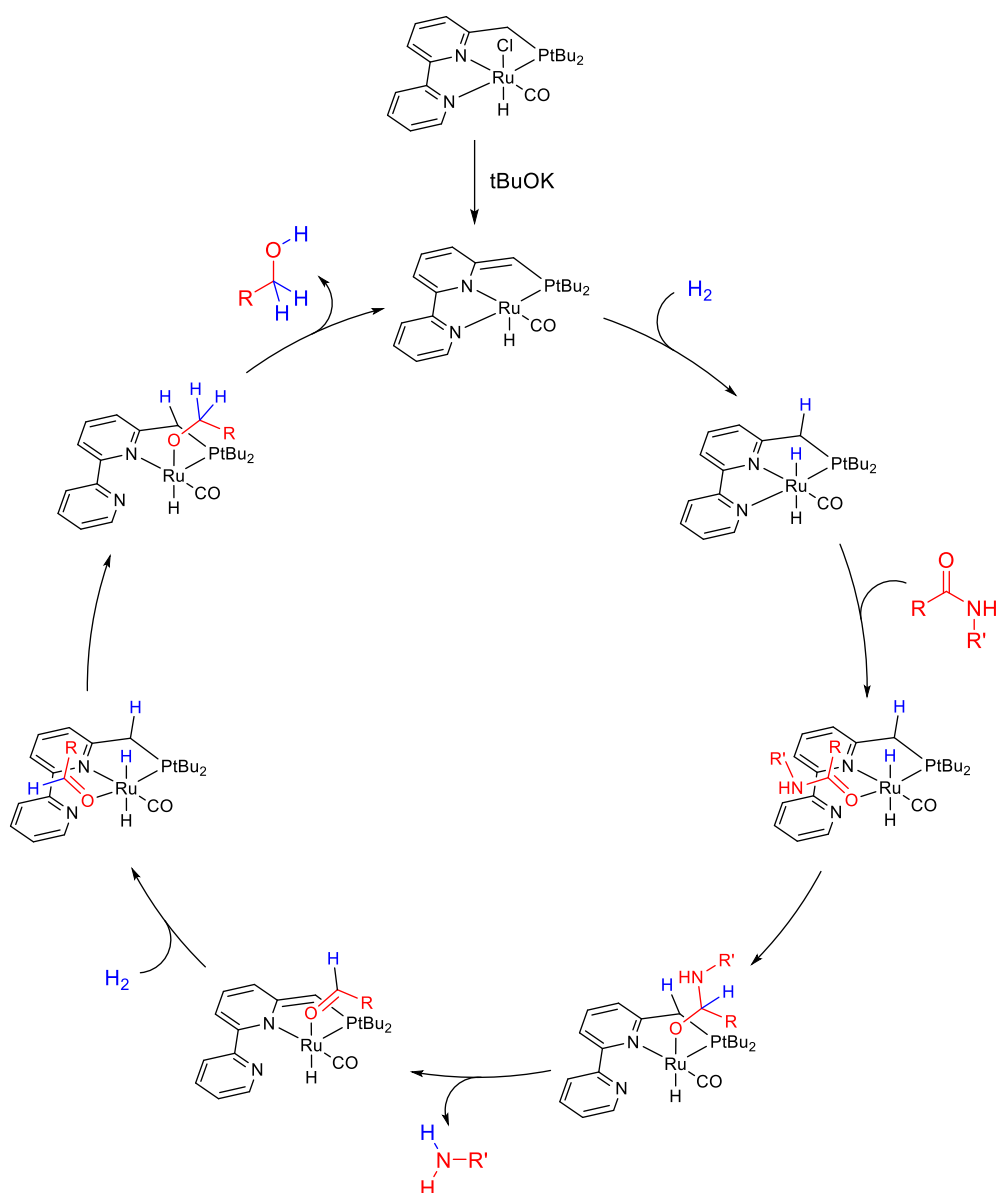
*Scheme 4.6 – Amide hydrogenation mechanism proposed by Milstein and coworkers, demonstrated with catalyst [RuCO(Cl)H(**L19**)], including base-activation and hydrogenation of ruthenium complex.*

An alternative proposed reason for the induction period is slow catalyst activation. In the literature, the Milstein group and others have reported several mechanistic investigations into the catalytic hydrogenative cleavage of amides and esters by asymmetric PNN complexes, exploring complexes containing secondary amine arms such as [RuCO(Cl)H(**L19**)], referred to as PNN[H] type complexes, and bipyridyl-based PNN[bpy] type complexes including [RuCO(Cl)H(**L20**]. These mechanisms involve a facile activation of catalyst already noted in section 1.3, where addition of base results in deprotonation at a carbon adjacent to binding phosphorus. The reaction then follows a catalyst cycle employing de- and re-aromatisation in a metal-ligand cooperative mechanism (Scheme 4.6)[38,40,41,44].

When considering PNN[H] species, deprotonation at the binding nitrogen of species is also possible, but DFT analysis reported by Kumar *et al*. demonstrates interchange with de-aromatised species is extremely low energy, thus may occur spontaneously (Scheme 4.7)[38].
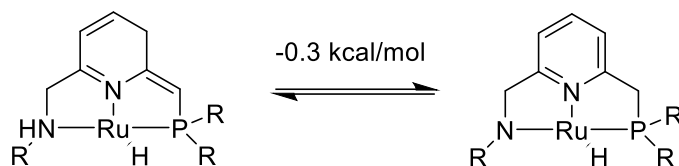
Scheme 4.7 - Interchange between de-aromatised active PNN[H] species and deprotonated PNN species, reported by Kumar et al[38].
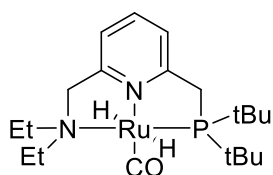
Figure 4.7 - Dihydride PNN[Et2] species isolated by Gusev (2020)[45].

The activated de-aromatised species is active for the heterolytic cleavage of H_2 with transfer of proton to ligand and hydride to the ruthenium centre. This H_2 activation step also appears facile, being observed experimentally at room temperature on an NMR scale with base-activated pyridine-based PNN[H] complexes, with Gusev noting the stability of the isolatable dihydride PNN[Et2] species shown in Figure 4.7 when stored in air overnight. DFT analysis seems to support this as formation of dihydride intermediate complexes from the activated catalyst is reported to be downhill for this family of species[38]. More recent work from both Milstein[41] and Gusev[46] suggests the subsequent coordination of an amide to reduced catalyst by an Ru-O interaction with substitution of the nitrogen binding arm of the ligand, followed by higher energy stepwise hydrogenation and substrate C-N dissociation to release an amine and aldehyde. Finally, a second hydrogenation of the catalyst enables aldehyde reduction. The generally low energy barriers of catalyst reduction and subsequent hydrogen activation suggest that the long incubation period observed in this work is not due to catalyst activation limiting reaction rate.

Therefore, the activation of the substrate appears to be limiting. This step is proposed to involve substitution of the Ru-N pendant arm, shown in Scheme 4.6, which may increase energy required for this step. However, experimental NMR scale investigations into activation of diamides and polyamides performed by Milstein and coworkers[38] showed room-temperature interaction between an aromatic diamide and base-activated PNN[H] complex [RuCO(Cl)H(PNN[tBu])] to form a dimeric complex in THF (Scheme 4.8). No such interaction with powder form nylon-6 at room

temperature was observed. When heated to 125 °C however, multiple species were observed in ^{31}P and ^{1}H NMR spectroscopy, suggesting that larger molecular weight amides coordinate less favourably. The de-coordination of a ligand nitrogen arm does not account for this difference between substrates. A potential alternative reason for this is simply poor substrate solubility, which may also be considered a limit in this work; DAE is poorly soluble in most non-protic solvents, including 1,4-dioxane. As both amine products in this instance are liquid, it is tentatively proposed that their production simply aids in solvation of starting material; this is supported by the results of the ethylenediamine spike.
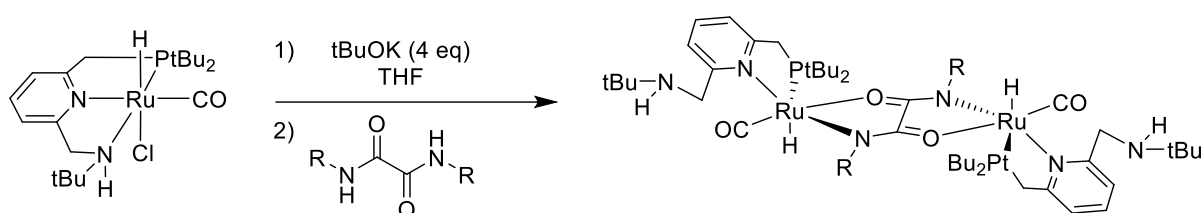
Scheme 4.8 - Interaction of [RuCO(Cl)H(PNN[tBu])] with diamide in THF reported by Milstein and coworkers[38].

R = Ph(p-OMe).

4.5.4   Catalyst Screen

A limited catalyst screen was performed using commercially available catalysts (summarised in Figure 4.8). Unfortunately, none showed significant change in starting material content, with only the PNP pincer complex [RuCO(Cl)H(**L21**)] showing trace amounts of ethanol and singly reduce product AEA produced.
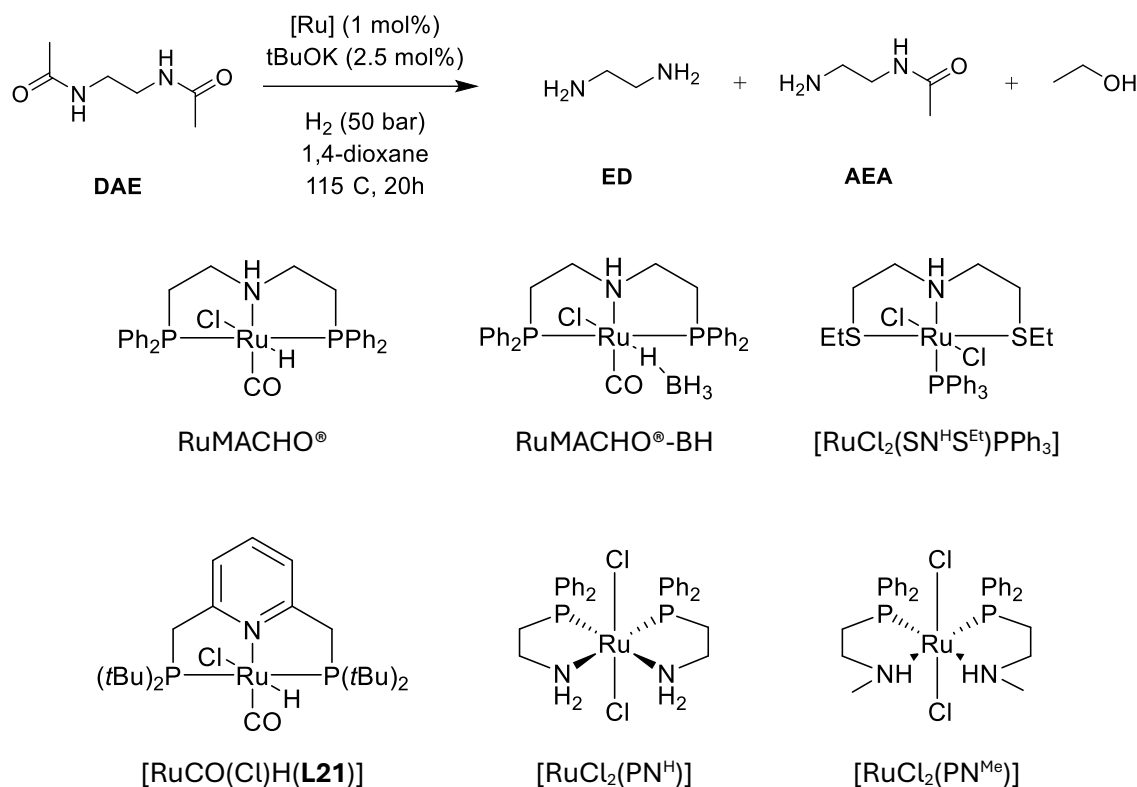
Figure 4.8 - Complexes tested in screen of commercial catalysts reported for ester hydrogenation.

The Milstein asymmetric PNN complex [RuCO(Cl)H(**L20**)] is clearly best in class for this transformation. Given the low success rate of catalysts already well-established to be effective for ester cleavage, investigation into the behaviour of novel complexes as direct hydrogenation catalysts was instead applied to the less strenuous ester hydrogenolysis.

4.6 Direct Hydrogenation of Esters

A model system for the hydrogenative cleavage of esters was developed for the investigation of the series of novel Ru(II) PNX catalysts presented in Chapter 2 as catalysts in direct hydrogenation systems. In this section, the results of these experiments are discussed. Additionally, a comparison between similar PNP, SNS and NNN systems as catalysts is explored.

4.6.1 Model System Development

The interest in the novel series of Ru(II) PNX (X = O, N, S) complexes as direct hydrogenation catalysts stems from the remarkable efficacy of similar PNO and PNN catalysts first reported by Clarke and coworkers in 2012[36], as discussed in Section 4.3.3. Their best system was later applied to the successful hydrogenative breakdown of PET[32].
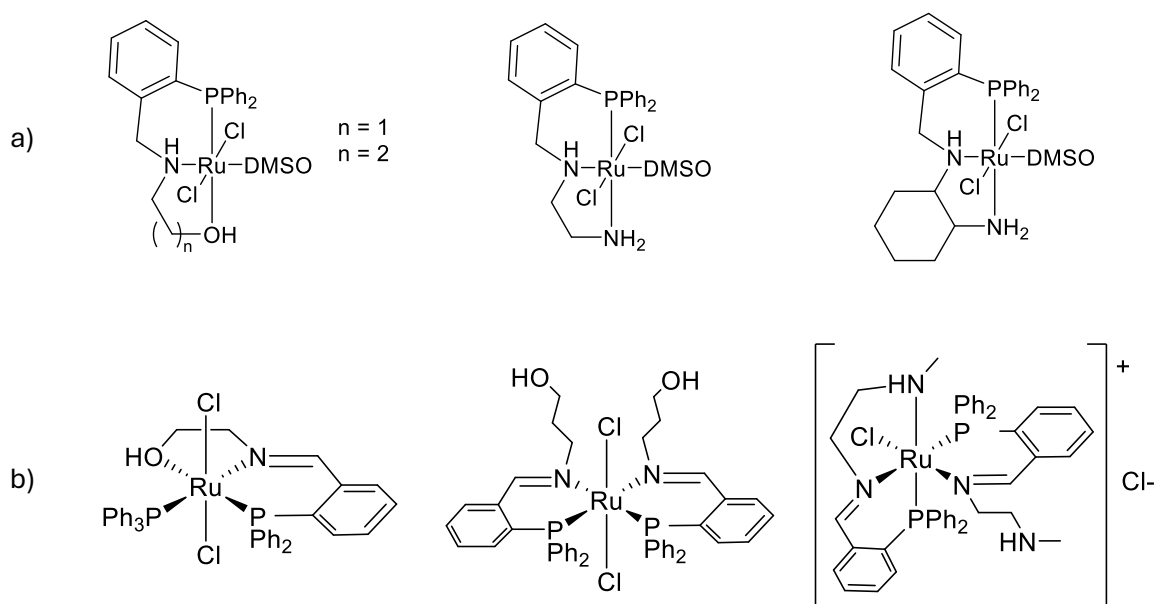
Figure 4.9 – a) Selection of complexes reported by Clarke and coworkers reported for hydrogenative cleavage of esters. b) This work.

Their complexes used the reduced forms of several ligands prepared in this work, employed as single tridentate ligands with ancillary chloride and DMSO ligands and provided early inspiration for the benefit of their modular, tuneable and straightfoward preparation. To appropriately compare the Clarke complexes with this work, a modified version of the model system selected by Clarke was reproduced here.
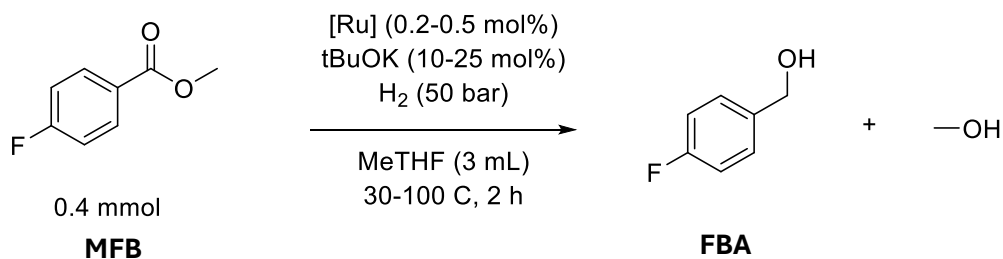
Scheme 4.9 - Model ester hydrogenation system as reported by Clarke et al.[32,36]

The substrate selected, methyl 4-fluorobenzoate (MFB) has the benefit of a fluorine tag, permitting simple monitoring by ^{19}F NMR spectroscopy. Additional quantitative ^{1}H NMR spectroscopy was performed against a mesitylene internal standard to corroborate obtained yields of 4-fluorobenzyl alcohol (FBA). The system was modified to accommodate alternative equipment in this work, and the solvent and temperature conditions were selected as a continuation of amide cleavage investigations.
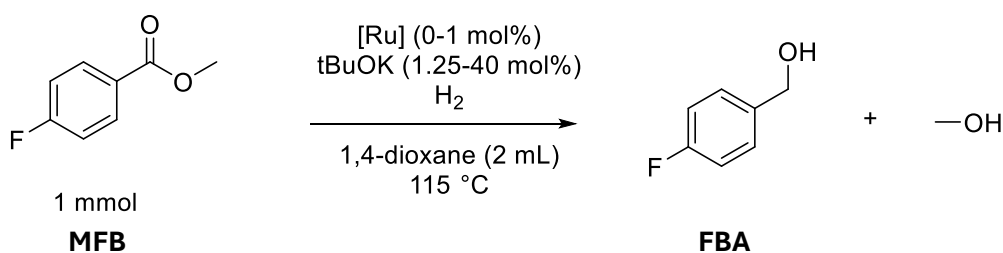
Scheme 4.10 - Model system developed for use in this work.

4.6.2 Conditions Screen

A series of reactions using the Milstein catalyst [RuCO(Cl)H(**L20**)] were performed to investigate the effects of base loading and run time on ester reduction. The results are summarised in Table 4.4.

*Table 4.4 - Conditions screening experiments of ester hydrogenolysis with Milstein catalyst RuCO(Cl)H(**L20**).*

Entry	Catalyst (mol%)	Base (mol%)	Run time / h	H$_2$ pressure / bar	FBA yield[a] / %
1	-	tBuOK (20)	2	50	0
2*	RuCO(Cl)H(**L20**) (1)	tBuOK (2.5)	20	50	23
3	RuCO(Cl)H(**L20**) (1)	tBuOK (2.5)	20	30	14
4	RuCO(Cl)H(**L20**) (1)	tBuOK (2.5)	20	50	32
5	RuCO(Cl)H(**L20**) (1)	tBuOK (2.5)	6	50	1
6	RuCO(Cl)H(**L20**) (1)	tBuOK (40)	2	50	>99
7	RuCO(Cl)H(**L20**) (0.5)	tBuOK (20)	2	50	>99
8	RuCO(Cl)H(**L20**) (0.5)	tBuOK (10)	2	50	>99
9	RuCO(Cl)H(**L20**) (0.5)	tBuOK (5)	2	50	98
10	RuCO(Cl)H(**L20**) (0.5)	tBuOK (2.5)	2	50	8
11	RuCO(Cl)H(**L20**) (0.5)	tBuOK (1.25)	2	50	1

[a]Yield of 4-fluorobenzyl alcohol as determined by ^{19}F NMR spectroscopy and ^{1}H NMR spectroscopy. *65 mL autoclave used.

4-Fluorobenzyl alcohol (FBA) was recovered as the sole fluorinated reduction product in all experiments; no side products were observed. Methanol was observed in typically slightly lower yields in quantitative ^{1}H NMR spectroscopy; this was attributed to its volatility. Standard vessel volume in this work was 100 mL; decreasing vessel size decreased product yield somewhat, though the depressive effect of decreasing H$_2$ pressure was more substantial. Interestingly, even at long run times, the high conversions observed in amide reductions were not seen until base

loadings were increased to base to catalyst ratio of at least 10:1 – this is higher than the standard base to catalyst molar ratio of 2:1 used in amide reductive cleavage (see Section 4.5.2). This is perhaps supportive of the previously proposed autocatalytic nature of amine substrates, whereby they operate by acting as an internal base (see Section 4.5.3). In ester cleavage, increasing base loadings seemed to entirely remove the 6 hour induction period discussed previously, and permitted much more convenient 2 hour run times. This was also noted in the literature for ester reduction[36], but contradicts the negative effect of increasing base loading seen in our earlier study on amide reduction (Table 4.2, Entry 4). The depressive effect of reducing base loading below 10 equivalents was dramatic at short run times.

4.6.3 Catalyst Screen

A selection of complexes prepared in Chapter 2 were screened for catalytic activity in the direct hydrogenative cleavage of methyl 4-fluorobenzoate (Figure 4.10). The results of these screening experiments are discussed in this section.
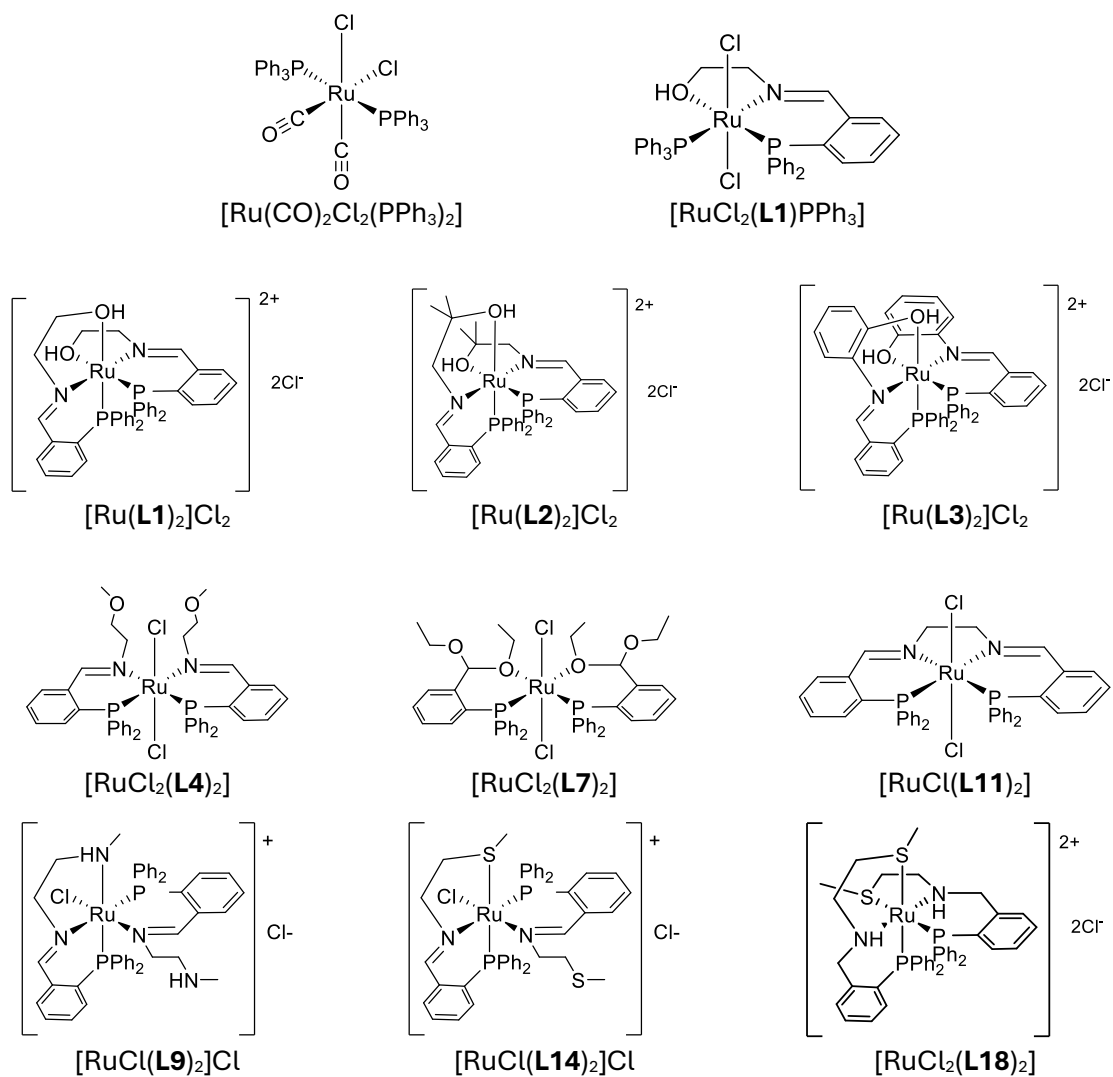
Figure 4.10 - Summary of catalysts tested in the hydrogenative cleavage of methyl 4-fluorobenzoate.
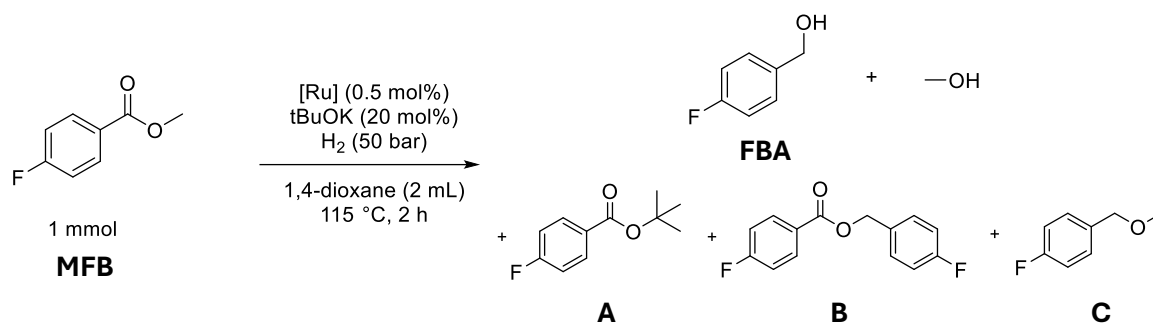
Scheme 4.11 - Conditions selected for catalyst screen of the reductive cleavage of methyl 4 fluorobenzoate. Observed side products A, B and C further discussed in section 4.6.5.

Table 4.5 – Results summary of conditions screening experiments of ester hydrogenolysis.

Entry	Catalyst (mol%)	Base (mol%)	Ester conversion / %	FBA (selectivity, %)	A	B	C
1	Ru(CO)$_2$Cl$_2$(PPh$_3$)$_2$ (0.5)	tBuOK (20)	6	-	6		
2	RuCl$_2$(**L1**)PPh$_3$ (0.5)	tBuOK (20)	25	4 (16)	1	12	7
3	[Ru(**L1**)$_2$]Cl$_2$ (0.5)	tBuOK (20)	29	6 (20)	2	16	6
4	[Ru(**L1**)$_2$]Cl$_2$ (0.5)	tBuOK (10)	19	3 (16)	3	12	
5	[Ru(**L1**)$_2$]Cl$_2$ (0.5)	tBuOK (5)	3	-	3		
6	[Ru(**L2**)$_2$]Cl$_2$ (0.5)	tBuOK (20)	17	3 (16)	7	6	2
7	[Ru(**L3**)$_2$]Cl$_2$ (0.5)	tBuOK (20)	8	-	8		
8	RuCl$_2$(**L6**)$_2$ (0.5)	tBuOK (20)	56	31 (54)		20	5
9	RuCl$_2$(**L6**)$_2$ (0.5)	NaOEt (20)	8	3 (38)		4	
10	RuCl$_2$(**L7**)$_2$ (0.5)	tBuOK (20)	5	-	5		
11	[RuCl(**L9**)$_2$]Cl (0.5)	tBuOK (20)	68	46 (68)		16	5
12	RuCl$_2$(**L11**) (0.5)	tBuOK (20)	100	100 (100)			
13	RuCl$_2$(**L11**) (0.5)	tBuOK (5)	8	8 (100)			
14	[RuCl(**L14**)$_2$]Cl (0.5)	tBuOK (20)	27	11 (41)	5	10	
15	[RuCl(**L14**)$_2$]Cl (0.5)	tBuOK (5)	3	-	3		
16	RuCl$_2$(**L18**)$_2$ (0.5)	tBuOK (20)	44	29 (66)	3	8	3
17	-	tBuOK (40)	6	-	6		

[a]Yields determined by ^{19}F NMR spectroscopy and ^{1}H NMR spectroscopy. **B** produced from 2 equivalents of starting ester. Selectivity reported as proportion of consumed ester.

A consistently observed trend is the lack of selectivity of the family of catalysts tested. All catalysts in this section which showed any activity at all for ester cleavage also resulted in the

production of at multiple unexpected side products, excluding only the PNNP complex [RuCl$_2$(**L11**)]. The nature of these side products is discussed in Section 4.6.5, but was particularly surprising as no side products were reported by Clarke and coworkers for this transformation[32,36], nor observed in the use of [RuCO(Cl)H(**L20**)] as catalyst (Section 4.5.2). Any attempts made to modify base or base loading in this series almost entirely stopped reactivity, demonstrating the critical nature of base in all catalytic systems – though it is noted that side product **A** is a direct product of reaction between base and the ester substrate (see Section 4.6.5).

The presence of a coordinated nitrogen in a ligand appears necessary for activity: use of the monodentate PPh$_3$ complex [Ru(CO)$_2$Cl$_2$(PPh$_3$)$_2$] and the PO complex [RuCl$_2$(**L7**)$_2$] did not catalyse any ester cleavage. This suggests either electronic or mechanistic importance of the Ru-N moiety. Although Milstein's proposed mechanisms (analogous between amide and ester cleavage, as shown in Scheme 4.6) don't typically involve the binding nitrogen of a ligand directly, the potential involvement of a ligand N-H in the mechanisms for ester (and amide) hydrogenation has been discussed in the literature by other authors to facilitate hydrogen transfer to a metal-coordinated substrate in multiple reports[45–48].

For example, a more recent DFT study from Chianese and coworkers proposes an alternative pathway whereby proton transfer to substrates is facilitated by the ligand N-H bond, largely through formation of N-H-X hydrogen bonds between ligand and substrate in an outer sphere mechanism (Scheme 4.12)[47]. Analysis of an osmium PNN complex by Gusev also proposes coordination of ethanol to a dihydride species by the central nitrogen donor, demonstrating that ligand interaction is not limited to pendant donor arms[45]. It is of course noted that not all active species contain a secondary amine, including [RuCO(Cl)H(**L20**)]. Hence, it is plausible multiple mechanisms may be at play, depending on the ligand structure. Regardless of mechanism, the presence of a Ru-N bond is consistent in literature species active for hydrogenative cleavage, so the apparent necessity in this work is perhaps unsurprising.
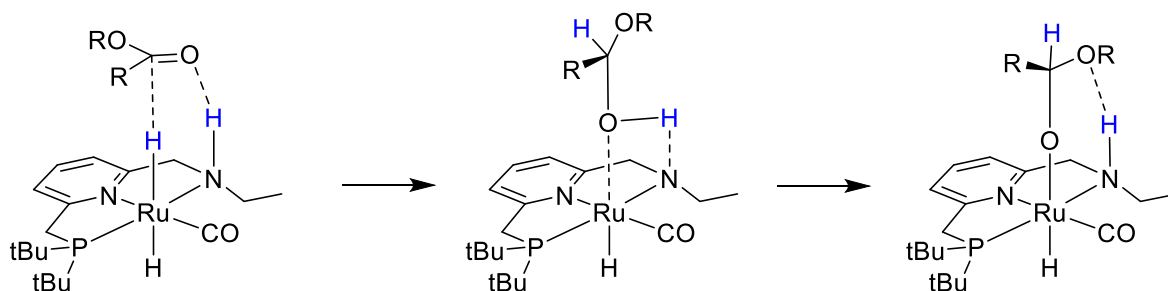
Scheme 4.12 - Proposed activation of ester to form acetal intermediate by dihydride Ru-PNN^H species with stabilising interactions with N-H donor arm, as proposed by Chianese and coworkers[47].

The family of bis-ligated tridentate PNO alcohol complexes are also all remarkably poor at ester hydrogenolysis. The aliphatic alcohol species all showed low yield of 4-fluorobenzyl alcohol and similar distribution of side products (Table 4.5, entries 2, 3, 6); the aromatic alcohol complex [Ru(**L3**)$_2$]Cl$_2$ showed no reductive activity (Table 4.5, entry 7). Substitution of the alcohol moiety for a methoxy group significantly improves catalytic activity, with moderate yield of desired 4-fluorobenzyl alcohol, but at low selectivity of 54 %.

Alteration between PNO, PNS and PNN species showed, as in literature, vast superiority of the PNN ligand type (Table 4.5 entries 8, 11 and 14), though again selectivity was only moderate in all examples. It is interesting to note that the PNN and PNO complexes [RuCl(**L9**)$_2$]Cl and [RuCl$_2$(**L6**)$_2$] inhibit production of side product **A**, *tert*-butyl 4-fluorobenzoate, which was produced by all other PNX complexes in this series. The PNNP pincer complex performed extremely well, but reduction in base loading showed poor performance compared to the Milstein complex [RuCO(Cl)H(**L20**)] (Table 4.5 entry 15, Table 4.4 entry 9).

Interestingly, the use of the reduced form of the PNS ligand **L14**, **L18**, significantly improved both 4-fluorobenzyl alcohol yield and selectivity; given the success of the analogous amine ligands reported by Clarke and coworkers for this transformation[32,36], and the aforementioned mechanistic relevance of the Ru-N-H moiety, it is proposed that the imine ligand may be undergoing reduction *in situ* to the amine before it becomes active for this direct reductive cleavage. Unfortunately, investigation into the post-reaction catalyst structure was not successful under the low catalyst loadings investigated, so this is not confirmed. Therefore, expansion of this set of [RuCl$_2$(PNX)$_2$] complexes to include their reduced amine forms could be interesting to pursue in future work, particularly if a comparison of the hydrogen gas activation by analogous amine and imine complexes could be studied.

4.6.4   Activation of PNN and PNNP complexes

Given the success of the PNNP complex [RuCl$_2$(**L11**)] in the hydrogenative ester cleavage reaction, the activation pathway of the complex was considered, in particular the relevance of imine or amine nitrogens. NMR scale experiments were conducted on the complex to study structural changes upon exposure to stoichiometric base and H$_2$ atmosphere. These investigations were also performed on Milstein species [RuCO(Cl)H(**L20**)]. Experiments were performed in freshly dried and degassed THF-d8 at room temperature in a J Youngs NMR tube. Use of a low pressure hydrogen Schlenk line allowed treatment of samples with H$_2$ gas at ambient pressure. Particular focus was paid to the hydride region and imine protons.

4.6.4.1 Reactions of [RuCO(Cl)H(**L20**)] with tBuOK and H_2

Signals of a particular interest in examination of [RuCO(Cl)H(**L20**)] were the phosphine ligand, the methylene protons, and any hydrides. When dissolved in freshly dried and degassed THF-d8, the Ru-H hydride signal was visible as a doublet at -14.75 ppm and Ru-P appeared in $^{31}P\{^1H\}$ NMR as a singlet at 104.5 ppm. When treated with superstoichiometric tBuOK, a colour change of the solution from orange to very dark purple-black was observed, and the expected doublet attributed to Ru-H was observed as a broad signal at -20.97 ppm. Upon treatment with H_2 in the presence of base, a further colour change to deep green was observed, and several $^{31}P\{^1H\}$ NMR signals appeared at low levels in the NMR spectrum. Notably, signals at 119.5 ppm and 94.5 ppm were observed. This seems reasonably concordant with a recent report by Gusev and coworkers, where they describe production of a dimeric system featuring hydride bridges (Scheme 4.13)[46], as opposed to the previously proposed (but never experimentally observed) [RuCOH$_2$(**L20**)]. Unfortunately conducting this study at room temperature also seemed to result in substantial complex decomposition and release of free ligand, making the ^1H NMR spectrum particularly difficult to interpret; Gusev and coworkers also note that substantial broadening in the spectrum was observed at room temperature. Several weak signals in the hydride region are apparent, but hydride signals concordant with those reported by Gusev could not be confidently determined.
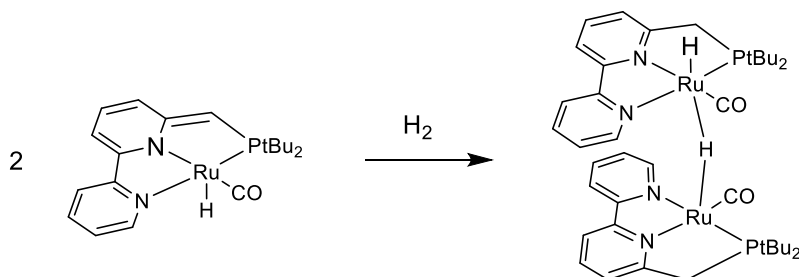
*Scheme 4.13 – Formation of dimeric complex with bridging hydride ligand by treatment of activated [RuCO(Cl)H(**L20**)] with H_2 gas, as reported by Gusev and coworkers[46].*

4.6.4.2 Reactions of [RuCl$_2$(**L11**)] with tBuOK and H_2

A similar attempt to monitor changes in the structure of [RuCl$_2$(**L11**)] was made. When dissolved in THF-d8, a red solution was formed which gave the expected key signals in ^1H NMR spectrum of the imine proton (8.97 ppm) and CH_2 bridge protons (4.18 ppm). In $^{31}P\{^1H\}$ NMR, the phosphine signal was visible as a singlet at 48.5 ppm. When placed under an H_2 atmosphere in the absence of base, no visible changes occurred to either solution or NMR signals. Upon treatment under N_2 atmosphere with stoichiometric *t*BuOK, a rapid colour change to form a green-black solution was observed and there was complete broadening of NMR signals in both ^1H and $^{31}P\{^1H\}$ NMR,

indicating the base had resulted in oxidation of the ruthenium centre to form a paramagnetic Ru(III) complex. When then placed under a H_2 atmosphere, a further colour change of solution to dark brown was observed, but NMR spectra remained broadened, indicating the continued presence of an Ru(III) complex. Attempts to produce crystals of either complex were unsuccessful, so unfortunately no further detail was obtained. However, the ready production of a Ru(III) complex suggests that [RuCl$_2$(**L11**)] readily changes oxidation state throughout the course of the catalytic cycle in a potential inner-sphere mechanism. However, little else can be elucidated from this data without further study.

4.6.5   Side Products

As is reported in Table 4.5, unexpected side products were observed in the ^{19}F NMR spectra of a number of these reactions, particularly during the use of the novel imine-based PNX catalysts developed in this work, accounting for up to 25 % of recovered material. Four different byproducts signals were observed in the ^{19}F NMR spectrum in addition to recovered starting material and the anticipated 4-fluorobenzyl alcohol product. These signals were identified using ^{1}H and ^{19}F NMR spectroscopy and GCMS analysis of crude product mixtures as the two transesterification products **A** and **B** listed in Figure 4.11. A third side product **C** was observed in some catalyst runs. No other impurities were noted.
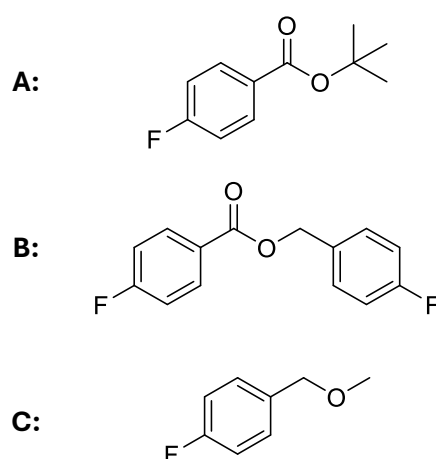
Figure 4.11 - Assigned identities of fluorine-containing impurities from the hydrogenolysis of methyl 4-fluorobenzoate.

Impurity **A** was identified by NMR spectroscopy and GCMS quite unexpectedly as the commercially available transesterification product *tert*-butyl 4-fluorobenzoate, clearly produced from the base additive. This is unusual as the *tert*-butoxide is typically non-nucleophilic due to its bulk, so the transformation was likely forced by the moderately high temperature and pressure of the system. The transformation is apparently secondary, and **A** was only seen any significant yield where ester cleavage product 4-fluorobenzyl alcohol yields were below 5 %. Regardless, yields of

A were always below 10 %. Ruthenium was not required for a low yield of **A** to be observed (Table 4.5, entry 17), and yields were no higher in the presence of ruthenium, suggesting this reaction is a simple base-catalysed transesterification with the alkoxide acting as nucleophile.

Impurity **B** was observed as having two signals in the ^{19}F NMR spectrum which were always produced together in equivalent yield at -105.6 and -113.5 ppm. Several shifted signals in the aromatic region and an additional distinctive singlet at 5.21 ppm in the ^{1}H NMR spectrum allowed identification as the cross-coupling product 4-fluorobenzyl 4-fluorobenzoate. **B** was only produced when 4-fluorobenyl alcohol was also produced, indicating that a benzyl reduction product is a reagent in the production of **B**. It is well understood that catalysts active for hydrogenative cleavage of esters (and amides) are frequently also active for the reverse dehydrogenative coupling[43,49], so a ruthenium catalysed coupling of two equivalents of alcohol product 4-fluorobenzyl alcohol to give **B** is possible, but this transformation is highly conditions dependent and the high hydrogen pressures disfavour the re-coupling of fully reduced alcohols in this system. It is also of course possible that base-catalysed transesterification between product and starting material occurs independently of the ruthenium catalyst, but the absence of **B** produced in systems effective for incomplete reductive cleavage (Table 4.4 entries 2-5) suggest the non-innocence of the metal complex. Therefore, it is most likely that a competitive reaction with a produced intermediate is occurring.
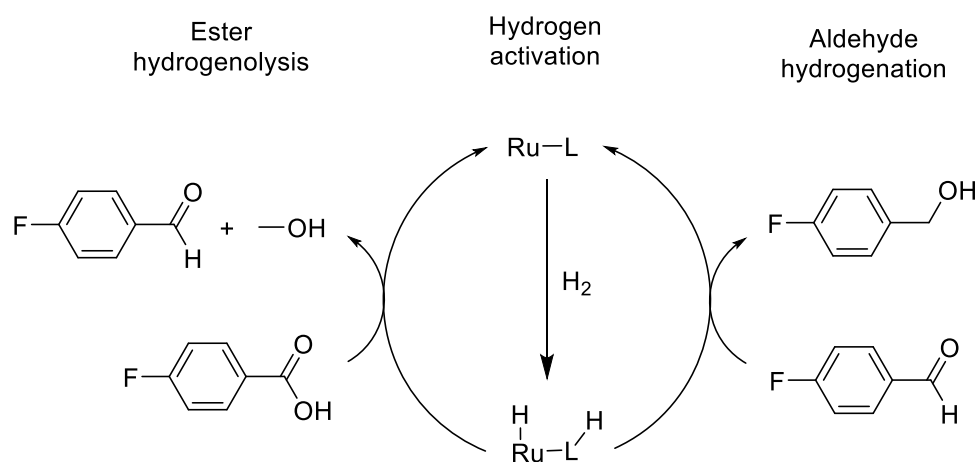
Scheme 4.14 - Catalytic cycle for ester hydrogenation with ruthenium catalyst.

Proposed mechanisms for the reductive cleavage of esters typically follow an analogous pathway to that proposed for amide reduction (Scheme 4.6), whereby a base-activated catalyst performs hydrolytic cleavage of H$_2$ gas in an initial step to give a metal hydride with the proton sitting somewhere on the ligand system. These hydrogen atoms are then transferred to the ester (or amide), performing C-O (or C-N) cleavage to produce an aldehyde and an alcohol, with the

aldehyde then reduced (summarised in Scheme 4.14)[44,45,47,50]. This system therefore gives the aldehyde 4-fluorobenzaldehyde as an intermediate product, susceptible to reaction. Reported DFT calculations of such transformations typically agree the reduction of the aldehyde is energetically much more favourable than the initial reduction of ester or amide[47,50], which explains the absence of accumulated aldehyde in product mixtures and indicates that a competitive Tishchenko aldehyde coupling is unlikely. It is disputed in similar systems whether aldehyde remains coordinated to the metal centre or is disassociated for the re-hydrogenation of the metal complex, but a coordinated aldehyde would be ideally activated for nucleophilic attack by a base-activated benzyl alcohol. If the catalysts explored in this work are inefficient in the activation of molecular hydrogen, particularly if intermediate aldehyde remains coordinated, reaction with nucleophilic alcohol could be competitive with reduction. This is therefore proposed as a potential pathway for the competitive production of **B** (Scheme 4.15). A similar pathway with attack by methanol may also occur, but as this would simply reproduce ester starting material it is not possible to confirm.
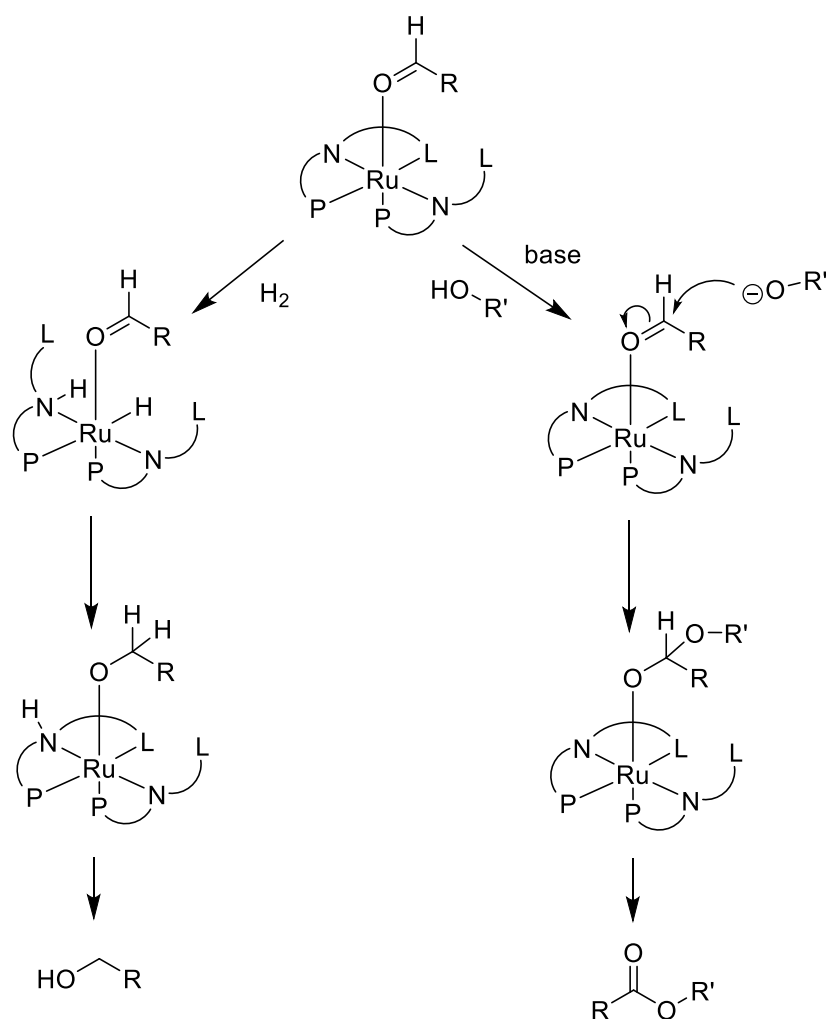
*Scheme 4.15 - Potential fate of coordinated aldehyde following initial C-O bond cleavage. Left: hydrogenation. Right: base-catalysed nucleophilic attack by alcohol to give starting material or **B**.*

Attempts to identify **C** were more difficult, as few distinctive peaks were visible in NMR spectroscopy. The position of the fluorine signal in ^{19}F NMR of -114.0 ppm is indicative of a retained 4-fluorobenzyl substructure, only slightly upfield of the signal observed for 4-fluorobenzyl alcohol. However, no clear signals in the shielded aliphatic region of ^{1}H NMR spectra were observed; only one significantly deshielded peak at 4.93 ppm was consistently present in reaction mixtures producing **C**. Additional impurity peaks attributed to **C** were observed in the aromatic region but overlap with other products made it impossible to obtain further information. The best guess for a potential product is the ether product 1-fluoro-4-(methoxymethyl)benzene, as the observed signals align reasonably well with literature values for this compound, on the assumption that the methyl protons are concealed beneath solvent 1,4-dioxane signals, though it is noted that the peak attributed to CH_2 appears slightly upfield of literature data. GCMS analysis supports this assignment, with an isolated fraction showing an observed mass/charge ratio of 141.07. The side production of this ether is

theoretically possible, either by dehydrogenative reduction of the ester carbonyl (though given reported mechanistic work this is considered unlikely for this system), or recombination of methanol and intermediate 4-fluorobenzaldehyde; there is little reported evidence of this occurring under direct reduction conditions, but has been previously reported to occur under hydroformylation conditions with a cobalt PNN pincer catalyst[51].

4.6.6 Symmetrical Ru(II) XNX (X = P,N,S) Complexes as Catalysts

It has been confirmed in the above investigations that ruthenium complexes featuring PNN type ligands consistently outperform species investigated which do not contain this substructure, a trend also noted in further literature studies with substantial investigation denoting the relevance of Ru-N binding in reaction mechanisms. It is noted that the asymmetric PNN ligands **L19** and **L20** have been extremely well explored in the literature for their activity in hydrogenations and dehydrogenation pathways. However, as previously discussed, the asymmetric ligand species reported by Milstein are frequently difficult to prepare in high purity and yield. Attempts to study the necessity of the asymmetrical nature of the investigated ligands were performed by a comparison of the behaviour of symmetrical species, analogous to the varied ligand arms of effective PNN complexes. Selected target ligands are summarised in Figure 4.12.
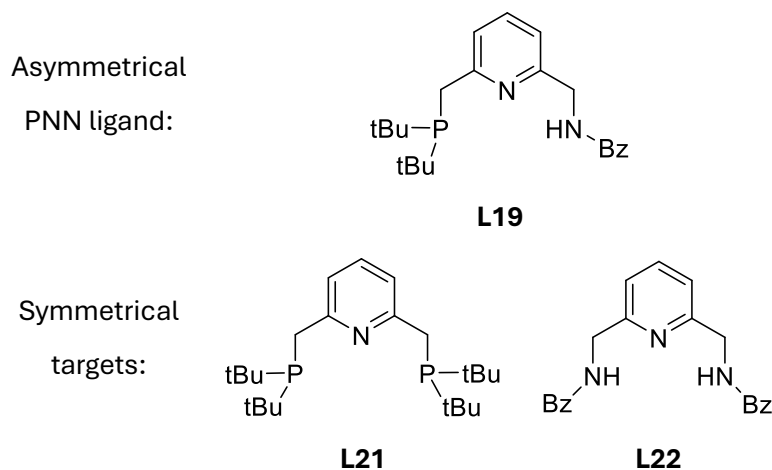
Figure 4.12 – PNN ligand **L19** and symmetrical analogues **L21** and **L22** investigated in this work.

The ligands **L21** and **L22** were prepared according to literature methods in good yields. **L21** was complexed readily in good yield with ruthenium precursor [RuCO(Cl)H(PPh$_3$)$_3$] to give the previously reported PNP complex [RuCO(Cl)H(**L21**)] as a yellow solid. Attempts to react **L22** with this precursor unfortunately provided a mixture of complexes which could not be separated by standard techniques. Greater success was gained from complexation with the precursor [RuCl$_2$(PPh$_3$)$_3$], and the apparently novel complex [RuCl$_2$(**L22**)PPh$_3$] was produced as a mixture of two isomers, as observed with two distinct singlet signals in the ^{31}P{^{1}H} NMR spectrum at

61.4 ppm and 50.7 ppm in a ratio of approximately 1:2. Identity was confirmed by HRMS. The two NMR signals are due to the two possible positions of the PPh$_3$ ancillary ligand, leading to two isomers where the chloride ligands are either *cis-* or *trans-* to one another; an analogous mixture is commonly observed with similar pyridyl SNS complexes[52]. In comparison with these systems, the more upfield signal is attributed to the *cis-* complex (δ: 50.7 ppm), whereas the minor downfield signal is attributed to the *trans-* complex (δ: 61.4 ppm). Similar reactions were attempted with terpyridine, but again, crude mixtures were obtained and further attempts to prepare such complexes were not performed.

[RuCO(Cl)H(**L21**)]   *cis*-[RuCl$_2$(**L22**)PPh$_3$]   *trans*-[RuCl$_2$(**L22**)PPh$_3$]
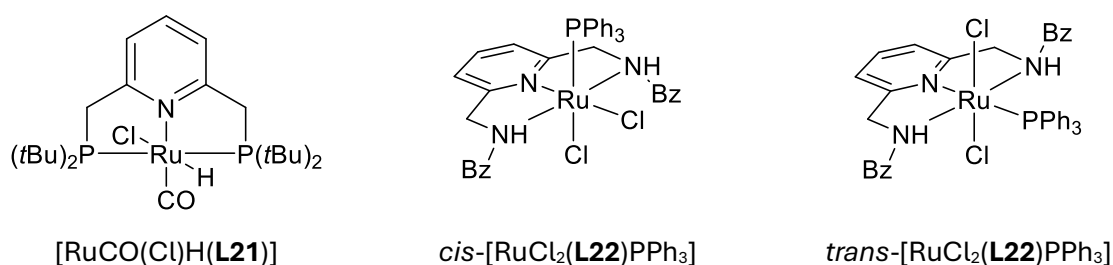
Figure 4.13 – PNP and NNN complexes prepared in this work.

Table 4.6 – Comparison of efficacy of symmetrical PNP and NNN complexes in model ester hydrogenation.

Entry	Catalyst (mol%)	Base (mol%)	4-fluorobenzyl alcohol (selectivity, %)	A	B	C
			Yield / %			
1	[RuCO(Cl)H(**L21**)] (0.5)	tBuOK (20)		13		
2	[RuCl$_2$(**L22**)PPh$_3$] (0.5)	tBuOK (20)	12		10	7

Here we have a reasonable representation of each ligand arm in the Milstein complex [RuCO(Cl)H(**L19**)], which is well established as highly effective in ester hydrogenative cleavage. A direct comparison of these two complexes shows no reduction of ester by the PNP complex, with instead the highest yield thus far seen of *tert*-butyl ester byproduct **A**. Moderate conversion of starting material to hydrogenation products was seen using the NNN[Bz] complex [RuCl$_2$(**L22**)PPh$_3$]. Selectivity towards 4-fluorobenzyl alcohol was poor however, producing both side products **B** and **C** as further reaction of produced 4-fluorobenzyl alcohol. The necessity of both N and P components is therefore clear in this pyridine backbone pincer type ligand, though the nitrogen pendant arm appears to have more importance.

4.6.7　Potential relevance of pyridine and N-H moieties

In contrast with the poor efficacy of the symmetrical pyridine backbone ligands discussed in section 4.6.6, several aliphatic amine-based symmetrical systems are well-established effective catalysts for direct hydrogenation of carbonyl compounds, including the commercially available Ru-MACHO® and [RuCl$_2$(SN^{H}S)PPh$_3$], reported in 2011 and 2013 respectively (Figure 4.14). These systems and feature a convenient symmetrical pincer structure with an aliphatic secondary amine backbone and R-substituted P or S arms. Indeed, the relevance of the N-H group has been established as a coordination agent, as previously discussed. However, the pyridine moiety is also frequently reported as integral in the de- and re-aromatisation activation process of the PNN complexes reported by Milstein, especially noting this activation is reported to involve specifically the P-adjacent methylene protons; notably, one of the best systems found in the literature is the Milstein complex [RuCO(Cl)H(**L20**)], which contains no N-H moiety at all.

To further examine this structure-activity relationship, the activity of pyridine-containing symmetrical PNP and SNS ligands are compared to their aliphatic analogues in the hydrogenative cleavage of esters. Initially, aliphatic species were screened.
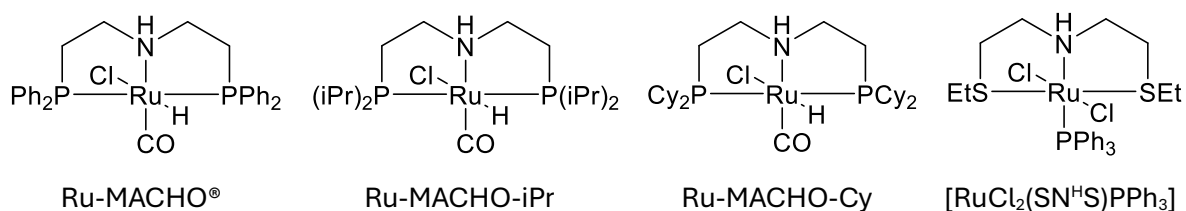
Figure 4.14 - Aliphatic PNP and SNS complexes tested in this work. Ru-MACHO and Ru-SNS obtained from commercial sources. Ru-MACHO^{Cy} and Ru-MACHO^{iPr} provided by Dr Katy Pellow, prepared according to literature procedures.

Table 4.7 - Comparison of efficacy of symmetrical aliphatic PNP and SNS complexes in model ester hydrogenation.

Entry	Catalyst (mol%)	Base (mol%)	4-fluorobenzyl alcohol (selectivity, %)	A	B	C
1	Ru-MACHO (0.5)	tBuOK (20)	92 (92)			8
2	Ru-MACHO^{iPr} (0.5)	tBuOK (20)	91 (91)			9
3	Ru-MACHO^{Cy} (0.5)	tBuOK (20)	91 (91)			9
4	Ru-SNS (0.5)	tBuOK (20)	100			

Both commercial systems were unsurprisingly found to completely convert starting ester. Interestingly, the Ru-SNS system was found to show complete conversion at 100 % selectivity towards the alcohol products, but Ru-MACHO gave the unexpected impurity **C** – identified in this work as 1-fluoro-4-(methoxymethyl)benzene – in almost 10 % yield. Altering R substituents on the MACHO ligand did not affect the activity or selectivity of this result.

Comparison with the pyridine-based analogues of these complexes was performed. These compounds are simply prepared, and ancillary ligands were kept analogous to the non-pyridine commercial samples. An expanded set of pyridine-based SNS complexes was prepared by Dr James Whitelegge and also applied to this system.

R = Et
nBu
tBu
Ph

[RuCl₂(**SNS**)PPh₃]   RuCl₂(SNS^{nBu})(DMSO)
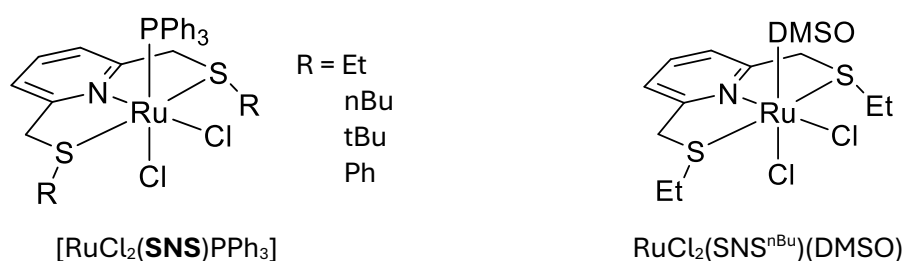
Figure 4.15 – Additional pyridine-based SNS examined for activity in direct hydrogenative cleavage. SNS complexes prepared by Dr James Whitelegge and existed as mixtures of cis- and trans- isomers, with cis the major component. [RuCl₂(SNS^{tBu})PPh₃] cis isomer only.

Table 4.8 - Comparison of efficacy of symmetrical pyridyl PNP, SNS and NNN complexes in model ester hydrogenation.

Entry	Catalyst (mol%)	Base (mol%)	4-fluorobenzyl alcohol (selectivity, %)	A	B	C
1	[RuCO(Cl)H(**L21**)] (0.5)	tBuOK (20)		13		
2	[RuCl₂(SNS^{Et})PPh₃] (0.5)	tBuOK (20)		5		
3	[RuCl₂(SNS^{nBu})PPh₃] (0.5)	tBuOK (20)		5		
4	[RuCl₂(SNS^{tBu})PPh₃] (0.5)	tBuOK (20)		4		
5	[RuCl₂(SNS^{Ph})PPh₃] (0.5)	tBuOK (20)		5		
6	[RuCl₂(SNS^{nBu})(DMSO)] (0.5)	tBuOK (20)		2		
7	[RuCl₂(**L22**)PPh₃] (0.5)	tBuOK (20)	12		10	7
[a]Yields determined by ¹⁹F NMR spectroscopy and ¹H NMR spectroscopy relative to starting ester. **B** produced from 2 equivalents of starting ester. Selectivity reported as proportion of consumed ester.						

As previously discussed, the PNP complex [RuCO(Cl)H(**L21**)] showed no activity towards hydrogenative cleavage, instead showing high activity for transesterification with potassium *tert*-butoxide; it is noted that yield relative to starting methyl 4-fluorobenzoate is 13 %, but this accounts for conversion of 65 % of base to transesterification product, given base loading of 20 %. The pyridine based SNS pincer complexes have been previously reported as poor catalysts for direct hydrogenation of esters under the milder conditions of 20 bar and 80 °C[52], but even under the more forcing conditions employed in this work this entire family of catalysts showed no activity towards hydrogen activation. Yield of transesterification product *tert*-butyl 4-fluorobenzoate is also reduced compared to analogous PNP species. Alteration of ancillary ligand from PPh_3 to DMSO did not alter activity. Interestingly, the only species showing any activity towards reduction remains the NNN complex [$RuCl_2$(**L22**)PPh_3], supporting the notion of catalytically relevant Ru-N-H moieties. Consequently, it may be interesting to pursue expansion of the NNN ligand set in future work to further explore this relationship and investigate other types of catalysis.

4.7 Conclusions and Further Work

The direct hydrogenative cleavage of amides and esters was investigated with application of a range of new Ru(II) pincer complexes. Investigations into the previously reported cleavage of a model diamide system using the PNN pincer complex [RuCO(Cl)H(**L20**)] identified a previously unreported induction period, attributed tentatively to poor substrate solubility, though an autocatalytic mechanism is also considered. Given the poor success of already known catalysts in the model amide hydrogenation, novel complexes were applied to a less challenging ester hydrogenative cleavage.

A selection of novel Ru(II) PNX (X = O, N, S) complexes prepared in this work were applied to the direct hydrogenative cleavage of a model ester system. Observed activity was moderate in several instances, but selectivity was consistently poor, with multiple alternative reaction pathways. Of the imine-containing systems investigated, PNN and PNNP complexes were the most active towards ester cleavage, with NMR scale investigation of PNNP complex [RuCl$_2$(**L11**)] suggesting an active Ru(III) species formed upon treatment with base. Bidentate PNO complex [RuCl$_2$(**L6**)$_2$] was also moderately effective. Comparison between imine and reduced forms of the PNS complex tested showed a marked improvement in activity when the reduced amine complex [RuCl$_2$(**L18**)$_2$] was applied. Further investigation of aliphatic and aromatic PNP, SNS and NNN complexes demonstrate an apparent reliance on the presence of N-H bonds for any reductive cleavage to be observed, with the only exception in this work being the highly active previously reported bipyridyl catalyst [RuCO(Cl)H(**L20**)]. Therefore, it is proposed reduction of the imine ligands occurs spontaneously under high hydrogen pressures to form an active amine-based species, though further work investigating longer run times and expanding the scope of amine-based complexes investigated would be needed to understand this process better. Additionally, further NMR scale investigations into the activation of hydrogen would be of interest, with particular focus on catalytically active PNN complexes. Given recently reported application of manganese featuring PNN pincer ligands in hydrogenative cleavage[53], application of the most active ligands in this work would be interesting to apply to alternative earth abundant metal species in further investigations.

4.8 References

1   T. M. Letcher, *Plastic Waste and Recycling: Environmental Impact, Societal Issues, Prevention, and Solutions*, 2020, 3–12.

2   R. Geyer, *Plastic Waste and Recycling*, 2020, 13–32.

3   R. Geyer, J. R. Jambeck and K. L. Law, *Sci Adv*, 2017, **3**, e1700782.

4   S. Freinkel, *Plastic: A Toxic Love Story*, Houghton Mifflin Harcourt, New York, New York, 2011.

5   Plastics – the fast Facts 2024 • Plastics Europe, https://plasticseurope.org/knowledge-hub/plastics-the-fast-facts-2024/, (accessed 1 March 2025).

6   How much oil is used to make plastic? - U.S. Energy Information Administration (EIA), https://www.eia.gov/tools/faqs/faq.php?id=34&t=6, (accessed 1 March 2025).

7   H. Wiesinger, Z. Wang and S. Hellweg, *Environ Sci Technol*, 2021, **55**, 9339–9351.

8   What is PlantBottle packaging?, https://www.coca-colacompany.com/about-us/faq/what-is-plantbottle-packaging, (accessed 1 March 2025).

9   L. V. Teixeira, J. V. Bomtempo, F. de A. Oroski and P. L. de A. Coutinho, *Sustainability 2023, Vol. 15, Page 4699*, 2023, **15**, 4699.

10   European Bioplastics, *Bioplastics Market Development Update 2022*, Berlin, 2022.

11   Polymer: Bio-Based/Degradables, https://www.bpf.co.uk/plastipedia/polymers/polymer-bio-based-degradables.aspx, (accessed 1 March 2025).

12   D. K. A. Barnes, F. Galgani, R. C. Thompson and M. Barlaz, *Philosophical Transactions of the Royal Society B: Biological Sciences*, 2009, **364**, 1985–1998.

13   J. Zalasiewicz, C. N. Waters, J. A. Ivar do Sul, P. L. Corcoran, A. D. Barnosky, A. Cearreta, M. Edgeworth, A. Gałuszka, C. Jeandel, R. Leinfelder, J. R. McNeill, W. Steffen, C. Summerhayes, M. Wagreich, M. Williams, A. P. Wolfe and Y. Yonan, *Anthropocene*, 2016, **13**, 4–17.

14   M. H. Rahman, P. R. Bhoi and P. L. Menezes, *Renewable and Sustainable Energy Reviews*, 2023, **188**, 113799.

15 S. Padmanabhan, K. Giridharan, B. Stalin, S. Kumaran, V. Kavimani, N. Nagaprasad, L. Tesfaye Jule and R. Krishnaraj, *Scientific Reports 2022 12:1*, 2022, **12**, 1–13.

16 *The Circular Economy for Plastics: A European Analysis*, 2024.

17 A. Bifulco, J. Chen, A. Sekar, W. W. Klingler, A. Gooneie and S. Gaan, *J Mater Sci Technol*, 2024, **199**, 156–183.

18 K. Ragaert, L. Delva and K. Van Geem, *Waste Management*, 2017, **69**, 24–58.

19 M. Niaounakis, in *Recycling of Flexible Plastic Packaging*, ed. M. Niaounakis, William Andrew Publishing, 2020, pp. 343–368.

20 L. Shen, E. Worrell and M. K. Patel, *Resour Conserv Recycl*, 2010, **55**, 34–52.

21 A. Bartl, in *Plastic Waste and Recycling*, ed. T. M. Letcher, Academic Press, 2020, pp. 251–279.

22 S. Siepen, O. Herweg, R. Mair and D. Popa, *How EPCs and equipment suppliers can capitalize on chemical recycling*, 2024.

23 M. Pohjakallio, T. Vuorinen and A. Oasmaa, in *Plastic Waste and Recycling: Environmental Impact, Societal Issues, Prevention, and Solutions*, Academic Press, 2020, pp. 359–384.

24 J. Aguado and D. P. Serrano, *Feedstock Recycling of Plastic Wastes*, The Royal Society of Chemistry, Cambridge, 1999.

25 B. Geyer, G. Lorenz and A. Kandelbauer, *Express Polym Lett*, 2016, **10**, 559–586.

26 World Intellectual Property Organization, WO/2015/173265, 2015.

27 H. Mitta, L. Li, M. Havaei, D. Parida, E. Feghali, K. Elst, A. Aerts, K. Vanbroekhoven and K. M. Van Geem, *Green Chemistry*, 2024, **27**, 10–40.

28 G. Squadrito, G. Maggio and A. Nicita, *Renew Energy*, 2023, **216**, 119041.

29 C. Wang and O. El-Sepelgy, *Curr Opin Green Sustain Chem*, 2021, **32**, 100547.

30 E. M. Krall, T. W. Klein, R. J. Andersen, D. S. Reader, B. C. Dauphinais, S. P. McIlrath, >Anne A. Fischer, M. J. Carney and N. J. Robertson, *Chemical Communications*, 2014, **50**, 4884–4887.

31 S. Westhues, J. Idel and J. Klankermayer, *Sci Adv*, 2018, **4**, eaat9669.

32   J. A. Fuentes, S. M. Smith, M. T. Scharbert, I. Carpenter, D. B. Cordes, A. M. Z. Slawin and M. L. Clarke, *Chemistry – A European Journal*, 2015, **21**, 10851–10860.

33   Y. Hu, S. Zhang, J. Xu, Y. Liu, A. Yu, J. Qian and Y. Xie, *Angewandte Chemie International Edition*, 2023, **62**, e202312564.

34   Z. Wei, H. Li, Y. Wang and Q. Liu, *Angewandte Chemie International Edition*, 2023, **62**, e202301042.

35   J. Zhang, G. Leitus, Y. Ben-David and D. Milstein, *J Am Chem Soc*, 2005, **127**, 10840–10841.

36   I. Carpenter, S. C. Eckelmann, M. T. Kuntz, J. A. Fuentes, M. B. France and M. L. Clarke, *Dalton Transactions*, 2012, **41**, 10136–10140.

37   M. Montag, J. Zhang and D. Milstein, *J Am Chem Soc*, 2012, **134**, 10325–10328.

38   A. Kumar, N. Von Wolff, M. Rauch, Y. Q. Zou, G. Shmul, Y. Ben-David, G. Leitus, L. Avram and D. Milstein, *J Am Chem Soc*, 2020, **142**, 14267–14275.

39   W. Zhou, P. Neumann, M. Al Batal, F. Rominger, A. S. K. Hashmi and T. Schaub, *ChemSusChem*, 2021, **14**, 4176–4180.

40   E. Balaraman, B. Gnanaprakasam, L. J. W. Shimon and D. Milstein, *J Am Chem Soc*, 2010, **132**, 16756–16758.

41   S. Kar, M. Rauch, A. Kumar, G. Leitus, Y. Ben-David and D. Milstein, *ACS Catal*, 2020, **10**, 5511–5515.

42   G. A. Filonenko, M. P. Conley, C. Copéret, M. Lutz, E. J. M. Hensen and E. A. Pidko, *ACS Catal*, 2013, **3**, 2522–2526.

43   P. Hu, Y. Ben-David and D. Milstein, *Angewandte Chemie*, 2016, **128**, 1073–1076.

44   C. Gunanathan and D. Milstein, *Acc Chem Res*, 2011, **44**, 588–602.

45   D. G. Gusev, *Organometallics*, 2020, **39**, 258–270.

46   L. N. Dawe, M. Karimzadeh-Younjali, Z. Dai, E. Khaskin and D. G. Gusev, *J Am Chem Soc*, 2020, **142**, 19510–19522.

47   J. Pham, C. E. Jarczyk, E. F. Reynolds, S. E. Kelly, T. Kim, T. He, J. M. Keith and A. R. Chianese, *Chem Sci*, 2021, **12**, 8477–8492.

48   M. K. Pandey and J. Choudhury, *ACS Omega*, 2020, **5**, 30775–30786.

49   M. H. G. Prechtl, K. Wobser, N. Theyssen, Y. Ben-David, D. Milstein and W. Leitner, *Catal Sci Technol*, 2012, **2**, 2039–2042.

50   H. Zhang, *Comput Theor Chem*, 2015, **1066**, 1–6.

51   F. G. Delolo, J. Fessler, H. Neumann, K. Junge, E. N. dos Santos, E. V. Gusevskaya and M. Beller, *Chemistry – A European Journal*, 2022, **28**, e202103903.

52   J. Schörgenhumer, A. Zimmermann and M. Waser, *Org Process Res Dev*, 2018, **22**, 862–870.

53   X. G. Li, F. Li, Y. Xu, L. J. Xiao, J. H. Xie and Q. L. Zhou, *Adv Synth Catal*, 2022, **364**, 744–749.

5 Experimental

5.1 General considerations

Unless otherwise specified, all procedures were carried out under an inert atmosphere of N_2 or Ar using standard Schlenk line or glovebox (MBraun O_2 < 0.1 ppm, H_2O < 0.1 ppm) techniques. Common solvents (acetonitrile, diethyl ether, toluene, dichloromethane, tetrahydrofuran, pentane and hexane) were obtained from a Grubbs-type purification system, stored under an inert atmosphere over 3 Å molecular sieves and degassed by N_2 sparge prior to use. Methanol, ethanol and 1,4-dioxane were obtained as extra dry methanol (99.9 %), extra dry ethanol (99.5 %) and extra dry 1,4-dioxane (99.5 %) stabilised with BHT from Acros Organics, transferred to storage under an inert atmosphere over 3 Å molecular sieves, and degassed by N_2 sparge prior to use. Deuterated solvents were obtained from commercial sources and were dried according to standard procedure (generally over CaH_2 or molecular sieves), degassed by freeze-pump-thaw and stored under inert conditions over 3 Å molecular sieves. Unless otherwise stated, reagents were purchased from commercial suppliers and used without further purification.

NMR spectra were recorded on a Bruker DPX 400 MHz, Bruker Avance 500 MHz or Bruker Avance 400 MHz instrument. ^{1}H and ^{13}C NMR spectroscopic data are reported in ppm relative to the residual solvent signal form the deuterated solvent, unless otherwise stated. Quantitative ^{1}H NMR spectroscopy using a pulse interval of D1 = 25 s was performed on a Bruker Avance 500 MHz or Bruker Avance 400 MHz. ^{31}P NMR are referenced relative to 85 % H_3PO_4 external standard. ^{19}F NMR are referenced relative to TFA external standard. Solid-state infrared (IR) absorption spectroscopy was recorded on an Agilent Cary 630 FTIR instrument in air. HRMS and LRMS analysis was conducted on a Waters XEVO spectrometer. Single crystal X-ray crystallography and structure determination was performed by Dr Benson Kariuki on an Agilent SupaNova Dual Atlas diffractometer, equipped with an Oxford Cryosystem cooling apparatus, using either Mo Kα or Cu Kα radiation.

5.2 Chapter 2 Experimental

Ethylenediamine was purified by distillation and stored under N_2 prior to use. All other liquid amines were degassed by freeze-pump-thaw with no further purification before use.

Ruthenium precursors [RuCl$_2$(p-cymene)]$_2$ and [RuCl$_2$(PPh$_3$)$_3$] were prepared according to literature procedures[1,2].

5.2.1 Synthesis of imine-based PNX (X=O,S,N) pincer ligands

5.1.1.1 Synthesis of **L1**
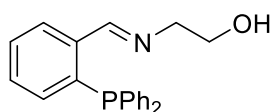
Adapted from literature procedure.[3]

Under an inert N_2 atmosphere, 2-(diphenylphosphino)benzaldehyde (5.0 g, 17.2 mmol) was stirred with ethanolamine (2.0 mL, 33.1 mmol) in toluene at 60 °C for 2 h. Once complete, as confirmed by ^{31}P NMR, the mixture was dried over NaSO$_4$. The crude mixture was filtered and volatiles were removed under high vacuum. The crude product was purified by recrystallisation from cold methanol and obtained as a white solid. Yield: 4.74 g, 14.2 mmol, 83 %.

Analysis in accordance with literature reports.[3]

^{1}H-NMR (400 MHz, CDCl$_3$) δ$_H$: 8.74 (d, J = 3.6 Hz, 1H), 7.81 (ddd, J = 7.7 Hz, J = 3.9 Hz, J = 1.4 Hz, 1H), 7.41 (td, J = 7.4 Hz, J = 1.3 Hz, 1H), 7.36-7.22 (m, 11H), 6.89 (ddd, J = 7.9 Hz, J = 4.7 Hz, J = 1.3 Hz, 1H), 3.70-3.58 (m, 4H), 1.72 (s, 1H) ppm. ^{31}P{^{1}H}-NMR (162 MHz, CDCl$_3$) δ$_P$: -10.7 ppm. ^{13}C{^{1}H}-NMR (101 MHz, CDCl$_3$) δ$_C$: 161.8 (d, J_{C-P} = 12.3 Hz), 139.2 (d, J_{C-P} = 16.4 Hz), 137.4 (d, J_{C-P} = 20.5 Hz), 137.3 (d, J_{C-P} = 8.7 Hz), 134.0, 133.9 (d, J_{C-P} = 19.9 Hz), 130.1, 129.4 (d, J_{C-P} = 4.1 Hz), 128.8, 128.7, 128.6 (d, J_{C-P} = 7.3 Hz), 62.9, 62.4 ppm. Selected IR data:, 3254 v(O-H) 1634 v(C=N) cm^{-1}.

5.1.1.2 Synthesis of **L2**
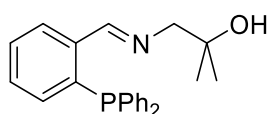
Under an inert N_2 atmosphere, 2-(diphenylphosphino)benzaldehyde (1.03 g, 3.55 mmol) was refluxed with 1-amino-2-methlypropan-2-ol (0.4 mL, 4.29 mmol) in methanol for 2 h. Once

complete, as confirmed by ^{31}P NMR, the mixture was dried over NaSO$_4$. The crude mixture was filtered and volatiles were removed under high vacuum. The crude product was purified by recrystallisation from cold methanol and obtained as a pale orange solid. Yield: 1.12 g, 3.09 mmol, 87 %.

^{1}H-NMR (400 MHz, CDCl$_3$) δ$_H$: 8.73 (d, J = 4.0 Hz, 1H), 7.85 (ddd, J = 7.6 Hz, J = 3.9 Hz, J = 1.5 Hz, 1H), 7.42 (td, J = 7.5 Hz, J = 1.4 Hz, 1H), 7.37-7.21 (m, 11H), 6.90 (ddd, J = 7.7 Hz, J = 4.5 Hz, J = 1.3 Hz, 1H), 3.44 (d, J = 1.4 Hz, 2H), 2.43 (s, 1H), 1.08 (s, 6H) ppm. ^{31}P{^{1}H}-NMR (162 MHz, CDCl$_3$) δ$_P$: -10.9 ppm. ^{13}C{^{1}H}-NMR (101 MHz, CDCl$_3$) δ$_C$: 161.4 (d, J_{C-P} = 12.8 Hz), 139.2 (d, J_{C-P} = 16.9 Hz), 137.3 (d, J_{C-P} = 21.5 Hz), 137.3 (d, J_{C-P} = 9.5 Hz), 134.0, 133.8, 130.2, 129.5 (d, J_{C-P} = 4.2 Hz), 128.8, 128.7, 128.6 (d, J_{C-P} = 7.2 Hz), 71.9, 70.1, 27.2 ppm. Selected IR data: 3370 v(O-H), 1631 v(C=N) cm^{-1}. HRMS (ES+/Q-TOF) m/z: [M+H]$^{+}$ Calcd for C$_{23}$H$_{25}$NOP 362.1674; Found 362.1671.

5.1.1.3   Synthesis of **L3**

Adapted from literature procedure.[4]

Under an inert N$_2$ atmosphere, 2-(diphenylphosphino)benzaldehyde (1.00 g, 3.45 mmol) was refluxed with 2-aminophenol (385 mg, 3.53 mmol) in methanol for 2 h. The product was isolated by filtration as a bright yellow solid with no further purification. Yield: 1.16 g, 3.04 mmol, 88 %.

Analysis in accordance with literature reports.[4]

^{1}H-NMR (400 MHz, CDCl$_3$) δ$_H$: 9.02 (d, J = 3.9 Hz, 1H), 7.98 (ddd, J = 7.7 Hz, J = 3.8 Hz, J = 1.4 Hz, 1H), 7.48 (td, J = 7.5 Hz, J = 1.3 Hz, 1H), 7.37-7.24 (m, 10H), 7.19 (d, J = 1.9 Hz, 1H), 7.12 (td, J = 7.3 Hz, J = 1.5 Hz, 1H), 7.07 (dd, J = 8.0 Hz, J = 1.5, 1H), 6.99 (ddd, J = 7.7 Hz, J = 4.6 Hz, J = 1.3 Hz, 1H), 6.93 (dd, J = 8.1 Hz, J = 1.4 Hz, 1H), 6.81 (td, J = 7.3 Hz, J = 1.4 Hz, 1H) ppm. ^{31}P{^{1}H}-NMR (162 MHz, CDCl$_3$) δ$_P$: -10.0 ppm. ^{13}C{^{1}H}-NMR (101 MHz, CDCl$_3$) δ$_C$: 156.5 (d, J_{C-P} = 11.0 Hz), 152.3, 138.9 (d, J_{C-P} = 15.6 Hz), 138.3 (d, J_{C-P} = 21.5 Hz), 137.0 (d, J_{C-P} = 8.72 Hz), 135.9, 134.6, 134.0, 133.8, 130.9-130.7 (m), 129.0-128.6 (m), 119.9, 116.1, 115.1 ppm. Selected IR data: 3278 v(O-H), 1633 v(C=N) cm^{-1}.

5.1.1.4   Synthesis of **L4**

Adapted from literature procedure.[3]

Under an inert N_2 atmosphere, 2-(diphenylphosphino)benzaldehyde (1.00 g, 3.45 mmol) was refluxed with 3-aminopropanol (0.40 mL, 5.23 mmol) in methanol for 2 h. All volatiles were removed under high vacuum. The product was isolated as a pale orange oil with no further purification. Yield: 1.15 g, 3.31 mmol, 96 %.

^{1}H-NMR (400 MHz, CDCl$_3$) δ_H: 8.87 (d, J = 4.8 Hz, 1H), 7.92 (ddd, J = 7.8 Hz, J = 4.0 Hz, J = 1.4 Hz, 1H), 7.41-7.24 (m, 12H), 6.88 (ddd, J = 7.7 Hz, J = 4.7 Hz, J = 1.4 Hz, 1H), 3.69-3.60 (m, 4H), 2.76 (s, 1H), 1.81-1.73 (m, 2H) ppm. ^{31}P{^{1}H}-NMR (162 MHz, CDCl$_3$) δ_P: -13.7 ppm. ^{13}C{^{1}H}-NMR (101 MHz, CDCl$_3$) δ_C: 160.1 (d, J_{C-P} = 21.3 Hz), 139.0 (d, J_{C-P} = 17.1 Hz), 137.5, 137.3, 136.4 (d, J_{C-P} = 9.4 Hz), 134.1, 133.9, 133.4, 130.4, 129.0, 128.9, 128.6 (d, J_{C-P} = 7.26 Hz), 128.5-128.2 (m), 128.7 (d, J_{C-P} = 4.3 Hz), 62.3, 59.8, 33.1 ppm. Selected IR data: 3278 v(O-H), 1636 v(C=N) cm^{-1}. HRMS (AP+/Q-TOF) m/z: [M+H]$^+$ Calcd for $C_{22}H_{23}NOP$ 348.1517; Found 348.1517.

5.1.1.5   Synthesis of **L5**

Adapted from literature procedure.[3]
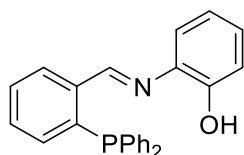
Under an inert N_2 atmosphere, 2-(diphenylphosphino)benzaldehyde (1.00 g, 3.45 mmol) was refluxed with 4-aminobutanol (0.45 mL, 4.88 mmol) in methanol for 2 h. All volatiles were removed under high vacuum. The product was isolated as an orange oil with no further purification. Yield: 1.24 g, 3.42 mmol, 99 %.

^{1}H-NMR (400 MHz, CDCl$_3$) δ_H: 8.93 (d, J = 5.1 Hz, 1H), 7.95 (ddd, J = 7.8 Hz, J = 4.0 Hz, J = 1.5 Hz, 1H), 7.42-7.23 (m, 12H), 6.87 (ddd, J = 7.8 Hz, J = 4.8 Hz, J = 1.3 Hz, 1H), 3.57-3.48 (m, 4H), 1.62-1.48 (m, 4H) ppm. ^{31}P{^{1}H}-NMR (162 MHz, CDCl$_3$) δ_P: -14.3 ppm. ^{13}C{^{1}H}-NMR (101 MHz, CDCl$_3$) δ_C: 159.9 (d, J_{C-P} = 23.2 Hz), 139.1 (d, J_{C-P} = 17.3 Hz), 137.5, 137.3, 136.3 (d, J_{C-P} = 9.4 Hz), 134.1, 133.9, 133.3, 130.4, 129.1, 128.9, 128.7, 128.6, 127.4 (d, J_{C-P} = 4.3 Hz), 62.6, 61.1, 31.2, 28.2 ppm. Selected IR data: 3291 v(O-H), 1636 v(C=N) cm^{-1}. HRMS (ES+/Q-TOF) m/z: [M+H]$^+$ Calcd for $C_{23}H_{25}NOP$ 362.1674; Found 362.1669.
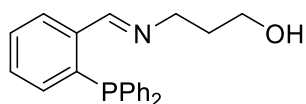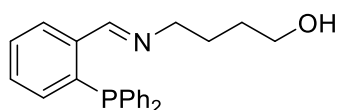
5.1.1.6   Synthesis of L6

Adapted from literature procedure.[3]

Under an inert N_2 atmosphere, 2-(diphenylphosphino)benzaldehyde (1.00 g, 3.45 mmol) was refluxed with 2-methoxyethylamine (0.40 mL, 4.60 mmol) in methanol for 2 h. All volatiles were removed under high vacuum. The product was isolated as an orange oil with no further purification. Yield: 1.16 g, 3.35 mmol, 97 %.

Analysis in accordance with literature reports.[5]

^{1}H-NMR (400 MHz, CDCl$_3$) δ_H: 8.91 (d, J = 4.8 Hz, 1H), 7.99 (ddd, J = 7.8 Hz, J = 3.9 Hz, J = 1.4 Hz, 1H), 7.40-7.21 (m, 12H), 6.86 (ddd, J = 7.7 Hz, J = 4.6 Hz, J = 1.3 Hz, 1H), 3.65 (td, J = 5.8 Hz, J = 1.3 Hz, 2H), 3.45 (t, J = 5.8 Hz, 2H), 3.22 (s, 3H) ppm. ^{31}P{^{1}H}-NMR (162 MHz, CDCl$_3$) δ_P: -13.8 ppm. ^{13}C{^{1}H}-NMR (101 MHz, CDCl$_3$) δ_C: 160.2 (d, J_{C-P} = 21.5 Hz), 138.4 (d, J_{C-P} = 17.2 Hz), 136.3 (d, J_{C-P} = 19.6 Hz), 135.6 (d, J_{C-P} = 9.6 Hz), 133.0 (d, J_{C-P} = 20.0 Hz), 132.3, 129.2, 127.8, 127.7, 127.5 (d, J_{C-P} = 7.1 Hz), 126.8 (d, J_{C-P} = 4.3 Hz), 71.1, 59.6, 57.7 ppm. Selected IR data: 1636 v(C=N) cm^{-1}.

5.1.1.7   Synthesis of L7
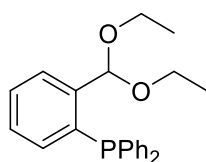
Under an inert N_2 atmosphere, 2-(diphenylphosphino)benzaldehyde (201 mg, 0.69 mmol) was refluxed in dry ethanol in the presence of [RuCl$_2$(p-cymene)]$_2$ (2 mg, 0.05 mol%) for 16 h. Reaction mixture was reduced to give a viscous orange oil with no further purification. NMR yield as determined by ^{31}P{^{1}H} relative to remaining 2-(diphenylphosphino)benzaldehyde: 84 %.

Analysis in accordance with literature reports.[6]

^{1}H-NMR (400 MHz, CDCl$_3$) δ_H: 7.75 (ddd, J = 7.8 Hz, J = 4.1 Hz, J = 1.4 Hz, 1H), 7.39 (td, J = 7.8 Hz, J = 1.4 Hz, 1H), 7.34-7.20 (m, 11H), 6.95 (ddd, J = 7.7 Hz, J = 4.4 Hz, J = 1.4 Hz, 1H), 6.12 (d, J = 5.8 Hz, 1H), 3.53-3.37 (m, 4H), 0.98 (t, J = 7.0 Hz, 1H) ppm. ^{31}P{^{1}H}-NMR (162 MHz, CDCl$_3$) δ_P: -17.2 ppm. ^{13}C{^{1}H}-NMR (101 MHz, CDCl$_3$) δ_C: 137.0 (d, J_{C-P} = 9.6 Hz), 135.3 (d, J_{C-P} = 17.2 Hz),

134.1, 133.9 (d, J_{C-P} = 19.7 Hz), 129.0, 128.5, 128.4, 128.3, 126.3 (d, J_{C-P} = 5.9 Hz), 100.0 (d, J_{C-P} = 23.8 Hz), 62.0, 14.8 ppm. Selected IR data: 1088 v(C-O), 1098 v(C-O), 1198 v(C-O) cm^{-1}.

5.1.1.8 Synthesis of **L8**
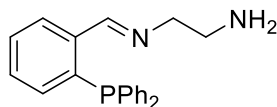
Adapted from literature procedure.[7]

Under an inert N_2 atmosphere, a solution of 2-(diphenylphosphino)benzaldehyde (2.00 g, 6.89 mmol) in THF was added dropwise over 3 h to a solution of excess ethylenediamine (4.0 mL, 59.9 mmol) in THF at room temperature. The mixture was stirred at room temperature for 2 h until reaction was complete, as confirmed by ^{31}P NMR. All volatiles were removed under high vacuum to give the crude product as a red oil with no further isolation achieved. NMR yield as determined by ^{31}P{^{1}H} NMR spectroscopy relative to remaining 2-(diphenylphosphino)benzaldehyde: 91 %.

^{1}H-NMR (400 MHz, CDCl$_3$) δ$_H$: 8.81 (d, J = 4.4 Hz, 1H), 7.90 (ddd, J = 7.6 Hz, J = 3.9 Hz, J = 1.4 Hz, 1H), 7.39 (td, J = 7.5 Hz, J = 1.3 Hz, 1H), 7.35-7.21 (m, 11H), 6.86 (ddd, J = 7.8 Hz, J = 4.6 Hz, J = 1.3 Hz, 1H), 3.52 (t, J = 5.6 Hz, 2H), 2.78 (t, J = 5.6 Hz, 2H) ppm. ^{31}P{^{1}H}-NMR (162 MHz, CDCl$_3$) δ$_P$: -12.5 ppm. HRMS (ES+/Q-TOF) m/z: [M+H]$^+$ Calcd for $C_{21}H_{22}N_2P$ 333.1521; Found 333.1522.
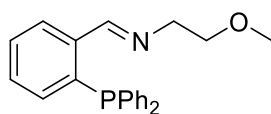
5.1.1.9 Synthesis of **L9**

Adapted from literature procedure.[8]

Under an inert N_2 atmosphere, 2-(diphenylphosphino)benzaldehyde (1.00 g, 3.45 mmol) was refluxed with N-methylethylamine (0.45 mL, 5.16 mmol) in toluene for 2 h. All volatiles were removed under high vacuum. The crude product was purified by recrystallisation from cold methanol and obtained as a beige solid mixture of two products. ^{1}H NMR spectroscopy showed a mixture of **L9a** and **L9b** in a ratio of approximately 1:2.3 with **L9b** as the major product. Yield: 905 mg, 2.61 mmol, 75 %.

Analytical data in accordance with literature reports.[8]

L9a: ^{1}H-NMR (400 MHz, CDCl$_3$) δ$_H$: 8.82 (d, J = 4.3 Hz, 1H), 7.80 (ddd, J = 7.7 Hz, J = 3.9 Hz, J = 1.5 Hz, 1H), 7.35-7.09 (m, 12H), 6.79 (ddd, J = 7.7 Hz, J = 4.6 Hz, J = 1.3 Hz, 1H), 3.55 (td, J = 5.6 Hz, J = 1.4 Hz, 1H), 2.61 (t, J = 5.5 Hz, 1H), 2.17 (s, 3H) ppm. ^{31}P{^{1}H}-NMR (162 MHz, CDCl$_3$) δ$_P$: -12.2 ppm. **L9b:** ^{1}H-NMR (400 MHz, CDCl$_3$) δ$_H$: 7.63 (ddd, J = 7.8 Hz, J = 4.1 Hz, J = 1.5 Hz, 1H), 7.35-7.09 (m, 12H), 6.84 (ddd, J = 7.7 Hz, J = 4.3 Hz, J = 1.4 Hz, 1H), 4.52 (d, J = 4.9 Hz, 1H), 3.25-3.14 (m, 2H), 3.03-2.95 (m, 1H), 2.31-2.23 (m, 1H), 1.80 (s, 3H) ppm. ^{31}P{^{1}H}-NMR (162 MHz, CDCl$_3$) δ$_P$: -17.2 ppm. Selected IR data:1655 v(C=N) cm^{-1}. HRMS (ES+/Q-TOF) m/z: [M+H]$^+$ Calcd for C$_{22}$H$_{24}$N$_2$P 347.1677; Found 347.1676.

5.1.1.10   Synthesis of **L10**
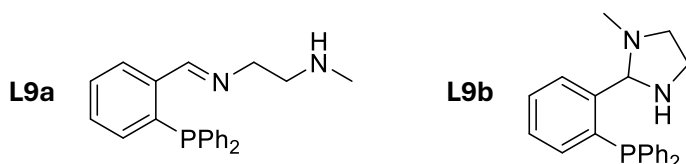

Adapted from literature procedure.[5]

Under an inert N$_2$ atmosphere, 2-(diphenylphosphino)benzaldehyde (1.00 g, 3.45 mmol) was refluxed with N,N-dimethylethylamine (0.55 mL, 5.04 mmol) in methanol for 2 h. All volatiles were removed under high vacuum. The product was isolated as a yellow-orange oil with no further purification. Yield: 1.20 g, 3.32 mmol, 96 %.

Analysis in accordance with literature reports.[5]

^{1}H-NMR (400 MHz, CDCl$_3$) δ$_H$: 8.90 (d, J = 4.9 Hz, 1H), 7.80 (ddd, J = 7.7 Hz, J = 4.0 Hz, J = 1.5 Hz, 1H), 7.40-7.23 (m, 12H), 6.86 (ddd, J = 7.8 Hz, J = 4.8 Hz, J = 1.4 Hz, 1H), 3.59 (td, J = 7.1 Hz, J = 1.4 Hz, 2H), 2.36 (t, J = 7.1 Hz, 2H), 2.18 (s, 6H) ppm.   ^{31}P{^{1}H}-NMR (162 MHz, CDCl$_3$) δ$_P$: -13.7 ppm. ^{13}C{^{1}H}-NMR (101 MHz, CDCl$_3$) δ$_C$: 160.5 (d, J_{C-P} = 21.6 Hz), 139.5 (d, J_{C-P} = 17.0 Hz), 137.3 (d, J_{C-P} = 19.3 Hz), 136.5 (d, J_{C-P} = 9.5 Hz), 134.1 (d, J_{C-P} = 20.0 Hz), 133.3, 130.3, 128.9, 128.8, 128.6 (d, J_{C-P} = 7.2 Hz), 127.6 (d, J_{C-P} = 4.4 Hz), 59.9, 59.5, 45.7 ppm.

5.1.1.11   Synthesis of **L11**

Under an inert N$_2$ atmosphere, 2-(diphenylphosphino)benzaldehyde (1.00 g, 3.45 mmol) was refluxed with ethylenediamine (1.4 mL, 20.98 mmol) in methanol for 2 h. All volatiles were

removed under high vacuum to give a yellow oil which solidified overnight to give a yellow solid. The crude product was purified by recrystallisation from cold methanol and obtained as a pale yellow solid. Yield: 889 mg, 1.47 mmol, 85 %.

Analytical data in accordance with literature reports.[9]

^{1}H-NMR (400 MHz, CDCl$_3$) δ$_H$: 8.78 (d, J = 4.6 Hz, 2H), 7.90 (ddd, J = 7.7 Hz, J = 3.9 Hz, J = 1.5 Hz, 2H), 7.37-7.21 (m, 24H), 6.86 (ddd, J = 9.5 Hz, J = 6.5 Hz, J = 1.9 Hz, 2H), 3.55 (s, 4H) ppm. ^{31}P{^{1}H}-NMR (162 MHz, CDCl$_3$) δ$_P$: -13.6 ppm. ^{13}C{^{1}H}-NMR (101 MHz, CDCl$_3$) δ$_C$: 161.0 (d, J_{C-P} = 20.7 Hz), 139.5 (d, J_{C-P} = 17.4 Hz), 137.4 (d, J_{C-P} = 19.8 Hz), 136.7 (d, J_{C-P} = 9.8 Hz), 134.0 (d, J_{C-P} = 20.0 Hz), 133.4, 130.1, 128.9, 128.8, 128.6 (d, J_{C-P} = 7.2 Hz), 127.8 (d, J_{C-P} = 4.3 Hz), 61.4 ppm. Selected IR data: 1655 v(C=N) cm^{-1}. HRMS (ES+/Q-TOF) m/z: [M+H]$^+$ Calcd for C$_{40}$H$_{35}$N$_2$P$_2$ 605.2275; Found 605.2274.

5.1.1.12   Synthesis of **L12**

Adapted from literature procedure.[3]

Under an inert N$_2$ atmosphere, 2-(diphenylphosphino)benzaldehyde (58 mg, 2.00 mmol) was refluxed with cysteamine (156 mg, 2.02 mmol) in methanol for 2 h. All volatiles were removed under high vacuum. The crude product was purified by recrystallisation from cold methanol and obtained as an off-white solid. Yield: 466 mg, 1.33 mmol, 67 %.

^{1}H-NMR (400 MHz, CDCl$_3$) δ$_H$: 7.67 (ddd, J = 7.9 Hz, J = 4.2 Hz, J = 1.3 Hz, 1H), 7.40-7.23 (m, 11H), 7.19 (td, J = 7.5 Hz, J = 1.3 Hz, 1H), 6.94 (ddd, J = 7.6 Hz, J = 4.2 Hz, J = 1.4 Hz, 1H), 6.21 (d, J = 6.5, 1H), 3.69-3.59 (m, 1H), 3.14-3.04 (m, 3H) ppm. ^{31}P{^{1}H}-NMR (162 MHz, CDCl$_3$) δ$_P$: -17.3 ppm. ^{13}C{^{1}H}-NMR (101 MHz, CDCl$_3$) δ$_C$: 145.1 (d, J_{C-P} = 23.3 Hz), 136.8 (d, J_{C-P} = 10.3 Hz), 134.3, 133.9 (d, J_{C-P} = 4.9 Hz), 133.7 (d, J_{C-P} = 4.9 Hz), 129.5, 128.7 (d, J_{C-P} = 5.7 Hz), 128.5 (m), 128.2, 126.2 (d, J_{C-P} = 5.2 Hz), 70.8 (d, J_{C-P} = 27.0 Hz), 53.2, 36.9 ppm.
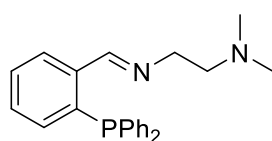
5.1.1.13   Synthesis of **L13**

Adapted from literature procedure.[3]

Under an inert N_2 atmosphere, 2-(diphenylphosphino)benzaldehyde (1.00 g, 3.45 mmol) was refluxed with 2-aminothiophenol (0.38 mL, 3.64 mmol) in methanol for 2 h. All volatiles were removed under high vacuum. The crude product was purified by recrystallisation from cold methanol and obtained as a pale green solid. Yield: 918 mg, 2.31 mmol, 67 %.

Analysis in accordance with literature reports.[10]

^{1}H-NMR (400 MHz, CDCl$_3$) δ_H: 7.98 (dd, J = 8.1 Hz, J = 4.4 Hz, 1H), 7.50-7.05 (m, 12H), 7.00-6.80 (m, 3H), 6.68 (t, J = 7.4 Hz, 1H), 6.53 (d, J = 7.8 Hz, 1H), 4.22 (s, 1H) ppm. ^{31}P{^{1}H}-NMR (162 MHz, CDCl$_3$) δ_P: -17.2 ppm.

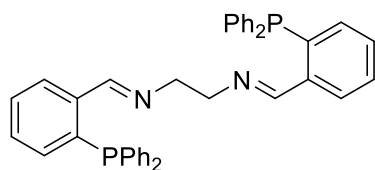## 5.1.1.14 Synthesis of **L14**

Adapted from literature procedure.[3]

Under an inert N_2 atmosphere, 2-(diphenylphosphino)benzaldehyde (1.00 g, 3.45 mmol) was refluxed with 2-(methylthio)ethylamine (0.45 mL, 4.84 mmol) in methanol for 2 h. All volatiles were removed under high vacuum. The product was isolated as a yellow oil with no further purification. Yield: 1.17 g, 3.21 mmol, 93 %.

^{1}H-NMR (400 MHz, CDCl$_3$) δ_H: 8.89 (d, J = 4.9 Hz, 1H), 7.97 (ddd, J = 7.7 Hz, J = 4.0 Hz, J = 1.4 Hz, 1H), 7.39 (td, J = 7.7 Hz, J = 1.5 Hz, 1H), 7.36-7.23 (m, 11H), 6.87 (ddd, J = 7.7 Hz, J = 4.7 Hz, J = 1.2 Hz, 1H), 3.68 (td, J = 7.0 Hz, J = 1.3 Hz, 2H), 2.56 (t, J = 7.0 Hz, 2H), 2.01 (s, 3H) ppm. ^{31}P{^{1}H}-NMR (162 MHz, CDCl$_3$) δ_P: -13.6 ppm. ^{13}C{^{1}H}-NMR (101 MHz, CDCl$_3$) δ_C: 160.8 (d, J_{C-P} = 21.4 Hz), 139.2 (d, J_{C-P} = 17.1 Hz), 137.5 (d, J_{C-P} = 19.6 Hz), 136.5 (d, J_{C-P} = 9.4 Hz), 134.0 (d, J_{C-P} = 20.1 Hz), 133.4, 130.4, 128.9, 128.8, 128.6 (d, J_{C-P} = 7.3 Hz), 127.7 (d, J_{C-P} = 4.3 Hz), 60.7, 34.7, 15.8 ppm. Selected IR data: 1636 v(C=N) cm^{-1}.

5.1.1.15 Synthesis of **L15**

Adapted from literature procedure.[3]

Under an inert N_2 atmosphere, 2-(diphenylphosphino)benzaldehyde (1.02 g, 3.52 mmol) was refluxed with 3-(methylthio)propylamine (0.40 mL, 3.57 mmol) in methanol for 2 h. All volatiles were removed under high vacuum. The product was isolated as a red oil with no further purification. Yield: 1.32 g, 3.48 mmol, 99 %.

^{1}H-NMR (400 MHz, CDCl$_3$) δ_H: 8.86 (d, J = 4.7 Hz, 1H), 7.93 (ddd, J = 7.8 Hz, J = 3.9 Hz, J = 1.5 Hz, 1H), 7.38 (td, J = 7.5 Hz, J = 1.3 Hz, 1H), 7.35-7.22 (m, 11H), 6.86 (ddd, J = 7.7 Hz, J = 4.6 Hz, J = 1.3 Hz, 1H), 3.56 (td, J = 6.7 Hz, J = 1.4 Hz, 2H), 2.30 (t, J = 7.1 Hz, 2H), 2.01 (s, 3H), 1.78 (p, J = 6.6 Hz, 2H) ppm. ^{31}P{^{1}H}-NMR (162 MHz, CDCl$_3$) δ_P: -13.4 ppm. ^{13}C{^{1}H}-NMR (101 MHz, CDCl$_3$) δ_C: 160.2 (d, J_{C-P} = 20.1 Hz), 139.5 (d, J_{C-P} = 17.2 Hz), 137.4 (d, J_{C-P} = 19.7 Hz), 136.7 (d, J_{C-P} = 9.6 Hz), 134.0 (d, J_{C-P} = 20.0 Hz), 133.4, 130.2, 128.9, 128.8, 128.6 (d, J_{C-P} = 7.1 Hz), 127.9 (d, J_{C-P} = 4.3 Hz), 60.0, 31.7, 29.9, 15.4 ppm. Selected IR data: 1636 v(C=N) cm^{-1}. HRMS (ES+/Q-TOF) m/z: [M+H]$^+$ Calcd for C$_{23}$H$_{25}$NPS 378.1445; Found 378.1443.
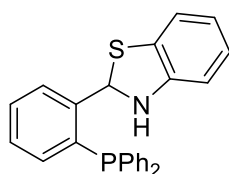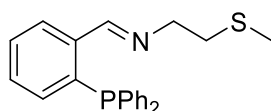
5.1.1.16 Synthesis of **L16**

Adapted from literature procedure.[3]

Under an inert N_2 atmosphere, 2-(diphenylphosphino)benzaldehyde (1.00 g, 3.46 mmol) was refluxed with 2-(methylthio)aniline (0.44 mL, 3.51 mmol) in toluene over 3 Å molecular sieves for 2 h. Once complete, as confirmed by ^{31}P{^{1}H} NMR, the crude mixture was filtered and all volatiles were removed under reduced pressure. The product was purified by recrystallisation from toluene and hexane, giving the product as a bright yellow solid with no further purification. Yield: 909 mg, 2.21 mmol, 64 %.

Analytical data in accordance with literature reports.[11]

^{1}H-NMR (400 MHz, CDCl$_3$) δ_H: 9.11 (d, J = 5.6 Hz, 1H), 8.39 (ddd, J = 7.8 Hz, J = 3.9 Hz, J = 1.4 Hz, 1H), 6.47 (t, J = 7.4 Hz, 1H), 7.39-7.29 (m, 11H), 7.17-7.14 (m, 2H), 7.05-7.00 (m, 1H), 6.93 (ddd, J = 7.7 Hz, J = 5.2 Hz, J = 1.4 Hz, 1H), 6.46 (m, 1H), 2.41 (s, 3H) ppm. ^{31}P{^{1}H}-NMR (162 MHz, CDCl$_3$) δ_P: -14.6 ppm. Selected IR data: 1616 v(C=N) cm^{-1}. HRMS (ES+/Q-TOF) m/z: [M+H]$^+$ Calcd for C$_{26}$H$_{23}$NPS 412.1289; Found 412.1295.

5.1.1.17   Synthesis of **L17**
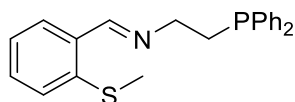
Adapted from literature procedure.[5]

Under an inert N_2 atmosphere, 2-(diphenylphosphino)ethylamine (742 mg, 3.24 mmol) was refluxed with 2-(methylthio)benzaldehyde (507 mg, 3.33 mmol) in methanol for 2 h. All volatiles were removed under high vacuum. The product was isolated as a white solid with no further purification. Yield: 1.05 g, 2.89 mmol, 89 %.

Analysis in accordance with literature reports.[5]

^{1}H-NMR (400 MHz, CDCl$_3$) δ_H: 8.71 (s, 1H), 7.77 (dd, J = 7.8 Hz, J = 1.6 Hz, 1H), 7.51-7.44 (m, 4H), 7.38-7.27 (m, 8H), 7.18 (td, J = 7.2 Hz, J = 1.5 Hz, 1H), 3.82-3.73 (m, 2H), 2.53-2.47 (m, 2H), 2.45 (s, 3H) ppm. ^{31}P{^{1}H}-NMR (162 MHz, CDCl$_3$) δ_P: -19.1 ppm. Selected IR data: 1627 v(C=N) cm^{-1}. HRMS (ES+/Q-TOF) m/z: [M+H]$^+$ Calcd for C$_{22}$H$_{23}$NPS 364.1289; Found 364.1287.

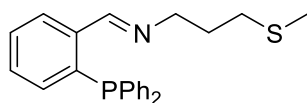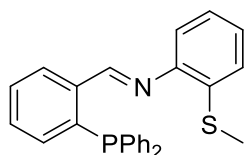### 5.1.1.18   Synthesis of **L18**
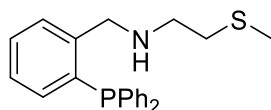
Adapted from literature procedure.[7]

Under an inert N_2 atmosphere, 2-(diphenylphosphino)benzaldehyde (1.99 g, 6.85 mmol) was refluxed with 2-(methylthio)ethylamine (0.70 mL, 7.48 mmol) in methanol for 2 h. Once complete, as confirmed by ^{31}P NMR, the mixture was stirred over NaBH$_4$ (400 mg, 10.6 mmol) at room temperature for 18 h. Unreacted NaBH$_4$ was quenched with addition of acetone (5 mL) and volatiles were removed under high vacuum. The resulting residue was dissolved in DCM, and washed once each with saturated NH$_4$Cl$_{(aq)}$ and DI H$_2$O under N$_2$ atmosphere. The organic phase was dried over MgSO$_4$, filtered, and solvent was removed under high vacuum, giving the product as a pale yellow oil with no further purification. Yield: 2.29 g, 6.26 mmol, 91 %.

^{1}H-NMR (400 MHz, CDCl$_3$) δ_H: 7.45 (dd, J = 7.8 Hz, J = 4.4 Hz, J = 1.4 Hz, 1H), 7.34-7.22 (m, 11H), 7.15 (td, J = 7.5 Hz, J = 1.4 Hz, 1H), 6.88 (ddd, J = 7.7 Hz, J = 4.5 Hz, J = 1.4 Hz, 1H), 3.99 (d, J = 1.7 Hz, 2H), 2.69 (t, J = 6.7 Hz, 2H), 2.44 (t, J = 6.7 Hz, 2H), 1.99 (s, 3H) ppm. ^{31}P{^{1}H}-NMR (162 MHz, CDCl$_3$) δ_P: -16.0 ppm. ^{13}C{^{1}H}-NMR (101 MHz, CDCl$_3$) δ_C: 144.4 (d, $J_{C\text{-}P}$ = 23.8 Hz), 136.8

(d, J_{C-P} = 10.0 Hz), 135.8 (d, J_{C-P} = 13.8 Hz), 133.9 (d, J_{C-P} = 19.9 Hz), 133.7, 129.1, 129.0, 128.8, 128.6 (d, J_{C-P} = 6.9 Hz), 127.3, 52.1 (d, J_{C-P} = 20.8 Hz), 47.3, 34.3, 15.3 ppm.

5.2.2 Synthesis of Ru(II) complexes

5.2.2.1 Synthesis of [RuCl$_2$(**L1**)PPh$_3$]
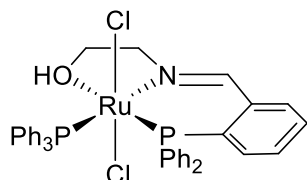
Under an inert N$_2$ atmosphere, RuCl$_2$(PPh$_3$)$_3$ (501 mg, 0.52 mmol) was refluxed with **L1** (238 mg, 0.71 mmol) in dry toluene for 16 h. The mixture was reduced to 50 % volume and the crude product precipitated with dry hexane. The product was recrystallised from DCM and hexane to give RuCl$_2$(**L1**)PPh$_3$ as a red solid. Yield: 229 mg, 0.30 mmol, 57 %.

Analysis in accordance with literature reports.[12]

^{1}H-NMR (400 MHz, CDCl$_3$) δ$_H$: 8.96 (d, J = 9.4 Hz, 1H), 7.56 (ddd, J = 7.8 Hz, J = 3.8 Hz, J = 1.4 Hz, 1H), 7.43 (tt, J = 7.4 Hz, J = 1.4 Hz, 1H), 7.37-6.97 (m, 27H), 4.38 (t, J = 5.3 Hz, 2H), 4.04 (q, J = 5.8 Hz, 2H), 3.09 (t, J = 6.2 Hz, 1H) ppm. ^{31}P{^{1}H}-NMR (162 MHz, CDCl$_3$) δ$_P$: 66.5 (d, J_{P-P} = 32.0 Hz), 34.5 (d, J_{P-P} = 32.0 Hz) ppm. Selected IR data: 3328 v(O-H), 1631 v(C=N) cm^{-1}. HRMS (ES+/Q-TOF) m/z: [M-Cl]$^+$ Calcd for C$_{39}$H$_{35}$NOP$_2$ClRu 732.0926; Found 732.0930. [M]$^+$ Calcd for C$_{39}$H$_{35}$NOP$_2$Cl$_2$Ru 767.0614; Found 767.0621.

5.2.2.2 Synthesis of [Ru(**L1**)$_2$]Cl$_2$
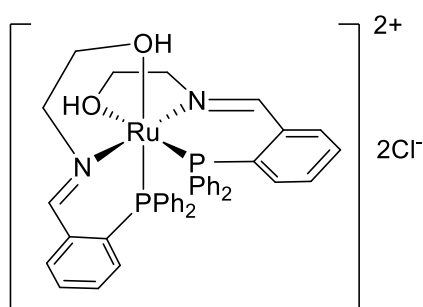
Under an inert N$_2$ atmosphere, [RuCl$_2$(p-cymene)]$_2$ (308 mg, 0.50 mmol) was refluxed with **L1** (802 mg, 2.40 mmol) in dry toluene for 16 h. The resulting precipitate was isolated by filtration and washed with toluene, giving [Ru(**L1**)$_2$]Cl$_2$ as a bright yellow solid. Yield: 557 mg, 0.66 mmol, 66 %.

^{1}H-NMR (400 MHz, CDCl$_3$) δ$_H$: 9.28 (s, 2H), 7.77 (m, 2H), 7.62 (t, *J* = 7.7 Hz, 2H), 7.45 (t, *J* = 7.5 Hz, 2H), 7.38-7.09 (m, 18H), 6.89 (t, *J* = 7.6 Hz, 2H), 6.75 (m, 2H), 4.28 (m, 2H), 4.12 (m, 2H), 3.43 (m, 2H), 3.31 (m, 2H) ppm. ^{31}P{^{1}H}-NMR (162 MHz, CDCl$_3$) δ$_P$: 61.2 ppm. Selected IR data: 1618 *v*(C=N) cm^{-1}. HRMS (ES+/Q-TOF) m/z: [M-Cl]$^+$ Calcd for C$_{42}$H$_{40}$N$_2$O$_2$P$_2$ClRu 803.1297; Found 803.1311. [M-2Cl]$^{2+}$ Calcd for C$_{42}$H$_{40}$N$_2$O$_2$P$_2$Ru 384.0804; Found 384.0832.

5.2.2.3 Synthesis of [Ru(**L2**)$_2$]Cl$_2$
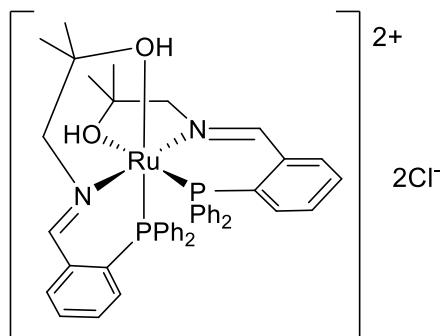
Under an inert N$_2$ atmosphere, [RuCl$_2$(*p*-cymene)]$_2$ (303 mg, 0.49 mmol) was refluxed with **L2** (805 mg, 2.23 mmol) in dry toluene for 16 h. The resulting precipitate was isolated by filtration and washed with toluene, giving [Ru(**L2**)$_2$]Cl$_2$ as a bright yellow solid. Yield: 436 mg, 0.49 mmol, 49 %.

^{1}H-NMR (400 MHz, CDCl$_3$) δ$_H$: 9.18 (s, 2H), 9.04 (br s, 2H), 7.71-6.80 (m, 22H), 4.78 (d, *J* = 13.4 Hz, 2H), 3.68 (d, *J* = 13.9 Hz, 2H), 1.83 (s, 6H), 1.25 (s, 6H) ppm. ^{31}P{^{1}H}-NMR (162 MHz, CDCl$_3$) δ$_P$: 58.9 ppm. Selected IR data: 1616 *v*(C=N) cm^{-1}. HRMS (ES+/Q-TOF) m/z: [M-2H]$^+$ Calcd for C$_{46}$H$_{46}$N$_2$O$_2$P$_2$Cl$_2$Ru 892.1455; Found 892.1458. [M-2Cl]$^{2+}$ Calcd for C$_{46}$H$_{48}$N$_2$O$_2$P$_2$Cl$_2$Ru 412.1172; Found 412.1187.

5.2.2.4 Synthesis of [Ru(**L3**)$_2$]Cl$_2$
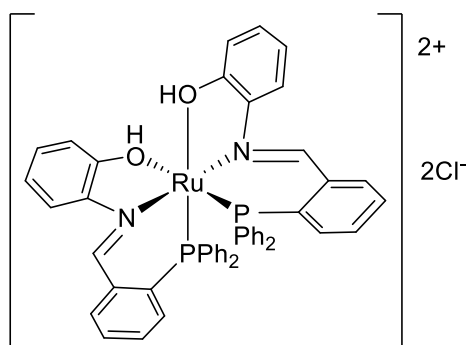
Under an inert N$_2$ atmosphere, [RuCl$_2$(*p*-cymene)]$_2$ (357 mg, 0.58 mmol) was refluxed with **L3** (1.06 g, 2.79 mmol) in dry toluene for 16 h. The resulting precipitate was isolated by filtration and washed with toluene, giving [Ru(**L3**)$_2$]Cl$_2$ as a dark brown solid. Yield: 901 mg, 0.96 mmol, 83 %.

^{1}H-NMR (400 MHz, DMSO-d6) δ$_H$: 9.60 (s, 2H), 8.19 (d, J = 7.9 Hz, 2H), 7.99 (d, J = 8.7 Hz, 2H), 7.75 (t, J = 7.5 Hz, 2H), 7.48 (t, J = 7.5 Hz, 2H), 7.28-6.99 (m, 8H), 7.04 (t, J = 7.3 Hz, 2H) 6.90 (t, J = 7.8 Hz, 4H) 6.86 (t, J = 7.0 Hz, 2H), 6.80-6.71 (m, 8H), 6.59 (t, J = 7.8 Hz, 2H), 6.25 (d, J = 8.3 Hz, 2H). ^{31}P{^{1}H}-NMR (162 MHz, DMSO-d6) δ$_P$: 58.7 ppm. Selected IR data: 1616 v(C=N) cm^{-1}.

5.2.2.5   Synthesis of [RuCl$_2$(**L4**)$_2$]
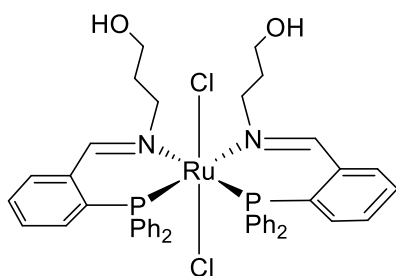
Under an inert N$_2$ atmosphere, [RuCl$_2$(p-cymene)]$_2$ (399 mg, 0.65 mmol) was refluxed with **L4** (1.08 g, 3.10 mmol) in dry toluene for 16 h. The resulting precipitate was isolated by filtration and washed with toluene, giving RuCl$_2$(**L4**)$_2$ as a dark red solid. The product was a mixture of the two species RuCl$_2$(**L4**)$_2$-a and RuCl$_2$(**L4**)$_2$-b in a molar ratio of 2:1. Yield: 783 mg, 0.90 mmol, 84 %.

RuCl$_2$(**L4**)$_2$-a: ^{1}H-NMR (400 MHz, CDCl$_3$) δ$_H$: 8.27 (s, 2H), 7.55-7.14 (m, 24H), 7.05 (t, J = 8.6 Hz, 2H), 6.91 (m, 2H), 4.23 (m, 2H), 2.91 (m, 2H), 2.79 (m, 2H), 2.67 (m, 2H) 1.45 (m, 2H), 1.15 (m, 2H) ppm. ^{31}P{^{1}H}-NMR (162 MHz, CDCl$_3$) δ$_P$: 30.8 ppm. ^{13}C{^{1}H}-NMR (101 MHz, CDCl$_3$) δ$_C$: 170.6, 139.5-127.2 (aromatic carbons), 58.7, 58.1, 35.3. RuCl$_2$(**L4**)$_2$-b: ^{1}H-NMR (400 MHz, CDCl$_3$) δ$_H$: 8.80 (d, J = 5.0 Hz, 2H), 7.55-7.14 (m, 22H), 6.82 (m, 4H), 6.58 (t, J = 7.8 Hz, 2H), 4.44 (m, 2H), 3.85 (m, 2H), 3.04 (m, 2H), 2.74 (m, 2H), 1.69 (m, 2H), 1.50 (m, 2H) ppm. ^{31}P{^{1}H}-NMR (162 MHz, CDCl$_3$) δ$_P$: 47.8 ppm. ^{13}C{^{1}H}-NMR (101 MHz, CDCl$_3$) δ$_C$: 171.4, 139.5-127.2 (aromatic carbons), 66.8, 57.9, 35.6 ppm. Selected IR data: 1616 v(C=N) cm^{-1}. LRMS (ES+/Q-TOF) m/z: [M]$^+$ Calcd for C$_{44}$H$_{44}$N$_2$O$_2$P$_2$Cl$_2$Ru 866.13; Found 866.13. [M-Cl]$^+$ Calcd for C$_{44}$H$_{44}$N$_2$O$_2$P$_2$ClRu 831.16; Found 831.16.

5.2.2.6   Synthesis of [RuCl$_2$(**L6**)$_2$]
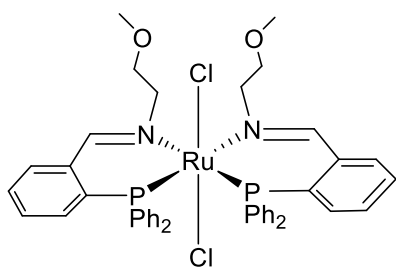
Under an inert N$_2$ atmosphere, [RuCl$_2$(p-cymene)]$_2$ (401 mg, 0.65 mmol) was refluxed with **L6** (1.08 g, 3.11 mmol) in dry toluene for 16 h. The resulting precipitate was isolated by filtration and washed with toluene, giving RuCl$_2$(**L6**)$_2$ as a red-orange solid. Yield: 654 mg, 0.75 mmol, 58 %.

^{1}H-NMR (400 MHz, CDCl$_3$) δ$_H$: 8.83 (d, J = 6.6 Hz, 2H), 7.55 (d, J = 5.5 Hz, 2H), 7.46-7.37 (m, 8H), 7.29-7.13 (m, 14H), 7.04 (t, J = 6.8 Hz, 2H), 6.57 (t, J = 7.8 Hz, 2H), 4.35 (d, J = 11.9 Hz, 2H), 3.81 (t, J = 10.8 Hz, 2H), 3.27 (d, J = 10.6 Hz, 2H), 2.94 (t, J = 10.5 Hz, 2H), 2.80 (s, 6H) ppm. ^{31}P{^{1}H}-NMR (162 MHz, CDCl$_3$) δ$_P$: 49.2 ppm. ^{13}C{^{1}H}-NMR (101 MHz, CDCl$_3$) δ$_C$: 172.5, 138.3-125.3 (aromatic carbons), 73.1, 63.5, 58.3 ppm. Selected IR data: 1616 v(C=N) cm^{-1}. HRMS (ES+/Q-TOF) m/z: [M]$^+$ Calcd for C$_{44}$H$_{44}$N$_2$O$_2$P$_2$Cl$_2$Ru 866.1299; Found 866.1320. [M-Cl]$^+$ Calcd for C$_{44}$H$_{44}$N$_2$O$_2$P$_2$ClRu 831.1610; Found 831.1621.

5.2.2.7 Synthesis of [RuCl$_2$(**L7**)$_2$]
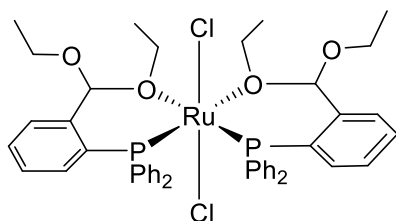
Under an inert N$_2$ atmosphere, [RuCl$_2$(p-cymene)]$_2$ (301 mg, 0.49 mmol) was refluxed with **L7** (750 mg, 2.06 mmol) in dry toluene for 16 h. The resulting precipitate was isolated by filtration and washed with toluene, giving RuCl$_2$(**L7**)$_2$ as a red solid. Yield: 338 mg, 0.38 mmol, 38 %.

^{1}H-NMR (400 MHz, CDCl$_3$) δ$_H$: 7.84 (d, J = 7.2 Hz, 2H), 7.40 (m, 2H), 7.30-7.16 (m, 14H), 7.04 (s, 2H), 7.01 (m, 10H), 4.53-3.63 (br m, 8H), 1.67-0.79 (br m, 12H) ppm. ^{31}P{^{1}H}-NMR (162 MHz, CDCl$_3$) δ$_P$: 46.7 ppm. Selected IR data: 1090s, 1146s, 1210 v(C-O) cm^{-1}. HRMS (ES+/Q-TOF) m/z: [M]$^+$ Calcd for C$_{46}$H$_{50}$O$_4$P$_2$Cl$_2$Ru 900.1605; Found 900.1611. [M-Cl]$^+$ Calcd for C$_{46}$H$_{50}$O$_4$P$_2$ClRu 865.1916; Found 865.1926.

5.2.2.8 Synthesis of [Ru(CO)$_2$Cl$_2$(PPh$_3$)$_2$]
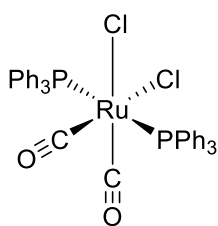
Under an inert N$_2$ atmosphere, [RuCl$_2$(p-cymene)]$_2$ (298 mg, 0.49 mmol) was refluxed with 2-(diphenylphosphino)benzaldehyde (601 mg, 2.07 mmol) in dry toluene for 16 h. The resulting

dark brown solution was reduced to 50 % volume and the product was precipitated with dry hexane. The product was isolated by filtration and washed with dry hexane, giving [Ru(CO)$_2$Cl$_2$(PPh$_3$)$_2$] as a beige solid. Yield: 399 mg, 0.53 mmol, 54 %.

^{1}H-NMR (400 MHz, CDCl$_3$) δ$_H$: 7.98-7.89 (m, 12H), 7.42-7.35 (m, 18H) ppm. ^{31}P{^{1}H}-NMR (162 MHz, CDCl$_3$) δ$_P$: 17.0 ppm. Selected IR data: 2061, 1998 v(C≡O) cm^{-1}. LRMS (ES+/Q-TOF) m/z: [M+Na]+ Calcd for C$_{38}$H$_{30}$Cl$_2$NaO$_2$P$_2$Ru 775.00; Found 775.00.

5.2.2.9 Synthesis of [Ru(CO)Cl$_2$(L7*)PPh$_3$]
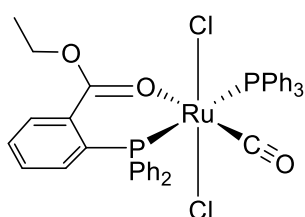
Under an inert N$_2$ atmosphere, [RuCl$_2$(p-cymene)]$_2$ (302 mg, 0.49 mmol) was refluxed with 2-(diphenylphosphino)benzaldehyde (602 mg, 2.07 mmol) in dry ethanol for 16 h. The resulting precipitate was isolated by filtration and washed with dry ethanol, giving [Ru(CO)Cl$_2$(L7*)PPh$_3$] as a yellow solid. Yield: 89 mg, 0.11 mmol, 11 %.

^{1}H-NMR (400 MHz, CDCl$_3$) δ$_H$: 8.07 (dd, J = 7.7 Hz, J = 3.2 Hz, 1H), 7.80 (m, 6H), 7.55-7.29 (m, 20H), 7.20-7.15 (m, 1H), 6.96 (tt, J = 7.7 Hz, J = 2.0 Hz, 1H), 3.44 (q, J = 7.2 Hz, 2H), 1.00 (t, J = 7.2, 3H) ppm. ^{31}P{^{1}H}-NMR (162 MHz, CDCl$_3$) δ$_P$: 34.1 (d, J = 356.4 Hz), 31.5 (d, J = 356.4 Hz) ppm. Selected IR data: 1938 v(C≡O), 1646 v(C=O) cm^{-1}. LRMS (ES+/Q-TOF) m/z: [M+Na]$^+$ Calcd for C$_{40}$H$_{34}$Cl$_2$NaO$_3$P$_2$Ru 819.03; Found 819.03. [M-Cl]$^+$ Calcd for C$_{40}$H$_{34}$ClO$_3$P$_2$Ru 761.07; Found 761.07.

5.2.2.10 Synthesis of [RuCl(L9)$_2$]Cl
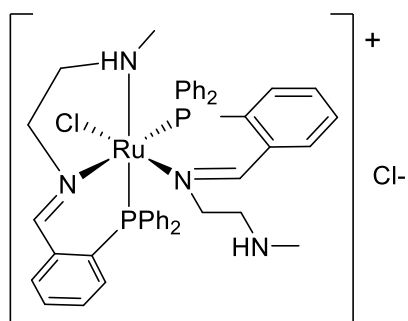
Under an inert N$_2$ atmosphere, [RuCl$_2$(p-cymene)]$_2$ (299 mg, 0.49 mmol) was refluxed with L9 (750 mg, 2.16 mmol) in dry toluene for 16 h. The resulting dark brown crude mixture was filtered

by cannula and washed with dry toluene. The filtrate was returned to reflux for a further 16 h. The resulting precipitate was isolated by filtration and washed with dry hexane, giving [RuCl(**L9**)$_2$]Cl as a yellow-orange solid. Yield: 173 mg, 0.20 mmol, 20 %.

^{1}H-NMR (400 MHz, CDCl$_3$) δ_H: 9.18 (d, J = 9.0 Hz, 1H), 8.79 (s, 1H), 8.35 (m, 1H), 7.83 (m, 1H), 7.67-7.44 (m, 6H), 7.42-7.08 (m, 10H), 7.04-7.82 (m, 8H), 6.08 (t, J = 8.0 Hz, 2H), 4.16 (d, J = 12.5 Hz, 1H), 3.97 (t, J = 11.8 Hz, 1H), 3.69-3.53 (m, 2H), 3.25 (t, J = 11.0 Hz, 1H), 2.67 (t, J = 12.9 Hz, 1H), 2.51 (s, 3H), 2.32 (m, 3H), 2.21 (d, J = 12.5 Hz, 1H), 1.69 (d, J = 17.6 Hz, 1H) ppm. ^{31}P{^{1}H}-NMR (162 MHz, CDCl$_3$) δ_P: 50.8 (d, J = 31.1 Hz), 35.7 (d, J = 31.1 Hz) ppm. ^{13}C{^{1}H}-NMR (101 MHz, CDCl$_3$) δ_C: 169.7, 169.3, 136.7-124.3 (aromatic carbons), 67.2, 60.4, 50.9, 44.4, 38.1, 32.4 ppm. Selected IR data: 1633 v(C=N) cm^{-1}. HRMS (ES+/Q-TOF) m/z: [M-Cl]$^+$ Calcd for C$_{44}$H$_{46}$N$_4$P$_2$ClRu 829.1930; Found 829.1939.

5.2.2.11 Synthesis of [RuCl(**L10**)(PPh$_3$^{CO})]
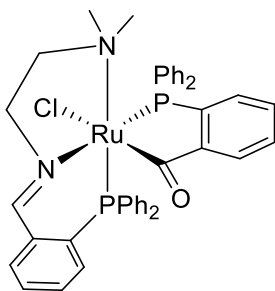
Under an inert N$_2$ atmosphere, [RuCl$_2$(p-cymene)]$_2$ (301 mg, 0.49 mmol) was refluxed with **L10** (1.10 g mg, 3.06 mmol, not pre-dried) in dry toluene for 16 h. The crude mixture was filtered, the resulting dark red filtrate was reduced to 50 % volume and the product was precipitated with dry hexane. The product was isolated by filtration and washed with dry hexane, giving RuCl(**L10**)(PPh$_3$^{CO}) as an orange-brown solid. Yield: 121 mg, 0.15 mmol, 15 %.

^{1}H-NMR (400 MHz, CDCl$_3$) δ_H: 8.80 (d, J = 7.9 Hz, 1H), 7.88 (m, 3H), 7.69-6.95 (m, 16H), 6.92 (t, J = 8.4 Hz, 2H), 6.86 (t, J = 7.5 Hz, 1H), 6.50 (m, 4H), 6.14 (t, J = 8.8 Hz, 2H), 4.61 (t, J = 11.1 Hz, 1H), 4.03 (d, J = 12.5 Hz, 1H), 2.60 (t, J = 11.3 Hz, 1H), 2.26 (d, J = 12.1 Hz, 1H), 1.84 (s, 3H), 1.70 (s, 3H) ppm. ^{31}P{^{1}H}-NMR (162 MHz, CDCl$_3$) δ_P: 59.3 (d, J = 35.1 Hz), 57.8 (d, J = 35.1 Hz) ppm. Selected IR data: 1625 v(C=N), 1541 v(C=O) cm^{-1}. HRMS (ES+/Q-TOF) m/z: [M-Cl]$^+$ Calcd for C$_{42}$H$_{39}$N$_2$OP$_2$Ru 751.1581; Found 751.1602.

5.2.2.12   Synthesis of [RuCl₂(**L10**)₂]
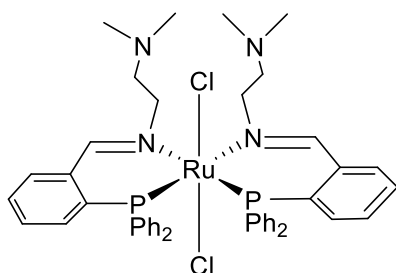
Under an inert N_2 atmosphere, [RuCl₂(*p*-cymene)]₂ (301 mg, 0.49 mmol) was refluxed with **L10** (1.03 g mg, 2.86 mmol, dried over Na_2SO_4) in dry toluene for 16 h. The resulting dark red solution was reduced to 50 % volume and the product was precipitated with dry hexane. The product was isolated by filtration and washed with dry hexane, giving RuCl₂(**L10**)₂ as a dark red solid. Yield: 204 mg, 0.23 mmol, 23 %.

^{1}H-NMR (400 MHz, CDCl₃) δ_H: 8.71 (s, 2H), 8.04 (m, 2H), 7.71 (m, 2H), 7.65-6.90 (m, 10H), 6.80 (m, 4H), 6.71 (m, 4H), 6.52 (m, 4H), 6.16 (m, 2H), 4.46 (m, 2H), 3.67 (m, 4H), 2.95 (m, 2H), 1.76 (s, 12H) ppm. ^{31}P{^{1}H}-NMR (162 MHz, CDCl₃) δ_P: 48.8 ppm. Selected IR data: 1617 v(C=N) cm⁻¹. HRMS (ES+/Q-TOF) m/z: [M+H]⁺ Calcd for $C_{46}H_{51}N_4P_2Cl_2Ru$ 893.2009; Found 893.2040. [M-Cl]⁺ Calcd for $C_{46}H_{50}N_4P_2ClRu$ 857.2243; Found 857.2269.

5.2.2.13   Synthesis of [RuCl₂(**L11**)]
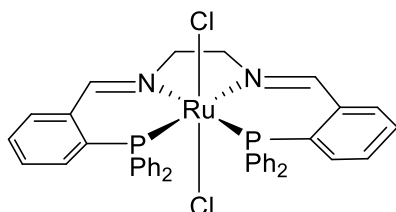
Prepared according to modified literature procedure.

Under an inert N_2 atmosphere, [RuCl₂(PPh₃)₃] (217 mg, 0.23 mmol) was refluxed with **L11** (151 mg, 0.25 mmol) in dry toluene for 3 h. The resulting precipitate was isolated by filtration and washed with dry Et₂O, giving [RuCl₂(**L11**)] as a red solid. Yield: 85 mg, 0.11 mmol, 48 %.

^{1}H-NMR (400 MHz, CDCl₃) δ_H: 9.00 (m, 2H), 7.59 (d, *J* = 7.6 Hz, 2H), 7.44 (t, *J* = 7.5 Hz, 2H), 7.32 (t, *J* = 7.6 Hz, 2H), 7.24 (t, *J* = 7.4 Hz, 4H), 7.20-7.10 (m, 4H), 7.01 (t, *J* = 7.2 Hz, 8H), 6.97-6.91 (m, 6H), 4.35 (s, 4H). ^{31}P{^{1}H}-NMR (162 MHz, CDCl₃) δ_P: 47.5 ppm. Selected IR data: 1634 v(C=N) cm⁻¹. HRMS (ES+/Q-TOF) m/z: [M]⁺ Calcd for $C_{40}H_{34}N_2P_2Cl_2Ru$ 776.0618; Found 776.0624. [M-Cl]⁺ Calcd for $C_{40}H_{34}N_2P_2ClRu$ 741.0929; Found 741.0939.

5.2.2.14   Synthesis of [RuCl(**L12**)(*p*-cymene)]Cl
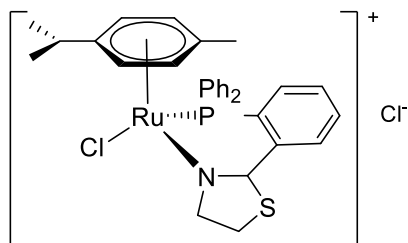
Under an inert N₂ atmosphere, **L12** (461 mg, 1.32 mmol) was added to a solution of [RuCl₂(*p*-cymene)]₂ (200 mg, 0.33 mmol) in dry toluene at room temperature and stirred for 2 h. The resulting precipitate was isolated by filtration and washed with dry toluene, giving [RuCl(**L12**)(*p*-cymene)] as a red-brown solid. Yield: 291 mg, 0.47 mmol, 72 %.

^{1}H-NMR (400 MHz, CDCl₃) δ$_H$: 7.82-7.10 (m, 14H), 6.31 (br d, 1H), 6.28 (br d, 1H), 5.63 (br d, 1H), 5.32 (br d, 1H), 4.78 (s, 1H), 3.83 (m, H), 3.71 (m, 1H), 3.55 (m, 1H), 3.13 (m, 1H), 2.74 (m, 1H), 1.94 (s, 3H), 1.25 (s, 3H), 1.19 (s, 3H) ppm. ^{31}P{^{1}H}-NMR (162 MHz, CDCl₃) δ$_P$: 36.2 ppm. LRMS (ES+/Q-TOF) m/z: [M-Cl]$^+$ Calcd for C₃₁H₃₄NPClRuS 620.09; Found 620.08.

5.2.2.15   Synthesis of [RuCl(**L12**)₂]Cl
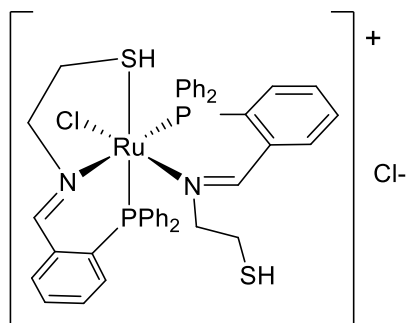
Under an inert N₂ atmosphere, hot solution of **L12** (699 mg, 2.00 mmol) in toluene was added to a solution of [RuCl₂(*p*-cymene)]₂ (251 mg, 0.41 mmol) in dry toluene at 110 °C and stirred at reflux for 20 h. The resulting precipitate was isolated by filtration and washed with dry toluene, giving [RuCl(**L12**)₂]Cl as a yellow-brown solid as a mixture of isomers. Yield: 291 mg, 0.47 mmol, 72 %.

NMR data attributed to major isomer [RuCl₂(**L12**)₂]-B:

^{1}H-NMR (400 MHz, CDCl₃) δ$_H$: 8.78 (s, 1H), 8.76 (s, 1H), 7.67-7.04 (m, H), 6.73 (m, 2H), 4.15-3.88 (m, 3H), 3.84-3.70 (m, 1H), 3.63-3.50 (m, 1H), 3.49-3.39 (m, 1H), 3.21-3.09 (m, 1H), 2.75-2.63 (m, 1H) ppm. ^{31}P{^{1}H}-NMR (162 MHz, CDCl₃) δ$_P$: 50.0 (d, J = 34.0 Hz), 24.2 (d, J = 34.0 Hz) ppm. Selected IR data: 1620 *v*(C=N) cm^{-1}. HRMS (ES+/Q-TOF) m/z: [M-Cl]$^+$ Calcd for C₄₂H₄₀N₂P₂S₂ClRu 835.08; Found 835.08.

5.2.2.16   Synthesis of [RuCl(**L14**)₂]Cl
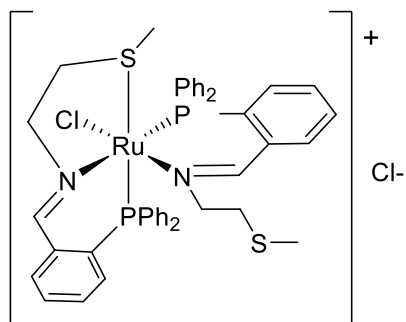
Under an inert N₂ atmosphere, [RuCl₂(*p*-cymene)]₂ (350 mg, 0.57 mmol) was refluxed with **L14** (0.99 g, 2.72 mmol) in dry toluene for 16 h. The resulting precipitate was isolated by filtration and washed with toluene, giving [RuCl(**L14**)₂]Cl as a bright yellow solid. Yield: 999 mg, 1.11 mmol, 97 %.

^{1}H-NMR (400 MHz, CDCl₃) δ_H: 9.15 (d, J = 8.5 Hz, 1H), 9.11 (d, J = 8.8 Hz, 1H), 8.38-8.27 (m, 1H), 8.00 (m, 1H), 7.93 (t, J = 8.2 Hz, 2H), 7.78 (m, 2H), 7.64 (t, J = 8.0 Hz, 1H), 7.51 (t, J = 7.5 Hz, 2H), 7.47-6.87 (m, 14H), 6.74 (t, J = 7.9 Hz, 1H), 6.50 (t, J = 8.8 Hz, 1H), 6.39 (t, J = 9.4 Hz, 1H), 5.91 (t, 7.0 Hz, 2H), 4.76-4.51 (m, 3H), 4.38 (m, 2H), 3.36 (m, 1H), 2.99 (m, 1H), 2.46 (m, 1H), 2.24 (s, 3H), 2.05 (s, 3H) ppm. ^{31}P{^{1}H}-NMR (162 MHz, CDCl₃) δ_P: 44.4 (d, J = 29.2 Hz), 41.4 (d, J = 29.2 Hz) ppm. Selected IR data: 1623 v(C=N) cm^{-1}. HRMS (ES+/Q-TOF) m/z: [M-Cl]$^+$ Calcd for C₄₄H₄₄N₂P₂S₂ClRu 863.1153; Found 863.1160.

5.2.2.17   Synthesis of [RuCl₂(**L15**)₂]
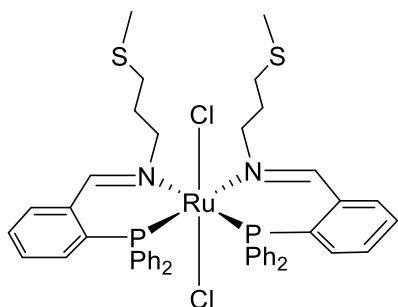
Under an inert N₂ atmosphere, [RuCl₂(*p*-cymene)]₂ (251 mg, 0.41 mmol) was refluxed with **L15** (713 mg, 1.89 mmol) in dry toluene for 16 h. The resulting dark red crude mixture was filtered by cannula, reduced to 50 % volume and the product precipitated with dry pentane. The product [RuCl₂(**L15**)₂] was isolated by filtration as a red-brown solid. Yield: 248 mg, 0.27 mmol, 33 %.

^{1}H-NMR (400 MHz, CDCl$_3$) δ_H: 8.75 (d, J = 5.8 Hz, 2H), 7.51 (m, 2H), 7.44-7.35 (m, 8H), 7.27-7.20 (m, 14H), 7.05 (t, J = 5.5 Hz, 2H), 6.59 (t, J = 7.9 Hz, 2H), 4.15 (td, J = 8.9 Hz, J = 4.8 Hz, 2H), 3.83 (q, J = 9.0 Hz, 2H), 2.25-2.11 (m, 4H), 1.84 (s, 6H), 1.85-1.74 (m, 2H), 1.37-1.27 (m, 2H). ^{31}P{^{1}H}-NMR (162 MHz, CDCl$_3$) δ_P: 48.7 ppm. Selected IR data: 1612 v(C=N) cm^{-1}. HRMS (ES+/Q-TOF) m/z: [M]$^+$ Calcd for C$_{46}$H$_{48}$N$_2$P$_2$S$_2$Cl$_2$Ru 926.1155; Found 926.1177. [M-Cl]$^+$ Calcd for C$_{46}$H$_{48}$N$_2$P$_2$S$_2$ClRu 891.1466; Found 891.1486.

5.2.2.18   Synthesis of [RuCl$_2$(**L17**)$_2$]
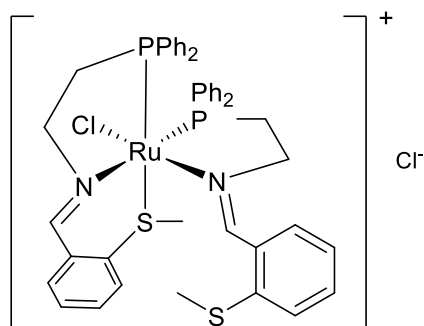
Under an inert N$_2$ atmosphere, [RuCl$_2$(*p*-cymene)]$_2$ (294 mg, 0.48 mmol) was refluxed with **L17** (749 mg, 2.06 mmol) in dry toluene for 16 h. The resulting dark red crude mixture was filtered by cannula and the resultant precipitate washed with dry toluene, giving [RuCl$_2$(**L17**)$_2$]-A as a dark red solid. The filtrate was reduced to 50 % volume and the product [RuCl$_2$(**L17**)$_2$]-B precipitated with dry hexane and isolated by filtration as a red solid.

[RuCl$_2$(**L17**)$_2$]-A: Yield: 145 mg, 0.16 mmol, 17 %. ^{1}H-NMR (400 MHz, CDCl$_3$) δ_H: 9.68 (s, 1H), 8.77 (s, 1H), 8.31-8.13 (m, 2H), 8.06-7.94 (m, 4H), 7.53-6.71 (m, 20H), 6.66 (t, J = 6.8 Hz, 2H), 5.37-5.18 (m, 1H), 4.83-4.40 (m, 3H), 4.40-4.13 (m, 3H), 3.75-3.46 (m, 1H), 3.15 (s, 3H), 2.36 (d, J = 1.8 Hz, 3H) ppm. ^{31}P{^{1}H}-NMR (162 MHz, CDCl$_3$) δ_P: 38.0 (d, J = 24.3 ppm), 33.7 (d, J = 24.3 ppm) ppm. Selected IR data: 1584 v(C=N) cm^{-1}. HRMS (ES+/Q-TOF) m/z: [M-Cl]$^+$ Calcd for C$_{44}$H$_{44}$N$_2$P$_2$S$_2$ClRu 863.1153; Found 863.1163.

[RuCl$_2$(**L17**)$_2$]-B: Yield: 346 mg, 0.39 mmol, 40 %. ^{1}H-NMR (400 MHz, CDCl$_3$) δ_H: 8.76 (d, J = 8.7 Hz, 1H), 8.25 (s, 1H), 6.76-6.69 (m, 6H), 7.48-7.09 (m, 20H), 6.94-6.83 (m, 2H), 4.53-4.41 (m, 2H), 3.13-3.03 (m, 2H), 2.66-2.54 (m, 4H), 2.39 (s, 3H), 2.05 (d, J = 2.4 Hz, 3H) ppm. ^{31}P{^{1}H}-NMR (162 MHz, CDCl$_3$) δ_P: 44.6 (d, J = 34.0 Hz), 30.0 (d, J = 34.0 Hz) ppm. Selected IR data: 1584 v(C=N) cm^{-1}. HRMS (ES+/Q-TOF) m/z: [M]$^+$ Calcd for C$_{44}$H$_{44}$N$_2$P$_2$S$_2$Cl$_2$Ru 899.0920; Found 899.0919. [M-Cl]$^+$ Calcd for C$_{44}$H$_{44}$N$_2$P$_2$S$_2$ClRu 863.1153; Found 863.1157.

5.2.2.19   Synthesis of [RuCl$_2$(**L18**)$_2$]
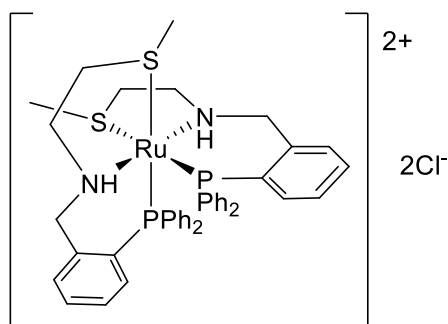
Under an inert N$_2$ atmosphere, [RuCl$_2$(*p*-cymene)]$_2$ (301 mg, 0.49 mmol) was refluxed with **L18** (922 mg, 2.52 mmol) in dry toluene for 16 h. The resulting precipitate was isolated by filtration and washed with toluene, giving [RuCl$_2$(**L18**)$_2$] as a yellow solid. Yield: 263 mg, 0.29 mmol, 30 %.

^{31}P{^{1}H}-NMR (162 MHz, Toluene) δ_P: 48.9 ppm. HRMS (ES+/Q-TOF) m/z: [M+H]$^+$ Calcd for C$_{44}$H$_{49}$N$_2$P$_2$S$_2$Cl$_2$Ru 903.1233; Found 903.1245

5.3 Chapter 3 Experimental

5.3.1   General Catalytic Procedure and Considerations

Catalytic reactions were performed in 100 mL Parr stainless steel autoclave reactors equipped with a PTFE sleeve and stirrer bar. Reactions were performed under N_2 atmosphere. The assembled reactor was placed in a pre-heated aluminium heat block and stirred at 500 rpm. Reactions were timed from when the reactor was added to the heat block.

Methanol and ethanol were obtained as extra dry methanol (99.9 %) and extra dry ethanol (99.5 %) from Acros Organics, transferred to storage under an inert atmosphere, over 3 Å molecular sieves and degassed by N_2 sparge prior to use. Sodium ethoxide and sodium methoxide were obtained from Alfa Aesar and stored in a glovebox. Sodium hydroxide pellets were crushed into a fine powder and dried under vacuum overnight before use. $RuCl_2(dppm)_2$ was prepared by Dr Richard Wingad.

Catalytic results were analysed using GC-FID on an Agilent 7820A GC equipped with a carbowax capillary column 30 m x 0.32 mm, I.D. 0.25 μm. Nitrogen carrier gas was used with the following method: starting oven temp 60 °C, hold at 60 °C for 5 min, heat to 220 °C at 30 °Cmin^{-1}, hold at 220 °C for 5 min. Details of sample preparation are given in section 5.3.4.1.

Ethanol conversion refers to the total conversion of ethanol to liquid products, as determined by GC analysis. Molar equivalence (mol%) is given relative to ethanol.

5.3.2   General procedure for Guerbet upgrading of ethanol to *n*-butanol

Under an N_2 atmosphere, a 100 mL Parr reactor was charged with catalyst (0.1 mol%), sodium ethoxide (583 mg, 8.6 mmol, 5 mol%), ethanol (10.0 mL, 171.3 mmol, 1.0 equiv.). The reactor was then sealed and transferred to a pre-heated heating block and heated at 150 °C for 20 h. After the reaction time was complete, the reactor was cooled in a water/ice bath and residual pressure was carefully vented. For post-reaction analysis, see section 5.3.4. Specific experimental details are given in Table 5.2.

5.3.3 General procedure for Guerbet upgrading of ethanol to isobutanol

Under an N_2 atmosphere, a 100 mL Parr reactor was charged with catalyst (0.1 mol%), sodium methoxide (1.851 g, 34.16 mmol, 200 mol%), ethanol (1.0 mL, 17.13 mmol, 1.0 equiv.) and methanol (10.0 mL, 247.13 mmol, 14.4 equiv.). The reactor was then sealed and transferred to a pre-heated heating block and heated at 180 °C for 20 h. After the reaction time was complete, the reactor was cooled in a water/ice bath and residual pressure was carefully vented. For post-reaction analysis, see section 05.3.4. Specific experimental details are given in Table 5.1.

Table 5.1 – Summary of results in the Guerbet coupling of methanol and ethanol to give isobutanol.

Catalyst (0.1 mol%)
Base (50-200 mol%)
180 °C

Catalyst	Base (mol%)	Temperature /°C	Time /h	Ethanol conversion[a] /%	Yield[b] (Selectivity[c]) / %			
					Isobutanol	1-propanol	2-methylbutan-1-ol	1-butanol
[RuCl₂(dppm)₂]	NaOMe (200)	180	20	100.0	58.5 (100.0)	-	-	-
[RuCl₂(dppm)₂]	NaOMe (200)	180	2	97.6	53.7 (98.3)	0.9 (1.7)	-	-
[RuCl₂(**L1**)PPh₃]	NaOMe (200)	180	20	95.8	36.4 (97.0)	-	2.3 (3.0)	-
[Ru(**L1**)₂]Cl₂	NaOMe (200)	180	20	91.5	42.5 (92.3)	1.8 (3.8)	3.6 (3.9)	-
[Ru(**L1**)₂]Cl₂	NaOMe (150)	180	20	85.2	32.2 (89.8)	2.0 (5.6)	3.3 (4.6)	-
[Ru(**L1**)₂]Cl₂	NaOMe (100)	180	20	43.8	10.4 (68.9)	4.0 (26.1)	1.5 (5.0)	-
[Ru(**L1**)₂]Cl₂	NaOMe (50)	180	20	39.5	12.5 (69.3)	3.4 (18.8)	3.9 (10.9)	-
[Ru(**L1**)₂]Cl₂	NaOH (200)	180	20	55.0	22.5 (76.5)	6.2 (21.1)	1.4 (2.4)	-
[Ru(**L2**)₂]Cl₂	NaOMe (200)	180	20	83.1	37.8 (86.4)	2.7 (6.2)	6.4 (7.4)	-
[Ru(**L3**)₂]Cl₂	NaOMe (200)	180	20	90.3	37.9 (91.1)	2.2 (5.2)	3.1 (3.7)	-
[RuCl₂(**L4**)₂]	NaOMe (200)	180	20	96.7	64.2 (93.8)	1.1 (1.6)	6.2 (4.6)	-

[RuCl₂(**L4**)₂]	NaOMe (150)	180	20	85.9	58.1 (87.4)	4.5 (6.8)	7.8 (5.8)	-
[RuCl₂(**L4**)₂]	NaOMe (100)	180	20	66.5	33.5 (72.5)	8.2 (17.7)	7.4 (8.1)	1.6 (1.7)
[RuCl₂(**L4**)₂]	NaOMe (50)	180	20	47.4	15.3 (55.8)	8.3 (30.2)	5.2 (9.6)	2.4 (4.4)
[RuCl₂(**L4**)₂]	NaOH (200)	180	20	66.8	30.4 (76.8)	8.3 (20.9)	1.8 (2.3)	-
[RuCl₂(**L6**)₂]	NaOMe (200)	180	20	95.7	50.7 (96.0)	0.8 (1.6)	2.5 (2.4)	-
[RuCl₂(**L6**)₂]	NaOMe (150)	180	20	90.6	52.6 (94.4)	1.5 (2.7)	3.3 (2.9)	-
[RuCl₂(**L6**)₂]	NaOMe (100)	180	20	76.9	41.9 (87.9)	3.8 (7.9)	4.0 (4.2)	-
[RuCl₂(**L6**)₂]	NaOMe (50)	180	20	28.6	3.8 (51.5)	2.8 (38.0)	0.9 (6.2)	0.6 (4.3)
[RuCl₂(**L6**)₂]	NaOH (200)	180	20	55.3	21.8 (80.6)	4.8 (17.6)	1.0 (1.8)	-
[RuCl₂(**L7**)₂]	NaOMe (200)	180	20	85.8	17.1 (90.4)	1.2 (6.4)	1.3 (3.4)	-
[Ru(CO)₂Cl₂(PPh₃)₂]	NaOMe (200)	180	20	85.9	31.9 (94.2)	1.5 (4.4)	0.9 (1.4)	
[RuCl(**L9**)₂]Cl	NaOMe (200)	180	20	94.8	36.4 (88.3)	1.2 (2.9)	7.3 (8.8)	
[RuCl₂(**L12**)₂]	NaOMe (200)	180	20	94.4	42.2 (95.1)	1.0 (2.2)	2.4 (2.7)	
[RuCl(**L12**)(*p*-cymene)]	NaOMe (200)	180	20	100.0	51.0 (98.8)	-	1.2 (1.2)	
[RuCl(**L14**)₂]Cl	NaOMe (200)	180	20	100.0	70.1 (98.1)	-	2.7 (1.9)	
[RuCl(**L14**)₂]Cl	NaOMe (150)	180	20	95.2	66.1 (95.3)	1.6 (2.3)	3.3 (2.4)	
[RuCl(**L14**)₂]Cl	NaOMe (100)	180	20	75.4	44.2 (83.4)	6.9 (13.0)	3.8 (3.6)	
[RuCl(**L14**)₂]Cl	NaOMe (50)	180	20	44.0	14.1 (55.5)	8.3 (32.6)	1.9 (3.8)	4.1 (8.1)
[RuCl(**L14**)₂]Cl	NaOMe (200)	180	6	100.0	66.0 (97.7)	-	3.1 (2.3)	-
[RuCl(**L14**)₂]Cl	NaOMe (200)	180	4	97.3	58.8 (96.4)	0.9 (1.5)	2.5 (2.1)	-
[RuCl(**L14**)₂]Cl	NaOMe (200)	180	2	91.3	50.2 (93.0)	2.3 (4.2)	3.0 (2.8)	-

[RuCl(**L14**)$_2$]Cl	NaOMe (200)	180	1	80.8	35.3 (84.3)	4.9 (11.7)	3.3 (4.0)	-
[RuCl(**L14**)$_2$]Cl	NaOH (200)	180	20	86.4	56.6 (95.4)	2.2 (3.7)	1.1 (0.9)	-
[RuCl$_2$(**L15**)$_2$]	NaOMe (200)	180	20	99.1	55.8 (98.8)	-	1.4 (1.2)	-
[RuCl$_2$(**L17**)$_2$]-A	NaOMe (200)	180	20	100.0	38.0 (99.2)	-	0.6 (0.8)	-
[RuCl$_2$(**L17**)$_2$]-B	NaOMe (200)	180	20	100.0	35.2 (100.0)	-	-	-
[RuCl$_2$(**L18**)$_2$]	NaOMe (200)	180	20	97.6	55.3 (96.7)	0.6 (1.0)	2.7 (2.3)	-

[a]Total ethanol conversion as determined by GC-FID. [b]Yield as determined by GC-FID. [c]Selectivity with respect to other liquid products.

Table 5.2 – Summary of results in the Guerbet ethanol coupling to n-butanol

Catalyst (0.1 mol%)
NaOEt (5 mol%)

2 ethanol (OH) → n-butanol (OH)

150 °C, 20 h

Catalyst	Base / mol%	Ethanol conversion[a] / %	Yield[b] (Selectivity[c]) / %						
			1-butanol	Ethyl acetate	2-butanol	2-ethyl butanol	1-hexanol	2-ethyl hexanol	1-octanol
[RuCl$_2$(dppm)$_2$]	NaOEt (5)	53.6	23.8 (79.9)	-	-	2.1 (4.7)	5.5 (12.2)	1.0 (1.6)	1.0 (1.6)
[Ru(CO)$_2$Cl$_2$(PPh$_3$)$_2$]	NaOEt (5)	38.8	13.9 (73.2)	0.4 (2.2)	-	2.0 (6.9)	3.7 (12.9)	1.0 (2.7)	0.8 (2.1)
[RuCl$_2$(**L1**)PPh$_3$]	NaOEt (5)	16.2	8.3 (83.5)	0.4 (4.4)	0.1 (1.1)	0.4 (2.7)	1.1 (7.0)	0.1 (0.7)	0.1 (0.6)
[Ru(**L1**)$_2$]Cl$_2$	NaOEt (5)	21.5	4.3 (73.9)	0.9 (15.3)	-	0.2 (2.8)	0.6 (6.6)	0.1 (0.9)	0.1 (0.5)
[Ru(**L2**)$_2$]Cl$_2$	NaOEt (5)	13.1	6.3 (73.7)	0.9 (10.1)	-	0.5 (3.8)	1.2 (9.6)	0.3 (1.7)	0.2 (1.1)
[Ru(**L3**)$_2$]Cl$_2$	NaOEt (5)	28.0	8.9 (83.6)	0.3 (2.6)	-	0.6 (3.7)	1.3 (8.2)	0.3 (1.3)	0.1 (0.6)
[RuCl$_2$(**L4**)$_2$]	NaOEt (5)	25.9	5.1 (67.6)	1.9 (25.1)	0.2 (2.9)	0.1 (1.3)	0.3 (3.0)	<0.1 (0.1)	-
[RuCl$_2$(**L6**)$_2$]	NaOEt (5)	25.2	6.8 (82.9)	0.8 (9.2)	-	0.3 (2.1)	0.6 (5.3)	0.1 (0.3)	<0.1 (0.2)
[RuCl$_2$(**L7**)$_2$]	NaOEt (5)	38.5	10.9 (76.1)	0.5 (3.5)	-	1.2 (5.4)	2.4 (11.4)	0.6 (2.0)	0.5 (1.6)
[RuCl(**L14**)$_2$]Cl	NaOEt (5)	26.8	6.9 (75.9)	1.0 (11.0)	0.7 (7.4)	0.2 (1.4)	0.4 (2.7)	0.1 (0.3)	0.2 (1.3)

[a]Total ethanol conversion as determined by GC-FID. [b]Yield as determined by GC-FID. [c]Selectivity with respect to other liquid products.

5.3.4   Post-Reaction Analysis

5.3.4.1   Liquid Product Analysis:

A portion of post-reaction crude mixture was neutralised by filtration through a 1 cm plug of acidic alumina and analysed by GC-FID (100 µL sample, 10 µL hexadecane standard, 1.6 mL Et_2O). Each liquid product was calibrated against hexadecane which was used as the standard. The calibration curve was obtained by plotting the ratios of the peak area $A_{sample}/A_{hexadecane}$ against the known concentration of sample, giving a best fit of $R^2 > 0.99$. The identity of the major products was also confirmed by ^1H and $^{13}C\{^1H\}$ NMR spectroscopy and GC-MS.
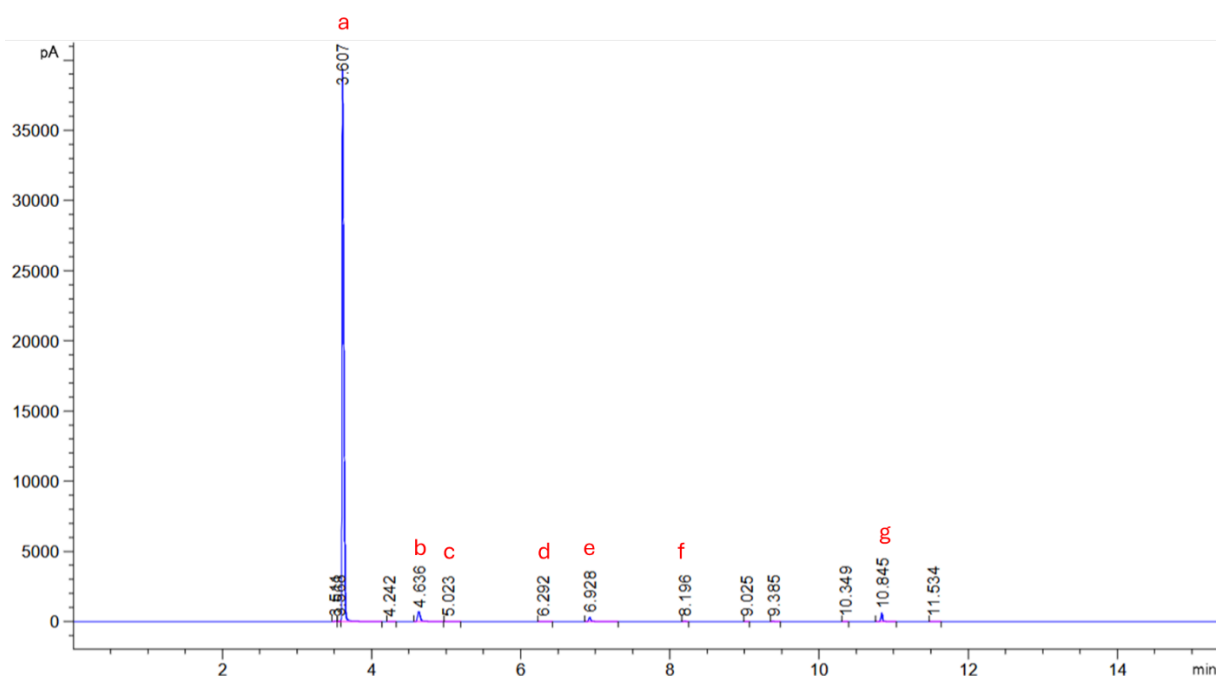
*Figure 5.1 - Example of an ethanol/methanol upgrading GC chromatogram. Conditions: methanol (10 mL, 247.13 mmol), ethanol (1 mL, 17.13 mmol), [RuCl$_2$(**L4**)$_2$] (0.1 mol%), NaOMe (200 mol%), 180 °C, 20 h. a = Diethyl ether (solvent), b = methanol, c = ethanol, d = 1-propanol, e = isobutanol, f = 2-methyl-1-butanol, g = hexadecane (standard).*
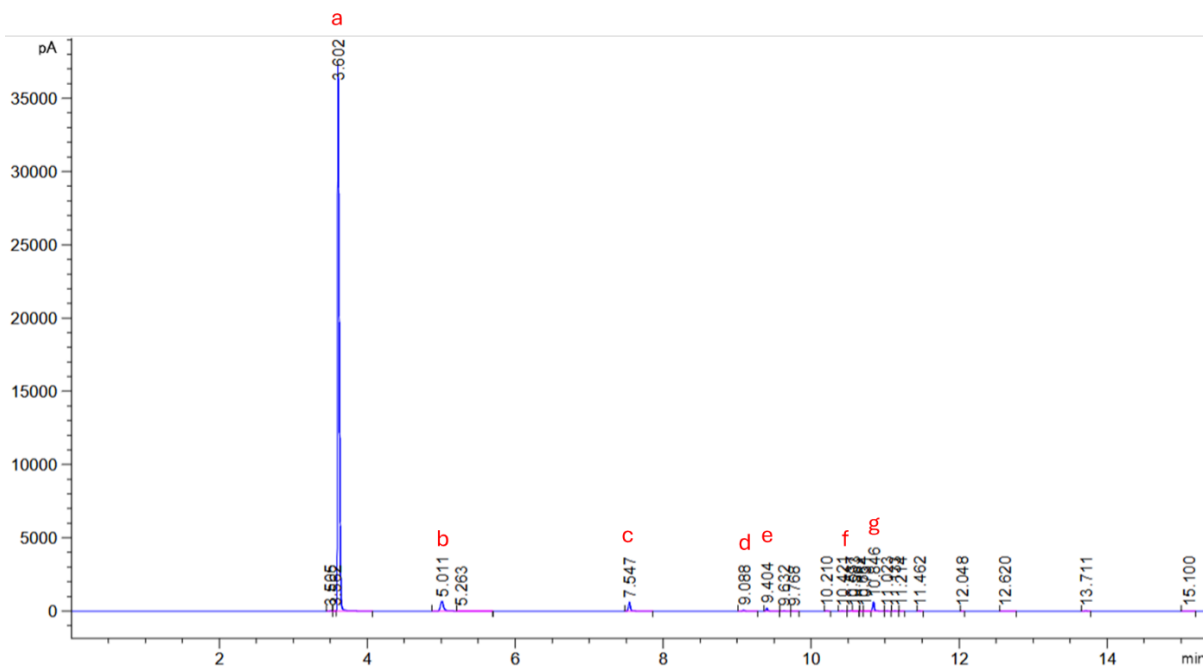
Figure 5.2 - Example of an ethanol upgrading GC chromatogram. Conditions: ethanol (10 mL, 171.3 mmol), [RuCl$_2$(dppm)$_2$] (0.1 mol%), NaOEt (10 mol%), 120 °C, 4 h. a = Diethyl ether (solvent), b = ethanol, c = n-butanol, d = 2-ethyl butanol, e = 1-hexanol, f = 2-ethyl hexanol, g = hexadecane (standard).

5.3.4.2   Solid Product Analysis:

The combined solid and liquid products from the PTFE sleeve were transferred directly into a round bottom flask and all volatiles were removed under reduced pressure. The solid was dried under vacuum for 16 h. The solid was stirred in toluene (30 mL) for 1 h at room temperature in air, then isolated by filtration and washed with toluene until washings ran clear. The solid was dried under vacuum for a further 6 h. The solid was analysed by ^{1}H NMR spectroscopy using a known amount of solid (approx. 20 mg) and DMSO as internal standard (20 mg) in D$_2$O. ^{1}H NMR spectroscopy, ^{13}C{^{1}H} NMR spectroscopy and ATR-FTIR spectroscopy were used to identify non-protonated solid residues.

Solid produced in the ethanol/methanol coupling catalysed by [RuCl(**L14**)$_2$]Cl:

^{1}H-NMR (400 MHz, CDCl$_3$) δ$_H$: 8.45 (s, HCOO$^-$), 1.91 (s, AcO$^-$, trace) ppm. ^{13}C{^{1}H}-NMR (101 MHz, CDCl$_3$) δ$_C$: 171.1 (HCOO$^-$), 168.2 (CO$_3{}^{2-}$), 22.9 (AcO$^-$, trace) ppm.

Solid produced in the ethanol homocoupling catalysed by [RuCl(**L14**)$_2$]Cl:

^{1}H-NMR (400 MHz, CDCl$_3$) δ$_H$: 1.91 (s, AcO$^-$) ppm. ^{13}C{^{1}H}-NMR (101 MHz, CDCl$_3$) δ$_C$: 181.4 (AcO$^-$), 23.3 (AcO$^-$) ppm.

5.3.5　NMR Experiments

Reactions were performed on [RuCl(**L14**)$_2$]Cl and [RuCl$_2$(**L18**)$_2$]. General procedures for reaction with methanol-d4 and sodium methoxide in methanol-d4 are below.

5.3.5.1　Reaction of Ru(II) complex in methanol-d4 general procedure

In a glovebox, a Youngs NMR tube was charged with ruthenium catalyst (approx. 13.5 mg, 15 µmol, 1.0 equiv.). Freshly dried and degassed methanol-d4 (1.0 mL) was added on a Schlenk line at room temperature. Initial ^{1}H and ^{31}P{^{1}H} NMR spectroscopy was performed. The NMR tube was then transferred to a 50 °C heat block for 16 h. ^{1}H and ^{31}P{^{1}H} NMR spectroscopy was performed again after heating was complete.

5.3.5.2　Reaction of Ru(II) complex with sodium methoxide in methanol-d4 general procedure

In a glovebox, a Youngs NMR tube was charged with ruthenium catalyst (approx. 13.5 mg, 15 µmol, 1.0 equiv.) and sodium methoxide (16.2 mg, 300 µmol, 20.0 equiv.). Freshly dried and degassed methanol-d4 (1.0 mL) was added on a Schlenk line at room temperature. Initial ^{1}H and ^{31}P{^{1}H} NMR spectroscopy was performed. The NMR tube was then transferred to a 50 °C heat block for 16 h. ^{1}H and ^{31}P{^{1}H} NMR spectroscopy was performed again after heating was complete.

5.4 Chapter 4 Experimental

Benzylamine and *tert*-butylamine were purified by distillation and stored under N_2 prior to use. 6-methyl-2,2'-bipyridine and 2,6-lutidine were degassed by freeze-pump-thaw and stored under N_2 with no further purification before use. Ruthenium precursor [RuCl$_2$(PPh$_3$)$_3$] was prepared according to literature procedures[1,2]. PtBu$_2$-BH$_3$ was prepared according to literature procedure[13]. All other reagents were purchased from commercial sources and used without further purification.

5.4.1   Catalyst Synthesis

5.4.1.1   Preparation of **L19**
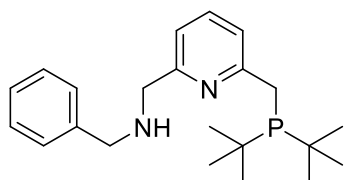
Adapted from literature procedures[13,14].

Under an inert N_2 atmosphere, n-butyllithium (3.60 mL, 2.60 M in hexane, 9.36 mmol) was added at -78 °C to a solution of PtBu$_2$-BH$_3$ (1.48 g, 9.29 mmol) in dry THF over 30 min. The mixture was stirred and allowed to warm to room temperature overnight. The resultant yellow solution was added by cannula to a solution of 2,6-bis(chloromethyl)pyridine (1.31 g, 7.44 mmol) in dry THF held at -78 °C. The mixture was stirred and allowed to warm to room temperature overnight. Volatiles were removed under reduced pressure and the crude product was purified by column chromatography   (silica,   DCM   eluent)   in   air   to   give 2-(chloromethyl)-6-(di-*tert*-butylphosphinomethyl)pyridine-BH$_3$ as   a   white   solid.   The intermediate product was stirred with benzylamine (8 mL, 73.2 mmol) under an inert N_2 atmosphere at 100 °C for 16 h. Excess benzylamine was removed under high vacuum at 60 °C. The resultant crude solid was extracted with dry hexane and filtered through celite. Volatiles were removed under vacuum to give the product as a viscous yellow oil. Yield: 0.78 g, 2.17 mmol, 29 %.

Analytical data in accordance with literature reports[14].

^{1}H-NMR (400 MHz, CDCl$_3$) δ$_H$: 7.53 (t, *J* = 7.6 Hz, 1H), 7.38-7.17 (m, 6H), 7.06 (d, *J* = 7.6 Hz, 1H), 3.87 (bd, 2H), 3.81 (bd, 2H), 3.06 (d, *J*$_{P-H}$ = 3.4 Hz, 2H), 1.16 (d, *J*$_{P-H}$ = 11.0 Hz, 18H) ppm. ^{31}P{^{1}H}-NMR (162 MHz, CDCl$_3$) δ$_P$: 36.3 ppm.

5.4.1.2 Preparation of **L20**
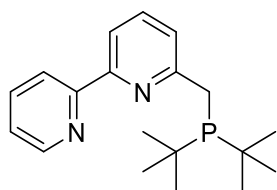
Adapted from literature procedure[15].

Under an inert N_2 atmosphere, lithium diisoproylamide (6.4 mL, 1.3 M in THF/hexanes, 8.32 mmol) was added at -78 °C to a solution of 6-methyl-2,2'-bipyridine (1.10 mL, 7.04 mmol) in dry Et_2O over 30 min and stirred for 45 min. Di-*tert*-butylchlorophosphine (1.2 mL, 6.32 mmol) in dry Et_2O was added dropwise. The mixture was stirred and allowed to warm to room temperature overnight, giving a very dark green solution. Excess LDA was quenched with degassed H_2O. The aqueous phase was extracted with 3 x 10 mL Et_2O. The organic phase was dried over Na_2SO_4 and filtered. Volatiles were removed under high vacuum to give the crude product as a yellow solid, which was purified by recrystallisation from cold dry MeOH to give the product as an off-white solid. Yield: 932 mg, 2.96, 47 %.

Analytical data in accordance with literature reports[15].

^{1}H-NMR (400 MHz, CDCl$_3$) δ$_H$: 8.66 (ddd, J = 4.8 Hz, J = 1.8 Hz, J = 0.9 Hz, 1H), 8.43 (dt, J = 8.0 Hz, J = 1.1 Hz, 1H), 8.16 (dt, J = 7.8 Hz, J = 1.0, Hz 1H), 7.79 (td, J = 7.5 Hz, J = 1.8 Hz, 1H), 7.70 (t, J = 7.7 Hz, 1H), 7.42 (dt, J = 7.7 Hz, J = 1.1 Hz 1H), 7.28 (ddd, J = 7.4 Hz, J = 4.8 Hz, J = 1.2 Hz, 1H), 3.15 (d, J = 3.3 Hz, 2H), 1.19 (d, J = 11.0 Hz, 18H) ppm. ^{31}P{^{1}H}-NMR (162 MHz, CDCl$_3$) δ$_P$: 37.2 ppm.

5.4.1.3 Preparation of **L21**
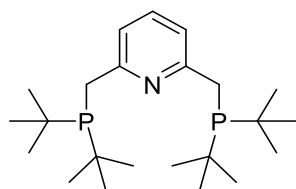
Prepared according to literature procedure[16].

Under an inert N_2 atmosphere, n-butyllithium (3.00 mL, 2.33 M in hexane, 6.99 mmol) was added at -78 °C to a solution of 2,6-lutidine (0.4 mL, 3.45 mmol) in dry Et_2O over 30 min. The mixture was stirred and allowed to warm to room temperature overnight. The resultant maroon solution was cooled to -78 °C and di-*tert*-butylchlorophosphine (1.35 mL, 7.11 mmol) in dry Et_2O was added

dropwise. The mixture was stirred and allowed to warm to room temperature overnight, giving a maroon solution. Excess n-butyllithium was quenched with 10 mL dry MeOH and volatiles were removed under reduced pressure. The crude solid was redissolved in dry Et_2O and filtered. The filtrate was reduced to dryness and the crude product was purified by recrystallisation from cold Et_2O giving the product as a white crystalline solid. Yield: 651 mg, 1.64, 48 %.

Analytical data in accordance with literature reports[16].

^{1}H-NMR (400 MHz, $CDCl_3$) δ_H: 7.44 (t, J = 7.7 Hz, 1H), 7.22 (d, J = 7.8 Hz, 2H), 2.99 (d, J = 3.5 Hz, 4H), 1.11 (d, J = 11.0 Hz, 36H) ppm. ^{31}P{^{1}H}-NMR (162 MHz, $CDCl_3$) δ_P: 35.8 ppm.

5.4.1.4   Preparation of **L22**
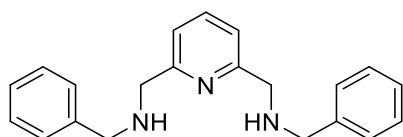
Under an inert N_2 atmosphere, benzylamine (0.66 mL, 6.04 mmol) was added to a solution of 2,6-pyridinedicarboxaldehyde (406 mg, 3.00 mmol) in dry methanol and stirred over Na_2SO_4 for 72 h. The mixture was then stirred over excess $NaBH_4$ (1.03 g, 27.2 mmol) for 3 h. The mixture was reduced to dryness to give a brown slurry. This slurry was dissolved in 15 mL 2.5 M HCl in air, then treated with 10 % NaOH solution until strongly basic. The aqueous solution was extracted with DCM, the organic phases combined, washed with DI H_2O, and dried over $MgSO_4$. The mixture was filtered and reduced to dryness to give L22 as a brown liquid which was stored under N_2. Yield: 643 mg, 2.02 mmol, 67 %.

^{1}H-NMR (400 MHz, $CDCl_3$) δ_H: 7.60 (t, J = 7.6 Hz, 1H), 7.39-7.29 (m, 8H), 7.25 (tt, J = 5.5 Hz, J = 1.6 Hz, 2H), 7.18 (d, J = 7.7 Hz, 2H), 3.92 (s, 4H), 3.85 (s, 4H), 2.14 (s, 2H) ppm. ^{13}C{^{1}H}-NMR (101 MHz, $CDCl_3$) δ_C: 159.3, 140.3, 136.8, 128.4, 128.3, 127.0, 120.5, 54.5, 53.6 ppm. HRMS (ES+/Q-TOF) m/z: [M+H]+ Calcd for $C_{21}H_{24}N_3$ 318.1970; Found 318.1965.

5.4.1.5   Preparation of [Ru(CO)Cl(H)(**L19**)]
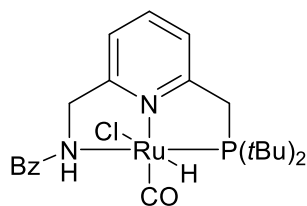
Prepared according to literature procedure[14].

Under an inert N_2 atmosphere, **L19** (150 mg, 0.42 mmol) was stirred with a suspension of [RuCO(Cl)H(PPh$_3$)$_3$] (227 mg, 0.24 mmol) in THF at 65 °C for 4 h. The mixture was reduced to 50 % volume and the crude product precipitated with dry hexane. The product was isolated by filtration as a yellow-orange solid and purified by recrystallisation from THF and dry Et$_2$O. Yield: 23 mg, 0.04 mmol, 18 %.

Analytical data in accordance with literature reports[14].

^{1}H-NMR (400 MHz, CDCl$_3$) δ_H: 7.81 (m, 1H), 7.48-7.18 (m, 6H), 7.00 (m, 1H), 4.80 (m, 2H), 4.16 (m, 1H), 4.09 (dd, J_{P-H} = 13.9 Hz, J_{H-H} = 11.2 Hz, 1H), 3.96 (dd, J_{P-H} = 15.9 Hz, J_{H-H} = 10.9 Hz, 1H), 3.78-3.66 (m, 2H), 1.47 (d, J_{P-H} = 13.6 Hz, 9H), 1.18 (d, J_{P-H} = 13.0 Hz, 9H), -15.41 (d, J_{P-H} = 23.7 Hz, 1H) ppm. ^{31}P{^{1}H}-NMR (162 MHz, CDCl$_3$) δ_P: 107.4 ppm. HRMS (ES+/Q-TOF) m/z: [M-Cl]+ Calcd for C$_{23}$H$_{34}$N$_2$OPRu 487.1452; Found 487.1451.

5.4.1.6   Preparation of [Ru(CO)Cl(H)(**L20**)]
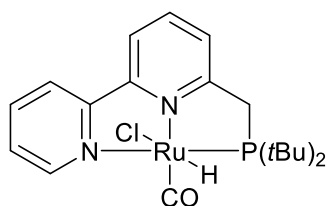
Adapted from literature procedure[15].

Under an inert N_2 atmosphere, **L20** (161 mg, 0.51 mmol) was stirred with a suspension of [RuCO(Cl)H(PPh$_3$)$_3$] (480 mg, 0.50 mmol) in THF at 65 °C for 4 h. The mixture was reduced to 50 % volume and the crude product precipitated with dry hexane. The product was isolated by filtration as an orange solid. Yield: 162 mg, 0.34 mmol, 67 %.

Analytical data in accordance with literature reports[15].

^{1}H-NMR (400 MHz, CDCl$_3$) δ_H: 9.20 (m, 1H), 7.95 (d, J = 7.9 Hz, 1H), 7.86 (d, J = 8.0 Hz, 1H), 7.80 (q, J = 7.7 Hz, 2H), 7.51 (d, J = 7.7 Hz, 1H), 7.39 (t, J = 6.5 Hz, 1H), 3.82-3.52 (m, 2H), 1.50 (d, J = 13.7 Hz, 9H), 1.24 (d, J = 13.1 Hz, 9H), -15.6 (d, J = 20.6 Hz, 1H) ppm. ^{31}P{^{1}H}-NMR (162 MHz, CDCl$_3$) δ_P: 103.8 ppm. HRMS (ES+/Q-TOF) m/z: [M-Cl]+ Calcd for C$_{20}$H$_{28}$N$_2$OPRu 445.0983; Found 445.0989. [M-H]+ Calcd for C$_{20}$H$_{27}$N$_2$OPClRu 479.0593; Found 479.0599.

5.4.1.7 Preparation of [Ru(CO)Cl(H)(**L21**)]
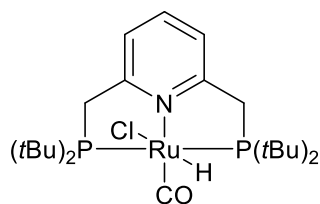
Prepared according to literature procedure[16].

Under an inert N_2 atmosphere, **L21** (213 mg, 0.54 mmol) was stirred with a suspension of [RuCO(Cl)H(PPh_3)_3] (461 mg, 0.48 mmol) in THF at 65 °C for 16 h. The mixture was reduced to 50 % volume and the crude product precipitated with dry hexane. The product was isolated by filtration as a yellow solid. Yield: 103 mg, 0.18 mmol, 38 %.

Analytical data in accordance with literature reports[17].

^{1}H-NMR (400 MHz, CDCl_3) δ_H: 7.47 (t, J = 7.6 Hz, 1H), 7.17 (d, J = 7.8 Hz, 2H), 3.93 (dt, J = 16.1 Hz, J = 3.4 Hz, 2H), 3.35 (dt, J = 16.1 Hz, J = 3.7 Hz, 2H), 1.48 (t, J = 6.7 Hz, 18H), 1.24 (t, J = 6.4 Hz, 18H), -14.42 (d, J = 20.7 Hz, 1H) ppm. ^{31}P{^{1}H}-NMR (162 MHz, CDCl_3) δ_P: 87.3 ppm. HRMS (ES+/Q-TOF) m/z: [M-Cl]+ Calcd for $C_{24}H_{44}NOP_2Ru$ 526.1942; Found 526.1948. [M-H]+ Calcd for $C_{24}H_{43}NOP_2ClRu$ 560.1552; Found 560.1556.

5.4.1.8 Preparation of [RuCl_2(**L22**)PPh_3]
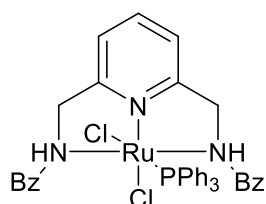
Under an inert N_2 atmosphere, **L22** (161 mg, 0.51 mmol) was refluxed with [RuCl_2(PPh_3)_3] (477 mg, 0.50 mmol) in dry toluene for 16 h. The solution was reduced to 30 % volume and the resultant precipitate was isolated by filtration as a yellow-brown solid, washed with dry Et_2O, as a mixture of two isomers of [RuCl_2(**L22**)PPh_3] in a ratio of 2:1. Yield: 260 mg, 0.35 mmol, 69 %.

Major isomer: ^{1}H-NMR (400 MHz, CDCl_3) δ_H: 7.86 (m, 6H), 7.47-7.12 (m, 22H), 6.87 (m, 2H), 4.01 (m, 4H), 3.74 (m, 4H) ppm. ^{31}P{^{1}H}-NMR (162 MHz, CDCl_3) δ_P: 50.7 ppm. Minor isomer: ^{1}H-NMR (400 MHz, CDCl_3) δ_H: 7.82 (m, 6H), 7.47-7.12 (m, 23H), 6.76 (m, 1H), 4.14 (m, 4H), 3.49 (m, 4H) ppm. ^{31}P{^{1}H}-NMR (162 MHz, CDCl_3) δ_P: 61.4 ppm. HRMS (ES+/Q-TOF) m/z: [M]+ Calcd for

C$_{39}$H$_{38}$N$_3$PCl$_2$Ru 751.1224; Found 751.1248. [M-Cl]+ Calcd for C$_{39}$H$_{38}$N$_3$PClRu 716.1535; Found 716.1530.

5.4.2   General Catalytic Procedure and Considerations

Catalytic reactions were performed in 100 mL or 60 mL Parr stainless steel autoclave reactors equipped with a PTFE sleeve and stirrer bar. Reactions were prepared under N$_2$ atmosphere and performed under H$_2$ atmosphere. Dry components were added in the glovebox. The sealed reactor was connected to a Schlenk line and high-pressure tubing, and the entire system was evacuated and refilled with atmospheric nitrogen three times. Liquid components were added under reverse flow of nitrogen. The reactor was charged with high pressure nitrogen and vented carefully (3 x 3 bar N$_2$), then charged with high pressure hydrogen and vented (3 x 3 bar H$_2$) to place the system under hydrogen atmosphere. The reactor was charged to the desired pressure with H$_2$ gas and sealed. The assembled reactor was placed in a pre-heated aluminium heat block and stirred at 600 rpm. Reactions were timed from when the reactor was added to the heat block.

1,4-Dioxane was obtained as extra dry 1,4-dioxane (99.5 %) stabilised with BHT from Acros Organics, transferred to storage under an inert atmosphere over 3 Å molecular sieves and degassed by N$_2$ sparge prior to use. Potassium *tert*-butoxide was obtained from Alfa Aesar and stored in a glovebox.

0.5 M stock solution of methyl 4-fluorobenzoate was prepared by degassing of 7.0 mL of methyl 4-fluorobenzoate by freeze-pump-thaw and subsequent dilution with 100.0 mL dry and degassed 1,4-dioxane. Concentration was confirmed by quantitative ^{1}H NMR spectroscopy against mesitylene internal standard.

Separate PTFE sleeves were used in Parr reactors for catalytic runs using different metals to prevent cross-contamination.

Molar equivalence (mol%) is given relative to substrate.

5.4.3   General procedure for direct hydrogenation of methyl 4-fluorobenzoate

Under an N$_2$ atmosphere, a 100 mL Parr reactor was charged with catalyst (0.5 mol%), potassium *tert*-butoxide (22.4 mg, 20 mmol, 20 mol%), and 2.0 mL 0.5 M methyl 4-fluorobenzoate solution in 1,4-dioxane (1.0 mmol). The reactor was flushed and carefully vented three times with 3 bar

N$_2$, then three times with 3 bar H$_2$. The reactor was charged with 50 bar H$_2$. The reactor was then sealed and transferred to a pre-heated heating block and heated at 115 °C for 20 h. After the reaction time was complete, the reactor was cooled in a water/ice bath and residual pressure was carefully vented.

5.4.3.1 Post-reaction analysis

Mesitylene standard (50 μL, 364 μmol) was added directly to the crude post-reaction mixture in air. An aliquot (~100 μL) was taken up in CDCl$_3$ and analysed by ^{19}F-NMR spectroscopy for conversion. Quantitative results were obtained by quantitative ^{1}H-NMR spectroscopy.

Table 5.3 - Summary of results in the direct hydrogenation of methyl 4-fluorobenzoate.

Catalyst (mol%)	Base (mol%)	Run time / h	H$_2$ pressure / bar	Methyl 4-fluorobenzoate recovery[a]	Yield[a] (selectivity) / %				
					4-fluorobenzyl alcohol	Other products	A -107 ppm	B[b] -113.6 ppm	C -114 ppm
[RuCO(Cl)H(**L20**)] (1)	tBuOK (2.5)	20	30	86	14 (100)	-			
*[RuCO(Cl)H(**L20**)] (1)	tBuOK (2.5)	20	50	77	23 (100)	-			
[RuCO(Cl)H(**L20**)] (1)	tBuOK (2.5)	20	50	68	32 (100)	-			
[RuCO(Cl)H(**L20**)] (1)	tBuOK (2.5)	6	50	99	1 (100)	-			
[RuCO(Cl)H(**L20**)] (1)	tBuOK (40)	2	50	0	100 (100)	-			
-	tBuOK (20)	2	50	94	0 (0)	6	6		

[RuCO(Cl)H(**L20**)] (0.5)	tBuOK (20)	2	50	0	100 (100)	-			
[RuCO(Cl)H(**L20**)] (0.5)	tBuOK (10)	2	50	0	100 (100)	-			
[RuCO(Cl)H(**L20**)] (0.5)	tBuOK (5)	2	50	2	98 (100)	-			
[RuCO(Cl)H(**L20**)] (0.5)	tBuOK (2.5)	2	50	92	8 (100)	-			
[RuCO(Cl)H(**L20**)] (0.5)	tBuOK (1.25)	2	50	99	1 (100)	-			
RuMACHO (0.5)	tBuOK (20)	2	50	0	92 (92)	8			8
RuMACHO^{iPr} (0.5)	tBuOK (20)	2	50	0	91 (91)	9			9
RuMACHO^{Cy} (0.5)	tBuOK (20)	2	50	0	91 (91)	9			9
[RuCO(Cl)H(**L21**)] (0.5)	tBuOK (20)	2	50	87	(0)	13	13		
[RuCl$_2$(SN^{H}S^{Et})PPh$_3$] (0.5)	tBuOK (20)	2	50	0	100 (100)	-			
[RuCl$_2$(SNS^{Et})PPh$_3$] (0.5)	tBuOK (20)	2	50	95	0 (0)	5	5		
[RuCl$_2$(SNS^{nBu})PPh$_3$] (0.5)	tBuOK (20)	2	50	95	0 (0)	5	5		
[RuCl$_2$(SNS^{tBu})PPh$_3$] (0.5)	tBuOK (20)	2	50	96	0 (0)	4	4		
[RuCl$_2$(SNS^{Ph})PPh$_3$] (0.5)	tBuOK (20)	2	50	95	0 (0)	5	5		
[RuCl$_2$(SNS^{nBu})(DMSO)] (0.5)	tBuOK (20)	2	50	98	0 (0)	2	2		
[RuCl$_2$(**L22**)PPh$_3$] (0.5)	tBuOK (20)	2	50	63	12 (29)	27		10	7
[Ru(CO)$_2$Cl$_2$(PPh$_3$)$_2$] (0.5)	tBuOK (20)	2	50	94	0 (0)	6	6		
[RuCl$_2$(**L1**)PPh$_3$] (0.5)	tBuOK (20)	2	50	75	4 (16)	21	1	6	7
[Ru(**L1**)$_2$]Cl$_2$ (0.5)	tBuOK (20)	2	50	71	6 (20)	24	2	8	6
[Ru(**L1**)$_2$]Cl$_2$ (0.5)	tBuOK (10)	2	50	81	3 (16)	16	3	6	
[Ru(**L1**)$_2$]Cl$_2$ (0.5)	tBuOK (5)	2	50	97	0 (0)	3	3		

[Ru(**L2**)$_2$]Cl$_2$ (0.5)	tBuOK (20)	6	50	83	3 (16)	16	7	3	2
[Ru(**L3**)$_2$]Cl$_2$ (0.5)	tBuOK (20)	2	50	92	0 (0)	8	8		
[RuCl$_2$(**L6**)$_2$] (0.5)	tBuOK (20)	2	50	44	31 (54)	26		10	5
[RuCl$_2$(**L6**)$_2$] (0.5)	NaOEt (20)	2	50	92	3 (38)	5		2	
[RuCl$_2$(**L7**)$_2$] (0.5)	tBuOK (20)	2	50	95	0 (0)	5	5		
[RuCl(**L9**)$_2$]Cl (0.5)	tBuOK (20)	2	50	32	46 (68)	22		8	5
[RuCl$_2$(**L11**)] (0.5)	tBuOK (20)	2	50	0	100	-			
[RuCl$_2$(**L11**)] (0.5)	tBuOK (5)	2	50	92	8	-			
[RuCl(**L14**)$_2$]Cl (0.5)	tBuOK (20)	2	50	73	11 (41)	16	5	5	
[RuCl(**L14**)$_2$]Cl (0.5)	tBuOK (5)	2	50	97	0 (0)	3	3		
[RuCl$_2$(**L18**)$_2$] (0.5)	tBuOK (20)	2	50	56	29 (66)	15	3	4	3

[a]Yield in the liquid phase as determined by {^{1}H}^{19}F NMR; corroborated with ^{1}H NMR against mesitylene internal standard. [b]Sum of yields <100 % as **B** produced from 2 equivalents of starting ester. Yield of **B** reported as proportion of theoretical yield. *65 mL Parr reactor.

5.4.4 General procedure for direct hydrogenation of N,N'-diacetylethylenediamine

Under an N_2 atmosphere, a 65 mL Parr reactor was charged with N,N'-diacetylethylenediamine (144 mg, 1.0 mmol), catalyst (0.5 mol%), potassium *tert*-butoxide (2.4 mg, 1.25 mmol, 1.25 mol%), and 2.0 mL 1,4-dioxane. The reactor was flushed and carefully vented three times with 3 bar N_2, then three times with 3 bar H_2. The reactor was charged with 50 bar H_2. The reactor was then sealed and transferred to a pre-heated heating block and heated at 115 °C for 20 h. After the reaction time was complete, the reactor was cooled in a water/ice bath and residual pressure was carefully vented.

5.4.4.1 Post-reaction analysis

Mesitylene standard (50 µL, 364 µmol) was added directly to the crude post-reaction mixture in air. The crude reaction mixture was homogenised with either DMSO-d6 (~2 mL) or $CDCl_3$ (~2 mL). An aliquot (~100 µL) was taken up in the NMR solvent and analysed by quantitative ^{1}H-NMR spectroscopy.

Table 5.4 - Summary of results in the direct hydrogenation of N,N'-diacetylethylenediamine.

Reaction scheme: **DAE** (1 mmol) → [Ru], tBuOK, H_2, 115 C, 1,4-dioxane (2 mL), 20h → **ED** + **AEA** + ethanol (OH)
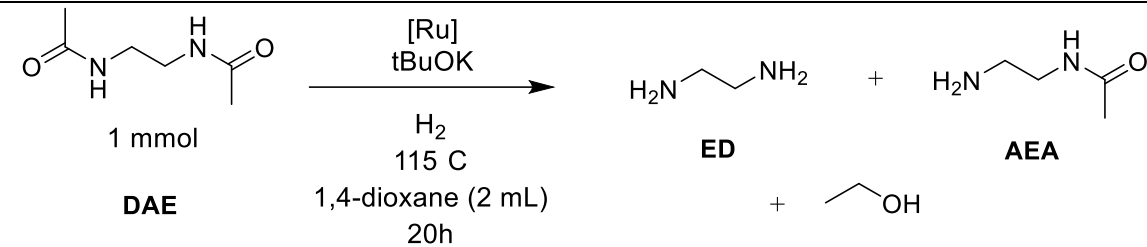
Catalyst (mol%)	Base (mol%)	Run time / h	H_2 pressure / bar	DAE conversion[a] / %	Yield[a] / %		
					AEA	ED	Ethanol[b]
-	-	20	50	3	0	0	0
[RuCO(Cl)H(**L20**)] (1)	tBuOK (2.5)	20	70	100	1	89	83
[RuCO(Cl)H(**L20**)] (1)	tBuOK (2.5)	20	50	100	5	95	71
[c][RuCO(Cl)H(**L20**)] (1)	tBuOK (2.5)	20	50	64	52	6	21
[RuCO(Cl)H(**L20**)] (0.5)	tBuOK (1.25)	20	50	98	21	70	76
[RuCO(Cl)H(**L20**)] (0.5)	tBuOK (5)	20	50	73	49	19	34
[e][RuCO(Cl)H(**L20**)] (0.5)	tBuOK (1.25)	20	40	87	49	27	37
[RuCO(Cl)H(**L20**)] (0.5)	tBuOK (1.25)	20	40	89	55	30	43
[f][RuCO(Cl)H(**L20**)] (0.5)	tBuOK (1.25)	20	50	4	0	0	0
[RuCO(Cl)H(**L20**)] (0.5)	tBuOK (1.25)	1	50	1	0	0	0

[RuCO(Cl)H(**L20**)] (0.5)	tBuOK (1.25)	2	50	4	0	0	0
[RuCO(Cl)H(**L20**)] (0.5)	tBuOK (1.25)	4	50	2	0	0	0
[RuCO(Cl)H(**L20**)] (0.5)	tBuOK (1.25)	6	50	4	0	0	0
[RuCO(Cl)H(**L20**)] (0.5)	tBuOK (1.25)	8	50	56	53	5	18
[RuCO(Cl)H(**L20**)] (0.5)	tBuOK (1.25)	12	50	94	48	44	56
[RuCO(Cl)H(**L20**)] (0.5)	tBuOK (1.25)	16	50	97	44	48	61
[g][RuCO(Cl)H(**L20**)] (0.5)	tBuOK (1.25)	6	50	51	44	100*	24
RuMACHO-BH (1)	tBuOK (2.5)	20	50	0	0	0	0
RuMACHO (1)	tBuOK (2.5)	20	50	3	0	0	0
[RuCl$_2$(PN)$_2$] (1)	tBuOK (2.5)	20	50	0	0	0	0
[RuCl$_2$(PN^{Me})$_2$] (1)	tBuOK (2.5)	20	50	0	0	0	0
[RuCO(Cl)H(**L21**)] (1)	tBuOK (2.5)	20	50	4	trace	0	3
[RuCl$_2$(SNS^{Et})PPh$_3$]	tBuOK (2.5)	20	50	1	0	0	trace

[a]Yield as determined by 1H NMR against mesitylene internal standard. [b]Ethanol conversion lower than amine products due to volatility. [c]6 mL solvent. [e]Reaction heating failure. [f]Room temperature reaction. [g]1 mmol ethylenediamine additive. ED yield includes additive; yield ED produced in reaction 0 %.

5.4.5 NMR Experiments

5.4.5.1 Reaction of [Ru(CO)Cl(H)(**L20**)] with H_2 in THF-d8

In a glovebox, [Ru(CO)Cl(H)(**L20**)] (7.2 mg, 15 μmol) was dissolved in freshly dried and degassed THF-d8 (0.75 mL). The resulting orange solution was filtered through glass filter paper into a Youngs NMR tube and sealed. Initial ^1H and $^{31}P\{^1H\}$ NMR spectroscopy was performed. The NMR tube was then placed under a H_2 atmosphere on a Schlenk line by freeze-pump-thaw; no colour change was observed. ^1H and $^{31}P\{^1H\}$ NMR spectroscopy was performed again under H_2 atmosphere.

5.4.5.2 Reaction of [Ru(CO)Cl(H)(**L20**)] with *t*BuOK and H_2 in THF-d8

In a glovebox, [Ru(CO)Cl(H)(**L20**)] (7.2 mg, 15 μmol, 1.0 equiv.) and potassium *t*-butoxide (3.4 mg, 30 μmol, 2.0 equiv.) was dissolved in freshly dried and degassed THF-d8 (0.75 mL). The resulting deep purple-black solution was filtered through glass filter paper into a Youngs NMR tube and sealed. Initial ^1H and $^{31}P\{^1H\}$ NMR spectroscopy was performed. The NMR tube was then placed under a H_2 atmosphere on a Schlenk line by freeze-pump-thaw; colour change to deep green-black solution was observed. ^1H and $^{31}P\{^1H\}$ NMR spectroscopy was performed again under H_2 atmosphere.

5.4.5.3 Reaction of [RuCl$_2$(**L11**)] with H_2 in THF-d8

In a glovebox, [RuCl$_2$(**L11**)] (11.6 mg, 15 μmol) was dissolved in freshly dried and degassed THF-d8 (0.75 mL). The resulting red solution was filtered through glass filter paper into a Youngs NMR tube and sealed. Initial ^1H and $^{31}P\{^1H\}$ NMR spectroscopy was performed. The NMR tube was then placed under a H_2 atmosphere on a Schlenk line by freeze-pump-thaw; no colour change was observed. ^1H and $^{31}P\{^1H\}$ NMR spectroscopy was performed again under H_2 atmosphere.

5.4.5.4 Reaction of [RuCl$_2$(**L11**)] with *t*BuOK and H_2 in THF-d8

In a glovebox, [RuCl$_2$(**L11**)] (11.6 mg, 15 μmol, 1.0 equiv.) and potassium *t*-butoxide (3.4 mg, 30 μmol, 2.0 equiv.) was dissolved in freshly dried and degassed THF-d8 (0.75 mL). The resulting deep green-black solution was filtered through glass filter paper into a Youngs NMR tube and sealed. Initial ^1H and $^{31}P\{^1H\}$ NMR spectroscopy was performed. The NMR tube was then placed under a H_2 atmosphere on a Schlenk line by freeze-pump-thaw; colour change to dark brown solution was observed. ^1H and $^{31}P\{^1H\}$ NMR spectroscopy was performed again under H_2 atmosphere.

5.5 Crystallographic Data

5.5.1   [RuCl$_2$(**L1**)PPh$_3$]
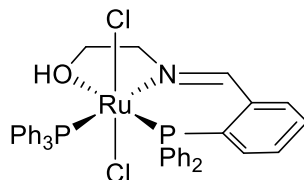
Empirical formula	C$_{43}$H$_{45}$Cl$_2$NO$_2$P$_2$Ru					
Formula weight	841.71					
Crystal system	Triclinic					
Space group	P-1					
Temperature / K	293(2)					
Cell lengths / Å	**a**	11.0169(9)	**b**	12.4651(6)	**c**	14.7974(7)
Cell angles / °	**α**	105.203(4)	**β**	96.307(5)	**γ**	94.052(5)
Volume / Å^3	1938.6(2)					
Z	2					
ρ$_{calc}$ / g cm^{-3}	1.442					
Absorption coefficient / mm^{-1}	0.663					
F(000)	868					
Crystal size / mm^3	0.520 x 0.240 x 0.180					
Radiation	Mo Kα (λ = 0.71073 Å)					
Θ range for data collection / °	3.344 to 29.810					
Index ranges	-14<=h<=14, -16<=k<=17, -17<=l<=19					
Reflections collected	17729					
Independent reflections	9186 [R$_{int}$ = 0.0585]					
Completeness to Θ = 25.242 °	99.7 %					
Data/restraints/parameters	9186 / 210 / 509					
Goodness-of-fit on F^2	1.024					
Final R indices [I > 2σ (I)]	R$_1$ = 0.0579, wR$_2$ = 0.1242					
Final R indices [all data]	R$_1$ = 0.1035, wR$_2$ = 0.1577					
Largest diff. peak and hole / e.Å^{-3}	0.780, -1.075					

5.5.2   [Ru(**L1**)$_2$]Cl$_2$
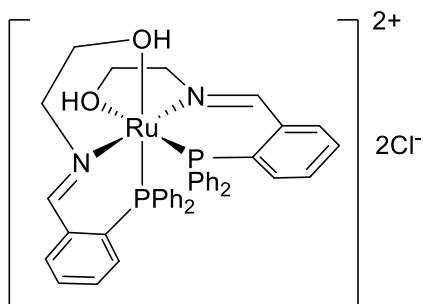
Empirical formula	C$_{46}$H$_{48}$Cl$_{10}$N$_2$O$_2$P$_2$Ru					
Formula weight	1178.37					
Crystal system	Orthorhombic					
Space group	Pcca					
Temperature / K	200(2)					
Cell lengths / Å	**a**	18.5551(3)	**b**	11.8697(2)	**c**	22.7454(3)
Cell angles / °	**α**	90	**β**	90	**γ**	90
Volume / Å^3	5009.53(13)					
Z	4					
ρ$_{calc}$ / g cm^{-3}	1.562					
Absorption coefficient / mm^{-1}	8.367					
F(000)	2392					
Crystal size / mm^3	0.150 x 0.110 x 0.040					
Radiation	Cu Kα (λ = 1.54184 Å)					
Θ range for data collection / °	3.724 to 72.813					
Index ranges	-21<=h<=22, -14<=k<=11, -23<=l<=27					
Reflections collected	17244					
Independent reflections	4933 [R$_{int}$ = 0.0316]					
Completeness to Θ = 67.684 °	100.0 %					
Data/restraints/parameters	4933 / 201 / 346					
Goodness-of-fit on F^2	1.087					
Final R indices [I > 2σ (I)]	R$_1$ = 0.0537, wR$_2$ = 0.1608					
Final R indices [all data]	R$_1$ = 0.0645, wR$_2$ = 0.1751					
Largest diff. peak and hole / e.Å^{-3}	1.017, -1.200					

5.5.3   [Ru(**L2**)₂]Cl₂
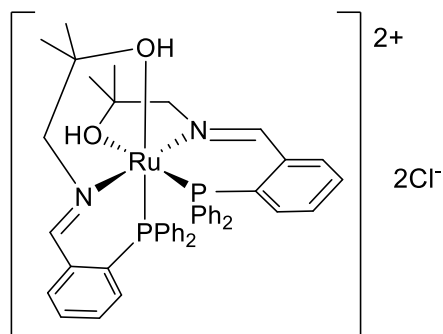
Empirical formula	C₄₉H₅₉Cl₂N₂O₄P₂Ru				
Formula weight	973.89				
Crystal system	Orthorhombic				
Space group	Fddd				
Temperature / K	293(2)				
Cell lengths / Å	**a**	18.3272(4)	**b**	25.2847(6)	**c** 43.6105(9)
Cell angles / °	**α**	90	**β**	90	**γ** 90
Volume / Å³	20209.0(8)				
Z	16				
ρ_{calc} / g cm⁻³	1.280				
Absorption coefficient / mm⁻¹	0.521				
F(000)	8112				
Crystal size / mm³	0.270 x 0.180 x 0.090				
Radiation	Mo Kα (λ = 0.71073 Å)				
Θ range for data collection / °	3.463 to 29.816				
Index ranges	-24<=h<=25, -34<=k<=33, -58<=l<=54				
Reflections collected	53675				
Independent reflections	6799 [R_{int} = 0.0363]				
Completeness to Θ = 25.242 °	99.7 %				
Data/restraints/parameters	6799 / 89 / 327				
Goodness-of-fit on F²	1.096				
Final R indices [I > 2σ (I)]	R_1 = 0.0364, wR_2 = 0.0965				
Final R indices [all data]	R_1 = 0.0511, wR_2 = 0.1093				
Largest diff. peak and hole / e.Å⁻³	0.620, -0.419				

5.5.4   [RuCl₂(**L6**)₂]
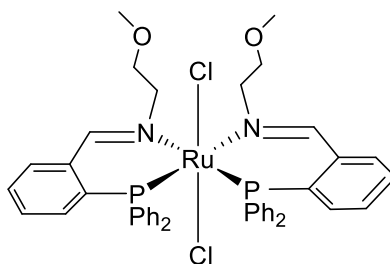
Empirical formula	$C_{45}H_{46}Cl_4N_2O_2P_2Ru$		
Formula weight	951.65		
Crystal system	Triclinic		
Space group	P-1		
Temperature / K	296(2)		
Cell lengths / Å	**a** 10.2045(4)	**b** 19.0335(6)	**c** 23.4195(10)
Cell angles / °	**α** 97.158(3)	**β** 102.301(4)	**γ** 93.616(3)
Volume / Å³	4390.8(3)		
Z	4		
ρ_{calc} / g cm⁻³	1.440		
Absorption coefficient / mm⁻¹	0.713		
F(000)	1952		
Crystal size / mm³	0.260 x 0.190 x 0.040		
Radiation	Mo Kα (λ = 0.71073 Å)		
Θ range for data collection / °	3.351 to 29.900		
Index ranges	-14<=h<=13, -23<=k<=25, -32<=l<=27		
Reflections collected	44063		
Independent reflections	21194 [R_{int} = 0.0782]		
Completeness to Θ = 25.242 °	99.7 %		
Data/restraints/parameters	21194 / 1130 / 1222		
Goodness-of-fit on F²	1.065		
Final R indices [I > 2σ (I)]	R_1 = 0.0834, wR_2 = 0.2009		
Final R indices [all data]	R_1 = 0.1348, wR_2 = 0.2442		
Largest diff. peak and hole / e.Å⁻³	1.616, -1.541		

5.5.5 [RuCl₂(L7)₂]
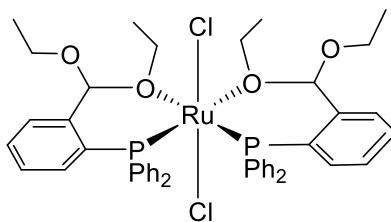
Empirical formula	$C_{46}H_{50}Cl_2O_4P_2Ru$				
Formula weight	900.77				
Crystal system	Monoclinic				
Space group	I2/a				
Temperature / K	200(2)				
Cell lengths / Å	**a** 22.3593(7)		**b** 11.3515(2)		**c** 35.4511(11)
Cell angles / °	**α** 90		**β** 107.620(3)		**γ** 90
Volume / Å³	8575.8(4)				
Z	8				
ρ_{calc} / g cm⁻³	1.395				
Absorption coefficient / mm⁻¹	0.607				
F(000)	3728				
Crystal size / mm³	0.450 x 0.180 x 0.140				
Radiation	Mo Kα (λ = 0.71073 Å)				
Θ range for data collection / °	3.499 to 29.833				
Index ranges	-30<=h<=29, -14<=k<=15, -45<=l<=42				
Reflections collected	45564				
Independent reflections	10994 [R_{int} = 0.0334]				
Completeness to Θ = 25.242 °	99.8 %				
Data/restraints/parameters	10994 / 0 / 500				
Goodness-of-fit on F²	1.089				
Final R indices [I > 2σ (I)]	R_1 = 0.0343, wR_2 = 0.0691				
Final R indices [all data]	R_1 = 0.0527, wR_2 = 0.0800				
Largest diff. peak and hole / e.Å⁻³	0.687, -0.558				

5.5.6 [Ru(CO)$_2$Cl$_2$(PPh$_3$)$_2$]
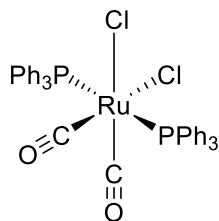
Empirical formula	C$_{38}$H$_{30}$Cl$_2$O$_2$P$_2$Ru				
Formula weight	752.53				
Crystal system	Monoclinic				
Space group	P2$_1$/n				
Temperature / K	200(2)				
Cell lengths / Å	**a** 10.40690(10)		**b** 25.6238(2)		**c** 12.55480(10)
Cell angles / °	**α** 90		**β** 100.4010(10)	**γ**	90
Volume / Å^3	3292.90(5)				
Z	4				
ρ$_{calc}$ / g cm^{-3}	1.518				
Absorption coefficient / mm^{-1}	6.533				
F(000)	1528				
Crystal size / mm^3	0.220 x 0.040 x 0.010				
Radiation	Cu Kα (λ = 1.54184 Å)				
Θ range for data collection / °	3.450 to 72.812				
Index ranges	-12<=h<=11, -31<=k<=31, -14<=l<=15				
Reflections collected	24916				
Independent reflections	6468 [R$_{int}$ = 0.0346]				
Completeness to Θ = 67.684 °	100.0 %				
Data/restraints/parameters	6468 / 0 / 406				
Goodness-of-fit on F^2	1.032				
Final R indices [I > 2σ (I)]	R$_1$ = 0.0233, wR$_2$ = 0.0524				
Final R indices [all data]	R$_1$ = 0.0295, wR$_2$ = 0.0547				
Largest diff. peak and hole / e.Å^{-3}	0.322, -0.376				

5.5.7   [Ru(CO)Cl$_2$(**L7***)PPh$_3$]
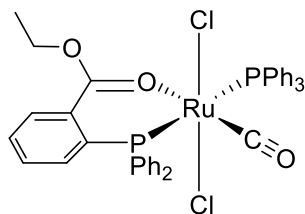
Empirical formula	C$_{40}$H$_{34}$Cl$_2$O$_3$P$_2$Ru				
Formula weight	796.58				
Crystal system	Monoclinic				
Space group	P2$_1$/n				
Temperature / K	200(2)				
Cell lengths / Å	**a**	12.05580(10)	**b**	21.0005(2)	**c** 13.9723(2)
Cell angles / °	**α**	90	**β**	95.0480(10)	**γ** 90
Volume / Å^3	3523.76(7)				
Z	4				
ρ$_{calc}$ / g cm^{-3}	1.502				
Absorption coefficient / mm^{-1}	6.161				
F(000)	1624				
Crystal size / mm^3	0.270 x 0.150 x 0.080				
Radiation	Cu Kα (λ = 1.54184 Å)				
Θ range for data collection / °	3.810 to 72.890				
Index ranges	-14<=h<=14, -25<=k<=25, -17<=l<=14				
Reflections collected	30818				
Independent reflections	6944 [R$_{int}$ = 0.0306]				
Completeness to Θ = 67.684 °	100.0 %				
Data/restraints/parameters	6944 / 0 / 434				
Goodness-of-fit on F^2	1.041				
Final R indices [I > 2σ (I)]	R$_1$ = 0.0244, wR$_2$ = 0.0588				
Final R indices [all data]	R$_1$ = 0.0305, wR$_2$ = 0.0630				
Largest diff. peak and hole / e.Å^{-3}	0.291, -0.441				

5.5.8 [RuCl(L9)₂]Cl
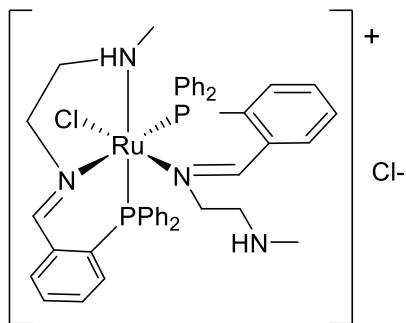
Empirical formula	$C_{45.71}H_{51.41}Cl_{6.41}N_4P_2Ru$				
Formula weight	1047.11				
Crystal system	Monoclinic				
Space group	P2₁/c				
Temperature / K	200(2)				
Cell lengths / Å	**a**	22.389(3)	**b**	12.6378(11)	**c** 19.356(3)
Cell angles / °	**α**	90	**β**	112.432(18)	**γ** 90
Volume / Å³	5062.4(13)				
Z	4				
ρ$_{calc}$ / g cm⁻³	1.374				
Absorption coefficient / mm⁻¹	6.488				
F(000)	2147				
Crystal size / mm³	0.160 x 0.040 x 0.030				
Radiation	Cu Kα (λ = 1.54184 Å)				
Θ range for data collection / °	4.099 to 75.209				
Index ranges	-27<=h<=27, -15<=k<=15, -15<=l<=23				
Reflections collected	27383				
Independent reflections	9606 [R$_{int}$ = 0.1451]				
Completeness to Θ = 67.684°	97.5 %				
Data/restraints/parameters	9606 / 21 / 545				
Goodness-of-fit on F²	1.022				
Final R indices [I > 2σ (I)]	R₁ = 0.1373, wR₂ = 0.3404				
Final R indices [all data]	R₁ = 0.2102, wR₂ = 0.4094				
Largest diff. peak and hole / e.Å⁻³	2.969, -1.242				

5.5.9 [RuCl(**L10**)(PPh$_3$^{CO})]
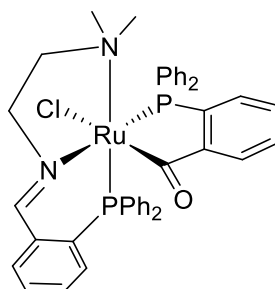
Empirical formula	C$_{44}$H$_{44}$ClN$_2$O$_{1.50}$P$_2$Ru				
Formula weight	823.27				
Crystal system	Monoclinic				
Space group	P2$_1$/c				
Temperature / K	200(2)				
Cell lengths / Å	**a** 18.0222(2)	**b** 9.86130(10)		**c** 22.5114(2)	
Cell angles / °	**α** 90	**β** 108.4150(10)		**γ** 90	
Volume / Å^3	3795.91(7)				
Z	4				
ρ$_{calc}$ / g cm^{-3}	1.441				
Absorption coefficient / mm^{-1}	5.088				
F(000)	1700				
Crystal size / mm^3	0.290 x 0.040 x 0.030				
Radiation	Cu Kα (λ = 1.54184 Å)				
Θ range for data collection / °	4.130 to 72.871				
Index ranges	-22<=h<=22, -12<=k<=11, -27<=l<=23				
Reflections collected	27792				
Independent reflections	7472 [R$_{int}$ = 0.0386]				
Completeness to Θ = 67.684 °	100.0 %				
Data/restraints/parameters	7472 / 61 / 489				
Goodness-of-fit on F^2	1.030				
Final R indices [I > 2σ (I)]	R$_1$ = 0.0286, wR$_2$ = 0.0708				
Final R indices [all data]	R$_1$ = 0.0352, wR$_2$ = 0.0754				
Largest diff. peak and hole / e.Å^{-3}	0.676 and -0.422				

5.5.10 [RuCl(**L14**)$_2$]Cl
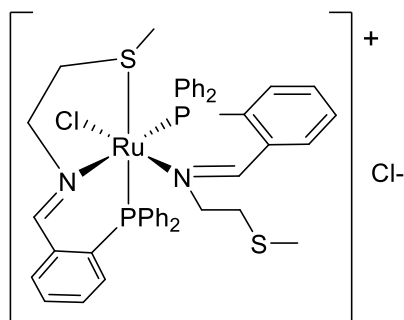
Empirical formula	C$_{46}$H$_{48}$Cl$_6$N$_2$P$_2$RuS$_2$				
Formula weight	1068.69				
Crystal system	Triclinic				
Space group	P-1				
Temperature / K	200(2)				
Cell lengths / Å	**a**	10.9056(4)	**b**	14.5979(6)	**c** 16.4130(6)
Cell angles / °	**α**	75.031(3)	**β**	86.147(3)	**γ** 88.813(3)
Volume / Å^3	2518.54(17)				
Z	2				
ρ$_{calc}$ / g cm^{-3}	1.409				
Absorption coefficient / mm^{-1}	7.080				
F(000)	1092				
Crystal size / mm^3	0.150 x 0.120 x 0.080				
Radiation	Cu Kα (λ = 1.54184 Å)				
Θ range for data collection / °	3.622 to 72.965				
Index ranges	-13<=h<=13, -14<=k<=18, -14<=l<=20				
Reflections collected	17860				
Independent reflections	9766 [R$_{int}$ = 0.0342]				
Completeness to Θ = 67.684 °	99.9 %				
Data/restraints/parameters	9766 / 75 / 563				
Goodness-of-fit on F^2	1.026				
Final R indices [I > 2σ (I)]	R$_1$ = 0.0397, wR$_2$ = 0.0998				
Final R indices [all data]	R$_1$ = 0.0491, wR$_2$ = 0.1066				
Largest diff. peak and hole / e.Å^{-3}	1.000, -0.770				

5.6 References

1   B. Holló, M. Krstić, S. P. Sovilj and K. Mészáros Szécsényi, *J Therm Anal Calorim*, 2013, **111**, 1927–1932.

2   H. Samouei and V. V. Grushin, *Organometallics*, 2013, **32**, 4440–4443.

3   J. Isai Ortega-Gaxiola, H. Valdés, E. Rufino-Felipe, R. A. Toscano and D. Morales-Morales, *Inorganica Chim Acta*, 2020, **504**, 119460.

4   A. Barandov and U. Abram, *Polyhedron*, 2009, **28**, 1155–1159.

5   M. E. Bluhm, O. Walter and M. Döring, *J Organomet Chem*, 2005, **690**, 713–721.

6   D. B. Grotjahn and H. C. Lo, *Organometallics*, 1996, **15**, 2860–2862.

7   J. A. Fuentes, S. M. Smith, M. T. Scharbert, I. Carpenter, D. B. Cordes, A. M. Z. Slawin and M. L. Clarke, *Chemistry – A European Journal*, 2015, **21**, 10851–10860.

8   C. Yang, Y. K. Cheung, J. Yao, Y. T. Wong and G. Jia, *Organometallics*, 2001, **20**, 424–429.

9   B. Tezcan, M. Kemal Yılmaz, G. Yakalı, M. Aygün and B. Güzel, *Inorganica Chim Acta*, 2022, **543**, 121155.

10   J. R. Dilworth, S. D. Howe, A. J. Hutson, J. R. Miller, J. Silver, R. M. Thompson, M. Harman and M. B. Hursthouse, *Journal of the Chemical Society, Dalton Transactions*, 1994, 3553–3562.

11   S. R. Bayly, A. R. Cowley, J. R. Dilworth and C. V. Ward, *Dalton Transactions*, 2008, 2190–2198.

12   K. Nakajima, S. Ishibashi, M. Inamo and M. Kojima, *Inorganica Chim Acta*, 2001, **325**, 36–44.

13   M. Gargir, Y. Ben-David, G. Leitus, Y. Diskin-Posner, L. J. W. Shimon and D. Milstein, *Organometallics*, 2012, **31**, 6207–6214.

14   E. Fogler,] Jai, A. Garg, P. Hu, G. Leitus, L. J. W. Shimon, D. Milstein, E. Fogler, J. A. Garg, P. Hu and D. Milstein, *Chemistry – A European Journal*, 2014, **20**, 15727–15731.

15   E. Balaraman, B. Gnanaprakasam, L. J. W. Shimon and D. Milstein, *J Am Chem Soc*, 2010, **132**, 16756–16758.

16   Z. Li, T. M. Rayder, L. Luo, J. A. Byers and C. K. Tsung, *J Am Chem Soc*, 2018, **140**, 8082–8085.

17   G. A. Filonenko, M. P. Conley, C. Copéret, M. Lutz, E. J. M. Hensen and E. A. Pidko, *ACS Catal*, 2013, **3**, 2522–2526.

18   C. Gemel, K. Folting and K. G. Caulton, *Inorg Chem*, 2000, **39**, 1593–1597.